UNIVERSITÀ DEGLI STUDI DEL MOLISE

Implementation and use of advanced constitutive models in numerical codes for the evaluation of the soil response under seismic loadings

Department of Biosciences and Territory

University of Molise

2022

Ph.D. Program in Biosciences and Territory

Thesis submitted in partial fulfillment of the requirements for the degree of

Doctor of Philosophy

SSD: ICAR/07 – GEOTECHNICS

Supervisor:

Prof. Filippo Santucci de Magistris

Coordinator:

Prof. Giovanni Fabbrocino

Candidate:

Tony Fierro

To my family

CONTENTS

ABSTRACT

The prediction of soil behaviour when seismic loads are applied is a challenging task to be achieved in Geotechnical Earthquake Engineering. However, when dynamic loadings are involved, low-to-high strain levels are reached. In this context, a key role is played by the numerical modelling, and different features are required to make it reliable: the soil should be modelled exploiting a solid constitutive framework, a widely tested software platform should be adopted, and the geometry of the problem under analysis should be correctly defined.

On these premises, the thesis focuses on the implementation and use of advanced constitutive models in an open-source numerical platform, namely OpenSees, to show their applicability to practical cases. Different scenarios mobilizing small-to-high strain levels are considered and an increasing complexity of the geometry of the problem is analyzed. Firstly, the most adopted constitutive models able to simulate granular soils behaviour under undrained conditions are reviewed; here, it emerged that SANISAND and PM4SAND only are available in OpenSees, while the NTUASand02 model has never been implemented in a finite element code to perform fully-coupled site response analysis. For this reason, the model has been added to the OpenSees framework, and the whole procedure to implement and validate the implementation is shown in detail. Drained and undrained, monotonic and cyclic, triaxial and direct simple shear tests have been performed to compare the elemental response obtained in OpenSees to that resulting from the original implementation. Furthermore, different integration schemes have been tested and the modulus reduction curve of Nevada sand has been simulated.

Then, the three constitutive models (SANISAND, PM4SAND, NTUASand02) have been tested in the simulation of the response of a 20-m thick column of Nevada sand. The comparison between the resulting responses has revealed satisfactory, especially under drained conditions and under undrained conditions at low-strain levels. When the shaking amplitude increases, soil liquefaction strongly affects the responses.

Then, two free-field centrifuge tests performed in the framework of LIQUEFACT project on Ticino Sand has been simulated. The centerline of the centrifuge box has

been modelled at the prototype scale and the soil non-linearity has been accounted for using PM4SAND. The results of the simulations highlighted that the acceleration time-series are correctly reproduced, while the excess pore water pressure time series are overestimated.

Finally, the paradigmatic case of the San Giuliano di Puglia basin is modelled exploiting the valuable computational capabilities of the single processor parallel interpreter OpenSeesSP on the DesignSafe-CI. In particular, in 2002, the Molise Earthquake caused the death of 27 children and a teacher in the newly built area of the town, while the historical core experienced limited damage. For this reason, the whole valley has been modelled in OpenSeesSP exploiting the most recent geotechnical data and the monitoring system installed in the town has been used as benchmark to validate the numerical model. The soil behaviour is modelled using the pressure-independent multi-yield constitutive model. Generally, a good agreement has been highlighted in the time domain by comparing recorded and simulated data, while the amplification factor profile is consistent to the damage distribution observed after the 2002 earthquake.

ACKNOWLEDGEMENTS

This thesis represents the culmination of a difficult path, started three years ago, and honestly, I was aware that it would have required strong efforts to me, but not so many. However, each journey gives the possibility to meet fantastic people and this is what happened to me.

First of all, I would like to express my deepest gratitude to Prof. Filippo Santucci de Magistris, my tutor and my academic father, whose support has been crucial for the finalization of the work. He gave to me his academic and human support for the whole period and broadcast me his love for research. Without his encouragement, this work would have never been possible. I would like to thank the coordinator of my Ph.D. program, Prof. Giovanni Fabbrocino: the scientific interaction with him has always been fruitful and stimulating.

Then, a great support was given to me by Dr. Maria Giovanna Durante from University of Calabria and Dr. Davide Noè Gorini from Sapienza University of Rome. Their priceless suggestions and their outstanding experience in the use of OpenSees has revealed vital for the current work.

Thanks to my collegues and friends Dr. Massimina Castiglia, Dr. Daniele Brigante and Eng. Stefano Ercolessi, who supported me in a part of this work. This interaction is the witness that real friends can be found even in the work environment.

I am grateful to Prof. Achilleas Papadimitriou (National Technical University of Athens), Prof. George Bouckovalas (National Technical University of Athens), Prof. Pedro Arduino (University of Washington, Seattle), and Dr. Alborz Ghofrani (University of Washington, Seattle): their suggestions allowed me to overcome some extremely hard moments in the development of the work.

Special thanks are due to the reviewers of this work, Prof. Adolfo Foriero (Université Laval, Quebec City) and Prof. Ferdinando Marinelli (University of Naples Federico II) for the precious pieces of advice they gave to me in order to improve the quality of the dissertation.

I would like to thank Prof. Alessandro Pagliaroli (University of Chieti-Pescara Gabriele d'Annunzio) and Dr. Giuseppe Scasserra (Italferr S.p.a.) who supported me in the early stage of the work.

Last but not least, this journey would not have been possible without the support of my family: my parents, my sister Miriana, my friends Maria and Memo, and my grandparents. A special thought goes to the angel who is watching us from Heaven: the family is always a light in the dark of the world.

LIST OF TABLES

LIST OF FIGURES

for tawny clay.

Figure C.3. Comparison between damping curves obtained by laboratory tests (blue curve; d'Onofrio et al., 2009) and by adopting the Darendeli (2001; red curve) formula for grey clay.

1 INTRODUCTION

Since the introduction of performance-based design in Earthquake Engineering, it was established that dynamic analyses (i.e., those that allow to understand both the failure modes and the extent of displacement, stress, ductility, and strain) are required for critical structures that should be designed with the target condition of minor or no damage and little or no loss of serviceability even for major earthquakes (see, for instance, PIANC, 2001). In this context, the prediction of soil behaviour under seismic loadings represents a challenging task and a major goal of Geotechnical Earthquake Engineering. The intrinsic variable nature of the imposed soil loading produces a wide range of mobilized strain levels: from low strains, when weak motions are applied, to high strains, when strong motions excite the soil and deviatoric-volumetric strain coupling takes place. In the latter case, some additional phenomena, such as soil liquefaction, could occur if the loading process involves undrained conditions and non-cohesive soils. In this case, the mathematical modelling of the granular medium response becomes more and more arduous to be conceived. For this reason, a lot of advanced constitutive models aiming at reproducing this complex stress-strain behaviour have been developed over the years, with an increasing reliability level. Bounding surface and multi-surface plasticity theories have performed successfully in this sense. Unfortunately, these models require a lot of parameters to work properly and the tests useful for the calibration procedure are not often available or difficult to be executed. On the other hand, even the description of a geotechnical problem when low strain levels are reached is non-trivial. In fact, in this case, the selection of advanced constitutive models could not be required, but the definition of the geometry and of the soil properties is extremely more relevant. Numerical modelling is vital in order to reproduce and predict soil behaviour under dynamic loadings. For valuable numerical modelling in geotechnical engineering, different aspects must be carefully evaluated: a reliable constitutive model should be chosen, well-founded soil characterization and a proper description of the geometry under analysis should be available, together with a widely consolidated software platform.

On these premises, this thesis focuses on the implementation and use of advanced constitutive models for the analysis of simple and complex geotechnical problems exploiting the OpenSees (Open System for Earthquake Engineering Simulation; McKenna, 1997) framework. OpenSees is thought to create serial and parallel finite element computer applications to simulate the response of structural and geotechnical systems under earthquake loadings. Although the framework was initially conceived for structural purposes only, its use for geotechnical applications is now increasingly widespread. Relevant studies can be found in Ramirez et al. (2018); Liu et al. (2020), Chen et al. (2021), Chen and Arduino (2021), Fasano et al. (2021), Özcebe et al. (2021), Gorini and Chisari (2022). In fact, OpenSees provides enormous capabilities in the performance of 2D and 3D fully-coupled non-linear analyses because some well-established constitutive models are implemented together with finite elements able to simulate the response of fluid saturated porous media. Despite its simulative potential, it is used mostly by researchers rather than practitioners. Since OpenSees was primarily conceived for research purposes, its use is not straightforward, as opposed to commercial codes, and the numerical modelling with this platform requires a background in both geomechanics and programming. The choice of the platform is absolutely not casual: the reliability, modularity, and flexibility of OpenSees in Earthquake Geotechnical Engineering applications want to be pointed out and its simulative potential in modelling simple problems with advanced constitutive models and complex geometries is highlighted. Last but not least, OpenSees is available at no cost for the users.

As it was mentioned before, constitutive modelling of soil behaviour represents one of the key aspects in Geotechnical Earthquake Engineering, mainly when high strain levels are reached, and when the undrained conditions are involved, precisely because some phenomena difficult to be mathematically modelled could arise. A valuable constitutive platform should satisfy both the requirements of the simplicity of implementation in numerical codes and reliability in simulating soil response. To this aim, OpenSees provides a database of constitutive models able to reproduce the response of granular soils under seismic loading in undrained conditions: in fact,

Pressure-Dependent Multi-Yield 02 (PDMY02), developed by Yang et al. (2008), SANISAND (Simple ANIsotropic SAND constitutive model) formulated by Dafalias and Manzari (2004), and the PM4SAND model conceived by Boulanger and Ziotopoulou (2017) have been already implemented and widely adopted in different studies. It is worth noticing that the reliability of a software platform can be dramatically increased by the addition of other constitutive models able to catch particular features of the soil behaviour.

Consequently, in this thesis, the procedure followed to implement a new advanced constitutive model in OpenSees, capable to describe the response of sands under cyclic loadings in undrained conditions, to enrich the previous database, is described. The selected model has been proposed by Papadimitriou and Bouckovalas (2002). In the following, the model will be referred as NTUASand02 in order to distinguish it from its modified version developed by Andrianopoulos et al. (2010) that, however, has a vanishing elastic region implemented. In fact, even if the model has been developed earlier if compared to the other constitutive frameworks available in OpenSees, it provides some remarkable features in the simulation of the response of granular soils at small shear strain levels allowing a non-linear hysteretic formulation for the strain rate of elastic states and in the modelling the fabric evolution macroscopically exploiting a scalar index. The model has been selected because this native version has never been adopted in finite element (FE) codes for the simulation of fully-coupled boundary value problems. In addition, the version modified by Andrianopoulos et al. (2010) has been proven able to simulate the uplift response of pipelines induced by soil liquefaction (see Marinatou et al., 2017).

To this aim, in the introductory Chapter 2, a brief description of the cornerstones of the plasticity theory is reported, followed by the analysis of the bounding surface plasticity theory on which framework the constitutive model proposed by Papadimitriou and Bouckovalas (2002) is developed. Then, the latter is illustrated together with the ones that are based on the bounding surface theory and are already available in OpenSees, namely SANISAND and PM4SAND. This choice was made because the use of

bounding surface constitutive models in OpenSees is less common if compared to the multi-surface approach (e.g., the one adopted for the development of other models available in OpenSees, like PDMY02).

Chapter 3 is mainly devoted to the Papadimitriou and Bouckovalas (2002) constitutive model. There, it is shown and described in detail the procedure adopted to implement the model in the OpenSees environment. Firstly, a brief introduction of the platform is provided, then the chapter focuses on the general approach required to add a new advanced soil material. The second part of the chapter deals with the specific functions implemented for the addition of NTUASand02 in both plane-strain and tri-dimensional conditions to the framework together with some details related to the integration schemes considered and to the elasto-plastic stiffness matrix, required to obtain the constitutive response.

The reliability of the implementation is evaluated in terms of elemental response and through the simulations of boundary value problems, site response of a soil column in this case. For this reason, Chapter 4 shows the results of some simple simulations obtained in OpenSees at the element level. The comparison between the response provided by the current implementation and the simulations available in the original paper, where the constitutive model is presented, together with results obtained from real tests are shown and critically discussed. In particular, drained and undrained cyclic simple shear tests and triaxial tests are reproduced to evaluate the reliability of the implementation and to detect eventual bugs in the code. Furthermore, this approach aims at evaluating the ability of both the model and the numerical framework to reliably predict the elemental behaviour of sands in cyclic conditions. However, even if the model is conceived to reproduce soil behaviour under dynamic loadings, it should be able to simulate the response under monotonic loadings as well. For this reason, monotonic undrained and drained triaxial tests have been performed. At the end, a key aspect to successfully predict soil behaviour under dynamic loadings is represented by the reproduction of modulus reduction curves. Consequently, the chapter ends with cyclic triaxial tests exploited to obtain the shear modulus decay curve of Nevada Sand.

Then, Chapter 5 represents a step further in terms of the degree of complexity of the analyzed problem. In fact, here, the seismic response of a 20 m homogeneous soil column of Nevada sand is taken into account and the two additional bounding surface constitutive models previously identified are considered to model soil beahviour (PM4SAND and SANISAND). In particular, the choice of Nevada sand is justified to avoid the introduction of any bias due to the calibration procedure and, as a consequence, calibrations available in the literature for the constitutive parameters are considered. Furthermore, it is interesting to understand how these parameters perform in site response analysis. On this basis, the constitutive parameters have been slightly modified to fit the initial conditions along with the soil profile. The chapter continues with a detail of the model of the column. The inputs to which the column has been subjected at the base are selected considering moderate PGA (about 0.1g) and a strong motion (0.345g), in order to investigate the performance of the Papadimitriou and Bouckovalas (2002) model under such conditions and to compare its response with the one provided by SANISAND and PM4SAND. Then, the philosophy followed in Chapter 4 has been adopted, performing analyses in both drained and undrained conditions.

The practical use of a reliable constitutive platform should be always oriented towards the simulation and reproduction of real problems. For this reason, the remaining part of the thesis is focused on the analysis of two classes of real problems in both controlled and in-situ conditions. In fact, Chapter 6 shows the implementation of free-field centrifuge tests performed in the framework of the LIQUEFACT project considering the site response of a soil column of Ticino sand. In the tests, different input motions aiming at inducing liquefaction have been applied to the centrifuge box. For this reason, considering free-field conditions, the centerline of the centrifuge box has been modelled using a soil column. Two input motions are considered in the simulations, and the soil response is modelled exploiting PM4SAND, which has been calibrated in previous studies for Ticino sand.

However, it could emerge that the constitutive behaviour of soils is the only crucial aspect to be carefully taken into account for in numerical simulations of real problems. This is absolutely not true. In fact, sometimes, when analyzing the real response of soil under seismic loadings, the selection of an advanced constitutive model could not be necessary, while the definition of the numerical model in the software framework together with the assignment and evaluation of the soil properties together with the realistic definition of initial conditions can reach more relevance. This generally happens when weak motions are considered, and the mobilized strain level is low. For this reason, in Chapter 7, the complex case-study of San Giuliano di Puglia has been implemented and analyzed in OpenSees. San Giuliano di Puglia experienced the collapse of an elementary school with the death of a teacher and 27 students in 2002 Molise Earthquake, and a very peculiar damage distribution was observed. In fact, the newly built area in the town was subjected to significant structural collapses, while limited damage took place in the historical core of the town. This was probably due to site effects. However, even if a large number of tests was available, the numerical model in terms of buried geometry and soil properties has been continuously re-evaluated, even on the basis of recordings deriving from the accelerometric network installed in the town. For this reason, in this study, it is very challenging to understand whether the previous findings have been confirmed, exploiting the numerical capabilities of OpenSees. Being the bi-dimensional model of the San Giuliano basin widely extended, High Performance Computing (HPC) resources are needed to analyze the model in reasonable computational time. To this aim, the parallel module of OpenSees (OpenSeesSP that stands for Single Parallel OpenSees Interpreter), implemented on the DesignSafe Cyber-Infrastructure (DesignSafe-CI), hosted at the Texas Advanced Computing Center (TACC), has been exploited. The soil has been modelled using the advanced multi-surface pressure-independent multi-yield constitutive framework and the eventual mobilization of non-linearity is critically investigated. Firstly, a background of the case-study is proposed, then, the soil properties of the different units are described together with the monitoring system installed in the town. Furthermore, a brief description of the equivalent linear analyses

performed at the site is provided and, finally, the nonlinear site response analyses are detailed, by keeping an eye on the implementation of the large numerical model of the valley and on the parameters assigned to the selected constitutive model. The chapter concludes through the explanation of some details on the resulting amplification and discussing the comparison with the linear elastic approach. The performance of the model is critically discussed.

At the end of the thesis, the conclusions of this study are summarised without neglecting some guidelines for further development of the research.

1.1 REFERENCES

Andrianopoulos K. I., Papadimitriou A. G., and Bouckovalas G. D. (2010). Bounding surface plasticity model for the seismic liquefaction analysis of geostructures. Soil Dynamics and Earthquake Engineering, 30(10): 895-911.

Chen L., Ghofrani A., and Arduino P. (2021). Remarks on numerical simulation of the LEAP-Asia-2019 centrifuge tests. Soil Dynamics and Earthquake Engineering, 2021, 142, 106541.

Chen L. and Arduino P. (2021). Implementation, verification and validation of the PM4SAND model in OpenSees. PEER Report No. 2021/02. Pacific Earthquake Engineering Research Center Headquarters, University of California, Berkeley, March 2021.

Dafalias Y.F. and Manzari M.T. (2004). Simple plasticity sand model accounting for fabric change effects, Journal of Engineering Mechanics 2004.

Fasano G., Nappa V., Özcebe A.G. and Bilotta E. (2021). Numerical modelling of the effect of horizontal drains in centrifuge tests on soil-structure interaction in liquefiable soils. Bulletin of Earthquake Engineering (2021) 19:3895–3931 https://doi.org/10.1007/s10518-021-01084-2.

Gorini D.N. and Chisari C. (2022). Impact of soil-structure interaction on the effectiveness of tuned mass dampers. Earthquake Engineering and Structural Dynamics, 2022.

Liu, H., Diambra, A., Abell J.A. and Pisanò, F. (2020). Memory-enhanced plasticity modeling of sand behaviour under undrained cyclic loading. J. Geotech. Geoenviron. Eng., 2020, 146(11): 04020122.

Marinatou S. M., Zontanou V. A., Chaloulos Y.K., and Bouckovalas G. D. (2017). Liquefaction induced uplift of pipelines: numerical modeling and parametric analyses. in Proceedings of the 3rd International Conference of Performance-Based Design in Earthquake Geotechnical Engineering, M. Taiebat, D. Wijewickreme, A. Athanasopoulos-Zekkos, and R. W. Boulanger, Eds., ,Vancouver, BC, USA, July 2017

McKenna F. (1997). Object-oriented finite element analysis: Frameworks for analysis, algorithms and parallel computing. Ph.D. dissertation, Univ. of California, Berkeley, CA.

Özcebe, A.G., Giretti, D., Bozzoni, F., Fioravante V. and Lai C.G. (2021). Centrifuge and numerical modelling of earthquake-induced soil liquefaction under free-field conditions and by considering soil–structure interaction. Bull. Earthquake Eng. 19, 47–75 https://doi.org/10.1007/s10518-020-00972-3.

Papadimitriou A. G. and Bouckovalas G. D. (2002). Plasticity model for sand under small and large cyclic strains: a multiaxial formulation, Soil Dynamics and Earthquake Engineering, 22: 191-204.

PIANC (2001). Seismic Design Guidelines for Port Structures. Working Group no. 34 of the Maritime Navigation Commission, International Navigation Association, 474 pp., Balkema, Lisse.

Ramirez J., Barrero R.A., Chen L., Dashti S., Ghofrani A., Taiebat M. and Arduino P. (2018). Site response in a layered liquefiable deposit: evaluation of different numerical tools and methodologies with centrifuge experimental results. J Geotech Geoenviron ASCE 2018;144(10) https://doi.org/10.1061/(ASCE)GT.1943-5606.0001947.

Yang, Z., Lu J. & Elgamal, A. 2008. OpenSees Soil Models and Solid-Fluid Fully Coupled Elements. User's Manual. v1.0. Department of Structural Engineering, University of California, San Diego.

1. INTRODUCTION

Ziotopoulou K. and Boulanger R.W. (2013). Numerical modeling issues in predicting postliquefaction reconsolidation strains and settlements. 10th International Conference on Urban Earthquake Engineering, March 1-2, Tokyo Institute of Technology, Tokyo, Japan, 469-475.

2 CONSTITUTIVE MODELING FOR SOIL LIQUEFACTION

2.1 INTRODUCTION

The reliable computational prediction of the response of soil subjected to dynamic excitation represents a key goal to be achieved in Geotechnical Earthquake Engineering. However, when sandy soils are involved together with undrained conditions, the numerical simulation of the problem widely increases its complexity. In fact, some additional aspects, peculiar to non-cohesive soils, such as soil liquefaction, need to be properly modelled in order to guarantee a reliable reproduction of the analyzed problem. Soil liquefaction is probably one of the most arduous and demanding physical phenomena to be modelled in Geotechnical Earthquake Engineering. This is due to the complexity of the phenomenon itself that renders it difficult to be mathematically conceived as well. In fact, even if largely investigated, it still represents a controversial topic.

The term liquefaction was firstly adopted by Terzaghi and Peck (1948) to refer to an abrupt change of loose sand into flows similar to those that take place in viscous fluids, triggered by a slight disturbance (Ishihara, 1993), and it was definitely coined by Mogami and Kubo (1953) with reference to earthquake loadings to indicate phenomena involving soil deformations induced by monotonic, transient, or repeated disturbance of saturated cohesionless soils under undrained conditions (Kramer, 1996). With the advent of increasingly capable numerical tools, the simulation of liquefaction-related phenomena is going to improve its reliability.

The following chapter aims at describing some advanced constitutive models widely adopted in the current practice to simulate the response of liquefiable soils subjected to dynamic excitations.

It is well-established that classical elastic perfectly-plastic models have been revealed to be able in the modelling of soil behaviour under monotonic loading, while they are not suitable to describe some basic phenomena related to the cyclic and dynamic excitations, including the mobilization of high plastic-strain levels in non-cohesive soils, such as liquefaction co-seismic effects (i.e., flow liquefaction or cyclic mobility). For this reason, a lot of constitutive frameworks were built specifically to fulfill this goal and to model the response of soils subjected to different initial conditions through a single set of parameters. The latter represents a challenging achievement because, if satisfied, it makes a constitutive model extremely versatile. However, these models should be oriented towards their use in numerical codes with a view to simulating liquefaction-related phenomena. For this reason, a balance between the analytical complexity of the formulations and the ease of implementation in numerical tools needs to be reached.

On the basis of the above-mentioned considerations, in this chapter, an overview of three largely adopted constitutive models based on the bounding surface concept is reported, starting from the analytical cornerstones of the plasticity theory up to a detailed description of each framework. The choice of the models is justified by their simulative capabilities, their effectiveness in reliably reproducing liquefiable sands behaviour and the relatively simple efforts required for the implementation in numerical codes, if compared to other constitutive platforms. Furthermore, on the basis of the analyzed literature, all of them have been revealed able to simulate boundary value problems involving liquefiable soils.

More specifically, in §2.2, the most relevant milestones on which plasticity theory is based are enumerated, in §2.3 some basic principles of the bounding surface theory are described, while in §2.4, the selected constitutive models are analyzed in detail.

2.2 BASIC ASPECTS OF THE PLASTICITY THEORY

In the following, for the sake of clarity, a brief review of the plasticity theory and a summary of the literature which brought to the formulation of advanced constitutive

models is reported. It is worth noting that tensors are written in bold. The general plasticity theory is described in a wide number of works, such as Lubliner (1990), Simo and Hughes (1987) and Jirasek and Bazant (2002), among others, while its application to geomechanics is reported in Vermeer and de Borst (1984), Zienkiewicz et al. (1999), Potts and Zdravkovic (1999), Wood (2004), and Yu (2006). Considering the aspects shown in the following, the interested reader can refer, among others, to Potts and Zdravkovic (1999), Wood (2004) and Yu (2006) for further and more detailed information.

2.2.1 BASIC STRESS AND STRAIN TERMS

Stress and strain tensors adopted for the models are reported in the following equations.

Stresses are effective by default and the prime symbol was removed. The superscripts e and p refer to elastic and plastic components of strain, respectively, while the general stress and strain tensors are expressed in the (x,y,z) space by σ_{ij} and ε_{ij}. The terms referred as σ_1, σ_2 and σ_3 indicate principal stresses. The basic stress tensors are reported in (2.1)-(2.4):

Stress tensor $\boldsymbol{\sigma}$:

$$\boldsymbol{\sigma} = \begin{bmatrix} \sigma_{xx} & \sigma_{xy} & \sigma_{xz} \\ \sigma_{yx} & \sigma_{yy} & \sigma_{yz} \\ \sigma_{zx} & \sigma_{zy} & \sigma_{zz} \end{bmatrix} \tag{2.1}$$

with mean stress p indicated as (2.2)

$$p = \frac{\sigma_{xx} + \sigma_{yy} + \sigma_{zz}}{3} \tag{2.2}$$

Deviatoric stress tensor $\mathbf{s}$:

$$\mathbf{s} = \boldsymbol{\sigma} - p\mathbf{I} = \begin{bmatrix} s_{xx} & s_{xy} & s_{xz} \\ s_{yx} & s_{yy} & s_{yz} \\ s_{zx} & s_{zy} & s_{zz} \end{bmatrix} = \begin{bmatrix} \sigma_{xx} - p & \sigma_{xy} & \sigma_{xz} \\ \sigma_{yx} & \sigma_{yy} - p & \sigma_{yz} \\ \sigma_{zx} & \sigma_{zy} & \sigma_{zz} - p \end{bmatrix} \tag{2.3}$$

Deviatoric stress ratio tensor **r**:

$$\mathbf{r} = \frac{\mathbf{s}}{p} = \begin{bmatrix} r_{xx} & r_{xy} & r_{xz} \\ r_{yx} & r_{yy} & r_{yz} \\ r_{zx} & r_{zy} & r_{zz} \end{bmatrix} = \begin{bmatrix} \frac{\sigma_{xx} - p}{p} & \frac{\sigma_{xy}}{p} & \frac{\sigma_{xz}}{p} \\ \frac{\sigma_{yx}}{p} & \frac{\sigma_{yy} - p}{p} & \frac{\sigma_{yz}}{p} \\ \frac{\sigma_{zx}}{p} & \frac{\sigma_{zy}}{p} & \frac{\sigma_{zz} - p}{p} \end{bmatrix} \tag{2.4}$$

where $\boldsymbol{\sigma}$, **s** and **r** are symmetric tensors.

The basic strain tensors are defined in (2.5)-(2.7):

Strain tensor $\boldsymbol{\varepsilon}$:

$$\boldsymbol{\varepsilon} = \begin{bmatrix} \varepsilon_{xx} & \varepsilon_{xy} & \varepsilon_{xz} \\ \varepsilon_{yx} & \varepsilon_{yy} & \varepsilon_{yz} \\ \varepsilon_{zx} & \varepsilon_{zy} & \varepsilon_{zz} \end{bmatrix} \tag{2.5}$$

with volumetric strain referred as (2.6):

$$\varepsilon_v = \mathrm{tr}(\boldsymbol{\varepsilon}) = \varepsilon_{xx} + \varepsilon_{yy} + \varepsilon_{zz} \tag{2.6}$$

Deviatoric strain tensor:

$$\mathbf{e} = \boldsymbol{\varepsilon} - \frac{\varepsilon_v}{3}\mathbf{I} = \begin{bmatrix} e_{xx} & e_{xy} & e_{xz} \\ e_{yx} & e_{yy} & e_{yz} \\ e_{zx} & e_{zy} & e_{zz} \end{bmatrix} = \begin{bmatrix} \varepsilon_{xx} - \frac{\varepsilon_v}{3} & \varepsilon_{xy} & \varepsilon_{xz} \\ \varepsilon_{yx} & \varepsilon_{yy} - \frac{\varepsilon_v}{3} & \varepsilon_{yz} \\ \varepsilon_{zx} & \varepsilon_{zy} & \varepsilon_{zz} - \frac{\varepsilon_v}{3} \end{bmatrix} \tag{2.7}$$

Note that in the following, the colon symbol : indicates the inner product of two tensors, i.e., the trace of their product. In particular, if **a** and **b** are two tensors, it yields $\mathbf{a}:\mathbf{b} = \mathrm{tr}(\mathbf{a}\cdot\mathbf{b}) = a_{ij}b_{ji}$. In addition, the symbol <> denotes the Maculey brackets and if x is a scalar, $\langle x \rangle = (x + |x|)/2$.

2.2.2 PLASTICITY THEORY

With a view to effectively describing the key aspects of the soil behaviour, also under monotonic loadings, the elastic models require the integration with the plasticity theory (Hill, 1950; Prager, 1955, Naghdi,1960), which, in turn, is based on the following assumptions:

1. Coincidence between incremental plastic strain and accumulated stress principal directions;
2. Existence of a yield function dependent on both stress state $\boldsymbol{\sigma}$ and state parameters $\mathbf{k}$, describing hardening or softening, defined as in (2.8):

$$\mathrm{f}(\boldsymbol{\sigma}, \mathbf{k}) = 0 \tag{2.8}$$

The latter must be convex and separates the purely elastic stress states, where $\mathrm{f}(\boldsymbol{\sigma}, \mathbf{k}) < 0$, from the elasto-plastic stress states $\mathrm{f}(\boldsymbol{\sigma}, \mathbf{k}) = 0$. In this case, the stress state is located on the yield surface and the consistency condition needs to be guaranteed (Prager, 1949) as it is expressed in (2.9):

$$\mathrm{df}(\boldsymbol{\sigma}, \mathbf{k}) = \frac{\partial \mathrm{f}(\boldsymbol{\sigma}, \mathbf{k})}{\partial \boldsymbol{\sigma}} \mathrm{d}\boldsymbol{\sigma} + \frac{\partial \mathrm{f}(\boldsymbol{\sigma}, \mathbf{k})}{\partial \mathbf{k}} \mathrm{d}\mathbf{k} = 0 \tag{2.9}$$

For the present applications, please note that all the stress quantities are effective. The condition $\mathrm{f}(\boldsymbol{\sigma}, \mathbf{k}) > 0$ is related to non-physical states, so it cannot be admittable. Consequently, the outward normal unit tensor to the yield surface can be expressed as in (2.10):

$$\mathbf{n} = \frac{\dfrac{\partial \mathrm{f}(\boldsymbol{\sigma}, \mathbf{k})}{\partial \boldsymbol{\sigma}}}{\left\| \dfrac{\partial \mathrm{f}(\boldsymbol{\sigma}, \mathbf{k})}{\partial \boldsymbol{\sigma}} \right\|} \tag{2.10}$$

where the denominator indicates the norm of $\frac{\partial \mathrm{f}(\boldsymbol{\sigma}, \mathbf{k})}{\partial \boldsymbol{\sigma}}$.

3. The additive decomposition of strain increments, which can be switched into an elastic and a plastic term, is valid (2.11):

$$\mathrm{d}\boldsymbol{\varepsilon} = \mathrm{d}\boldsymbol{\varepsilon}^{\mathbf{e}} + \mathrm{d}\boldsymbol{\varepsilon}^{\mathbf{p}} \tag{2.11}$$

In (2.11), $\mathrm{d}\boldsymbol{\varepsilon}$, $\mathrm{d}\boldsymbol{\varepsilon}^{\mathbf{e}}$ and $\mathrm{d}\boldsymbol{\varepsilon}^{\mathbf{p}}$ are the total strain, elastic strain and plastic strain tensors increments, respectively. Furthermore, the additive decomposition of strains (cf. (2.11)) can be written in incremental form by switching the total strain increment into a volumetric term (see (2.12)) and a deviatoric term (2.13):

$$\mathrm{d}\varepsilon_{\mathrm{v}} = \mathrm{d}\varepsilon_{\mathbf{v}}^{\mathrm{e}} + \mathrm{d}\varepsilon_{\mathbf{v}}^{\mathrm{p}} \tag{2.12}$$

$$\mathrm{d}\mathbf{e} = \mathrm{d}\mathbf{e}^{\mathrm{e}} + \mathrm{d}\mathbf{e}^{\mathrm{p}} \tag{2.13}$$

Then, the stress rate can be expressed in terms of strain increment through the following hypoelastic relationship (2.14):

$$\mathrm{d}\boldsymbol{\sigma} = \mathbf{D}^{\mathrm{e}}(\boldsymbol{\sigma})\mathrm{d}\boldsymbol{\varepsilon}^{\mathbf{e}} = \mathbf{D}^{\mathrm{e}}(\boldsymbol{\sigma})[\mathrm{d}\boldsymbol{\varepsilon} - \mathrm{d}\boldsymbol{\varepsilon}^{\mathrm{p}}] \tag{2.14}$$

In (2.14), $\mathbf{D}^{\mathrm{e}}(\boldsymbol{\sigma})$ is the fourth order elastic tangent stiffness tensor and it depends on the current stress.

4. Existence of a flow rule. The former describes the plastic strain evolution and can be expressed by the following (2.15):

$$\mathrm{d}\boldsymbol{\varepsilon}^{\mathbf{p}} = \Lambda \frac{\partial \mathrm{g}(\boldsymbol{\sigma}, \mathbf{k})}{\partial \boldsymbol{\sigma}} \tag{2.15}$$

where $\mathrm{g}(\boldsymbol{\sigma}, \mathbf{k})$ represents the plastic potential function, Λ is a scalar value called plastic multiplier and $\mathbf{k}$ indicates the state variables vector, as in (2.8). The plastic multiplier determines the plastic strain increment modulus, while $\frac{\partial \mathrm{g}(\boldsymbol{\sigma},\mathbf{k})}{\partial \boldsymbol{\sigma}}$ is the outward normal vector to the plastic potential surface and defines its components.

Then, the outward normal unit tensor to the plastic potential function $\mathbf{n}_g$ can be expressed as in (2.16):

$$\mathbf{n}_g = \frac{\frac{\partial g(\boldsymbol{\sigma}, \mathbf{k})}{\partial \boldsymbol{\sigma}}}{\left\| \frac{\partial g(\boldsymbol{\sigma}, \mathbf{k})}{\partial \boldsymbol{\sigma}} \right\|} \tag{2.16}$$

Note that the state parameters are constant for perfect plasticity, while they vary with the plastic strain otherwise.

It is worth noting that some simplifying assumptions can be considered, such as associate flow hypothesis that stems from the condition $f(\boldsymbol{\sigma}, \mathbf{k}) = g(\boldsymbol{\sigma}, \mathbf{k})$. This assumption practically means a coincidence between yield surface and plastic potential functions. On the contrary, the flow is said to be non-associated.

5. Existence of a hardening rule, which describes the evolution of the state parameters, and, consequently, of the yield surface as a function of the plastic strain increments. The hardening law can be expressed as (2.17):

$$d\mathbf{k}(\boldsymbol{\sigma}, \mathbf{k}) = \Lambda \mathbf{h}(\boldsymbol{\sigma}, \mathbf{k}) \tag{2.17}$$

and $\mathbf{h}(\boldsymbol{\sigma}, \mathbf{k})$ depends on the current stress and state parameters.

From a mathematical point of view, the hardening law practically describes the evolution of the yield surface that can translate and/or expand. It defines the post-yielding behaviour of the constitutive model. Consequently, the hardening can be either isotropic or kinematic. The kinematic hardening (or softening) takes place when a translation of the hardening surface in the stress space occurs and any variation of its dimension or shape is forbidden, while the isotropic hardening (or softening) takes place when the yield surface expands (or contracts) without translating and keeping its shape, its center and its normal unit vectors. When both these behaviours take place, the model is said to exhibit mixed hardening. All the models considered in this study provide a kinematic

hardening rule. The kinematic hardening was first proposed by Prager (1955), which developed the first simple kinematic hardening rule. To this aim, the yield surface can be described as in (2.18):

$$f(\boldsymbol{\sigma} - \boldsymbol{\alpha}, \mathbf{k}) = m \tag{2.18}$$

where $\boldsymbol{\alpha}$ is the anisotropy back-stress tensor that expresses the evolution of the center of the yield surface and m is a material constant representing its size, which remains unchanged.

With reference to the plastic multiplier Λ, it must satisfy the so-called Kuhn-Tucker conditions enumerated in (2.19):

$$\Lambda \geq 0; \qquad f(\boldsymbol{\sigma}, \mathbf{k}) \leq 0; \qquad \Lambda f(\boldsymbol{\sigma}, \mathbf{k}) = 0 \tag{2.19}$$

This means that plastic strain can take place only when the current stress state is on the yield surface. The concept expressed in (2.19) is reflected in the fact that the plastic multiplier is equal to zero for elastic states while, if the yield function reaches zero (i.e., the stress state is on the yield surface), the plastic multiplier is activated, triggering in this way the development of plastic strain (cf. (2.15)). The basic assumptions of the plasticity theory are graphically shown in Figure 2.1.

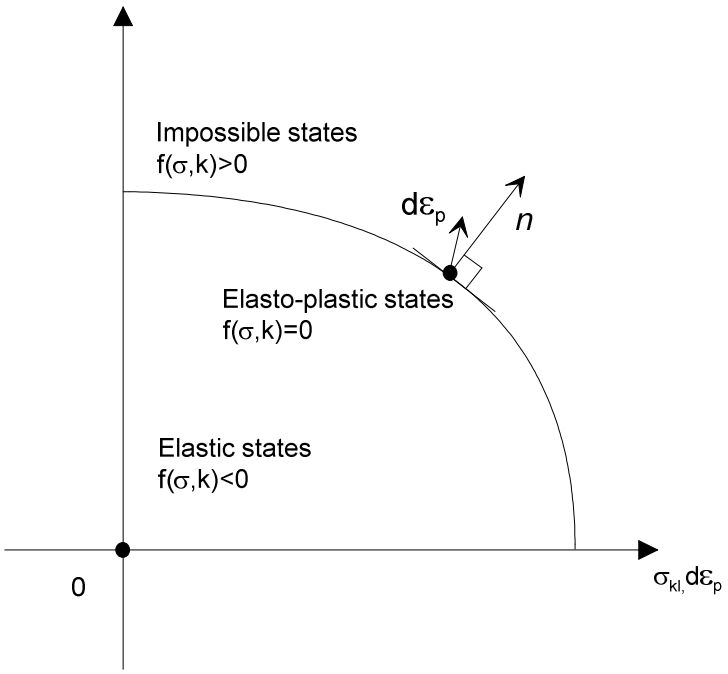

Figure 2.1. Basic assumptions of the plasticity theory.

By applying the consistency condition in (2.9), together with the expression of stress increments (2.14) and the flow rule (2.15), the plastic multiplier can be expressed as (2.20):

$$\Lambda = \frac{\frac{\partial \mathbf{f}(\boldsymbol{\sigma}, \mathbf{k})}{\partial \boldsymbol{\sigma}} \mathbf{D}^{e} \, d\boldsymbol{\varepsilon}}{\frac{\partial \mathbf{f}(\boldsymbol{\sigma}, \mathbf{k})}{\partial \boldsymbol{\sigma}} \mathbf{D}^{e} \frac{\partial \mathbf{g}(\boldsymbol{\sigma}, \mathbf{k})}{\partial \boldsymbol{\sigma}} + K_{p}} \tag{2.20}$$

K_p is called plastic modulus and in terms of internal variables, by applying consistency condition, is expressed in (2.21):

$$K_{p} = -\frac{1}{\Lambda} \frac{\partial f(\boldsymbol{\sigma}, \mathbf{k})}{\partial \mathbf{k}} d\mathbf{k} \tag{2.21}$$

By substituting the expression of the plastic multiplier into (2.14), the so-called elasto-plastic stiffness matrix, that is a fourth order tensor, can be defined as (2.22):

$$\mathbf{D}^{ep} = \mathbf{D}^{e} - \frac{\left(\mathbf{D}^{e}\frac{\partial \mathbf{g}(\boldsymbol{\sigma},\mathbf{k})}{\partial \boldsymbol{\sigma}}\right)\left(\frac{\partial \mathbf{f}(\boldsymbol{\sigma},\mathbf{k})}{\partial \boldsymbol{\sigma}}\mathbf{D}^{e}\right)}{\frac{\partial \mathbf{f}(\boldsymbol{\sigma},\mathbf{k})}{\partial \boldsymbol{\sigma}}\mathbf{D}^{e}\frac{\partial \mathbf{g}(\boldsymbol{\sigma},\mathbf{k})}{\partial \boldsymbol{\sigma}} + \mathrm{K_p}} \tag{2.22}$$

The evaluation of the elasto-plastic stiffness matrix is crucial in the implementation of constitutive models in numerical codes, so further details are provided in §3.

The plasticity theory assumes a drastic separation between elastic and elasto-plastic states. However, for soils, it is observed that irreversible strains can arise also for low stress levels, especially in case of cyclic excitations. Consequently, the soil non-linearity takes place even for low stress level. In this sense, the development of excess pore water pressure in undrained conditions plays a key role. For the above-mentioned reasons, the classical elasto-plasticity is not suitable to reproduce the main features of the soil response under cyclic loadings.

In order to successfully reproduce these aspects, the latter must be integrated with additional concepts, such as bounding surface theory and critical state of soil mechanics (CSSM).

2.3 BOUNDING SURFACE PLASTICITY THEORY

With the adoption of a single yield surface, the comparison between numerical and experimental results shows a wider elastic domain compared to that obtained from lab tests (Yu, 2006). For this reason, to overcome this limitation, one of the most widespread approaches is represented by the bounding surface theory (Dafalias and Popov, 1976; Krieg, 1975; Dafalias, 1986). The presentation of the concept is detailed in Dafalias and Popov (1976), while the mathematical description of the problem is reported in Dafalias (1986). However, different authors worked on this theoretical framework (see Prevost, 1997; 1986; Mroz et al., 1978; 1981; Hashiguchi, 1985; 1988; Al-Tabbaa and Wood, 1989; Gajo and Wood, 1999; Rouainia and Wood, 2000).

The starting hypothesis of this approach states that considering a stress state inside or on the bounding surface, a mapping rule will associate an "image" stress state $\boldsymbol{\sigma}^{\mathbf{b}}$ on

the bounding surface and the distance between the above-mentioned stress states is a measure of the plastic response of the system. More specifically, the theory assumes that the post-yielding behaviour, in terms of plastic modulus, is connected to the distance between the current stress state and the "image" stress state on the bounding surface. More the latter is high more the material behaves as stiff (Yu, 2006). The bounding surface divides the physical states from impossible states, but some modifications have been made on this point, allowing the bounding surface to be momentarily crossed (see Andrianopoulos et al., 2010).

A bounding surface is defined similarly to a yield surface, as follows ((2.23); cf. Potts and Zdravkovic, 1999):

$$f\left(\boldsymbol{\sigma}^{\mathbf{b}}, \mathbf{k}\right) = 0 \tag{2.23}$$

A plastic potential, a plastic modulus and a hardening law are defined for the bounding surface. A unit tensor $\mathbf{n_L}$ representing the loading direction can be defined. The above-mentioned quantities are reported in Figure 2.2.

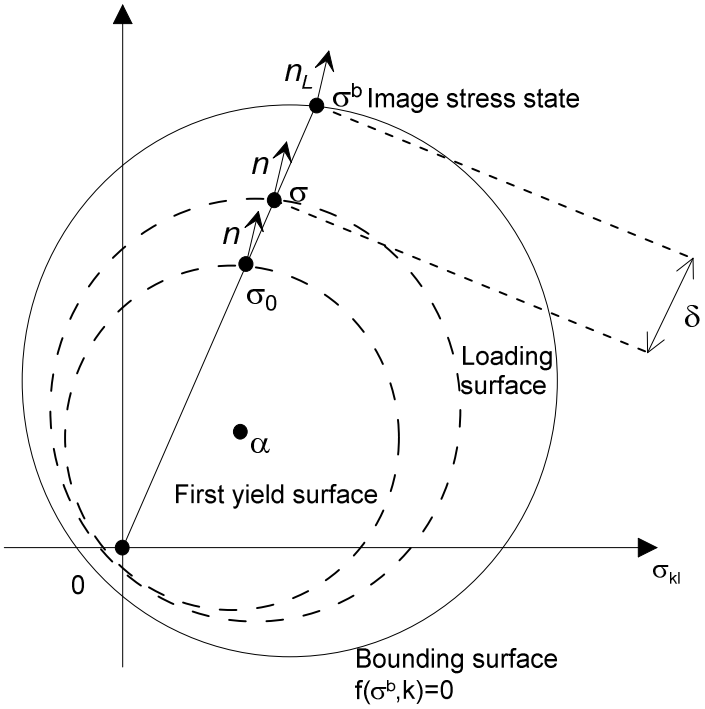

Figure 2.2. Schematic plot of the bounding surface (adapted from Dafalias, 1986 and Potts and Zdravkovic, 1999).

As it is clearly shown in Figure 2.2, if the stress state of the soil is on the bounding surface, the latter behaves as a yield surface, while, differently from the latter, plastic strain can take place whether the stress state is inside the bounding surface but on the yield surface. During unloading, the soil behaves elastically, otherwise its behaviour is elasto-plastic.

A continuous non-invertible mapping rule is required to relate the current stress states $\boldsymbol{\sigma}$ to the image stress state $\boldsymbol{\sigma^b}$ on the bounding surface and to estimate the distance among them. The distance between these two states can be calculated as in (2.24):

$$\delta = \left\| \boldsymbol{\sigma^b} - \boldsymbol{\sigma} \right\| \tag{2.24}$$

When such a relationship is determined, the loading index is the gradient of the bounding surface and it depends on δ. In this way, the distance between the current and the image stress states influences the hardening response of the soil. Analyzing more in detail the situation shown in Figure 2.2, the soil element is loaded in its loading

history and its stress state moves from the initial condition σ_0 on the yield surface towards the stress state σ. A first yield surface is defined homeothetically from the bounding surface and, consequently, it has the same shape of the bounding surface but scaled down and intersects the stress state before loading σ_0. When the stress state of the soil reaches σ, if unloaded, the behaviour is purely elastic, while the yield surface evolves based on its hardening rule otherwise. The condition in Figure 2.2 implicitly shows the so-called radial mapping rule, which is the simplest conceived mapping rule. In fact, the latter takes place when the "image" stress state lies on the intersection between the straight line passing through the stress state and the origin of axes and the bounding surface. It is worth noting that the latter has been proved to satisfactorily reproduce a lot of stress paths in many applications (Potts and Zdravkovic, 1999).

Furthermore, the homeotethism between the bounding surface and the yield surface guarantees the identity between their gradients. Obviously, the hardening law of the yield surface is in turn connected to distance and plastic modulus on the bounding surface (Potts and Zdravkovic, 1999).

2.4 ADVANCED CONSTITUTIVE MODELS FOR LIQUEFACTION PROBLEMS

All the constitutive models analyzed in this study are based on the constitutive framework developed by Manzari and Dafalias (1997), where the main constitutive ingredients for the application of the bounding surface theory to model sand behaviour were first thoroughly summarized. Another key aspect that renders this approach very suitable for the simulation of elasto-plastic soil response is the introduction of the critical state theory in the model and the possibility to simulate a wide variety of stress paths with a single set of parameters. In fact, efforts have been originally made by Roscoe et al. (1963) and Roscoe and Burland (1968) to apply the elasto-plasticity in the CSSM. However, these formulations have been revealed able to capture the monotonic response of clays, but if considering sands in undrained conditions (i.e., generated excess pore water pressures drastically influence the response of the soil),

the CSSM alone with the classical elasto-plasticity is not enough to mathematically model soil response. In addition, for sands at different densities (see Zeng and Arulanandan, 1993), different calibrations of the same constitutive models are often needed (Dafalias and Manzari, 1997). In conclusion, the constitutive model developed by Manzari and Dafalias (1997) was the first to overcome all the above-enumerated limitations, in the sense that it has revealed able to reproduce even the response of sands under undrained conditions, and a single set of parameters successfully captured the response at different densities and confining pressures.

The latter consists of a two-surface plasticity formulation integrated with the critical state theory developed in the deviatoric stress ratio space. The formulation of this constitutive model was thought mainly to be able to simulate different loading conditions, such as drained and undrained, cyclic and monotonic with a single set of constitutive parameters. The multiaxial formulation is developed in the deviatoric plane (π-plane) while the triaxial one is referred to the p-q plane that is a cross section of the multiaxial space. Being the multiaxial formulation the key for the implementation of the models in numerical codes, the latter will be explained in the following.

This model consists of three different surfaces (critical state surface, dilatancy surface and bounding surface) plus the yield surface (see Figure 2.3). The surfaces are conical but not circular except for the yield surface.

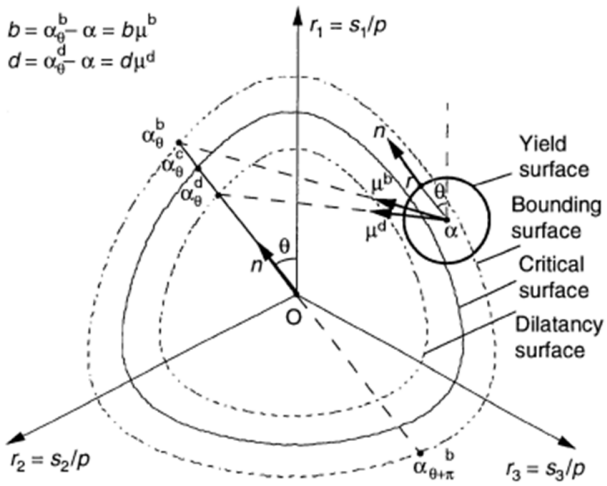

Figure 2.3. Reproduction of the four surfaces (from Manzari and Dafalias, 1997).

Here, the yield surface is represented by a circle with a "diameter" directly related to the constitutive parameter m, while its location in the plane is defined through the back-stress ratio α.

Figure 2.3 clearly shows that the former three surfaces are wedge-shaped in the π-plane. In particular, the openings of the dilatancy and the bounding surfaces depend on the stress ratio at the critical state, which is kept constant.

The loading direction is adopted to map the conjugate critical, bounding and dilatancy back-stress ratios α^i (with i=b,c,d; cfr. Figure 2.3). The dependency of the latter on the Lode angle generates the wedge shape of the surfaces on the π-plane, differently from the yield surface, where its formulation is independent from the Lode angle. This choice is well-explained in Manzari and Dafalias (1997): the Lode angle independency of the yield surface was adopted in order to avoid the introduction of the Lode angle in the gradient of the yield surface, which would have extremely complicated the evaluation of the derivatives; overall, this formulation resulted able to reproduce a wide variety of stress paths. The signs of the distances d^i between the current back-stress ratio α and its images α^i define whether the soil is looser or denser than critical, hardens or softens, is dilative or contractive.

A unique critical state surface is assumed and in order to express "how far" the current state is from the critical state and to evaluate whether the current state is looser or denser than critical, as it was mentioned before, the well-known state parameter ψ developed by Been and Jeffries (1985) is adopted (2.25):

$$\psi = e - e_{cs} \tag{2.25}$$

where e is the current void ratio and e_{cs} is the critical void ratio calculated through the critical state line in the e-ln(p) plane.

The dilatancy surface is based on the concept of phase transformation line developed by Ishihara et al. (1975) that separates the states characterized by contractive behaviour (inside) from those with dilative behaviour (outside). The role of the bounding surface has already been explained in §2.3.

On the basis of Wood et al. (1994) where it is assumed that a virtual bounding stress ratio can be associated to the critical stress ratio and to be consistent with the critical state of soil mechanics in order to avoid unrealistic unlimited dilation at critical state, the surfaces are interrelated among others. In particular, bounding and dilatancy surfaces are dependent on the state parameter ψ.

It is worth noting that some enhancements were made in the evolution of the original Manzari and Dafalias (1997) constitutive model. In fact, as stated in Dafalias et al. (2003), the cyclic response of sands is strictly related to the loading direction with reference to a preferred fabric orientation. For this reason, the following constitutive models take into account for this feature through an anisotropic fabric tensor **F**.

The most adopted constitutive models in numerical simulations and, consequently, implemented into codes based on this approach are NTUASand (adopted to identify the model developed by Papadimitriou and Bouckovalas, 2002 and the following versions), SANISAND (Dafalias and Manzari, 2004) and PM4SAND (Boulanger and Ziotopoulou, 2017). For this reason, the latter are considered in the present study.

Consequently, a brief review of the main features of these models are reported in the following.

2.4.1 THE PAPADIMITRIOU AND BOUCKOVALAS MODEL (NTUASAND02, 2002)

As for all the constitutive platforms based on the bounding surface theory and analyzed in this thesis, the one proposed by Papadimitriou and Bouckovalas (2002) was developed with a view to describing non-cohesive soil behaviour under cyclic loadings. At variance with the approach proposed by Manzari and Dafalias (1997), this model combines the bounding surface theory for high strains with an hypoelastic hysteretic Ramberg-Osgood (1943) formulation for lower strain levels and represents the multiaxial formulation of the model previously developed by Papadimitriou et al. (2001). The shear strain threshold value beyond which any degradation of the shear stiffness is due to irreversible strains is considered through the volumetric strain threshold γ_{tv}. The plastic modulus is capable to simulate the microstructure effect macroscopically, while a kinematic hardening model is adopted. The constitutive framework has shown satisfactory results in terms of shear strain and pore water pressures evolution with the number of cycles and in terms of liquefaction resistance estimation. In addition, as it was mentioned before, an empirical index takes into account for the fabric evolution.

In this model, the critical state line in the e-ln(p) plane is expressed as in (2.26):

$$e_{cs} = (e_{cs})_a - \lambda \ln(\frac{p}{p_{atm}}) \tag{2.26}$$

where p_{atm} represents the atmospheric pressure, while $(e_{cs})_a$ and λ are model constants to be calibrated, as usually done for constitutive models that include critical state framework, on the basis of monotonic element tests reaching critical state conditions (Papadimitriou et al., 2001). As in Manzari and Dafalias (1997), four surfaces are defined in the model: critical, bounding, dilatancy and yield surfaces.

A sketch of these surfaces is reported in Figure 2.4 for both p-q plane and deviatoric plane (referred as π-plane).

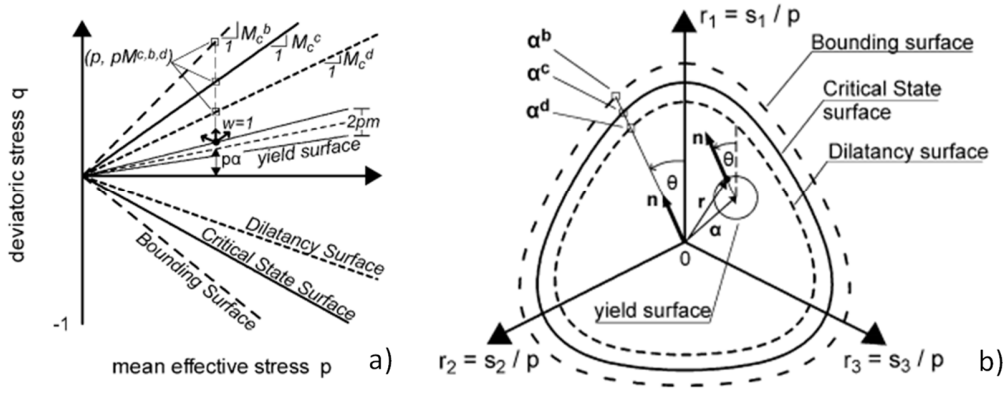

Figure 2.4. Constitutive framework in both triaxial (a) and deviatoric (b) planes (from Papadimitriou and Bouckovalas, 2002).

As it is clear from Figure 2.4, the former three surfaces are conical but not circular and this obviously yields to different slopes of their projections on the p-q plane ($M_c^i \neq M_e^i$, with i=c,b,d) in compression and extension. The above-mentioned projections represent the deviatoric stress ratios. Consequently, the latter are interrelated as it emerged from (2.27) and (2.28):

$$M_{c,e}^b = M_{c,e}^c + k_{c,e}^b \langle -\psi \rangle \tag{2.27}$$

$$M_{c,e}^d = M_{c,e}^c + k_{c,e}^d \psi \tag{2.28}$$

where k_c^b and k_c^d are model constants.

To calibrate these parameters, monotonic compression tests, at least two, are needed. The tests need to start from different conditions in terms of void ratios. The calibration procedure consists in relating the dilatancy (η_{dil}, i.e., the stress ratio corresponding to the phase transformation) and the peak (η_{peak}) stress ratios to their initial value of the state parameter ψ_0. The procedure adopted for Nevada Sand on k_c^b is reported in Figure 2.5. An analogous procedure needs to be applied for k_c^d.

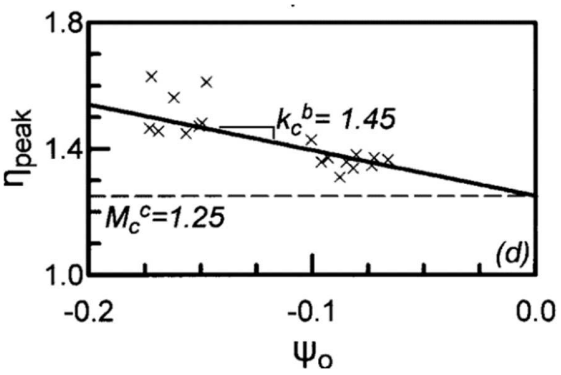

Figure 2.5. Calibration procedure for k_c^b (from Papadimitriou et al., 2001).

In order to avoid the introduction of additional issues related to the calibration of two extra parameters, for practical applications, a good approximation to express $k_e^{b,d}$ is (2.29):

$$k_e^{b,d} = c^c k_c^{b,d} \tag{2.29}$$

In (2.29) c^c represents the ratio $c^c = M_e^c/M_c^c$ that written in a compact form considering even bounding and dilatancy stress ratios becomes $c^{c,b,d} = M_e^{c,b,d}/M_c^{c,b,d}$.

Using the theory of elasticity, the evolution laws of mean pressure and deviatoric stress can be expressed as follows in (2.30) and (2.31):

$$dp = K_t d\varepsilon_v^e \tag{2.30}$$

$$d\mathbf{s} = 2G_t d\mathbf{e}^e \tag{2.31}$$

In the abovementioned equations, the moduli are defined as in (2.32) and (2.33) in function of the classical theory of elasticity and are connected through the Poisson's ratio ν:

$$K_t = G_t \frac{2(1+\nu)}{3(1-2\nu)} \tag{2.32}$$

$$G_t = \frac{G_{max}}{T} = \left(\frac{B p_{atm}}{0.3 + 0.7 e^2} \sqrt{\frac{p}{p_{atm}}} \right) \left(\frac{1}{T} \right) \tag{2.33}$$

This formulation of elastic moduli governs shear modulus degradation and hysteretic damping development for small-to-medium cyclic shear strains.

The equation of G_{max} was inherited by Hardin (1978) and T evolves as in (2.34):

$$T = \begin{cases} 1 + \kappa \left(\frac{1}{a_1} - 1 \right) \left(\frac{\chi_r^0}{\eta_1} \right)^{\kappa - 1}, \text{first shearing} \\ 1 + \kappa \left(\frac{1}{a_1} - 1 \right) \left(\frac{\chi_r^{SR}}{2\eta_1} \right)^{\kappa - 1}, \text{shear reversal} \end{cases} \leq 1 + \kappa \left(\frac{1}{a_1} - 1 \right) \tag{2.34}$$

Here, η_1 is (2.35):

$$\eta_1 = \frac{\tau_1}{p_{SR}} = a_1 \left(\frac{G_{max}^{SR}}{p_{SR}} \right) \gamma_1 \tag{2.35}$$

It is worth noting that the above-mentioned formulation of the evolution of shear modulus reminds the well-known Ramberg-Osgood approach.

The variables B, a_1 and γ_1 are model constants, p_{atm}= 98.1 kPa is the atmospheric pressure and T is a scalar variable which introduces shear modulus degradation as a function of the distance between the current deviatoric stress ratio (**r**) and its value at the last load reversal ($\mathbf{r}^{ref}$) on the π-plane of the deviatoric stress-ratio space. To this aim, two main reference states are considered through the stress scalar parameter χ_r^{ref} reported in (2.36):

$$\chi_r^{ref} = \left[0.5 \cdot \left(\mathbf{r} - \mathbf{r}^{ref} \right) : \left(\mathbf{r} - \mathbf{r}^{ref} \right) \right]^{0.5} \tag{2.36}$$

In fact, $\mathbf{r}^{ref}$ corresponds to $\mathbf{r}^0$ (i.e., its value after consolidation) if the first shearing path is taking place and $\chi_r^{ref} = \chi_r^0$, otherwise it assumes the value $\mathbf{r}^{SR}$ of the deviatoric stress ratio at last shear reversal ($\chi_r^{ref} = \chi_r^{SR}$). Consequently, the parameters p_{SR} and

G_{max}^{SR}correspond to the value of p and G_{max} at the last load reversal state. The value of κ is chosen to be 2 as in Papadimitriou and Bouckovalas (2002).

The model constants to be calibrated are, consequently, B, γ_1, a_1, and ν. The parameter B requires a fitting procedure of small-strain tests to be estimated. For example, resonant column tests are suitable to determine its value. In the following Figure 2.6, the calibration of B is clearly explained: in particular, when T=1 (that correctly represents first shearing conditions) the following equality is valid (2.37):

$$B\sqrt{\frac{p}{p_{atm}}} = \frac{G_{max}}{p_{atm}}(0.3 + 0.7e^2) \qquad (2.37)$$

Different resonant column tests at different confining pressures (p) are required in order to evaluate G_{max}. By interpolating the obtained results, the value of $\frac{G_{max}}{p_{atm}}(0.3 + 0.7e^2)$ corresponding to $\sqrt{\frac{p}{p_{atm}}} = 1$ is the value of B to be adopted as it was made in Papadimitriou et al. (2001) for Nevada Sand (see Figure 2.6).

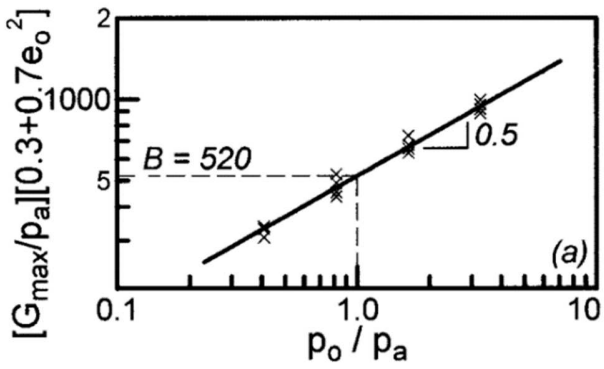

Figure 2.6. Calibration procedure for B (from Papadimitriou et al., 2001).

It is worth noting that a value 2 or 3 times lower is required for monotonic shearing.

The parameter γ_1 indicates the characteristic strain where $G_t = G_{min}$ (see, for instance, Figure 2.7). Practically, it represents the threshold value in terms of shear strain beyond which any variation in shear stiffness is due to plastic strain only. According to Vucetic

(1994), who defined this parameter as γ_{tv}, this value belongs to the range 0.0065%-0.025% for silts and non-plastic sands. In absence of any further information, the value of 0.025% can be chosen. As a consequence, the value of a_1 is selected by fitting the data from resonant column tests as it is highlighted in Figure 2.8 for Nevada sand. It is worth noting that values ranging from 0.55 to 0.75 are generally appropriate for sands (Vucetic and Dobry, 1991; Ishibashi and Zhang, 1993).

Finally, the Poisson's ratio ν can be estimated exploting small strain measurements.

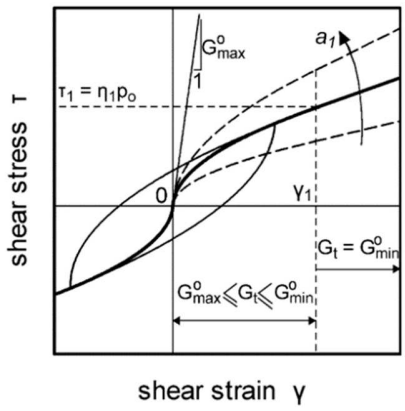

Figure 2.7. Interpretation of the non-linear elastic formulation adopted in the model (from Papadimitriou et al., 2001).

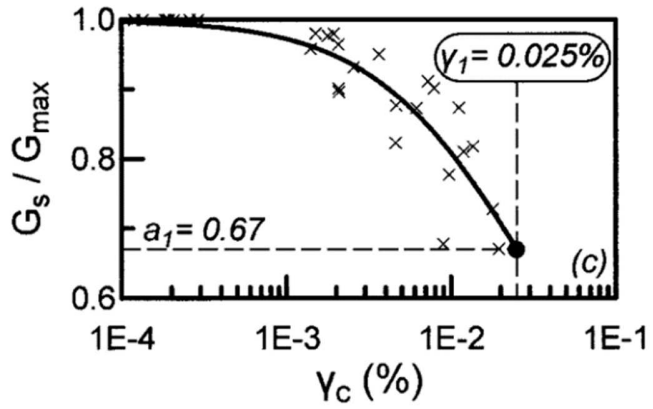

Figure 2.8. Calibration procedure for a_1 (from Papadimitriou et al., 2001).

The yield function assumes the same functional form as in the original work made by Manzari and Dafalias (1997) as expressed in (2.38):

$$f = [(\mathbf{s} - p\boldsymbol{\alpha}) : (\mathbf{s} - p\boldsymbol{\alpha})]^{0.5} - \sqrt{\frac{2}{3}} mp = 0 \tag{2.38}$$

where m is a material constant (typically m=0.06-0.07 and a good estimation of this coefficient can be assumed as $0.05M_c^c$; Papadimitriou et al., 2001; Manzari and Dafalias, 1997) and $\boldsymbol{\alpha}$ is the deviatoric back-stress ratio tensor characterizing the axis of the yield surface. The parameter m represents the size of the yield surface and it assumes a constant value since isotropic hardening is not considered in the model. Furthermore, to give stability to the model, a low value of m must be considered (Papadimitrou, 2020).

Being kinematic hardening allowed in the model, the back-stress ratio $\boldsymbol{\alpha}$ can evolve according to the hardening rule.

It is worth noting the definition of the normal to the yield surface **L**, defined as follows (2.39):

$$\mathbf{L} = \mathbf{n} - \frac{V}{3}\mathbf{I} \tag{2.39}$$

where **n** represents the unit deviatoric stress ratio tensor and the position **n**:**n**=1 is valid. In (2.39), tensor **I** indicates the second order identity tensor, whereas **n** physically indicates the component of the loading direction **L** that lies on the π-plane of the **r**-space and it is defined in the following form (2.40):

$$\mathbf{n} = \frac{\mathbf{r} - \boldsymbol{\alpha}}{\sqrt{2/3}m} \tag{2.40}$$

On the other hand, V can be written as in (2.41):

$$V = \boldsymbol{\alpha} : \mathbf{n} + \sqrt{2/3}m = \mathbf{n} : \mathbf{r} \tag{2.41}$$

As it is reported in Manzari and Dafalias (1997), the shape of the yield surface is circular and this choice was made by the Authors in order to avoid any dependence of

the latter on the Lode Angle, whose role will be described in a while, and on the third order invariants. Either a more accurate shape of the yield surface or a volumetric hardening could have been considered, but this would have affected the definition of loading direction dramatically, increasing its complexity, with small benefits (see Egglezos and Bouckovalas, 1999).

As it was mentioned in §2.3, a mapping rule is required in order to relate the current back-stress tensor to its "images" on the bounding, dilatancy and critical surfaces. To this aim, the Lode angle, calculated starting from the stress ratio tensor $\bar{\mathbf{r}} = \mathbf{r} - \boldsymbol{\alpha}$ is adopted. It can be evaluated in terms of second and third stress ratio tensor invariants (2.42):

$$\cos 3\theta = \frac{3\sqrt{3}}{2}\frac{\bar{J}_3}{\bar{J}_2^{\,3/2}} \tag{2.42}$$

Here, $\bar{J}_2$ and $\bar{J}_3$ are referred to as the second and third invariants of the stress ratio tensor $\bar{\mathbf{r}}$ and are defined as $\bar{J}_2 = \frac{1}{2}\bar{\mathbf{r}}:\bar{\mathbf{r}}$ and $\bar{J}_3 = \frac{1}{2}\bar{\mathbf{r}}:\bar{\mathbf{r}}:\bar{\mathbf{r}}$.

The image deviatoric back-stress ratio tensors can be expressed as (2.43) and (2.44):

$$\boldsymbol{\alpha}^{c,b,d} = \sqrt{2/3}\alpha_\theta^{c,b,d}\mathbf{n} \tag{2.43}$$

where

$$\alpha_\theta^{c,b,d} = g\left(\theta, c^{c,b,d}\right)M_c^{c,b,d} - m \tag{2.44}$$

The function $g\left(\theta, c^{c,b,d}\right)$ that expresses the correlation between back-stress ratios and Lode angle is defined as follows (2.45):

$$g\left(\theta, c^{c,b,d}\right) = \frac{2c^{c,b,d}}{\left[\frac{(1+c^{c,b,d})}{2} - \frac{(1-c^{c,b,d})}{2}\cos 3\theta\right]} - \left[\frac{1+c^{c,b,d}}{2} + \frac{1-c^{c,b,d}}{2}\cos 3\theta\right] \tag{2.45}$$

The plastic strain rate can be calculated on the basis of the following flow rule (2.46):

$$d\boldsymbol{\varepsilon}^{\mathbf{p}} = \langle \Lambda \rangle \mathbf{R} = \langle \Lambda \rangle \left[\mathbf{n} + \frac{D\mathbf{I}}{3} \right] \tag{2.46}$$

The tensor **R** indicates the plastic strain increment direction, while Λ is the plastic multiplier (2.47):

$$\Lambda = \frac{\mathbf{L}: d\boldsymbol{\sigma}}{K_p} = \frac{2G_t \mathbf{n}: d\mathbf{e} - VK_t d\varepsilon_v}{K_p + 2G_t - VK_t D} \tag{2.47}$$

On the basis of (2.47), plastic volumetric strain rate can be expressed as (2.48):

$$d\varepsilon_v^p = \langle \Lambda \rangle D \tag{2.48}$$

where

$$D = A_0 d^d \tag{2.49}$$

It is worth noticing that the position (2.46) highlights that a non-associative flow rule is adopted being V≠-D. In addition, to avoid the unrealistic case of dilation when $\psi > 0$, meaning a looser-than-critical state (cf. (2.26)) and $d^d < 0$ (contractive behaviour), the additional condition of D=0 must be introduced until one of the inequalities ends to hold. This condition is required when a state looser than critical is reached with a stress ratio higher than M_c^d. In fact, on plastic loading without load reversal causing softening, additional dilation could occur for looser-than-critical states. If the state parameter ψ increases, the stress ratio M_c^d increases as well but due to softening the stress ratio decreases. Consequently, it could happen that the stress ratio is inside the dilatancy surface and consolidation will follow the initial dilation leading to critical state. However, it is improbable that even a small amount of dilation precedes consolidation for a looser-than-crtical state, and the above-mentioned restriction is required (Manzari and Dafalias, 1997).

Here, A_0 represents a positive model constant, while d^d is the distance between the current stress state and the dilatancy surface (2.50):

$$d^d = \left(\boldsymbol{\alpha}^d - \boldsymbol{\alpha}\right): \mathbf{n} \tag{2.50}$$

The parameter A_o can be calibrated using stress-dilatancy data with small sampling interval (in ε_v-ε_q plane) in drained triaxial tests, plotting the value of the current stress-ratio vs. the ratio between ε_v^p and ε_q^p. exploiting constant-p drained triaxial tests.

Then, the plastic modulus K_p is defined as (2.51):

$$K_p = p h_b h_f d^b \tag{2.51}$$

where d^b represents the distance between the current stress state and the bounding surface (2.52):

$$d^b = \left(\boldsymbol{\alpha}^b - \boldsymbol{\alpha}\right): \mathbf{n} \tag{2.52}$$

The plastic modulus is strictly connected to the distance d^b as in the bounding surface philosophy and when the latter is negative, it leads K_p to be negative as well. This was made to simulate post-peak shear strain softening. The first scalar h_b introduces the interpolation rule of the model, as in (2.53) and (2.54):

$$h_b = h_0 \left(\frac{p}{p_{atm}}\right)^{\mu-1} \frac{|d^b|}{\langle d^b_{ref} - |d^b| \rangle} \tag{2.53}$$

$$d^b_{ref} = \sqrt{2/3}\left(\alpha^b_\theta + \alpha^b_{\theta+\pi}\right) \tag{2.54}$$

and h_0 is a model constant, while the constant μ is assumed to be μ=1. Obviously, $\alpha^b_{\theta+\pi} = g\left(\theta + \pi, c^b\right) M^b_c - m$ and $\cos 3(\theta + \pi) = -\cos 3\theta$. The constant h_0 can be determined by trial-and-error procedure through the fitting of both effective stress path and stress-strain cycles of monotonic tests (either triaxial or simple shear). The first cycle of large strain cyclic tests can be adopted.

The scalar h_f represents one of the main enhancements of the model with respect to the Manzari and Dafalias (1997) version and acts as an indicator of the effect of sand fabric evolution during shearing on plastic strain rate (2.55):

$$h_f = \frac{1 + \langle \mathbf{F}: \mathbf{I} \rangle^2}{1 + \langle \mathbf{F}: \mathbf{n} \rangle} = \frac{1 + \langle f_p \rangle^2}{1 + \langle \mathbf{f}: \mathbf{n} \rangle} \tag{2.55}$$

where $\mathbf{F}$, $\mathbf{f}$ (deviatoric part of $\mathbf{F}$) and f_p are defined as follows in (2.56) and (2.57):

$$\mathbf{F} = \mathbf{f} + \left(f_p/3\right)\mathbf{I} \tag{2.56}$$

$$f_p = \mathrm{tr}(\mathbf{F}) = \mathbf{F}: \mathbf{I} \tag{2.57}$$

whose evolution rates are (2.58) and (2.59):

$$df_p = H d\varepsilon_v^p \tag{2.58}$$

$$d\mathbf{f} = -H\langle -d\varepsilon_v^p \rangle [C\mathbf{n} + \mathbf{f}] \tag{2.59}$$

C and H are defined as (2.60) and (2.61):

$$C = \max\left|f_p\right|^2 \tag{2.60}$$

$$H = H_0 \left(\frac{\sigma_{1o}}{p_{atm}}\right)^{-\xi} \langle -\psi_0 \rangle \tag{2.61}$$

where H_0 and ξ are material positive constants, while ψ_0 and σ_{10} are the values of the state parameter and the major principal effective stress at consolidation, respectively. This solution enables the dependency of the fabric on the initial stress state. The formulation shown in (2.55) for h_f is adopted, as it is clearly explained in Papadimitriou and Bouckovalas (2002), in order to trigger the development of the denominator in (2.55) only after a shear reversal that follows a dilative state. This meets findings from different studies highlighting a stiffer response of sands for small amplitude unloading-reloading cycles and more compliant responses when cycles are characterized by high

amplitude and shear reversal takes place beyond the dilatancy surface (Papadimitriou, 1999; Papadimitriou et al., 2001, Ladd et al., 1977; Ishihara et al., 1975; Nemat-Nasser and Tobita, 1982).

In the model, the stress evolution rate is reported in (2.62):

$$d\boldsymbol{\sigma} = 2G_t d\mathbf{e} + K_t d\varepsilon_v \mathbf{I} - \langle \Lambda \rangle (2G_t \mathbf{n} + K_t D \mathbf{I}) \tag{2.62}$$

and the hardening rule is expressed as (2.63):

$$d\boldsymbol{\alpha} = \langle \Lambda \rangle h_b h_f (\boldsymbol{\alpha}^b - \boldsymbol{\alpha}) \tag{2.63}$$

For the sake of clarity, it is worthwhile to note that the effect of the fabric is accounted for by considering the **F** tensor in the definition of plastic modulus.

The constant H_o can be determined by fitting cyclic undrained simple shear tests or at least two cyclic undrained triaxial tests. In particular, the excess pore water pressure buildup needs to be achieved during cyclic loading. The last model parameter is ξ, which can be set to 1 as in Andrianopoulos et al. (2010b).

The model above-described was implemented in Abaqus by Miriano (2010) in its original version (i.e., the version described in this chapter) in order to study the dynamic behaviour of flexible retaining structures in sandy soils in drained conditions. In addition, the constitutive model was implemented in FLAC3D by Andrianopoulos (2010b) in a modified version (Andrianopoulos et al., 2010a), to improve its computational capability. The main changes made by Andrianopoulos et al. (2010b) consisted of the prevision of a vanishing elastic region that collapses into a point in the π-plane and a discontinuously relocatable stress projection center connected to the last shear reversal point adopted for mapping the current stress state on the three surfaces. In the verification and validation procedure of the model in FLAC3D, the constitutive framework was adopted to simulate tests at the element level and with centrifuge apparatus performed during the VELACS (Verification of Liquefaction Analysis by Centrifuge Studies) project (Arulmoli et al., 1992). In order to distinguish the different

versions of the model, the one developed by Papadimitriou and Bouckovalas (2002) will be referred in the following as NTUASand02.

In addition, the constitutive model was studied and implemented into the finite element code Imperial College Finite Element Program (ICFEP) by Taborda et al. (2014). After a review of the original version of the model, some critical aspects were identified, and some modifications were applied to the model. Two different yield surfaces were assumed at low stress levels, the shape of the critical state line in the e-ln(p) plane was changed and the hardening modulus formulation has been improved.

The model in its original formulation has never been tested in site response analysis in undrained conditions and boundary value problems were analyzed only by Miriano (2010) in Abaqus. To the Author's knowledge, differently from the most common constitutive models, the original version of the NTUASand constitutive model is not available for any numerical platform. For this reason, and with a view to testing its performance in boundary value problems, the latter will be implemented in a flexible numerical code in the framework of this thesis.

This is the reason why a detailed description of the structure of the constitutive framework has been provided in this paragraph highlighting the calibration procedure that the user needs to adopt as well. For this reason and for the sake of brevity, the other constitutive models analyzed in this study will be only briefly presented in the following paragraphs.

2.4.2 THE SANISAND MODEL (2004)

The second model considered in the thesis was developed by the efforts conducted by Dafalias and Manzari (2004) and it belongs to the SANISAND (Simple ANIsotropic models for SAND) family of constitutive models developed by prof. Dafalias and his coworkers that found its basis on the Manzari and Dafalias (1997) model.

It is a critical-state compatible, bounding surface constitutive framework developed to model liquefiable soils behaviour. Some key and innovative aspects are related to a modified Lode angle expression for the development of the mapping rule and to

account macroscopically for the fabric evolution during the dilatant phase upon shear reversal. Its basic features are reported in Figure 2.9.

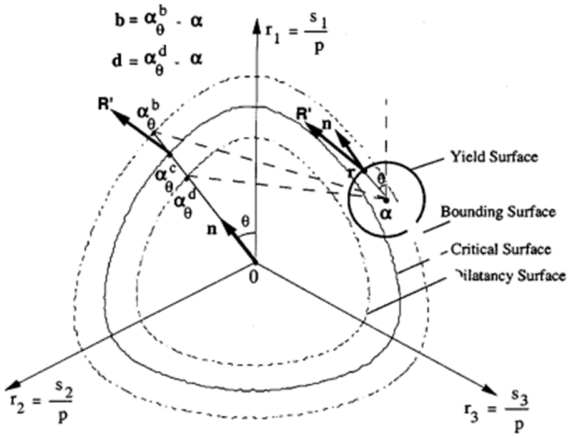

Figure 2.9. Schematic of the SANISAND constitutive model structure (from Dafalias and Manzari, 2004).

The critical state line is expressed in function of the critical void ratio as in Li and Wang (1998), as it is clearly highlighted in (2.64):

$$e_{cs} = e_0 - \lambda_c \left(\frac{p}{p_{atm}}\right) \tag{2.64}$$

where e_0, λ_c and ξ (which is 0.7 for most sands) are material parameters. Differently from what was observed in (2.26), a linear dependency of the critical void ratio from the mean effective pressure p is provided.

The deviatoric bounding and dilatancy stress ratios are expressed as in (2.65) and (2.66):

$$M^b = M \cdot \exp\left(-n^b \psi\right) \tag{2.65}$$

$$M^d = M \cdot \exp\left(n^d \psi\right) \tag{2.66}$$

Here, n^b and n^d are positive constants, and M is the critical stress ratio. Note that for the same quantities, the model developed by Papadimitriou and Bouckovalas (2002)

defines linear relationships between stress ratios and state parameter (cf. (2.27) and (2.28)), while, in this case, the dependency assumes an exponential form.

The shear modulus is defined as in (2.67) and the bulk modulus is reported in (2.68):

$$G = G_0 p_{atm} \frac{(2.97 - e)^2}{1 + e} \left(\frac{p}{p_{atm}}\right)^{0.5} \tag{2.67}$$

$$K = G \frac{2(1 + \nu)}{3(1 - 2\nu)} \tag{2.68}$$

where G_0 is a material constant, ν is the Poisson's ratio and p_{atm} is the reference pressure (1bar = 101.3kPa). It is worth noting that a different elastic shear modulus expression if compared to (2.33) is provided. The equation (2.67) derives from Richart et al. (1970) and Li and Dafalias (2000).

The yield function is defined in the same manner of Papadimitriou and Bouckovalas (2002), discussed in (2.38), and reported in (2.69) for the sake of clarity:

$$f = [(\mathbf{s} - p\boldsymbol{\alpha}) : (\mathbf{s} - p\boldsymbol{\alpha})]^{0.5} - \sqrt{\frac{2}{3}} mp = 0 \tag{2.69}$$

with

$$\mathbf{n} = \frac{\mathbf{s} - p\boldsymbol{\alpha}}{\|\mathbf{s} - p\boldsymbol{\alpha}\|} \tag{2.70}$$

As in NTUASand02, a non-associated flow rule is provided in (2.71):

$$d\boldsymbol{\varepsilon}^{\mathbf{p}} = \langle L \rangle \mathbf{R} = \langle L \rangle \left[\mathbf{R}' + \frac{D\mathbf{I}}{3}\right] \tag{2.71}$$

It is worth noting that in NTUASand02 the deviatoric part of **R** is **n**, while in SANISAND it is **R'** so that **R'**≠**n**.

The rate of plastic deviatoric strain follows the law in (2.72):

$$\mathrm{d}\mathbf{e}^{\mathrm{p}} = \langle \mathrm{L} \rangle \mathbf{R}' = \langle \mathrm{L} \rangle \left[\mathrm{B}\mathbf{n} - \mathrm{C}\mathbf{n}^2 + \frac{\mathbf{I}}{3} \right] \tag{2.72}$$

In the previous (2.71), the direction of deviatoric plastic strain rate depends on B and C, which are in turn related to the Lode angle θ as follows in (2.73) and (2.74), while in the previous model they depend on the normal to the yield surface only (cf. (2.46)):

$$\mathrm{B} = 1 + \frac{3}{2}\frac{1-\mathrm{c}}{\mathrm{c}}\mathrm{g}(\theta, \mathrm{c})\cos 3\theta \tag{2.73}$$

$$\mathrm{C} = 3\sqrt{\frac{3}{2}}\frac{1-\mathrm{c}}{\mathrm{c}}\mathrm{g}(\theta, \mathrm{c}) \tag{2.74}$$

where c represents the ratio between triaxial extensive and compressive strengths, and it is $\mathrm{c} \leq 1$. In addition, a modified definition of the Lode angle if compared to (2.42) is reported in (2.75), while the interpolation function g(θ,c) assumes the functional form defined by Argyris et al. (1974; see (2.76)).

$$\cos 3\theta = \sqrt{6}\mathrm{tr}\mathbf{n}^3 \tag{2.75}$$

$$\mathrm{g}(\theta, \mathrm{c}) = \frac{2\mathrm{c}}{(1+\mathrm{c}) - (1-\mathrm{c})\cos 3\theta} \tag{2.76}$$

The rate of plastic volumetric strain follows the law shown in (2.77):

$$\mathrm{d}\varepsilon_{\mathrm{v}}^{\mathrm{p}} = \langle \mathrm{L} \rangle \mathrm{D} \tag{2.77}$$

In (2.77), the volumetric term assumes the form of (2.78) and the terms appearing in this equation are in (2.79) and (2.80).

$$\mathrm{D} = \mathrm{A}_{\mathrm{d}}\left(\boldsymbol{\alpha}_{\theta}^{\mathrm{d}} - \boldsymbol{\alpha}\right) : \mathbf{n} \tag{2.78}$$

$$\mathrm{A}_{\mathrm{d}} = \mathrm{A}_0(1 + \langle \mathbf{z} : \mathbf{n} \rangle) \tag{2.79}$$

$$\boldsymbol{\alpha}_{\theta}^{d} = \sqrt{\frac{2}{3}}\left[g(\theta, c) \cdot M \cdot \exp\left(n^{d}\psi\right) - m\right]\mathbf{n} \tag{2.80}$$

A_0 and n^d are material constants and $\mathbf{z}$ is defined as the fabric-dilatancy tensor whose rate is expressed by (2.81) in a purely deviatoric form, differently from (2.56):

$$d\mathbf{z} = -c_{\mathbf{z}}\langle -d\varepsilon_{\mathbf{v}}^{p}\rangle(z_{max}\mathbf{n} + \mathbf{z}) \tag{2.81}$$

where c_z and z_{max} are material constants (z_{max}=4.0-5.0 for most sands). The formulation reported is analogous to the one indicated in (2.59) for NTUASand02; however, for the latter, the parameter C that scales $\mathbf{n}$ is updated (2.60), while for SANISAND it is assumed to be constant (z_{max}).

The hardening rule is expressed by (2.82):

$$d\boldsymbol{\alpha} = \langle L\rangle\frac{2}{3}h\left(\boldsymbol{\alpha}_{\theta}^{b} - \boldsymbol{\alpha}\right) \tag{2.82}$$

The parameters appearing in (2.82) are reported in (2.83) and (2.84)

$$\boldsymbol{\alpha}_{\theta}^{b} = \sqrt{\frac{2}{3}}\left[g(\theta, c) \cdot M \cdot \exp\left(-n^{b}\psi\right) - m\right] \tag{2.83}$$

$$h = \frac{G_0 h_0 (1 - c_h e)\left(\frac{p}{p_{atm}}\right)^{-0.5}}{(\boldsymbol{\alpha} - \boldsymbol{\alpha}_{in}):\mathbf{n}} \tag{2.84}$$

where c_h, h_0 and n^b are material constants. Indeed, $\boldsymbol{\alpha}_{in}$ is the value of $\boldsymbol{\alpha}$ when a new loading process triggers and it is also updated when $(\boldsymbol{\alpha} - \boldsymbol{\alpha}_{in}):\mathbf{n}$ becomes negative.

The loading index can be calculated as in (2.85):

$$L = \frac{1}{K_p}\frac{\partial f}{\partial \boldsymbol{\sigma}}:d\boldsymbol{\sigma} = \frac{2G\mathbf{n}:d\mathbf{e} - K\mathbf{n}:\mathbf{r}d\varepsilon_v}{K_p + 2G(B - Ctr\mathbf{n}^3) - KD\mathbf{n}:\mathbf{r}} \tag{2.85}$$

and the plastic modulus is expressed by (2.86):

$$K_p = \frac{2}{3} ph\left(\boldsymbol{\alpha}_{\boldsymbol{\theta}}^{\mathbf{b}} - \boldsymbol{\alpha}\right) : \mathbf{n} \tag{2.86}$$

Finally, the stress increment can be calculated as (2.87):

$$d\boldsymbol{\sigma} = 2Gd\mathbf{e} + Kd\varepsilon_v \mathbf{I} - \langle L \rangle \left(2G \left[B\mathbf{n} - C\left(\mathbf{n}^2 - \frac{\mathbf{I}}{3} \right) \right] + KD\mathbf{I} \right) \tag{2.87}$$

This model was implemented by Cheng et al. (2014) in FLAC, while an external umat routine (i.e., the subroutine required for the implementation of an additional constitutive model) written in Fortran for Abaqus was developed by Martinelli et al. (2015) and it is available at www.soilmodels.com; the same routine was adapted by Masin to include the model in Plaxis. Finally, Ghofrani (2016) tested this constitutive framework in the simulation of centrifuge tests with OpenSees and the details of the implementation are reported in Ghofrani (2018), where the development of the new ManzariDafalias class is discussed. In very recent times, the SANISAND model has been modified including the memory surface concept to simulate cyclic ratcheting and the SANISAND-MS material was conceiveed by Liu and Pisanò (2019). The latter has been implemented in OpenSees and has been made available at the end of 2021.

2.4.3 THE PM4SAND MODEL (2017)

PM4SAND is the acronym of the bounding surface constitutive model developed and improved by Ziotopoulou and Boulanger at UCDavis (see, for instance, Boulanger, 2010; Boulanger and Ziotopoulou, 2012; Boulanger and Ziotopoulou, 2015 and Ziotopoulou and Boulanger, 2017). The constitutive framework is based on the SANISAND model.

Differently from the above-mentioned models, PM4SAND was thought to be calibrated on the basis of classical in-situ tests (e.g., standard penetration tests, cone penetration tests, shear wave velocity measurements) and its formulation was not produced in the π-plane, but a plane-strain formulation only (in the $\mathbf{r}_{xx}$-$\mathbf{r}_{yy}$ plane) of the model was developed. In the following, the key equations only will be analyzed for the

sake of brevity, while the interested reader can refer to Ziotopoulou and Boulanger (2017).

Some key additions were made in order to consider a fabric history and fabric cumulative indices, while dilatancy expression is splitted into both volumetric expansion and contraction terms. A schematic of the model is reported in Figure 2.10.

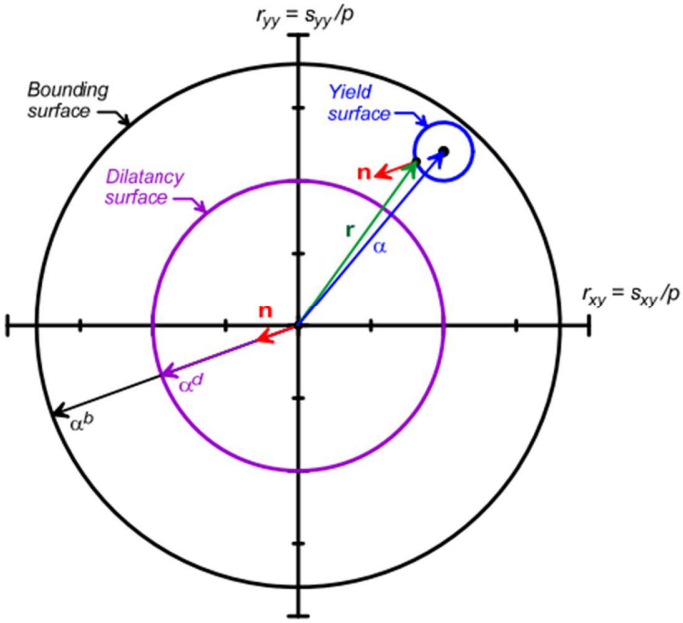

Figure 2.10. Schematic of the bounding, dilatancy and yield surfaces for PM4SAND model (from Boulanger and Ziotopoulou, 2017).

In PM4SAND, the state parameter is expressed as in Bolton (1986) in terms of relative density (2.88):

$$\xi_R = D_{R,cs} - D_R \tag{2.88}$$

The term $D_{R,cs}$ can be expressed as in (2.89):

$$\xi_R = \frac{R}{Q - \ln\left(100\frac{p}{p_{atm}}\right)} \tag{2.89}$$

where Q and R are fitting parameters evaluated by Bolton (1986) as 10 and 1.0, respectively, for quarzitic sands.

The critical state stress ratio is calculated as in (2.90) with an explicit dependency on the critical state friction angle:

$$M = 2\sin\phi_{cv} \tag{2.90}$$

and Φ_{cv} is the critical state effective friction angle that must be assigned as a model parameter. The critical stress ratio is adopted to determine bounding and dilatancy stress ratios as in (2.91) and (2.92), where an exponential functional form dependent on the state parameter is assumed along the lines of Dafalias and Manzari (2004) as in (2.65) and (2.66):

$$M^b = M \cdot \exp\left(-n^b \xi_R\right) \tag{2.91}$$

$$M^d = M \cdot \exp\left(n^d \xi_R\right) \tag{2.92}$$

with n^b and n^d model constants. Consequently, bounding and dilatancy surfaces can be mapped in terms of back-stress ratios (see (2.93) and (2.94)) following the philosophy of the bounding surface theory:

$$\boldsymbol{\alpha^b} = \sqrt{1/2}\left[M^b - m\right]\mathbf{n} \tag{2.93}$$

$$\boldsymbol{\alpha^d} = \sqrt{1/2}\left[M^d - m\right]\mathbf{n} \tag{2.94}$$

From the observation of Figure 2.10 and considering (2.93) and (2.94), it is clear that the surfaces are circular in the deviatoric plane and not wedge-shaped as in NTUASand02 and SANISAND. This is due to the choice of the Authors to remove the Lode angle dependency in the definition of the above-mentioned surfaces for the sake of simplicity (cf. (2.43),(2.44), and (2.83))

A strategy to track the initial back-stress ratio is adopted and an apparent part of the initial back-stress ratio ($\boldsymbol{\alpha}_{in}$), referred as $\boldsymbol{\alpha}_{in}^{app}$ is individuated to avoid over-stiffening at shear reversal. A non-associated flow rule is adopted as (2.46), while the hardening rule expressed by (2.82) is considered in the model and K_p is calculated as in (2.86).

Differently from the original Dafalias and Manzari (2004) formulation, the parameter h is expressed as (2.95):

$$h = \frac{3}{2}\frac{K_p}{p(\boldsymbol{\alpha}^b - \boldsymbol{\alpha}):\mathbf{n}} \tag{2.95}$$

An additional parameter z_{cum} expresses the norm of the absolute changes in the fabric tensor **F**, whose evolution is defined in (2.96):

$$d\mathbf{F} = -\frac{c_z}{1 + \langle\frac{z_{cum}}{2z_{max}} - 1\rangle}\frac{\langle -d\varepsilon_v^p\rangle}{D}(z_{max}\mathbf{n} + \mathbf{F}) \tag{2.96}$$

where z_{max} is the maximum value ever attained by **F** and c_z regulates the rate of evolution of **F**. Finally, the constitutive platform defines a stress-ratio and fabric-dependent shear modulus G as (2.97):

$$G = G_0 p_{atm}\left(\frac{p}{p_{atm}}\right)^{1/2} C_{SR}\left(\frac{1 + \frac{z_{cum}}{z_{max}}}{1 + \frac{z_{cum}}{z_{max}}C_{GD}}\right) \tag{2.97}$$

In the latter expression, C_{SR} takes into account for the stress ratio effects and C_{GD} considers the degradation of G at high values of z_{cum}.

A valuable improvement brought by the model in comparison to the previous constitutive frameworks consists of the possibility to take into account for the post-liquefaction reconsolidation strains. Being the latter essentially due to sedimentation, the additive decomposition into elastic and plastic strains is not suitable to model this aspect and, consequently, they are difficult to be simulated numerically. Furthermore, it was observed by the Authors that post-liquefaction strains predicted at element level by different constitutive frameworks are about an order of magnitude lower than those experimentally measured (Ziotopoulou and Boulanger 2013; Howell et al., 2014).

For this reason, the Authors adopted a pragmatic approach by providing an additional feature that can be activated after the strong-shaking phase, during the simulation. In fact, the post-shaking elastic moduli are reduced considering a parameter identified as F_{sed} whose value is reduced when z_{cum} increases (cf. (2.98) and (2.99)):

$$G_{post-shaking} = F_{sed}G \tag{2.98}$$

$$K_{post-shaking} = F_{sed} K \tag{2.99}$$

The constitutive model has been implemented in FLAC2D by the Authors of the model and the details of the implementation in the finite-difference code are reported in Boulanger and Ziotopoulou (2017). The model has also been implemented in Plaxis by Vilhar et al. (2018), while Chen and Arduino (2021) added the new multiaxial material PM4SAND in OpenSees. Additional applications and details with reference to the implementation in OpenSees are in Chen (2020).

2.5 REFERENCES

Al-Tabbaa A. and Wood D. M. (1989). An experimentally based bubble model for clay. In: Pietrusczczak, S., Pande, G. N. (Eds.), NUMOG III. Elsevier Applied Science.

Andrianopoulos K. I., Papadimitriou A. G. and Bouckovalas G. D. (2010a). Explicit integration of bounding surface model for the analysis of earthquake soil liquefaction, International Journal for Numerical and Analytical Methods in Geomechanics, 34 (15): 1586-1614.

Andrianopoulos K. I., Papadimitriou A. G. and Bouckovalas G. D. (2010b). Bounding surface plasticity model for the seismic liquefaction analysis of geostructures, Soil Dynamics and Earthquake Engineering, 30(10): 895-911.

Argyris J.H., Faust G., Szimmat J., Warnke P. and William K. (1974). Recent developments in finite element analyses of prestressed concrete reactor vessels. Nuclear Engineering and Design 28:42-75.

Arulmoli K., Muraleetharan K.K., Hossain M.M. and Fruth L.S. (1992). VELACS verification of liquefaction analyses by centrifuge studies -Laboratory Testing Program – Soil Data Report, Research Report, The Earth. Technology Corporation.

Been K. and Jefferies M. G. (1985). A state parameter for sands. Geotechnique, London, 35(2), 99–112.

Bolton M.D. (1986). The strength and dilatancy of sands. Géotechnique 36(1):65–78.

Boulanger R.W. and Ziotopoulou K. (2013). Formulation of a sand plasticity plane-strain model for earthquake engineering applications. Soil Dyn Earthq Eng 53:254–267.

Boulanger R.W. and Ziotopoulou K. (2015). PM4Sand (Version 3): A sand plasticity model for earthquake engineering applications.

Boulanger R.W. (2010). Sand Plasticity Model for Non-linear Seismic Deformation Analyses. In: International Conferences on Recent Advances in Geotechnical Earthquake Engineering and Soil Dynamics. Missouri University of Science and Technology.

Boulanger R.W. and Ziotopoulou K (2017). PM4Sand (version 3.1): A sand plasticity model for earthquake engineering applications. Report No. UCD/CGM-17/01, Center for Geotechnical Modeling, Department of Civil and Environmental Engineering, University of California, Davis, CA, March, 112 pp.

Chen L. (2020). Implementation, Verification, Validation, and Application of Two Constitutive Models for Earthquake Engineering Applications. Ph.D. Thesis. University of Washington, Seattle.

Chen L. and Arduino P. (2021). Implementation, verification and validation of the PM4SAND model in OpenSees. PEER Report No. 2021/02. Pacific Earthquake Engineering Research Center Headquarters, University of California, Berkeley, March 2021.

Cheng Z., Dafalias M. and Manzari M.T. (2013). Application of SANISAND Dafalias-Manzari model in FLAC3D. The 3rd International FLAC/DEM Symposium, Hangzhou, China, Vol:Continuum and Distinct Element Numerical Modeling in Geomechanics – 2013.

Dafalias Y.F. (1986). Bounding surface plasticity. I: Mathematical foundation and hypoplasticity. Journal of Engineering Mechanics, Vol. 112, No. 9, September, 1986. ©ASCE, ISSN 0733-9399/86/0009-0966/$01.00. Paper No. 20918.

Dafalias Y.F., Li X.S., Manzari M.T., Papadimitriou A.G. and Wang Z.L. (2003). Generic and non-traditional constitutive ingredients in sand plasticity modelling. International Workshop on Prediction and Simulation Methods in Geomechanics, ISSMGE/TC34, Athens.

Dafalias Y.F. and Manzari M.T. (2004). Simple plasticity sand model accounting for fabric change effects, Journal of Engineering Mechanics 2004.

Dafalias Y.F. and Popov E.P. (1976). A model of nonlinearly hardening materials for complex loadings, Acta. Mech., Vol 21, 173-192.

Egglezos, D. N. and Bouckovalas, G. D. (1999). Permanent strain and pore pressure relations for cyclic loading of sand. Proc., 2nd Int. Conf. on Earthquake Geotech. Engrg., Vol. 1, 131–136.

Gajo A. and Wood D. M. (1999). A kinematic hardening constitutive model for sands: the multiaxial formulation. Int. J. Num. Anal. Meth. Geomech. 23, 925-965.

Ghofrani A. (2018). Development of Numerical Tools For the Evaluation of Pile Response to Laterally Spreading Soi. Ph.D. Thesis, The University of Washington, Seattle.

Ghofrani A. and Arduino P. (2016). Prediction of LEAP centrifuge test results using a pressure-dependent bounding surface constitutive model Soil Dynamics and Earthquake Engineering (2016), http://dx.doi.org/10.1016/j.soildyn.2016.12.001.

Hardin B.O. (1978). The nature of stress-strain behaviour of soils, State-of-the-art report. Proceedings of the ASCE Specialty Conference on Earthquake Engineering and Soil Dynamics, Pasadena, p. 3-90.

Hashiguchi K. (1985). Two- and three-surface models of plasticity. In: V Int. Conf. Num. Meth. in Geomechanics. Balkema, Rotterdam, Nagoya, Japan.

Hashiguchi K. (1988). Mathematically consistent formulation of elastoplastic constitutive equations. In: VI Int. Conf. Num. Meth. in Geomechanics. Balkema, Rotterdam, Innsbruck, Austria.

Hill R. (1950). The mathematical theory of plasticity, Oxford Univ. Press, 1950.

Howell R., Rathje, E. M. and Boulanger, R. W. (2014). Evaluation of simulation models of lateral spread sites treated with prefabricated vertical drains. Journal of

Geotechnical and Geoenvironmental Engineering, ASCE, 04014076, 10.1061/(ASCE)GT.1943-5606.0001185.

Ishibashi I. and Zhang X. (1993). Unified dynamic shear moduli and damping ratios of sand and clay. Soils and Foundations 1993;33(1):182–91.

Ishihara K. (1993). Liquefaction and flow failure during earthquakes. Geotechnique 43, No. 3, 351-415.

Ishihara K., Tatsuoka F. and Yasuda, S. (1975). Undrained deformation and liquefaction of sand under cyclic stresses. Soils and Found., Tokyo, 15(1), 29–44.

Jirasek M., and Bazant Z. P. (2002). Inelastic Analysis of Structures. Wiley, Chichester.

Kramer S. L. (1996). Geotechnical Earthquake Engineering. Prentice Hall, 653 pp.

Krieg R.D. (1975). A practical two-suraface plasticity theory, J. Appl. Mech., Vol 42, 641-646.

Ladd C.C., Foott R., Ishihara K., Schlosser F. and Poulos H.G. (1977). Stress-deformation and strength characteristics, State-of-art report. Proceedings of the Ninth International Conference on Soil Mechanics and Foundation Engineering, Tokyo, 2, 1977, p.421-94.

Li X. S. and Dafalias Y. F. (2000). Dilatancy for cohesionless soils. Geotechnique, 50(4), 449–460.

Li X. S. and Wang Y. (1998). Linear representation of steady-state line for sand. J. Geotech. Geoenviron. Eng., 124(12), 1215–1217.

Liu H. Y. and Pisanò F. (2019). Prediction of oedometer terminal densities through a memory-enhanced cyclic model for sand. Géotechnique Letters, 9(2), 81-88.

Lubliner J. (1990). Plasticity Theory. McMillan Publishing Company.

Manzari M.T. and Dafalias Y.F. (1997). A critical state two-surface plasticity model for sands, Geotechnique, London, 47(2), 255–272.

Martinelli M., Miriano C., Tamagnini C. and Masin D. (2015). Implementation of SANISAND model as ABAQUS umat and PLAXIS user defined subroutines.

Miriano C. (2010). Numerical modelling of the seismic response of flexible retaining structures. Ph.D. Thesis, Sapienza University of Rome. (in Italian).

Mogami T. and Kubo K. (1953). The behaviour of soil during vibration. Proc. 3rd Int. Conf. Soil Mech., 1, 152-153.

Mroz Z., Norris V. A. and Zienkiewicz O. C. (1978). An anisotropic hardening model for soils and its application to cyclic loading. Int. J. Num. Anal. Meth. Geomech. 2, 203-221.

Mroz Z., Norris V. A. and Zienkiewicz O. C. (1981). An anisotropical critical state model for soils subject to cyclic loading. Geotechnique 31 (4), 451-469.

Naghdi P. M. (1960). Stress-strain relations in plasticity and thermoplasticity plasticity, Proc. Symp. Nuw. Struct. Mech., 2nd, 1960 p. 121.

Nemat-Nasser S. and Tobita Y. (1982). Influence of fabric in liquefaction and densification potential of cohesionless sand. Mech Mater ; 1:43-62.

Papadimitriou A. G. and Bouckovalas G. D. (2002). Plasticity model for sand under small and large cyclic strains: a multiaxial formulation, Soil Dynamics and Earthquake Engineering, 22: 191-204.

Papadimitriou A. G., Bouckovalas G. D. and Dafalias Y. F. (2001). Plasticity model for sand under small and large cyclic strains, Journal of Geotechnical and Geoenvironmental Engineering, ASCE, 127(11): 973-983.

Papadimitriou A.G. (1999). Elastoplastic modelling of monotonic and dynamic behaviour of soils. Doctorate Thesis, Department of Geotechnical Engineering, Faculty of Civil Engineering, National Technical University of Athens, June 1999 (in Greek).

Papadimitriou A.G. (2020). Personal Communication.

Potts D.M. and Zdravkovic L. (1999). Finite element analysis in geotechnical engineering: Theory. London: Thomas Telford.

Prager, W. (1949). Recent developments in the mathematical theory of plasticity, J. Appl. Phys. 20:3 (1949), 235–241.

Prager, W. (1955). Probleme der Plastizitätstheorie, Birkhäuser, Basel (in German).

Prevost J. H. (1977). Mathematical modelling of monotonic and cyclic undrained clay behaviour. Int. J. Num. Anal. Meth. Geomech. 1, 195-216.

Prevost J. H. (1986). Constitutive equations for pressure-sensitive soils: theory, numerical implementation, and examples. In: Dungar, R., Studer, J. A. (Eds.), Geomechanical Modelling in Engineering Practice. Balkema, Rotterdam.

Ramberg W. and Osgood W. R. (1943). Description of stress-strain curve by three parameters. Technical Note 902, National Advisory Committee for Aeronautics, Washington, D.C.

Richart F. E., Jr., Hall J. R. and Woods R. D. (1970). Vibration of soils and foundations. International series in theoretical and applied mechanics, Prentice-Hall, Englewood Cliffs, N.J.

Roscoe K. H., Schofield A. N. and Thurairajah, A. (1963). Yielding of clays in states wetter than critical. Geotechnique 13, No. 3, 211–240.

Roscoe, K. H. and Burland, J. B. (1968). On the generalized stress–strain behavior of wet clays. In Engineering plasticity (eds J. Heyman & F. A. Leckie), pp. 535–609. Cambridge University Press.

Rouainia M. and Wood D. M. (2000). A kinematic hardening constitutive model for natural clays with loss of structure. Geotechnique 50 (2), 153-164.

Simo J. C. and Hughes T. J. R. (1987). General return mapping algorithms for rate-independent plasticity. In: Desai, C., et al. (Eds.), Constitutive Laws for Engineering Materials. Elsevier Science Publishing, Horton, Greece.

Taborda D.M.G., Zdravković L., Kontoe S. and Potts D.M. (2014). Computational study on the modification of a bounding surface plasticity model for sand, Computers and Geotechnics, 94, 22-30.

Terzaghi K. and Peck R. (1948). Soil mechanics in engineering practice. 2nd ed, p. 108. Chichester: Wiley.

Vermeer P. A. and de Borst R. (1984). Non-associated plasticity for soils, concrete and rock. HERON 29 (3), 1-64.

Vilhar G., Brinkgreve R.B.J. and Zampich L. (2018). Plaxis. The PM4SAND model. Plaxis.

Vucetic M. and Dobry R. (1991). Effect of soil plasticity on cyclic response. Journal of Geotechnical Engineering, ASCE 1991;117(1):89–107.

Wood D.M., Belkheir K. and Liu D.F. (1994). Strain softening and state parameters for sand modelling. Geotechnique 44, No. 2, 335–339.

Wood D.M. (2004). Geotechnical Modelling. Spon Press, Oxfordshire, UK.

Yu H.S. (2006). Plasticity and Geotechnics. Springer Science, New York.

Zeng X. and Arulanandan K. (1993). Overview of calibration of constitutive models and soil parameters. In Verification of numerical procedures for the analysis of soil liquefaction problems, ol. 2 (eds Arulanandan and Scott). Rotterdam: Balkema.

Zienkiewicz O. C., Chang C. T., Pastor M., Schreer M. and Shiomi, T. (1999). Computational Geomechanics (with special reference to earthquake engineering). Wiley & Son.

Ziotopoulou K. and Boulanger R.W. (2013). Numerical modeling issues in predicting postliquefaction reconsolidation strains and settlements. 10th International Conference on Urban Earthquake Engineering, March 1-2, Tokyo Institute of Technology, Tokyo, Japan, 469-475.

3 IMPLEMENTATION OF A NEW MULTIAXIAL CONSTITUTIVE MODEL IN A FINITE ELEMENT CODE

3.1 INTRODUCTION

In the Geotechnical Earthquake Engineering field, a lot of numerical codes based on Finite Difference and Finite Element strategies have been developed and their reliability in liquefaction problems is continuously increasing. In particular, strong efforts have been performed in simulating boundary value problems through fully-coupled nonlinear effective stress analyses that are able to reproduce the interaction between mechanical response and pore pressure developments (Andrianopoulos et al., 2010). Among the most used codes one can find Plaxis (Brinkgreve et al., 2021) and FLAC (Itasca, 2019), both with their bi- and tri-dimensional versions. The former exploits the Finite Element (FE) approach while the latter adopts the Finite Difference (FD) scheme. In this study, it has been decided to move towards the adoption of an open-source finite element platform developed primarily for research purposes. For this reason, OpenSees (McKenna, 1997; McKenna et al., 2000) has been selected.

As it was widely explained in the Introduction of this thesis, the choice can be justified by the flexibility of the OpenSees framework and to its extremely high simulative potential. In addition, the open-sourceness of the code played a key role for this selection. In fact, the source code and its programming environment was designed to be freely accessed by external users in order to improve its simulative capability. Furthermore, numerous studies were successfully performed with a view to reproducing liquefaction-related phenomena adopting different constitutive models (see, for instance, Ghofrani and Arduino, 2016; McAllister et al., 2016; Carey and Kutter, 2017; Ramirez et al., 2018; Chen et al., 2021; Liu et al., 2020; Chen and Arduino, 2021; Fasano et al., 2021).

Generally, the main goal of the constitutive models, when formulated, consists of their integration in numerical codes so that they can be successfully adopted in simulations of real problems. In this manner, the models increase their reliability. On the other hand, their formulation can be improved by the users in order to take into account for additional features. For this reason, the validation of a constitutive model can be thought as a continuously ongoing process.

A constitutive model can be considered actually effective only if it is able to reproduce a large variety of real problems and it can interact with different numerical platforms in a relatively simple way: when formulated, an eye should always be kept on the complexity of its implementation in FE or FD codes.

On this basis, the constitutive models mentioned in §2.4 meet these requirements and this is the reason why they have been selected for the analyses included in this thesis. Furthermore, it is worth noting that SANISAND and PM4SAND are already available in OpenSees (cf. §2.4.2 and §2.4.3 for the references). On the other hand, the model proposed by Papadimitriou and Bouckovalas (2002) is not available in the numerical platform. Therefore, in this study, it was decided to add a new material in OpenSees. It was identified with the acronym NTUASand02. This acronym cannot be found in literature, and it was assigned to distinguish it from the version of the model implemented in FLAC by Andrianopoulos et al. (2010).

The current chapter provides a brief description of the OpenSees environment in §3.2, while in §3.3, a description on how to implement a new constitutive model in OpenSees is developed. Furthermore, in §3.4, the implementation of NTUASand02 constitutive model is analyzed in detail, in §3.5 some theoretical insights relative to the integration of the elasto-plastic stiffness matrix are provided, and, finally, in §3.6 the commands useful to take advantage for the NTUASand02 class in OpenSees are shown.

3.2 THE OPENSEES ENVIRONMENT

All the computational activities to model and simulate the response of liquefiable soils using different constitutive platforms are performed here adopting the Open System for

Earthquake Engineering Simulation, usually known as OpenSees (McKenna, 1997; McKenna et al., 2000). It is an object-oriented, open-source software framework, developed with a view to reproducing the response of a large number of problems, such as geotechnical and structural systems subjected to a wide range of hazards exploiting the Finite Element theory. It is designed to be flexible, extensible and portable (McKenna, 2011).

It is mainly written in C++, but uses several numerical libraries written in Fortran and C for implemented materials, linear equation solving and finite element routines (https://opensees.berkeley.edu). The framework was developed by Frank McKenna and Gregory L. Fenves with funding from PEER (Pacific Earthquake Engineering Research Center of University of California, Berkeley). A reference manual was developed by Mazzoni et al. (2007).

OpenSees is primarily an interpreter, and it is conceived to be highly modular in order to make the users able to extend and integrate the code. In addition, it exploits the object-oriented programming model (OOP) of the C++ language. Consequently, various objects are implemented and are thought to be able to communicate with each other to provide the desired functionality (McKenna, 2011). Objects are organized hierarchically, and they represent instances of a class, separate and independent, and their behaviour is defined by the corresponding class. The interpreter reads scripts written using the Tcl programming language. Not only does it have the advantage to be simple-to-learn, but it also is very powerful with a small number of rules provided to describe the syntax which allows the development of programs in multiple platforms (http://wiki.tcl-lang.org). Furthermore, each command relies on a C++ procedure written in the source code of the OpenSees library.

This modularity is integrated into a superior software design which allows the composition of the object, making the users able to combine the different components on the basis of their own problem. Overall, the main added-value of this framework consists of being completely open-source. Consequently, its library of components is ever-growing and allows a wide amount of different and various simulations. In addition, if on one hand the use of a command-driven language could be more difficult

to be dealt with, on the other hand, it guarantees the development of more versatile input files. In fact, it is not a black-box, in so far as the user has the full control of the instructions the code is executing. Again, the possibility of freely integrating into OpenSees a new material, element, or analysis object renders the framework a very useful and powerful tool to reliably simulate different classes of problems (McKenna, 2011). In Figure 3.1, the typical structure of an OpenSees input file is provided.

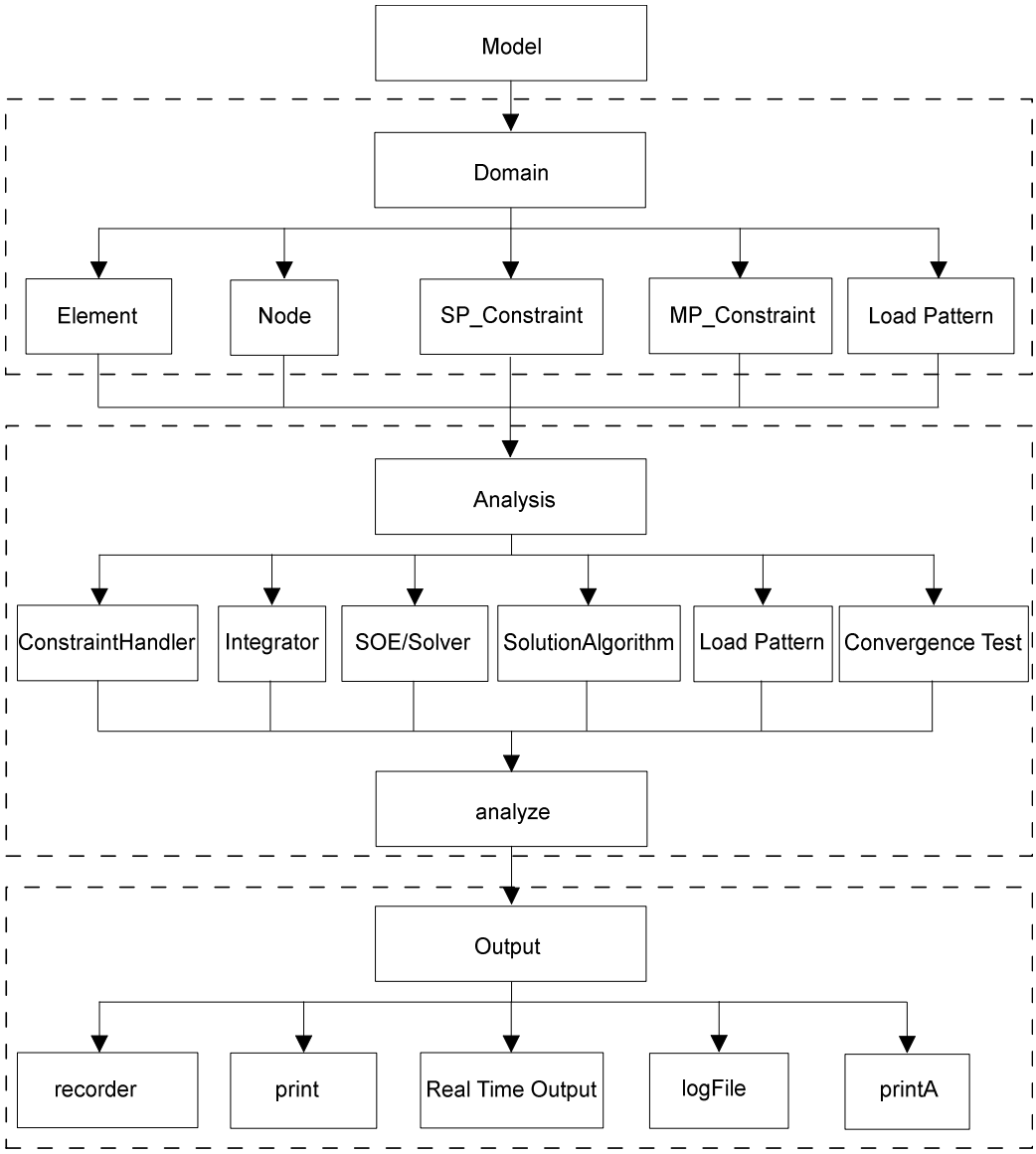

Figure 3.1. OpenSees input file structure (adapted from https://opensees.berkeley.edu).

As it is highlighted in Figure 3.1, first of all, the domain under analysis can be built by defining elements, nodes, boundary conditions and external loads to be applied to the model. Subsequently, the analysis object is built by defining all the component objects that construct the type of analysis of the system under study. Then, the analyze() command is used to perform the so-defined analysis type and the output commands allow the users to monitor the status of the quantities that describe the type of problem. Among them, the recorders are objects that give the response of an element or node in terms of a requested quantity.

Furthermore, another strength of this software is that it is conceived with a view to guaranteeing the implementation of serial and parallel computer applications. To this aim, two applications are developed as extensions of this basic interpreter to allow parallel computation: OpenSeesSP and OpenSeesMP. The former (OpenSeesSP) is used for very large models, while the latter is mainly adopted for parametric studies. A brief description of OpenSeesSP is provided in §7.6.1.

However, as repeatedly stressed, the most important feature of OpenSees with reference to this study consists of the possibility to freely add a new material without changing any feature of the framework.

3.3 IMPLEMENTATION OF A NEW MATERIAL IN OPENSEES

OpenSees was structured in a manner that the implementations of materials and elements are kept separate. This allows the user to take advantage of the possibility to implement a new material without changing elements codes and, obviously, vice-versa. A key role to accomplish this feature is played by the C++ programming language supporting data encapsulation and run-time binding.

Here, a brief review of the structure that a new material abstraction should contain if a developer aims at implementing it into the OpenSees framework is provided. All the details reported here are from Scott and Fenves (2001), and from the OpenSees online documentation. The purpose of the paragraph is to sum up some of the features needed to implement a new model for geotechnical applications.

3. IMPLEMENTATION OF A NEW MULTIAXIAL CONSTITUTIVE MODEL IN A FINITE ELEMENT CODE

Three material abstractions are available in OpenSees and are referred to as UniaxialMaterial, SectionForceDeformation and nDMaterial. The former refers to mono-dimensional material models, such as stress-strain or force-deformation. The SectionForceDeformation material reproduces the plate and beam-column force-deformation response. On the contrary, the abstraction adopted to implement the constitutive model referred herein as NTUASand02 is nDMaterial. The latter provides the stress-strain response in a multidimensional element. This represents the reason why the constitutive equations of the model must be written in a tensor form.

In the implementation procedure of new multiaxial material in OpenSees, two different files are needed: the header (.h) where all the methods (i.e., functions belonging to the same class) and member variables (i.e., variables directly associated to this class) are declared and a .cpp file where the script is executed, and the functions are contained. Some differences occur whether the problem to analyze is bi- or tri-dimensional. For this reason, if both plane-strain and tri-dimensional formulations need to be added, additional files can be provided representing material subclasses: two .h header files and two .cpp files containing the declaration of the functions to describe both the formulations of the model (.h files) and their expressions (.cpp files). It is worth noting that the addition of these files is not mandatory, and the distinction can be also made in the main .h and .cpp files.

With reference to the header file, generally, it contains the declaration of all the public variables that are allowed to be accessed by different parts of the framework. Here, the classical C++ libraries are recalled, such as those required for the input-output operations (i.e., iostream.h, fstream.h) and those useful for the mathematical operations (math.h) as well as those libraries defined into OpenSees with reference to the nDMaterial class (nDMaterial.h) and for tensor operations (Vector.h and Matrix.h).

On the other hand, the nDMaterial interface .cpp file contains the definition of all the constitutive equations of the material model. All data or methods are public because no protected or private data or methods are considered. The constructor is here defined and when the material is created for the first time, it is called. Its role consists in the initialization of variables defined in the header file. Among these, optional parameters

could be defined. In addition to the input parameters required for a certain constitutive model, others required for the material identification (i.e., tags, being the nDMaterial a "tagged object" in Opensees; Scott and Fenves, 2011) and for the integration of the stiffness matrix (e.g., integration schemes, when needed) are provided. Note that, among others, an integer identifier, called tag, must be associated with each material object into OpenSees. The latter plays the role to uniquely refer to the object. The counterpart of the constructor object is the destructor and represents the method to be called before an object is destroyed.

The getCopy() method referred to the nDMaterial class must be implemented. In fact, it is defined to create a new instance by cloning a called object and, consequently, by keeping the same properties. In this manner, the constructor creates the object, and all the previously defined variables are copied in the latter.

The commitState(), revertToLastCommit() and revertToStart() methods are involved in the definition of the state variables values. In particular, commitState() sets all the history variables to their trial values and is called once the convergence is achieved in a load step and here the updating of all history variables takes place; revertToLastCommit() is called if convergence is not achieved, while revertToStart() set all the variables to 0.0. The getType() and getOrder() methods are related to the type of analyzed problem to be sent back in a vector form.

The virtual method getStressToRecord(), which is defined "virtual" because it can be overridden by a subclass of nDMaterial only, sends the committed state to the finite element. The committed state is assembled and the method sends the output values to the recorder through the getState() method where state variables are plotted.

The setResponse() and getResponse() methods are related to the Response class. In fact, these methods contain the quantities that can be called by the element recorders.

The recvSelf() method plays the role to get a vector containing the current values of the internal variables, while the sendSelf() method sends data and assigns values to internal variables. Both of them work across the Channel Object. The Print() method writes material tag, material name and material parameters to the output stream. Furthermore, the getEStrain(), getPStrain(), getStress() and getTangent() methods are

virtual methods whose role consists in sending back elastic strain and plastic strain tensors, stress tensor and tangent stiffness tensor, respectively, all of them written in Voigt notation.

Finally, setParameter() and updateParameter() play a key role in reliability analysis in the sense that they can assign a value to a certain parameter before or after an analysis stage.

Obviously, the newly added material must be integrated into the OpenSees framework. To do this and to enable the parsing, an additional if statement must be added to the TclModelBuilderNDMaterial. In the following §3.4, the implementation of NTUASand02 in OpenSees is detailed, by keeping an eye on the differences with the codes of other bounding surface models, such as SANISAND and PM4SAND.

3.4 IMPLEMENTATION OF THE NTUASAND02 CLASS IN OPENSEES

In §2.4, it was highlighted that two constitutive models of the SANISAND family for liquefaction problems are already available in the OpenSees framework: SANISAND (Dafalias and Manzari, 2004) and PM4SAND (Boulanger and Ziotopoulou, 2017). The implementation of these materials represents the culmination of strong efforts performed by the University of Washington Research Group directed by Prof. Pedro Arduino. This group also improved the availability of finite elements for liquefaction analyses for both bi- and tri-dimensional conditions. In fact, quadrilateral and hexahedral elements, with pore pressure degree of freedom were developed using the single-stabilization point technique (see, for instance, McGann et al., 2012; 2015).

Being NTUASand02 part of the SANISAND family of constitutive models, the selection of the same structure adopted in the implementation of PM4SAND and SANISAND is natural, and it is inherited to build the code of the model developed by Papadimitriou and Bouckovalas (2002). For this reason, in this study, the open-sourceness of OpenSees was crucial, and the works made by Ghofrani (2018), and Chen and Arduino (2021) inspired and mostly guided the Author in the implementation of the new material. More specifically, these codes are contained in a folder of the

OpenSees source code identified as UWMaterials where UW stems for the University of Washington.

In the implementation procedure of the NTUASand02 class, all the member variables are initialized through the initialize() method. In particular, material constants, tensors describing the state of the material and quantities related to the integration schemes are here initialized and their values are declared. In addition to the input parameters required for the constitutive model $(\nu, M_c^c, \lambda, (e_{cs})_a, h_o, A_o, B,\ a_1, \gamma_1, M_e^c, k_c^d, k_c^b, H_o, \varsigma)$, others necessary for the integration of the elasto-plastic matrix (integration schemes and tolerances) are defined. Additional parameters such as density and initial void ratio needed in the equations are declared. Additional variables are defined as members in the code $(\sigma_{1o}, \psi_o, C, d\chi_e, \eta_1, \chi_r)$. A boolean variable defining whether the first shear is taking place or not is implemented (mIsFirstShear) and this is required for the definition of the the paraelastic formulation of the model.

The tensors here initialized are stress, strain, fabric, and back-stress. Once the analysis starts, the trial strain is got from the finite element considering either bi- or tri-dimensional formulation based on the problem type. The instructions of the setTrialStrain() method are contained in both additional .cpp files of plane strain and 3D formulations of the constitutive model, so that the subclasses of NTUASand02 called NTUASand02PlaneStrain and NTUASand023D are derived.

Once the trial strain is obtained, its values in Voigt notation are exploited to enter in the integrate() method. Here, a switch is built: the integration can be performed using either the elastic (elastic_integrator()) or the elastoplastic tangent stiffness (explicit_integrator()) matrix. In the latter case, the entire elasto-plastic formulation of the model is activated, while in the former, the elastic moduli only are required (see (2.32) and (2.33)). Here, different explicit integration schemes are implemented in the .cpp files. This aspect will be discussed in §3.5.

Furthermore, through the updateMaterialStage() command, common to the elasto-plastic constitutive models for sands, the switch from elastic to elasto-plastic

integration can be parsed and this can be directly written in the Tcl file. It is worth noting that the source code of SANISAND provides a third option consisting in the implementation of the implicit Closest Point Projection Method (Ortiz and Simo, 1986) with an added secondary yield surface that represents a tension cut-off (Ghofrani, 2018). Further details on the latter integration scheme are provided by Ghofrani (2018). The tension cut-off is needed because the constitutive models cannot deal with mean pressures lower than zero and, consequently, with tensile stresses. However, it could happen that in undrained conditions and boundary value problems (for example, consider the finite elements closer to the surface in the case of a free-field sand column subjected to a strong motion input in undrained conditions), low confinement and contractive behaviour could lead to the inadmittable condition $p \leq 0$. To this aim, Ghofrani (2018) added a secondary yield surface with the role of limiting the effective stress at the value of p_{min}, which assumes in this case the value of 0.1‰ times the atmospheric pressure. In the OpenSees implementation of PM4SAND, its value corresponds to $p_{atm}/200$. The necessity to avoid the possibility of mean pressure lower than zero lead Taborda et al. (2014) to introduce an additional yield surface to the NTUASand02 constitutive model. The determination of this value is discussed because it is stated that small values of p_{min} do not avoid issues related to the precision loss, while high values alter the constitutive formulation (Taborda et al., 2014). For this reason, the Authors performed a parametric study with different p_{min} values (0.1 kPa, 1.0 kPa and 10.0 kPa). It emerged that for p_{min} corresponding to 10.0 kPa, lower deformation if compared to 0.1 kPa and 1.0 kPa were obtained. On the other hand, very slight differences arise considering either 0.1 kPa or 1.0 kPa. In conclusion, they asserted that a low value must be assigned. In the implementation of the NTUASand02 constitutive model in OpenSees, a simpler strategy is adopted to manage the condition $p < p_{min}$. In this case, the mean pressure p has been simply cut to the value of p_{min} (i.e., if $p < p_{min}$, then $p = p_{min}$)

Finally, if the convergence is achieved, the obtained values of stress, strain, back-stress and fabric tensors are committed, otherwise, the step analysis is repeated once more.

Here, a crucial point of the implementation is represented by the adopted integration scheme, whose role is clarified in §3.5.

All the equations provided and described in §2.4.1 must be implemented and, for this reason, additional methods have the role to define the values of variables required to update the element state. To this aim, for example, the method g() calculates the interpolation function expressed by (2.45), while the yield surface (2.38) is evaluated through the GetF() method. The state parameter (2.25) is calculated by the method GetPsi() and the normal to the yield surface **n** is evaluated by GetNormalToYield() (cf. (2.40)). Elastic moduli are calculated in GetElasticModuli() following (2.32) and (2.33). It is worth noting that this method evaluates whether the first shearing is taking place, or the material has just experienced a shear reversal. To this aim, an additional member variable called mConsolidationStage() is implemented in the code. When the variable is set to 0, it means that a gravity analysis is going to be performed, while when it is switched to 1, the system is subjected to a dynamic loading. Taking advantage of the parsing, from the Tcl file, the value of this variable can be changed when the gravity analysis ends. In this manner, eventual early identifications of shear reversals are carefully avoided and an additional tolerance to be calibrated is not introduced.

Then, GetLodeAngle() determines the current Lode Angle in terms of invariants (2.42): it first checks whether the mean pressure is lower than p_{min}, then it calculates $\bar{\mathbf{r}}$ and consequently, invariants in terms of $\bar{\mathbf{r}}$ as well. Then, an if statement evaluates the load condition of the element (i.e., if gravity or dynamic loadings are applied on the element) and finally, being $\cos(3\theta)$ bounded in the interval range [1,-1], these limits are checked. In the end, the value of $\cos(3\theta)$ is returned.

More complex is the role of GetStateDependent(). It applies the mapping rule and evaluates the plastic flow in the constitutive model. In fact, all the stress-ratios and related quantities are here computed (cf. (2.27),(2.28), and (2.29)), in order to obtain the image back-stress ratios for the mapping rule (2.43) through the interpolation function (2.44). Furthermore, the distances from the current back-stress ratio and its

images on bounding and dilatancy surfaces are computed as well. In addition, the scalar value h_f (2.55) that accounts for the fabric evolution method and the magnitude of plastic (2.46) volumetric strains are here evaluated.

As it was repeatedly stressed in this chapter, a crucial point consists of the integration methods choice. The following paragraph describes this issue in detail.

3.5 INTEGRATION OF NONLINEAR CONSTITUTIVE EQUATIONS

The strong non-linearity described mathematically by the bounding surface constitutive models just enumerated translates into the impossibility to integrate analytically the constitutive relationships. Consequently, given an unknown strain increment, as usual in numerical codes, the corresponding stress increment is obtained by integrating the differential constitutive equations numerically. These differential equations consist in hardening rules and plastic potential gradients.

Numerical integration schemes can be subdivided into explicit methods and implicit methods. The former methods integrate equations at known stress states with consequent no iteration strictly required to predict final stress and, generally, consistency condition is not assured. This phenomenon is called yield surface drift. For this reason, it is prudent to provide the existence of a simple stress correction in order to assure that the stress state lies on the yield surface (Sloan et al., 2001). On the contrary, implicit methods compute the solution by considering iterative strategies where all the unknown variables are calculated at the end of the step increment. This guarantees that consistent stress states are automatically furnished in output. In this work, three explicit algorithms have been implemented for the NTUASand02 constitutive model, on the basis of Ghofrani (2018) and Chen and Arduino (2021): Forward Euler, Modified Euler and 4^{th} order Runge-Kutta. Some additional evaluations have also been performed with the implementation of the explicit Runge-Kutta-England (Sloan et al., 1987), Runge-Kutta-Dormand-Prince (Sloan et al., 2001) and the implicit Backward Euler Closest Point Projection Method (Ortiz and Simo, 1986) but no reliable results were obtained at the time of writing this document. The latter

integration scheme was implemented as in Ghofrani (2018), and the derivatives of the constitutive equations needed for its implementation are reported in Appendix A.
On the basis of what above mentioned, Forward Euler, Modified Euler and 4th order Runge-Kutta integration schemes are briefly reported in the following. For further details see Ghofrani (2018) and Chen and Arduino (2021).

3.5.1 FORWARD EULER

The set of ordinary differential equations to be solved with the above-mentioned integration schemes can be expressed in vector terms as in (3.1), while the initial conditions are summarized in (3.2):

$$\dot{\mathbf{u}} = \mathbf{f}(\mathbf{u}) \tag{3.1}$$

$$\mathbf{u}(\mathbf{0}) = \mathbf{0} \tag{3.2}$$

In the previous (3.1) and (3.2), $\mathbf{u}$ is a k-component vector with component $u_1,\ldots,u_k$, where a generic u_j refers to a single variable whose value must be predicted by the integration scheme, while $\mathbf{f}(\mathbf{u})$ is a vector containing nonlinear functions $f_1(\mathbf{u}),\ldots,f_k(\mathbf{u})$ of the variables $u_1,\ldots,u_k$.

The local truncation error of an integration scheme can be evaluated through the difference between the actual solution of the differential equations and the solution predicted by the integration scheme. It depends on the discretization of the solution domain and if the latter is identified as t, it is divided into k steps of amplitude Δt, and the error is $o(\Delta t)^2$, the method is referred to as first order accurate. Furthermore, if the error is $o(\Delta t)^3$, the scheme is said to be 2nd order accurate and so on. In the first order Forward Euler method, if $\mathbf{u^n}$ represents the value of $\mathbf{u}$ at the *n*-th step, the differential of $\mathbf{u}$ can be expressed, using Taylor's expansion and neglecting $o(\Delta t)^2$ together with higher order terms, as (3.3):

$$du(t_n) = \frac{du(t_n)}{dt_n} = f(u_n) \cong \frac{u^{n+1} - u^n}{\Delta t} \tag{3.3}$$

Consequently, the approximated solution is given in (3.4):

$$u^{n+1} = u^n + \Delta t f(u^n) \tag{3.4}$$

In order to properly work, the Forward Euler scheme needs small increments because it has a really small stability region and usually it drifts from the yield surface (Ghofrani, 2018).

3.5.2 MODIFIED EULER WITH SUBSTEPPING

The so-called Modified Euler integration scheme is a second-order accurate scheme, and it was developed by Sloan et al. (2001) based on Sloan (1987). The main enhancements consist in the implementation of a substepping technique with an error control and the use of a drift correction in order to satisfy the consistency condition.
The method performs calculations in two different steps. The former allows the calculation of the solution using the Forward Euler technique at half the step amplitude with the calculation of the differential function, which is used to identify the resulting solution for the next step. The whole method is summarized in the steps shown in (3.5) and (3.6):

$$\hat{u}^{n+1/2} = u^n + \frac{\Delta t}{2} f(u^n) \tag{3.5}$$

$$u^{n+1} = u^n + \Delta t f\left(\hat{u}^{n+1/2}\right) \tag{3.6}$$

A measure of the local truncation error E can be estimated on the basis of the ratio between u^{n+1} and $\hat{u}^{n+1/2}$, while the current strain increment is modified iteratively based on E in the following manner of (3.7):

$$\Delta\varepsilon^m = \beta \Delta\varepsilon^c \tag{3.7}$$

where $\Delta\varepsilon^{m}$ represents the modified strain increment, obtained from the current strain increment $\Delta\varepsilon^{c}$. In addition, the coefficient β to evaluate the step amplitude at the step n+1 is estimated through the local error E and a fixed tolerance STOL as it is expressed in (3.8):

$$\beta = 0.8\left(\frac{\mathrm{STOL}}{\mathrm{E}}\right)^{0.5} \tag{3.8}$$

The coefficient β is constrained between the values 0.1 and 2 in Sloan et al. (2001), while experience suggests reducing these boundaries to 0.1 and 0.5 (see Anandarajah, 2011).

This algorithm also provides a procedure to calculate the transition from elastic to elasto-plastic states and a correction of the stress response to the yield surface to guarantee a consistent solution. In fact, when the current stress $\boldsymbol{\sigma_n}$ lies within the region of the yield surface, an elastic predictor $\boldsymbol{\sigma}_{n+1}^{tr,e}$must be evaluated in order to check whether the state has switched from elastic to plastic. If $\boldsymbol{\sigma_n}$ is inside the yield surface and $\boldsymbol{\sigma}_{n+1}^{tr,e}$ lies inside it as well, the whole step is elastic, while if $f\left(\boldsymbol{\sigma}_{n+1}^{tr,e}, \boldsymbol{\alpha}\right) > 0$, the state is composed, on the basis of additive decomposition, by an elastic and a plastic part. The condition $f\left(\boldsymbol{\sigma}_{n+1}^{tr,e}, \boldsymbol{\alpha}\right) > 0$ can be replaced by $f\left(\boldsymbol{\sigma}_{n+1}^{tr,e}, \boldsymbol{\alpha}\right) >$ FTOL, where FTOL is a small tolerance assumed to be $1x10^{-7}$ for NTUASand02 because Sloan et al. (2001) suggested to take this value between $1x10^{-6}$ and $1x10^{-9}$. Worth noticing that this parameter is included among the optional parameters and its value can be chahnged by the user. Consequently, the intersection with the yield surface must be found to apply a plastic correction. This consists in finding the value of the scalar α so that the following (3.9) is satisfied:

$$f\left(\boldsymbol{\sigma_n} + \alpha\left(\boldsymbol{\sigma}_{n+1}^{tr,e} - \boldsymbol{\sigma_n}\right)\right) = 0; \quad \alpha \in [0; 1] \tag{3.9}$$

This can be made by exploiting the root-finding Pegasus procedure developed by Dowell and Jarratt (1972) for its unconditional convergence and for the lack of necessity to use derivatives. Attention must be paid if loading or unloading conditions

take place because the procedure changes accordingly. This approach is required because when elasto-plastic unloading occurs with an angle higher than 90° between the gradient of the yield surface $\partial \mathbf{f} / \partial \boldsymbol{\sigma}$ and the trial elastic stress increment, if the latter is outside the yield surface, the yield surface can be crossed twice. This condition cannot happen under elasto-plastic loading.

The interested reader can refer to Dowell and Jarratt (1972), while for its implementation in the integration of the elasto-plastic matrix for critical state constitutive models, Sloan et al. (2001) provide the full description of the algorithm.

However, at the end of each step, the drift (i.e., the divergence of the calculated state of stress from the yield surface) may take place and a correction of the response to the yield surface is needed. This can be made on the basis of Sloan et al. (2001), where the yield surface expression may be expanded in Taylor series and on the basis of the assigned increment, an unknown multiplier can be evaluated iteratively so that consistent response can be obtained.

3.5.3 4th ORDER RUNGE-KUTTA

The 4th order Runge-Kutta explicit integration scheme has also been implemented to integrate NTUASand02 on the basis of Chen and Arduino (2021). The four algorithm phases are reported in (3.10), (3.11), (3.12) and (3.13), respectively.

$$\hat{u}^{n+1/2} = u^n + \frac{\Delta t}{2} f(u^n) \tag{3.10}$$

$$\tilde{u}^{n+1/2} = u^n + \frac{\Delta t}{2} f\left(\hat{u}^{n+1/2}\right) \tag{3.11}$$

$$\tilde{u}^n = u^n + \Delta t f\left(\tilde{u}^{n+1/2}\right) \tag{3.12}$$

$$u^{n+1} = u^n + \frac{\Delta t}{6} f(u^n) + 2f\left(\hat{u}^{n+1/2}\right) + 2f\left(\tilde{u}^{n+1/2}\right) + f(\tilde{u}^n) \tag{3.13}$$

3.5.4 MATERIAL TANGENT STIFFNESS MATRIX

The formulation of the elasto-plastic constitutive matrix is clearly described in Potts and Zdravkovic (1999) and, for the sake of clarity it is briefly reported here with all the steps that must be followed to obtain it, as it is reported in (2.22) . It is the key ingredient for the relationship between incremental stresses and incremental strains, as shown in §2.2. This relationship can be written as follows in (3.14):

$$\Delta\boldsymbol{\sigma} = \mathbf{D}^{ep}\Delta\boldsymbol{\varepsilon} \tag{3.14}$$

Being valid the additive decomposition of strains (cf. (2.11)), the incremental strains can be split into an elastic part ($\boldsymbol{\Delta\varepsilon^e}$) and a plastic part ($\boldsymbol{\Delta\varepsilon^p}$):

$$\Delta\boldsymbol{\varepsilon} = \Delta\boldsymbol{\varepsilon}^e + \Delta\boldsymbol{\varepsilon}^p \tag{3.15}$$

Consequently, the relationship between the elastic strain increment and the incremental stresses yields to the (3.16):

$$\Delta\boldsymbol{\sigma} = \mathbf{D}\,\Delta\boldsymbol{\varepsilon^e} \tag{3.16}$$

In (3.16), **D** is the fourth-order tensor elastic stiffness matrix that in Voigt notation is a 6x6 tensor that assumes the form in (3.17).

$$\mathbf{D} = \begin{bmatrix} K+\frac{4}{3}G & K-\frac{2}{3}G & K-\frac{2}{3}G & 0 & 0 & 0 \\ K-\frac{2}{3}G & K+\frac{4}{3}G & K-\frac{2}{3}G & 0 & 0 & 0 \\ K-\frac{2}{3}G & K-\frac{2}{3}G & K+\frac{4}{3}G & 0 & 0 & 0 \\ 0 & 0 & 0 & G & 0 & 0 \\ 0 & 0 & 0 & 0 & G & 0 \\ 0 & 0 & 0 & 0 & 0 & G \end{bmatrix} \tag{3.17}$$

Combining the latter two (3.15) and (3.16), the incremental stresses can be alternatively written in the function of the plastic strains as (3.18):

$$\Delta\boldsymbol{\sigma} = \mathbf{D}\,(\Delta\boldsymbol{\varepsilon} - \Delta\boldsymbol{\varepsilon}^{\mathbf{p}}) \tag{3.18}$$

Furthermore, by applying the flow rule, plastic strain increments can be written on the basis of the plastic potential function gradient $\frac{\partial P(\boldsymbol{\sigma},\boldsymbol{\alpha})}{\partial\boldsymbol{\sigma}}$, where P represents the plastic potential function and $\boldsymbol{\alpha}$ represents hardening parameters, as (3.19):

$$\Delta\boldsymbol{\varepsilon}^{\mathbf{p}} = \Lambda\,\frac{\partial P(\boldsymbol{\sigma},\boldsymbol{\alpha})}{\partial\boldsymbol{\sigma}} \tag{3.19}$$

Λ is a scalar representing the plastic multiplier.

In addition, the latter (3.16), (3.18), and (3.19) can be combined yielding the (3.20):

$$\Delta\boldsymbol{\sigma} = \mathbf{D}\,\Delta\boldsymbol{\varepsilon} - \mathbf{D}\,\Lambda\,\frac{\partial P(\boldsymbol{\sigma},\boldsymbol{\alpha})}{\partial\boldsymbol{\sigma}} \tag{3.20}$$

Applying the consistency condition, in order to guarantee that in plasticity the stress state must satisfy the latter, one can write (3.21):

$$df(\boldsymbol{\sigma},\boldsymbol{\alpha}) = \frac{\partial f(\boldsymbol{\sigma},\boldsymbol{\alpha})}{\partial\boldsymbol{\sigma}}\Delta\boldsymbol{\sigma} + \frac{\partial f(\boldsymbol{\sigma},\boldsymbol{\alpha})}{\partial\boldsymbol{\alpha}}\Delta\boldsymbol{\alpha} \tag{3.21}$$

The (3.21) can be rearranged yielding the (3.22):

$$\Delta\boldsymbol{\sigma} = -\frac{\frac{\partial f(\boldsymbol{\sigma},\boldsymbol{\alpha})}{\partial \alpha}}{\frac{\partial f(\boldsymbol{\sigma},\boldsymbol{\alpha})}{\partial \boldsymbol{\sigma}}}\Delta\boldsymbol{\alpha} \tag{3.22}$$

Then, by combining (3.20) and (3.22), in order to calculate the plastic multiplier Λ, one has, consequently, (3.23), (3.24) and (3.25):

$$\mathbf{D}\,\Delta\boldsymbol{\varepsilon} - \mathbf{D}\,\Lambda\,\frac{\partial P(\boldsymbol{\sigma},\boldsymbol{\alpha})}{\partial \boldsymbol{\sigma}} = -\frac{\frac{\partial f(\boldsymbol{\sigma},\boldsymbol{\alpha})}{\partial \boldsymbol{\alpha}}}{\frac{\partial f(\boldsymbol{\sigma},\boldsymbol{\alpha})}{\partial \boldsymbol{\sigma}}}\Delta\boldsymbol{\alpha} \tag{3.23}$$

$$\mathbf{D}\,\Delta\boldsymbol{\varepsilon} = \Lambda\left(\mathbf{D}\,\frac{\partial P(\boldsymbol{\sigma},\boldsymbol{\alpha})}{\partial \boldsymbol{\sigma}} - \frac{1}{\Lambda}\frac{\frac{\partial f(\boldsymbol{\sigma},\boldsymbol{\alpha})}{\partial \boldsymbol{\alpha}}}{\frac{\partial f(\boldsymbol{\sigma},\boldsymbol{\alpha})}{\partial \boldsymbol{\sigma}}}\Delta\boldsymbol{\alpha}\right) \tag{3.24}$$

$$\Lambda = \frac{\mathbf{D}\,\Delta\boldsymbol{\varepsilon}}{\mathbf{D}\,\frac{\partial P(\boldsymbol{\sigma},\boldsymbol{\alpha})}{\partial \boldsymbol{\sigma}} - \frac{1}{\Lambda}\frac{\frac{\partial f(\boldsymbol{\sigma},\boldsymbol{\alpha})}{\partial \boldsymbol{\alpha}}\Delta\boldsymbol{\alpha}}{\frac{\partial f(\boldsymbol{\sigma},\boldsymbol{\alpha})}{\partial \boldsymbol{\sigma}}}} \tag{3.25}$$

Then, multiplying both numerator and denominator by $\frac{\partial f(\boldsymbol{\sigma},\boldsymbol{\alpha})}{\partial \boldsymbol{\sigma}}$, and assuming that $K_p = -\frac{1}{\Lambda}\frac{\partial f(\boldsymbol{\sigma},\boldsymbol{\alpha})}{\partial \boldsymbol{\alpha}}\Delta\boldsymbol{\alpha}$, the plastic multiplier assumes the form of the (3.26):

$$\Lambda = \frac{\frac{\partial f(\boldsymbol{\sigma},\boldsymbol{\alpha})}{\partial \boldsymbol{\sigma}}\mathbf{D}}{\frac{\partial f(\boldsymbol{\sigma},\boldsymbol{\alpha})}{\partial \boldsymbol{\sigma}}\mathbf{D}\,\frac{\partial P(\boldsymbol{\sigma},\boldsymbol{\alpha})}{\partial \boldsymbol{\sigma}} + K_p}\Delta\boldsymbol{\varepsilon} \tag{3.26}$$

Finally, by substituting (3.26) in (3.20), the (3.27) is obtained:

$$\Delta\boldsymbol{\sigma} = \mathbf{D}\,\Delta\boldsymbol{\varepsilon} - \frac{\mathbf{D}\,\frac{\partial P(\boldsymbol{\sigma},\boldsymbol{\alpha})}{\partial \boldsymbol{\sigma}}\frac{\partial f(\boldsymbol{\sigma},\boldsymbol{\alpha})}{\partial \boldsymbol{\sigma}}\mathbf{D}}{\frac{\partial f(\boldsymbol{\sigma},\boldsymbol{\alpha})}{\partial \boldsymbol{\sigma}}\mathbf{D}\,\frac{\partial P(\boldsymbol{\sigma},\boldsymbol{\alpha})}{\partial \boldsymbol{\sigma}} + K_p}\Delta\boldsymbol{\varepsilon} \tag{3.27}$$

A direct consequence of the (3.27) is that the elasto-plastic stiffness matrix can be expressed as in (3.28):

$$\Delta\boldsymbol{\sigma} = \mathbf{D}^{\mathbf{ep}}\Delta\boldsymbol{\varepsilon} = \left(\mathbf{D} - \frac{\mathbf{D}\,\dfrac{\partial \mathrm{P}(\boldsymbol{\sigma},\boldsymbol{\alpha})}{\partial\boldsymbol{\sigma}}\dfrac{\partial \mathrm{f}(\boldsymbol{\sigma},\boldsymbol{\alpha})}{\partial\boldsymbol{\sigma}}\mathbf{D}}{\dfrac{\partial \mathrm{f}(\boldsymbol{\sigma},\boldsymbol{\alpha})}{\partial\boldsymbol{\sigma}}\mathbf{D}\,\dfrac{\partial \mathrm{P}(\boldsymbol{\sigma},\boldsymbol{\alpha})}{\partial\boldsymbol{\sigma}} + \mathrm{K_p}}\right)\Delta\boldsymbol{\varepsilon} \tag{3.28}$$

More specifically, referring to the NTUASand02 constitutive model, the following positions of (3.29) and (3.30) hold.

$$\frac{\partial \mathrm{f}(\boldsymbol{\sigma},\boldsymbol{\alpha})}{\partial\boldsymbol{\sigma}} = \mathbf{n} - \frac{\mathrm{V}}{3}\mathbf{I} \tag{3.29}$$

$$\frac{\partial \mathrm{P}(\boldsymbol{\sigma},\boldsymbol{\alpha})}{\partial\boldsymbol{\sigma}} = \mathbf{R} \tag{3.30}$$

Consequently, the elasto-plastic stiffness matrix can be expressed in the form of the (3.31).

$$\mathbf{D}^{\mathbf{ep}} = \frac{\left(\left(\mathbf{n} - \frac{\mathrm{V}}{3}\mathbf{I}\right):\mathbf{D}\right)\cdot(\mathbf{D}:\mathbf{R})}{\left(\mathbf{n} - \frac{\mathrm{V}}{3}\mathbf{I}\right):\mathbf{D}:\mathbf{R} + \mathrm{K_p}} \tag{3.31}$$

3.6 TCL COMMANDS

The NTUASand02 material, whose implementation has been described in this chapter, can be called through the OpenSees Tcl interpreter by using the following command.

```
nDMaterial NTUASand02  $matTag $nu $VoidRatio $Mc $lambda_c $ecs_a \\
$P_atm $m $h0 $A0 $B $a1 $gamma1 $Me $k_bc $k_dc $H0 $zeta \\
$SoilDen < $kappa $integrationScheme>
```

Here, $matTag is the material tag. The parameters inside <> are optional, so that if no values are assigned to $kappa, it is set to 2.0, as in Papadimitriou and Bouckovalas (2002). Furthermore, the different integration schemes can be selected, by assigning the following values to the $integrationScheme variable: 5 for Forward Euler, 1 for

Modified Euler with substepping, and 4 for fourth-order Runge-Kutta. The Modified Euler integration scheme with substepping is set as default. Obviously, the other integration schemes are implemented as well, and they will be object of future studies. Even the tolerances STOL and FTOL can be modified as additional parameters.

Among the different outputs that can be calculated for each element, the stress and strain vectors in Voigt notation can be obtained through the following commands.

```
recorder Element –ele $nElem –time –file stress.out stress

recorder Element –ele $nElem –time –file strain.out strain
```

where $nElem represents the tag of the desired element.

The use of nonlinear elastic or elastoplastic formulation of the material can be considered through the switching of the updateMaterialStage command from 0 to 1 as follows.

For elastic formulation:

```
updateMaterialStage –material $matTag –stage 0
```

For elastoplastic formulation:

```
updateMaterialStage –material $matTag –stage 1
```

Finally, the dynamic phase of the load can be activated using the command reported in the following.

```
updateMaterials –material $matTag ConsolidationStage 1
```

In the following chapters, some analyses performed using this implementation are shown.

3.7 REFERENCES

Anandarajah, A. (2011). Computational methods in elasticity and plasticity: solids and porous media. Springer-Verlag New York, New York.

Andrianopoulos K. I., Papadimitriou A. G., Bouckovalas G. D. (2010) Explicit integration of bounding surface model for the analysis of earthquake soil liquefaction,

International Journal for Numerical and Analytical Methods in Geomechanics, 34 (15): 1586-1614.

Brinkgreve R.B.J., Engin E. and Swolfs W.M. (2021). Plaxis V21.01 2021. Delft, Plaxis bv.

Carey, T.J. and Kutter B.L. (2017). Comparison of liquefaction constitutive models for ahypothetical sand; In: Proceedings of Geotechnical Frontiers 2017 GSP 281.

Chen L., Ghofrani A., and Arduino P. (2021). Remarks on numerical simulation of the LEAP-Asia-2019 centrifuge tests. Soil Dynamics and Earthquake Engineering, 2021, 142, 106541.

Chen L. and Arduino P. (2021). Implementation, verification and validation of the PM4SAND model in OpenSees. PEER Report No. 2021/02. Pacific Earthquake Engineering Research Center Headquarters, University of California, Berkeley, March 2021.

Chen, L., Ghofrani, A. and Arduino, P. (2019). Prediction of LEAP-UCD-2017 centrifuge test results using two advanced plasticity sand models. In B. Kutter et al. (Eds.), Model tests and numerical simulations of liquefaction and lateral spreading: LEAP-UCD-2017. New York: Springer.

Dowell M. and Jarratt P. (1972). The Pegasus method for computing the root of an equation, BIT, Vol. 12, pp. 503-8.

Fasano G., Nappa V., Özcebe A.G., Bilotta E. (2021). Numerical modelling of the effect of horizontal drains in centrifuge tests on soil-structure interaction in liquefiable soils. Bulletin of Earthquake Engineering (2021) 19:3895–3931 https://doi.org/10.1007/s10518-021-01084-2.

Ghofrani A. (2018). Development of Numerical Tools For the Evaluation of Pile Response to Laterally Spreading Soi. Ph.D. Thesis, The University of Washington, Seattle.

Ghofrani A. and Arduino P. (2016). Prediction of LEAP centrifuge test results using a pressure-dependent bounding surface constitutive model Soil Dynamics and Earthquake Engineering (2016), http://dx.doi.org/10.1016/j.soildyn.2016.12.001.

Itasca Consulting Group, Inc. (2019). FLAC — Fast Lagrangian Analysis of Continua, Ver. 8.1. Minneapolis: Itasca.

Liu, H., Diambra, A., Abell J.A., Pisanò, F. (2020). Memory-enhanced plasticity modeling of sand behaviour under undrained cyclic loading. J. Geotech. Geoenviron. Eng., 2020, 146(11): 04020122.

Mazzoni S., McKenna F., Scott M.H., Fenves G.L. and Jeremic B. (2007). OpenSees command language manual. Pacific Earthquake Engineering Research Center. University of California, Berkeley.

McAllister G., Taiebat M., Ghofrani A., Chen L. and Arduino P. (2015). Nonlinear site response analyses and high dilation pulses. In: Proceedings of GeoQuèbec 2015. Challenges from North to South.

McGann C. R., Arduino P. and Mackenzie-Helnwein P. (2012). Stabilized single-point 4-node quadrilateral element for dynamic analysis of fluid saturated porous media. Acta Geotechnica, 7(4), 297-311.

McGann C. R., Arduino P. and Mackenzie-Helnwein P. (2015). A stabilized single-point finite element formulation for three-dimensional dynamic analysis of saturated soils. Computers and Geotechnics 66, 126–141.

McKenna F. (1997). Object-oriented finite element analysis: Frameworks for analysis, algorithms and parallel computing. Ph.D. dissertation, Univ. of California, Berkeley, CA.

McKenna F. (2011). OpenSees: A Framework for Earthquake Engineering Simulation. Earthquake Engineering Simulation. 1521-9615/11/$26.00 2011 IEEE. Copublished by the IEEE CS and the AIP.

McKenna F., Fenves G. L., Scott M. H. and Jeremić B. (2000). Open system for earthquake engineering simulation. http:// opensees.berkeley.edu.

Ortiz M., Simo J. C. (1986). An analysis of a new class of integration algorithms for elastoplastic constitutive relations. International Journal for Numerical Methods in Engineering, 23 (3). pp. 353-366. ISSN 0029-5981.

Papadimitriou A. G., Bouckovalas G. D. (2002). Plasticity model for sand under small and large cyclic strains: a multiaxial formulation, Soil Dynamics and Earthquake Engineering, 22: 191-204.

Potts D.M., Zdravkovic L. (1999). Finite element analysis in geotechnical engineering: Theory. London: Thomas Telford.

Ramirez J., Barrero R.A., Chen L., Dashti S., Ghofrani A., Taiebat M. and Arduino P. (2018). Site response in a layered liquefiable deposit: evaluation of different numerical tools and methodologies with centrifuge experimental results. J Geotech Geoenviron ASCE 2018;144(10) https://doi.org/10.1061/(ASCE)GT.1943-5606.0001947.

Scott M.H. and Fenves G. (2001). How to introduce a New Material into OpenSees. Version 1.1. August, 21, 2001. PEER, University of California, Berkeley.

Sloan S.W., Abbo A.J. and Sheng D. (2001). Refined explicit integration of elastoplastic models with automatic error control. Eng Comput 2001;18(1/2):121–94. http://dx.doi.org/10.1108/02644400110365842.

Sloan, S.W. (1987). Substepping schemes for the numerical integration of elastoplastic stress strain relations, International Journal for Numerical Methods in Engineering, Vol. 24, pp. 893-911.

Taborda D.M.G., Zdravković L., Kontoe S., Potts D.M. (2014). Computational study on the modification of a bounding surface plasticity model for sand, Computers and Geotechnics, 94, 22-30.

4 VALIDATION AND VERIFICATION OF THE NTUASAND02 CONSTITUTIVE MODEL IN OPENSEES

4.1 INTRODUCTION

In this chapter, the most relevant tests performed to verify and validate the implementation of the constitutive model proposed by Papadimitriou and Bouckovalas (2002) into the OpenSees framework (identified through the code NTUASand02, as it was stressed in §2.4.1) are presented. Verification and validation should be distinguished: verification aims at detecting eventual programming bugs in the source code, while validation is the process playing the role to assess whether a real phenomenon could be accurately reproduced (Chen and Arduino, 2021). For this reason, the verification and validation procedure is here conducted at the element level by performing drained and undrained, monotonic and cyclic triaxial tests and direct simple shear tests. To this aim, elemental responses simulated in various papers adopting different versions of the model are reproduced. The tests simulated in this work are reported in Papadimitriou and Bouckovalas (2002), in Papadimitriou et al. (2001), and in Andrianopoulos et al. (2010a), in the verification procedure of the respective versions of the constitutive model. As it was discussed in §2.4.1, the model has already been implemented in Abaqus by Miriano (2010) and a constitutive driver exploiting the Bardet and Choucair (1991) procedure was built by Martinelli in the context of the same work developed by Miriano (2010). On the contrary, in Andrianopoulos et al. (2010b), the model was modified considering a different mapping rule and a vanishing elastic region and it was implemented in the FLAC code (Andrianopoulos et al., 2010a). For the above-mentioned reasons, the latter works will be re-called in this chapter and comparisons will be presented. One cyclic triaxial liquefaction test, one undrained cyclic direct simple shear test, three undrained

monotonic triaxial tests and two drained monotonic triaxial tests performed within the VELACS project (see Arulmoli et al., 1992) are employed to verify the implementation in OpenSees. In addition, one cyclic direct simple shear test and one cyclic triaxial test are simulated in drained conditions to verify whether the model can reproduce certain stress paths, even without the pore water pressure development. Furthermore, different finite elements available in the OpenSees framework are adopted. A general good agreement between simulated and target curves provided by the various Authors is reached. However, the discrepancies that eventually arise can be related either to the different finite element frameworks (e.g., Abaqus and OpenSees) or to the different solution strategies (e.g., finite elements and finite difference). Furthermore, these discrepancies should be small or neglectable. It is worth noting that neither all the details on the integration strategy taken into account in the original implementation of the model nor some details on the initial conditions assumed for the testing procedure are provided in Papadimitriou and Bouckovalas (2002), whose simulations are selected as the benchmark. Some results of the study are shown in Fierro et al. (2022). In absence of any further indication, the analyses reported in the following chapters are conducted using the Modified Euler scheme with substepping.

4.2 ELEMENT TESTS

The first task that a new constitutive model implemented within a numerical code should be able to fulfill consists in the simulation of the response of soil at the element level. This is required because the first step of the validation of the model is oriented towards the testing of homogeneous conditions: in fact, homogeneous boundary conditions should lead to a homogeneous response in terms of stress and state variables at each integration point. For example, a crucial point is represented by its ability to reproduce the stress paths and the stress-strain response obtained in drained and undrained cyclic triaxial and direct simple shear loading conditions. Obviously, with reference to the specific constitutive model accounted for in this study, its main goal is the reproduction of the soil response in undrained conditions at high strain levels, when

soil liquefaction is triggered. However, at the same time, the model should be able to reproduce even the response under monotonic loadings with and without the pore water pressure development. To this aim, the verification and validation procedure of the implementation in OpenSees have been based on the tests summarized in Table 4.1. In particular, Table 4.1 reports all the tests performed to validate the implementation of the model in OpenSees. In addition, the undrained cyclic triaxial and undrained monotonic triaxial tests are reproduced in drained conditions too, in order to investigate whether the model is able to correctly catch the stress paths with drainage allowed. Furthermore, the undrained and drained monotonic triaxial tests performed in Papadimitriou et al. (2001) and in Andrianopoulos et al. (2010a) are adopted to reach two goals: on the one hand, they certify the suitability of the implementation to reproduce the response under monotonic loadings, on the other hand, they validate the different integration schemes implemented in the code.

Table 4.1. Element tests simulated for the verification and validation of the model.

Test Type	Test Reference	Simulation Reference	Confining Pressure (kPa)	Initial Void Ratio (-)
Undrained Cyclic Triaxial	Arulmoli et al. (1992)	Papadimitriou and Bouckovalas (2002)	80	0.73
Undrained Cyclic Direct Simple Shear			160	0.66
Undrained Monotonic Triaxial		Papadimitriou et al. (2001)	160 / 80 / 40	0.66
Drained Monotonic Triaxial		Andrianopoulos et al. (2010a)	80	0.66 / 0.73
Drained Cyclic Triaxial	Arulmoli et al. (1992)	Papadimitriou and Bouckovalas (2002)	80	0.73
Drained Monotonic Triaxial		Papadimitriou et al. (2001)	80	0.66

The constitutive parameters assigned to the NTUASand02 material for the testing procedures are obtained from the calibration reported in Papadimitriou and Bouckovalas (2002) for Nevada sand. It is worth noting that the sole parameter B varies as a function of the test type: it assumes the value of 520 in the case of cyclic test and

its value is set to 200 for monotonic tests. Its role has been explained in §2.4.1. For the sake of clarity, all the assigned parameters are reported in the following Table 4.2.

Table 4.2. Parameters adopted for NTUASand02 within the verification and validation procedure of the OpenSees implementation.

Parameter	**Value**	**Unit**	**Meaning**
$(e_{cs})_a$	0.809	[-]	CSL Location in the e-ln(p) space
λ	0.022	[-]	CSL Location in the e-ln(p) space
M_c^c	1.25	[-]	Critical state strength in triaxial compression
M_e^c	0.9	[-]	Critical state strength in triaxial extension
B	520 - 200	[-]	Elastic shear modulus constant
a_1	0.67	[-]	Non-linearity of the elastic shear modulus
γ_1	0.00025	[-]	Strain limit of elastic modulus degradation
ν	0.31	[-]	Poisson's ratio
k_c^b	1.45	[-]	Effect of ψ on peak stress ratio
k_c^d	0.3	[-]	Effect of ψ on stress ratio at PT
A_o	2.1	[-]	Dilatancy constant
h_o	5000	[-]	Plastic modulus constant
H_o	68000	[-]	Fabric index constant
ζ	1.0	[-]	Effect of major principal stress on fabric index
e_{init}	0.66 – 0.73	[-]	Initial void ratio
p_{atm}	98.1	[kPa]	Atmospheric pressure
m	0.0625	[-]	Yield surface constant
ρ	2.0	[ton/m^3]	Soil density

Finally, in the following paragraphs, a detailed description of each test is reported.

4.3 FINITE ELEMENTS ADOPTED IN THE SIMULATIONS

The numerical simulations of the above-mentioned tests are performed by considering the different finite elements available in the OpenSees framework in order to observe the different responses. The plane-strain conditions are reproduced using four node quadUP, SSPquadUP (see McGann et al., 2012), and nine four node quadUP elements.

Briefly, the four node quadUP element is a plane-strain element that adopts the bilinear isoparametric formulation and it was developed to reproduce the response of solid-fluid fully coupled material under dynamic loading. It relies on a mixed displacement-pressure u-p formulation (where u stands for the displacement degrees-of-freedom and p stands for the pore water pressure degree-of-freedom) based on the Biot's theory (1941), then adapted by Zienkiewicz and Shiomi (1984). In particular, the element provides four nodes, and each node has 3 degrees of freedom (DOFs): two for the displacements (horizontal and vertical) and one for the pore water pressure. The stress-strain response is calculated at four integration points. An extension of the quadUP element is represented by the SSPquadUP element that includes additional physical hourglass stabilization to allow the single point integration (SSP). Consequently, the stress-strain response is calculated at an integration point located at the center of the element. This feature is of vital importance to save computational time that represents a non-trivial aspect in the analysis of large domains. In particular, volumetric locking and shear locking are avoided by setting the shear strain and the volumetric dilation generated by hourglass modes to zero. In addition, equal-order interpolation is applied for all the DOFs, but a non-residual stabilization of the fluid phase avoids the instability in the incompressible-impermeable limit, also known as inf-sup or Babuška-Brezzi condition (Brezzi and Fortin, 1991). This goal is reached through the use of a stabilization coefficient, referred to as α, and depending on the height of the finite element, the speed of the elastic wave propagation and the mass density of the solid phase (McGann et al., 2012). The nine-four node quadUP element represents a nine-nodes plane-strain quadrilateral element, where the nodes at the corners have 3 DOFs and the other nodes are equipped with displacement DOFs only.

With reference to the hexhedral elements, SSPbrick, SSPbrickUP elements (McGann et al., 2015), and brickUP element are considered for the simulations. The former basically consists of an eight-nodes tri-dimensional hexahedral element, with each node having three displacement degrees-of-freedom. In this case, the response is calculated once more at a point located at the center of the element, while the

stabilization is allowed using the parameter α, function of the height of the finite element, and of the bulk and shear moduli of the solid phase of the soil. The SSPbrickUP element differs from the SSPbrick because it provides an additional pore pressure degree-of-freedom at each node. The response under undrained conditions considering hexahedral elements is analyzed also with brickUP elements: the latter is an eight-node linear isoparametric element with three DOFs for displacement and one DOF for pore water pressure; the response is given at the eight Gauss points because the single-stabilization point technique is not provided.

Figure 4.1 reports a sketch of the finite elements previously described.

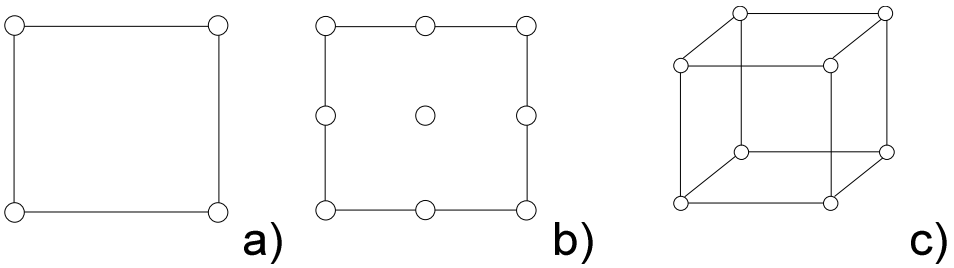

Figure 4.1. Schematic of SSPquadUP and quadUP elements (a), nine-four nodes quadUP element (b) and SSPbrick, SSPbrickUP, and brickUP element (c).

4.4 DRAINED MONOTONIC TRIAXIAL TESTS SIMULATIONS

Two drained monotonic triaxial tests are analyzed to check the goodness of the implementation and to verify the model. These tests were exploited by Andrianopoulos et al. (2010a). Both tests are performed during the VELACS project (Arulmoli et al., 1992) at 80 kPa confining pressure and both 60% and 40% relative density on Nevada Sand, meaning 0.73 and 0.66 void ratios, respectively. The SSPbrick element was adopted to reproduce drained conditions. The test set up consists in the application of the confining pressure through nodal loads and in the following stage, a monotonic displacement increment is applied in the vertical direction. A load-control integrator with a Newton algorithm is exploited, while the mapping between the DOFs and equation number (numberer command in OpenSees) is constructed by considering a reverse Cuthill-McKee scheme (Cuthill and McKee, 1969). The linear system of

equations is built using the BandGeneral SOE. The ConsolidationStage flag (see §3.4 and §3.6 for further details) is switched at the end of consolidation. Finally, constraints are enforced through the Transformation constraint handler and the norm displacement increment test with a tolerance of 1 $x10^{-5}$ controls the convergence of the analysis.

The comparison is reported in terms of volumetric vs. axial strain in Figure 4.2. In Figure 4.2a, the simulated results with the current implementation in OpenSees (OpenSEES Implementation) are shown, while in Figure 4.2b, the simulations conducted by Andrianopoulos et al. (2010a) in FLAC are compared to the curves resulting from the laboratory tests performed in the framework of the VELACS project (Experimental Data).

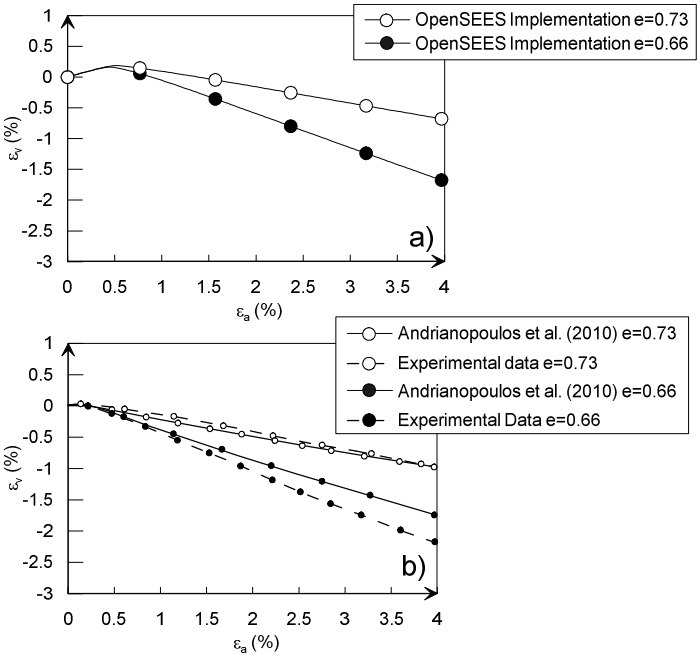

Figure 4.2. Drained monotonic triaxial tests performed at 80kPa initial confining pressure and both 0.73 and 0.66 void ratios: OpenSees implementation (a); simulations by Andrianopoulos et al. (2010b).

A general agreement is observed between the simulations provided by Andrianopoulos et al. (2010b) and the current implementation of the model considering the reached volumetric strain.

Then, a monotonic triaxial test is here reproduced in drained conditions considering a mean effective confining pressure of 80 kPa. Such a test has not been conducted in the framework of the VELACS project and it has been performed in order to understand whether the theoretical response of this loading condition is correctly reproduced. In this case, the drained conditions are guaranteed by fixing pore water pressure degrees of freedom of each node. The deviatoric stress vs axial strain curve and the stress path are shown in Figure 4.3, considering a unit brickUP element, and in Figure 4.4, considering the SSPbrickUP element. The test set up consists in the application of the confining pressure through nodal loads, then a deviatoric load is applied vertically to the upper nodes only.

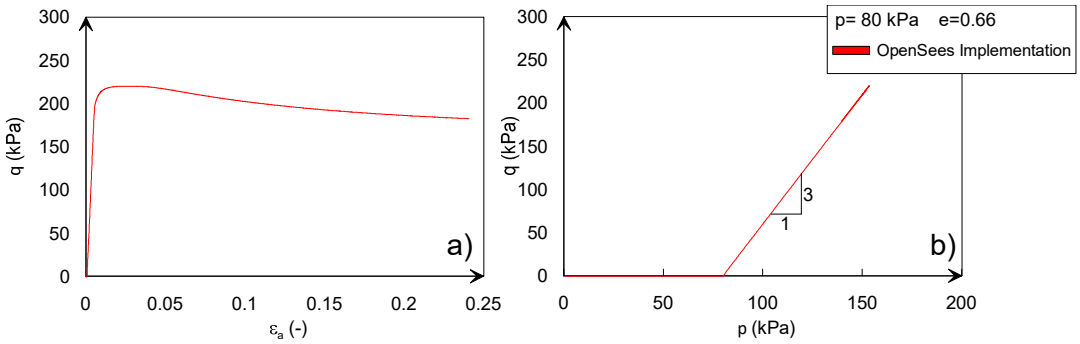

Figure 4.3. Deviatoric stress vs axial strain curve (a) and stress path (b) in drained triaxial test at 80 kPa confining pressure and 0.66 void ratio using brickUP element.

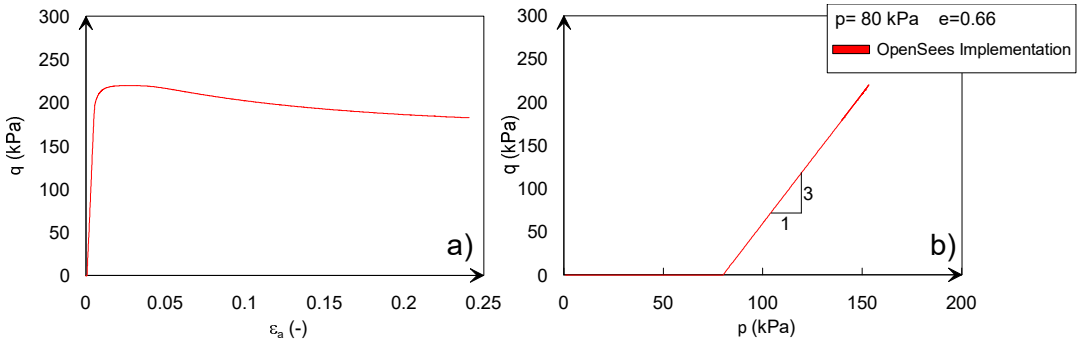

Figure 4.4. Deviatoric stress vs axial strain curve (a) and stress path (b) in drained triaxial test at 80 kPa confining pressure and 0.66 void ratio using SSPbrickUP element.

The curves observed in Figure 4.3 and Figure 4.4 highlight the same response considering both the elements and the reliability of the model to simulate drained

response: in fact, in Figure 4.3a and Figure 4.4a, the typical response of a dilative sand is reproduced, while in Figure 4.3b and Figure 4.4b the 3:1 slope of the stress path in drained conditions under monotonic loading is well caught.

4.5 UNDRAINED MONOTONIC TRIAXIAL TESTS SIMULATIONS

The second step of the verification procedure to validate the current implementation consists in the reproduction of undrained monotonic triaxial tests. For example, Miriano (2010) shows the comparison of the simulations conducted adopting the umat routine in Abaqus with those reported in Papadimitriou et al. (2001), where the tri-axial formulation of the constitutive model is presented. The tests were performed with an initial void ratio equal to 0.66 at different confining pressures (p=40 kPa, p=80 kPa, p=160 kPa). These tests are reproduced by implementing a Tcl script in OpenSees and adopting both brickUP and SSPbrickUP hexahedral elements. The load-control test is conducted using an explicit Newmark integrator with the γ and β parameters equal to 0.5 and 0.25, respectively. The norm displacement increment test with a tolerance of $1x10^{-5}$ controls the convergence of the analysis.

The response in terms of deviatoric stress versus axial strain is reported in Figure 4.5 and Figure 4.6.

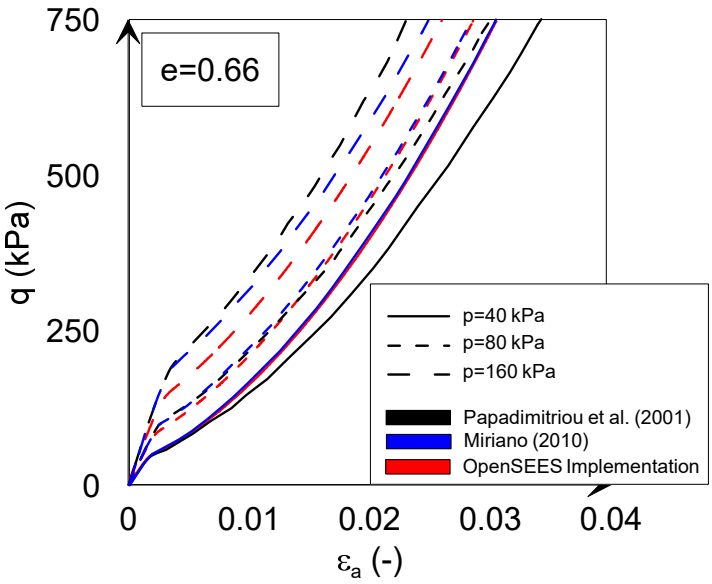

Figure 4.5. Simulations of undrained monotonic triaxial tests at different confining pressures (40 kPa, 80 kPa, and 160 kPa) using the implemented constitutive model with brickUP hexahedral elements (red curve).

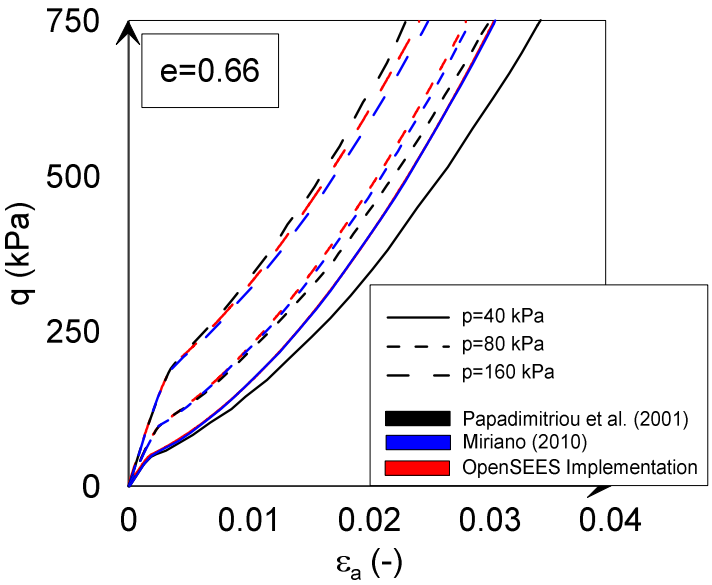

Figure 4.6. Simulations of undrained monotonic triaxial tests at different confining pressures (40 kPa, 80 kPa, and 160 kPa) using the implemented constitutive model with SSPbrickUP hexahedral elements (red curve).

The undrained monotonic tests show a complete agreement in the comparison between the results obtained with the current implementation and those resulting from the implementation provided by Miriano (2010). In addition, a perfect correspondence is obtained in the cases of mean effective consolidation pressures of 40 kPa and 80 kPa between the current implementation using both the finite elements and Miriano (2010), while some slight differences emerge for p=160 kPa. In this case, the current implementation with SSPbrickUP has a stiffer response, closer to the original implementation, if compared to the results obtained by Miriano (2010) and the simulations deriving from the use of the brickUP element. Generally, all the simulations (included Miriano, 2010) show a stiffer response if compared to the original implementation of the model for the cases of p=40 kPa and p=80kPa, while the response is softer for 160 kPa mean effective pressure.

The test with a mean pressure of 80 kPa is also performed at the element level in OpenSees using the SSPbrickUP element to validate the response obtained adopting the three implemented integration schemes: Modified Euler with stress correction (set as the default scheme in the code), Forward Euler and 4^{th} order Runge-Kutta. The tests are also conducted using Runge-Kutta-Dormand-Prince and Runge-Kutta-England schemes, but convergence issues arised and the response is not judged reliable at the time of writing this work. In Figure 4.7 the responses obtained adopting the different integration schemes are reported. More in detail, all the schemes reproduce a satisfactory agreement in the deviatoric stress-axial strain curves (Figure 4.7a), which is evident even considering a zoom-in limiting the strain level (Figure 4.7b)

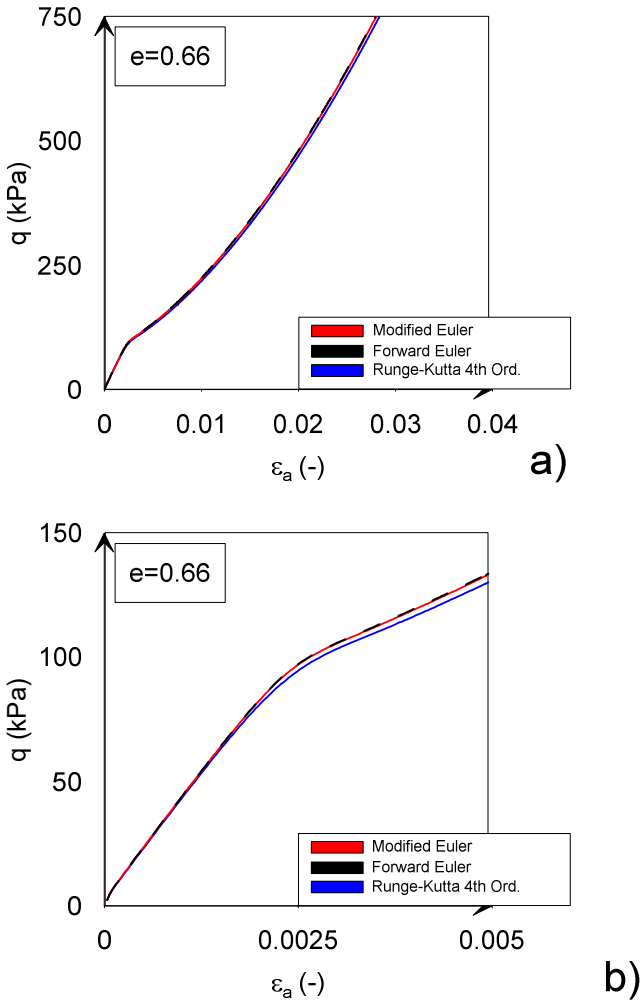

Figure 4.7. Comparison between the simulations of the undrained monotonic triaxial test at 80 kPa confining pressure using different integration schemes.

4.6 UNDRAINED CYCLIC DIRECT SIMPLE SHEAR TESTS SIMULATIONS

The undrained cyclic direct simple shear (DSS) test reported in Arulmoli et al. (1992) is adopted to validate the constitutive model in Papadimitriou and Bouckovalas (2002). The load-control test was performed on a soil sample of 60% relative density, which corresponds to a 0.66 initial void ratio for Nevada Sand. The test is identified as 60-09 in the VELACS report. For the sake of clarity, an extract of the report is shown in the following Figure 4.8.

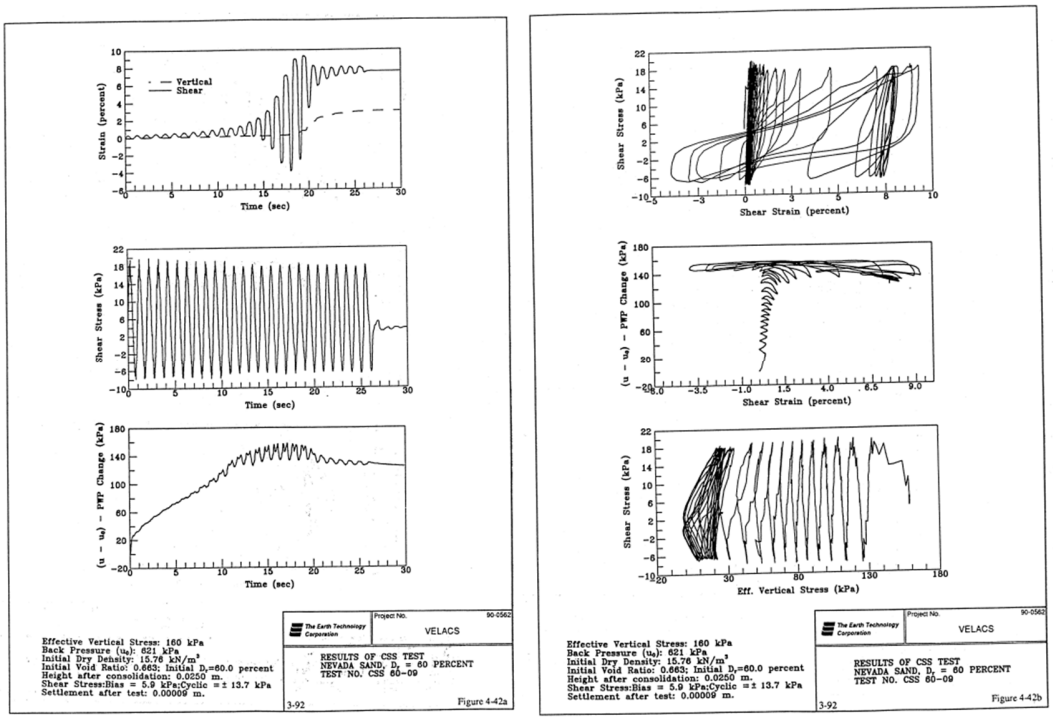

Figure 4.8. Extract of the cyclic direct simple shear test 60-09 from VELACS report (from Arulmoli et al., 1992).

The test was performed applying an effective consolidation stress of 160 kPa with a load bias of 5.9 kPa (i.e., non-zero shear stress during this stage is applied). The dynamic stage of the test is performed through a cyclic shear stress with a frequency of 1 Hz, a duration of 26 s and an amplitude of 13.7 kPa.

The numerical simulations of the test are performed by considering the different finite elements available in the OpenSees framework in order to observe the different responses. The plane-strain conditions are reproduced using four node quadUP, SSPquadUP (see McGann et al., 2012), nine four node quadUP elements and, for the sake of comparison, SSPbrickUP element (McGann et al., 2015).

In order to reproduce the laboratory tests, loads are applied as nodal forces to the plane-strain elements. Nodal forces are calculated by multiplying the desired pressure by the tributary area of each node. More in detail, in the consolidation stage, vertical nodal loads are applied to the upper nodes with a non-zero shear stress (i.e., horizontal forces are applied to the upper nodes of the elements). The base nodes are not allowed to move

and both translational DOFs are constrained, while upper nodes' translational DOFs are tied together to reproduce the pure shearing conditions. The pore water pressures of both couples of nodes are tied together. For the sake of clarity, the load configuration of the four-nodes quadUP element and for the four-nodes stabilized single point quadrilateral u-p (SSPquadUP) element is shown in Figure 4.9.

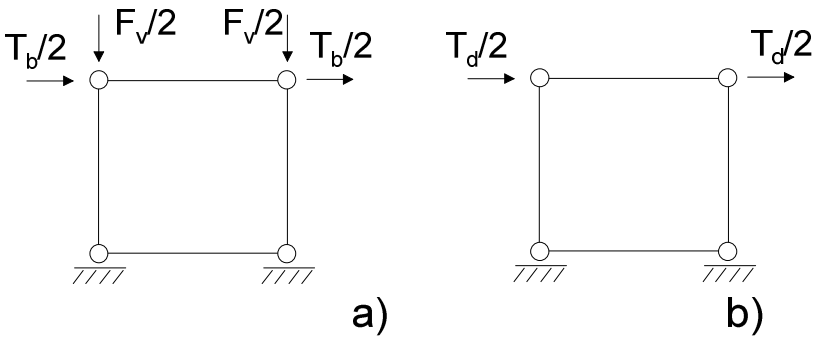

Figure 4.9. Load conditions for the plane-strain quadUP element and for the plane-strain SSPquadUP element in both consolidation (a) and dynamic (b) stages of the test.

Furthermore, the assigned intrinsic permeability is 5.6×10^{-6} m^3s/ton calculated by $k_{in} = k_{real}/(\rho_f \cdot g)$, where ρ_f represents the water density and g is the gravity acceleration. Being OpenSees unitless, the units must be selected accordingly. For this reason, the reference units are kN, m and s. As a consequence, material densities are assigned in $tons/m^3$. A quad element with a length of 0.1 m per side and the same thickness is implemented. The time step is assigned to be 0.0001s because the explicit Newmark integrator with the γ and β parameters equal to 0.5 and 0.25, respectively to ensure unconditional stability, is adopted. A small initial mass- and initial stiffness-proportional Rayleigh damping is added to ensure numerical stability. The ConsolidationStage flag (see §3.4 and §3.6 for further details) is switched at the end of consolidation. The mapping between the DOFs and equation number (numberer command in OpenSees) is constructed by considering a reverse Cuthill-McKee scheme (Cuthill and McKee, 1969), while the linear system of equations is built using the profileSPD SOE. A variable transient analysis is conducted in the dynamic stage, while a transient analysis is performed during the consolidation stage. Finally, constraints are

enforced through the Plain constraint handler and the norm displacement increment test with a tolerance of 1 $x10^{-5}$ controls the convergence of the analysis.

The simulations of the undrained cyclic direct simple shear test are reported in terms of τ-σ_y and τ-γ curves. In Figure 4.10, the element tests using different finite elements are reported. The obtained curves are compared to those in the original work of Papadimitriou and Bouckovalas (2002; indicated as "Papadimitriou and Bouckovalas 2002" in the figure) and the results obtained through the Abaqus umat by Miriano (2010).

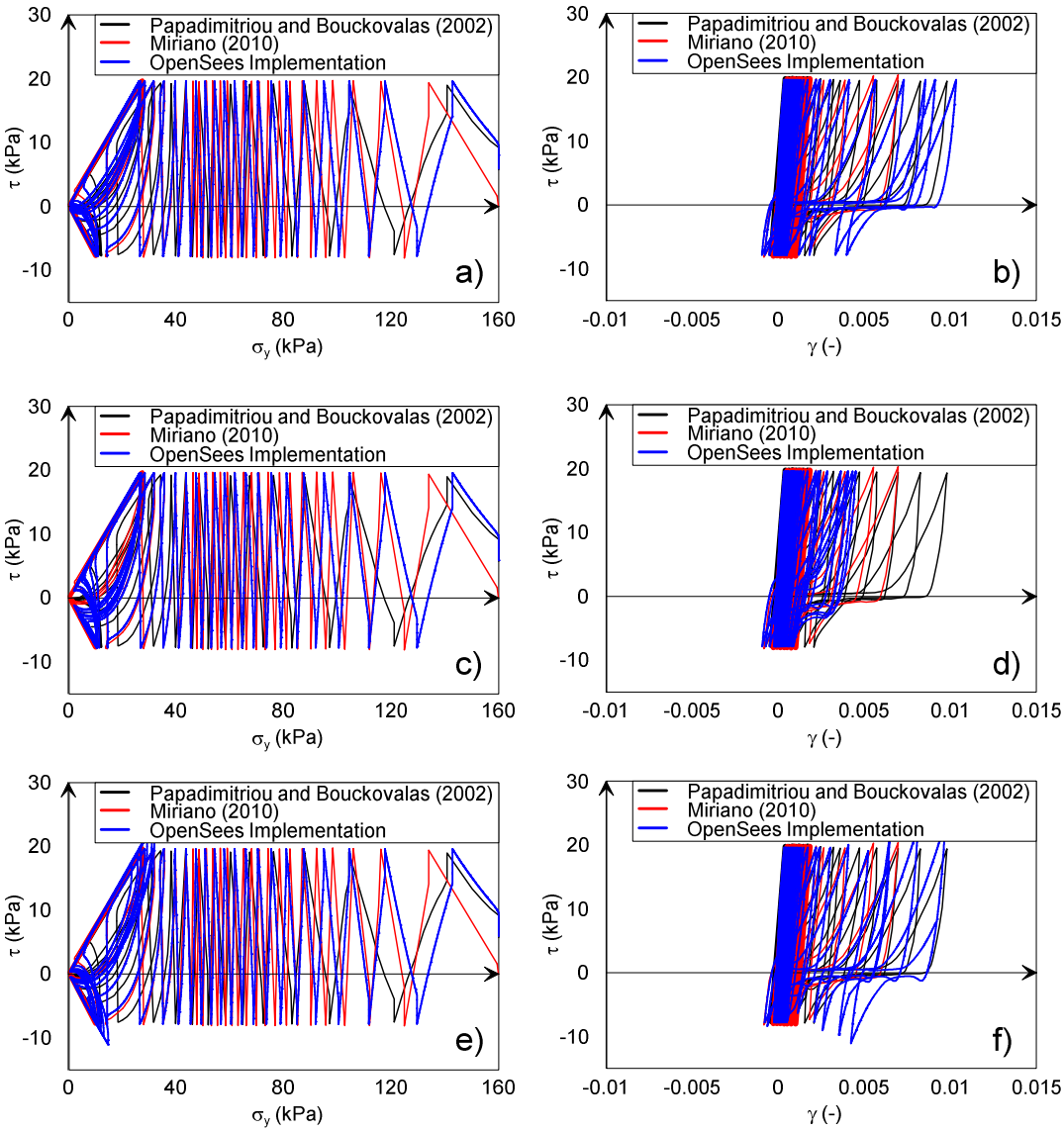

Figure 4.10. τ-σ_y and τ-γ curves for the cyclic undrained DSS test obtained from Papadimitriou and Bouckovalas (2002; black curves), Miriano (2010; red curves), and current implementation (blue curves) using quadUP (a)-(b), SSPquadUP (c)-(d), and nine-four quadUP (e)-(f) elements.

Observing the stress paths and the stress-strain response reported in Figure 4.10, a satisfactory accordance seems to be reached between the benchmarks and the current simulations. In particular, the simulations performed in OpenSees show a good fitting with those performed in Abaqus by Miriano (2010). However, both of them exhibit a stiffer response at low strain levels, if compared to the original implementation. It is worth noting that the details on the implementation of the original model are not

provided. Considering all the finite elements, in all cases, the response at high strain levels is well caught. Particularly, the typical butterfly-shaped stress-path is well simulated. Among them, the nine-four node quadUP element exhibits some problems (i.e., the stress amplitude is not well caught), while at high strain levels the SSPquadUP element shows a stiffer response in terms of the hysteretic loop, if compared to the quadUP element, which generally presents the best agreement with both the original implementation and the Abaqus implementation. The discrepancies that obviously arise can be connected to the different implementation strategies adopted.

In order to verify the sensitivity of the response to the discretization of the domain under study, the same test is performed by meshing the numerical model using multiple elements. In particular, the single element has been discretized considering 2x2 and 4x4 quadUP elements, as it is illustrated in Figure 4.11.

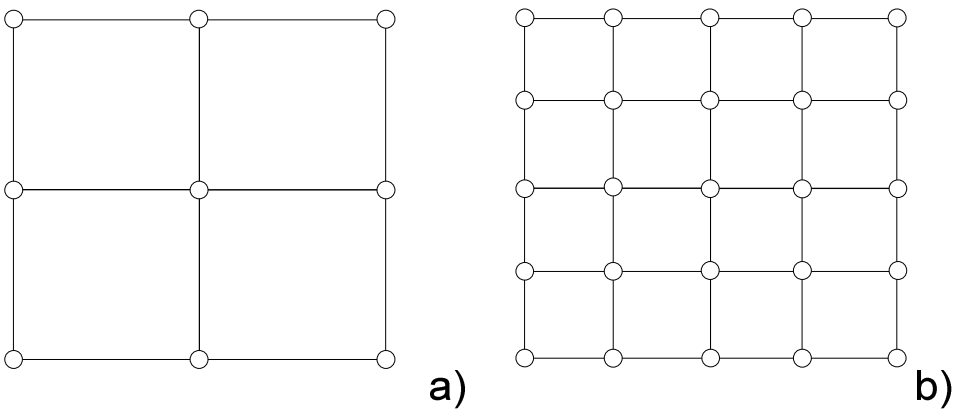

Figure 4.11. Domain discretization for the DSS test: 2x2 domain (a) and 4x4 domain (b).

Consequently, the dimensions of each element sides correspond to 0.05 m and 0.025 m, respectively. The obtained curves in terms of stress path and hysteretic loop are reported in Figure 4.12 and Figure 4.13.

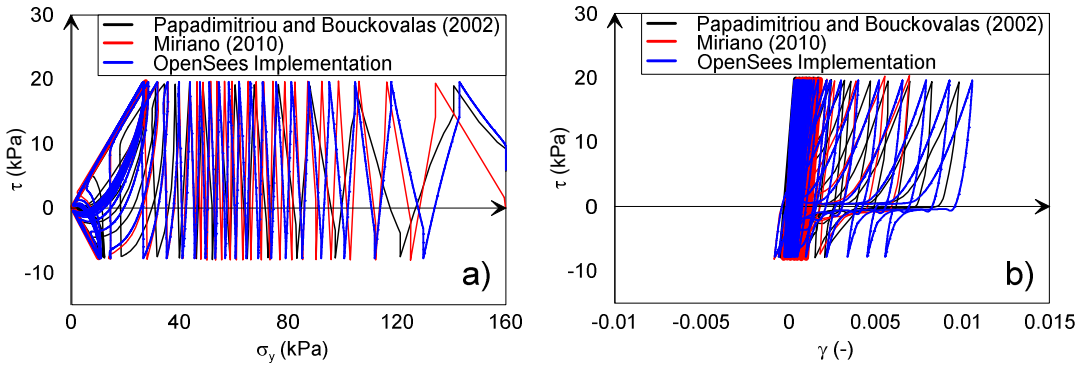

Figure 4.12. τ-σ_y and τ-γ curves from the simulation of the undrained cyclic DSS test considering 2x2 meshed domain.

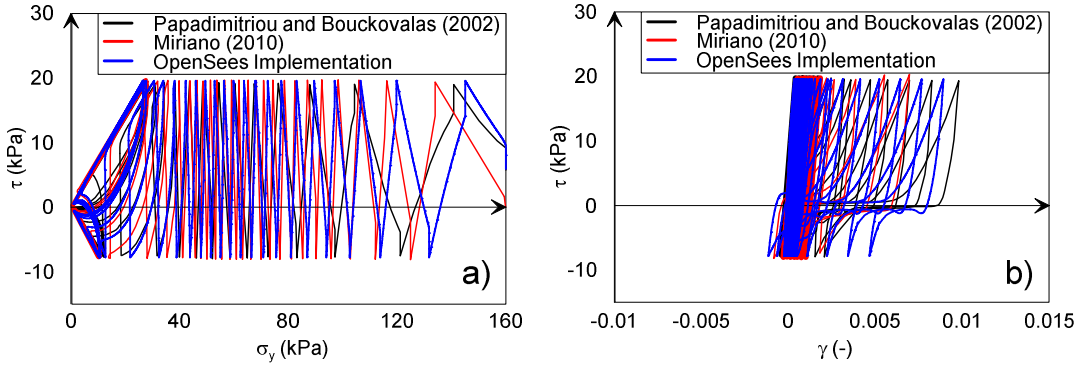

Figure 4.13. τ-σ_y and τ-γ curves from the simulation of the undrained cyclic DSS test considering 4x4 meshed domain.

As it can be expected, the response is more accurate at the high strain levels, and it is basically the same observed using the single element and the response is homogeneous at the integration points.

In Figure 4.14, the development of pore water pressures in time and with respect to the shear strain is shown. The response is obtained by using the quadUP single element.

The resulting response is the one typically expected in such tests, and this strengthens the implementation of the model.

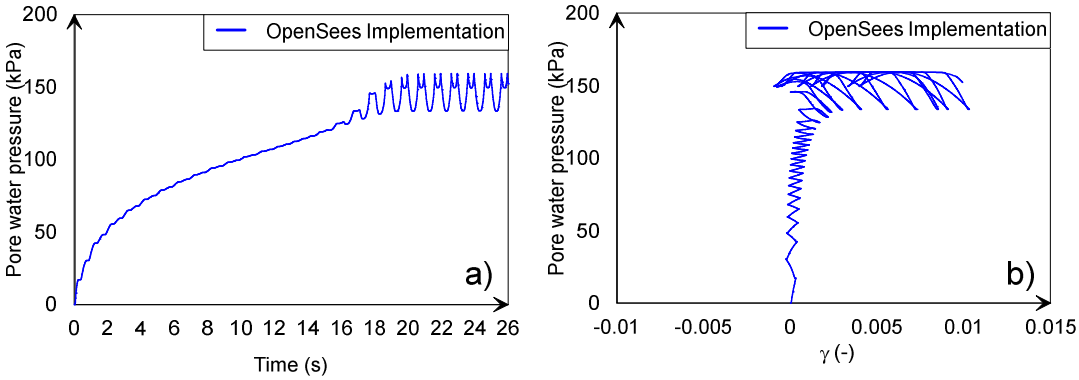

Figure 4.14. Results in terms of pore water pressure vs time (a) and pore water pressure vs shear strain (b) from the simulation of the undrained cyclic DSS test using quadUP element.

On the other hand, in Figure 4.15, the development of shear stress versus time is reported to demonstrate the correct application of the load.

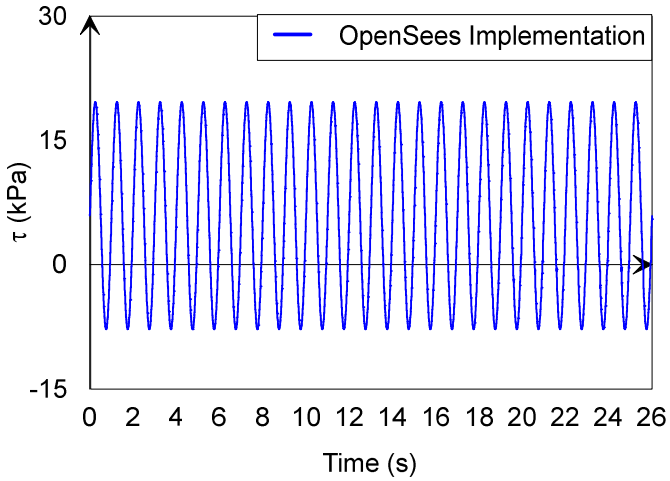

Figure 4.15. τ-time curve obtained from undrained cyclic DSS test simulation.

Finally, as it was mentioned before, the response obtained using the plane-strain quadrilateral element is compared to that obtained reproducing the plane-strain conditions with SSPbrickUP element. In particular, the nodal forces are applied on the top nodes of the element, while the element itself is constrained to avoid any out-of-plane displacement. The so-obtained stress paths and hysteretic loops are reported in

Figure 4.16, and a perfect agreement between the response obtained using SSPquadUP element and SSPbrickUP element is noticed.

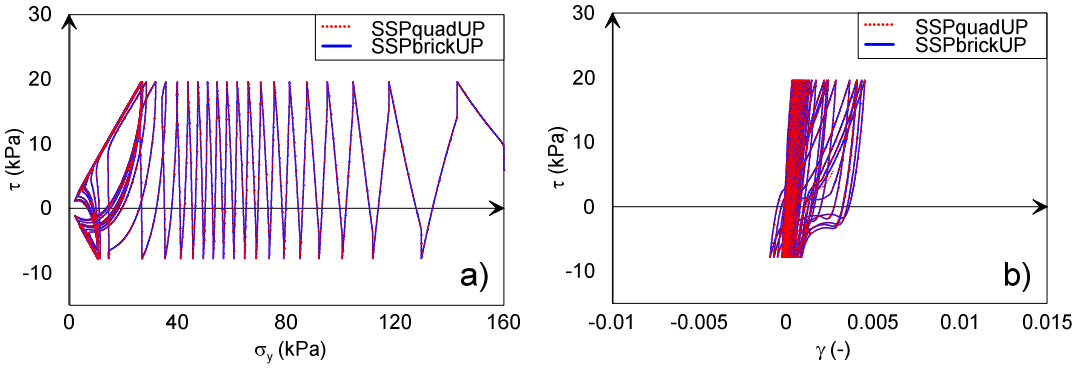

Figure 4.16. Stress path (a) and hysteretic loop (b) obtained using both SSPbrickUP and SSPquadUP to simulate undrained cyclic DSS test.

4.7 UNDRAINED AND DRAINED CYCLIC TRIAXIAL TESTS SIMULATIONS

Another test exploited by Papadimitriou and Bouckovalas (2002) to validate their constitutive model is here simulated. In particular, an undrained cyclic triaxial test performed on a 2.5 in x 1.0 in sample with 40% relative density (which corresponds to a 0.73 initial void ratio) executed during the VELACS project (Arulmoli et al., 1992), and there indicated as test 40-73, is considered. In the test, the loading process consists of an anisotropic consolidation of 80 kPa mean effective pressure with 26 kPa offset, followed by a cyclic deviatoric load of 43.1 kPa at 1 Hz frequency.

As it was done for the previous test, an extract from the VELACS report is shown in the following Figure 4.17.

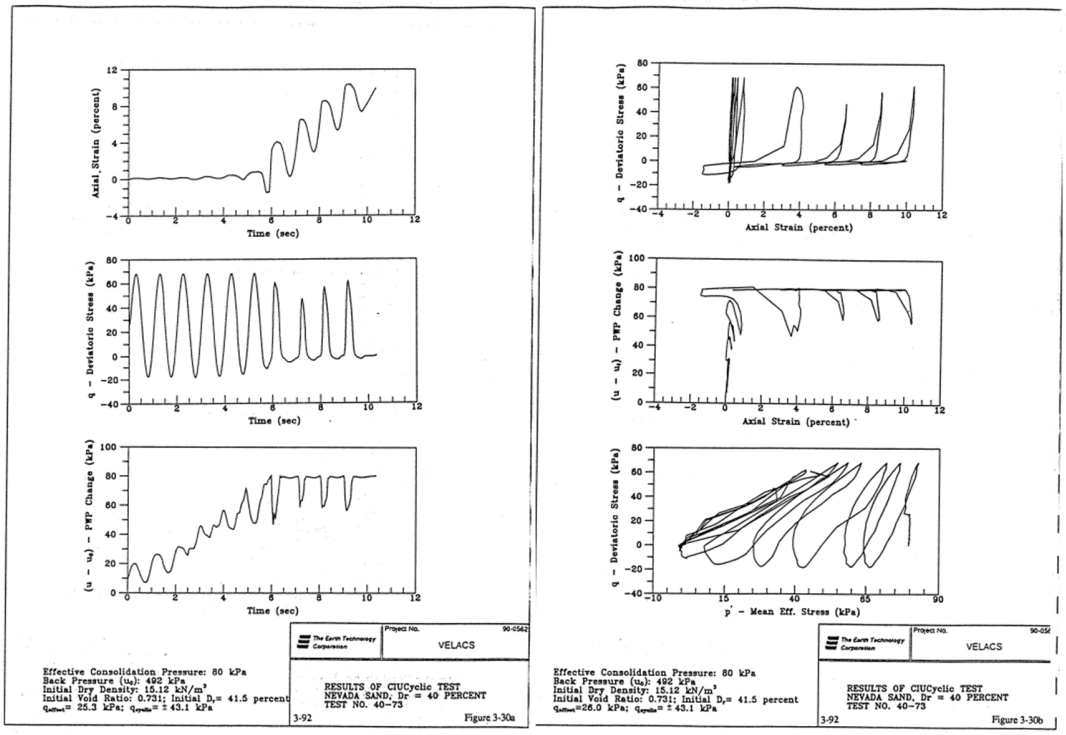

Figure 4.17. Extract of the cyclic triaxial test 40-73 from VELACS report.

Due to the impossibility to reproduce pure triaxial loading conditions with plane-strain elements, numerical simulations are performed by comparing the response obtained using both SSPbrickUP and brickUP elements.

The numerical model has the same dimensions of the elements adopted to perform the DSS tests (0.1 x 0.1 x 0.1 m^3). During the consolidation stage, the ConsolidationStage flag is set to 0 as usual and the same analysis parameters adopted to perform the DSS test are used for Nevada sand. A sketch with the load conditions of the hexahedral element is presented in Figure 4.18, for both consolidation and dynamic stages.

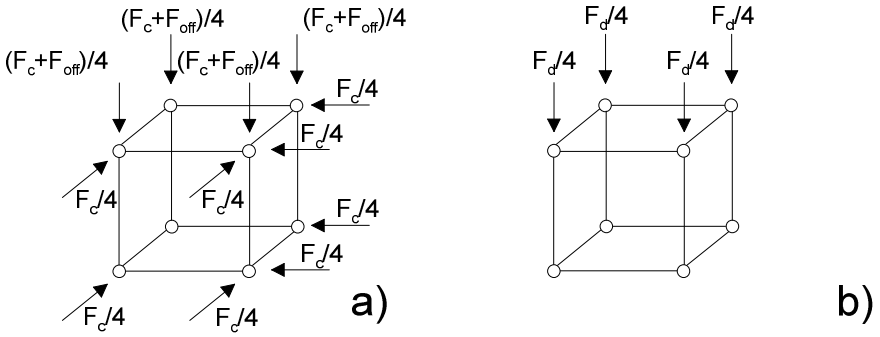

Figure 4.18. Load conditions for the brickUP element and SSPbrickUP element in both consolidation (a) and dynamic (b) stages of the test.

Figure 4.19 and Figure 4.20 show the comparison between the simulations performed in Papadimitriou and Bouckovalas (2002; P&B2002 in the Figures), and the response obtained by the simulations of the undrained cyclic triaxial test using both brickUP and SSPbrickUP elements in OpenSees, respectively.

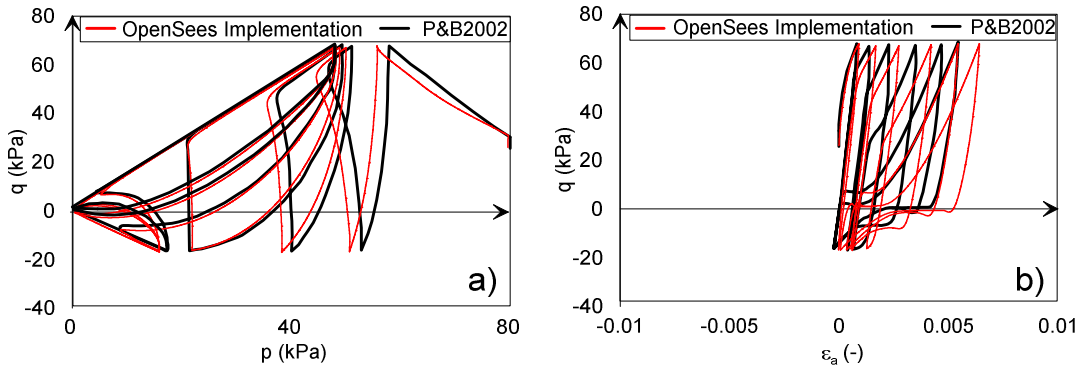

Figure 4.19. Stress path (a) and stress-strain (b) curves obtained adopting a 3D brickUP element.

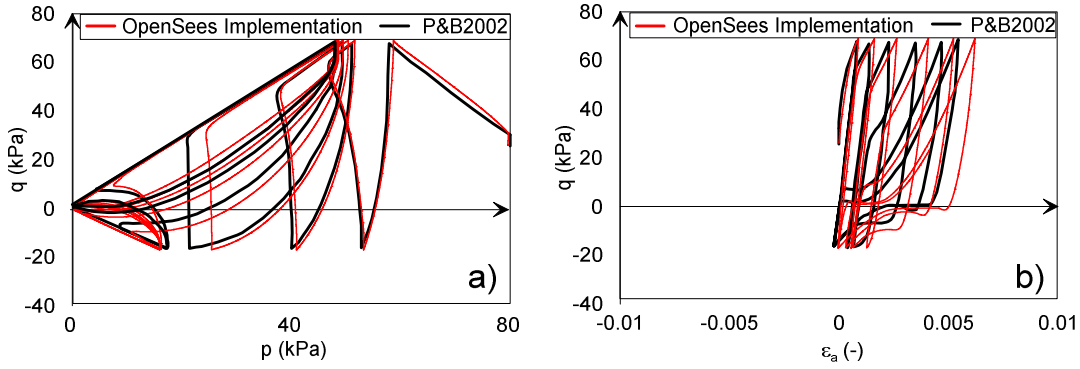

Figure 4.20. Stress path (a) and stress-strain (b) curves obtained adopting a 3D SSPbrickUP element.

Considering the latter results, the congruence between target and simulations seems to dramatically improve with respect to the DSS test, even if discrepancies are still observed and can be related to the different integration strategies adopted.

Finally, the same test is performed in drained conditions by constraining excess pore water pressure DOFs to zero at each node. In the following Figure 4.21 and Figure 4.22, the stress paths are shown using both the analyzed hexahedral finite elements.

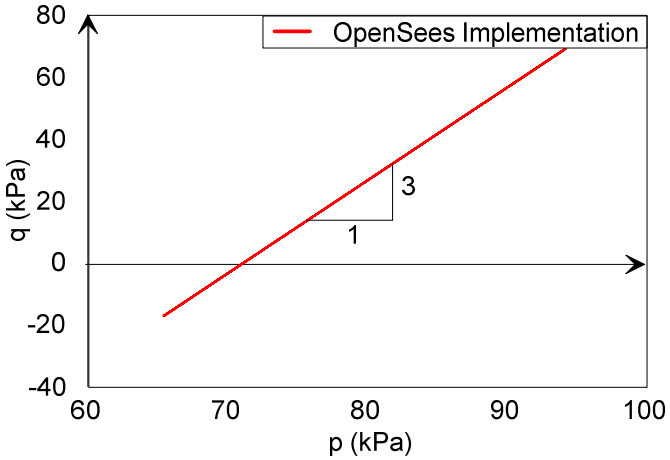

Figure 4.21. Stress path obtained adopting a 3D brickUP element.

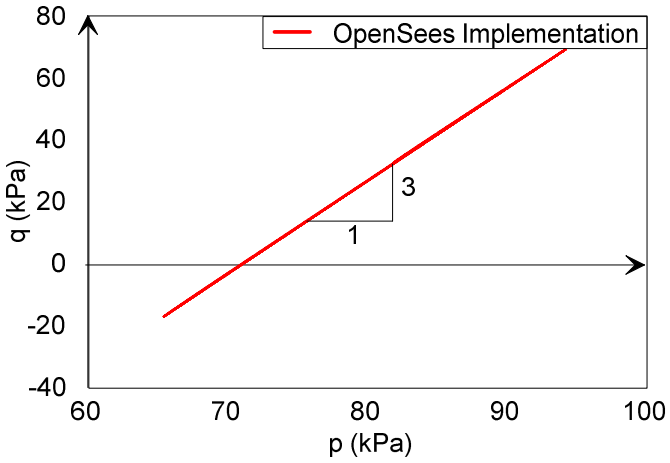

Figure 4.22. Stress path obtained adopting a 3D SSPbrickUP element.

In Figure 4.21 and Figure 4.22, both the finite elements exhibit the same behaviour and, in particular, the stress path shows the expected 3:1 slope.

4.8 MODULUS REDUCTION CURVE SIMULATIONS

A new constitutive model added to a numerical framework should be able even to catch the modulus reduction curve of a tested soil. To understand whether the current implementation can catch this aspect, an undrained cyclic isotropically consolidated triaxial test is here performed.

The displacement control cyclic triaxial test is performed by applying an effective consolidation stress of 180 kPa. The load is applied by progressively increasing the nodal forces and 100 steps are performed. Then, additional 50 steps are done to let the model rest and to eventually damp out waves. At the end of this stage, the pore water pressure DOFs are unconstrained, so that the pore water pressure can freely develop. After this activation, additional 50 steps are performed. Finally, the dynamic stage is conducted, where the deviatoric stress is applied along the vertical z-axis. The test was performed adopting the SSPbrickUP element.

The modulus reduction curves are calculated based on the results of the cyclic phase. The deviatoric stress is calculated as in (4.1):

$$q = \sigma_z - \sigma_x \tag{4.1}$$

and, consequently, the maximum and minimum values of q are evaluated as well as it is done for the axial strain, for each cycle. This was made in order to obtain the secant shear modulus for the i-th cycle (4.2):

$$G_{s,i} = \frac{1}{3}\frac{\Delta q_i}{\Delta \varepsilon_{a,i}} \tag{4.2}$$

where $\Delta q_i = q_{max,i} - q_{min,i}$ and $\Delta \varepsilon_{a,i} = \varepsilon_{a,max,i} - \varepsilon_{a,min,i}$.

Consistently, the shear strain is evaluated as (4.3):

$$\gamma_i = \Delta \varepsilon_{a,i}(1 + \nu) \tag{4.3}$$

Figure 4.23 shows the hysteretic loops obtained from the cyclic triaxial test, while Figure 4.24 and Figure 4.25 show the results in terms of G_s and $G_s/G_{s,max}$, extrapolated adopting the procedure described in this paragraph.

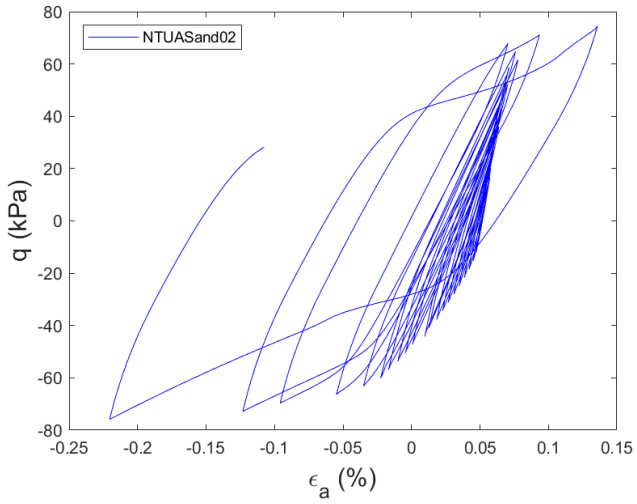

Figure 4.23. Hysteretic loop in terms of deviatoric stress-axial strain obtained from the cyclic triaxial test.

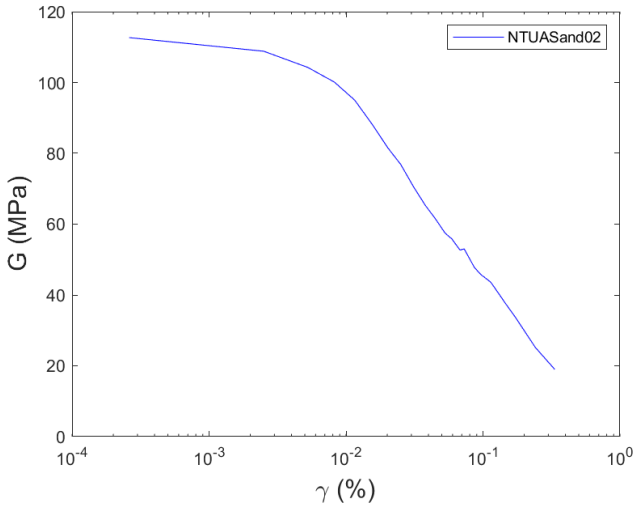

Figure 4.24. G_s vs. shear strain curve resulting from the triaxial test.

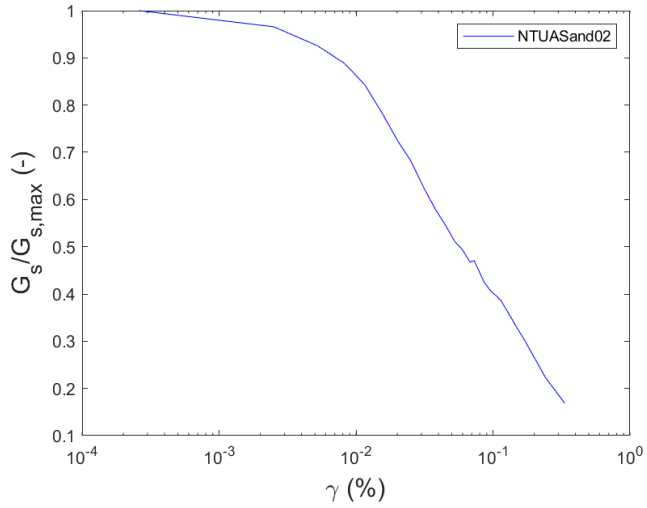

Figure 4.25. $G_s/G_{s,max}$ vs. shear strain curve resulting from the triaxial test.

The curves obtained in this manner in Figure 4.24 and Figure 4.25 highlight the suitability of the current implementation in simulating the modulus reduction curves of a soil sample.

The review of the simulations performed using the implemented NTUASand02 constitutive model in OpenSees just described highlights that the elemental response of soil under different monotonic and cyclic, drained and undrained loading conditions is well reproduced by the adopted framework. In addition, all the analyzed elements exhibit a reliable response in the different loading conditions.

4.9 DISCUSSION

The tests illustrated in this chapter are selected on the one hand to evaluate the goodness of the implementation of the constitutive model in OpenSees; on the other hand, they are willing to demonstrate the ability of the model to simulate a wide range of loading conditions at the element level. In particular, the response obtained in OpenSees is compared to the simulations performed in the original paper proposed by Papadimitriou and Bouckovalas (2002) and to the one resulting in real tests. Additionally, the simulations provided by Miriano (2010) in the framework of the implementation of the same model in Abaqus are shown as well.

Overall, different finite elements provided in OpenSees are tested under both drained and undrained conditions and a very good and satisfactory accordance is obtained. The simulations in case of monotonic and cyclic triaxial tests showed excellent results, with some slight differences with reference to the benchmark that can be related to the different numerical platforms exploited. Even the implemented integration schemes gave satisfactory accordance and the implementation revealed to be able to reproduce the modulus reduction curve under cyclic triaxial loading conditions.

Differences are also observed when undrained direct simple shear tests are simulated in the framework of the comparison with the benchmark (Papadimitriou and Bouckovalas, 2002). However, studies previously performed on the same constitutive model (Miriano, 2010) evidenced the same differences encountered in this study. It is worth noting that no additional pieces of information are provided in Papadimitriou and Bouckovalas (2002) on the implementation procedure of the model (for example, whether a constitutive driver or a finite element platform is exploited), and the differences in the results can be due to this aspect. On the other hand, the discrepancies obtained between the current implementation results and those presented in Miriano (2010) can be related either to the different finite element frameworks (e.g., Abaqus and OpenSees) or to the different approaches (e.g., finite elements and finite differences).

Another crucial result highlights that the capabilities and the flexibility for the implementation of user-defined materials make OpenSees an extremely valuable tool for Geotechnical Earthquake Engineering applications and for the evaluation of the performances of geotechnical systems.

As a result, it can be stated that the model is successfully verified and its application to boundary value problems is needed.

4.10 REFERENCES

Andrianopoulos K. I., Papadimitriou A. G., Bouckovalas G. D. (2010a). Explicit integration of bounding surface model for the analysis of earthquake soil liquefaction,

International Journal for Numerical and Analytical Methods in Geomechanics, 34 (15): 1586-1614.

Andrianopoulos K. I., Papadimitriou A. G., Bouckovalas G. D. (2010b). Bounding surface plasticity model for the seismic liquefaction analysis of geostructures, Soil Dynamics and Earthquake Engineering, 30(10): 895-911.

Arulmoli K., Muraleetharan K., Hosain, M., and Fruth, L. (1992). Velacs laboratory testing program, soil data report. Rep. to the National Science Foundation, Earth Technology Corporation, Irvine, CA.

Bardet J. P. and Chouchair W. (1991). A linearized integration technique for incremental constitutive equations. Int. J. Num. Anal. Meth. Geomech. 15, 1-19.

Biot M.A. (1941) General theory of three-dimensional consolidation. Journal of Applied Physics 12, 155. https://doi.org/10.1063/1.1712886.

Brezzi F. and Fortin M. (1991). Mixed and hybrid finite element methods. Springer, New York.

Chen L. and Arduino P. (2021). Implementation, verification and validation of the PM4SAND model in OpenSees. PEER Report No. 2021/02. Pacific Earthquake Engineering Research Center Headquarters, University of California, Berkeley, March 2021.

Cuthill E. and McKee J. (1969). Reducing the bandwidth of sparse symmetric matrices. In Proc. 24th Nat. Conf. ACM, pages 157-172, 1969.

Fierro T., Ercolessi S., Castiglia M., Santucci de Magistris F. and Fabbrocino G. (2022; in print). Implementation and verification of an advanced bounding surface constitutive model. Proceedings of the 4th International Conference on Performance-based Design in Earthquake Geotechnical Engineering. Beijing, July 15-17, 2022.

McGann C. R., Arduino P. and Mackenzie-Helnwein P. (2012). Stabilized single-point 4-node quadrilateral element for dynamic analysis of fluid saturated porous media. Acta Geotechnica, 7(4), 297-311.

McGann C. R., Arduino P. and Mackenzie-Helnwein P. (2015). A stabilized single-point finite element formulation for three-dimensional dynamic analysis of saturated soils. Computers and Geotechnics 66, 126–141.

Miriano C. (2010). Numerical modelling of the seismic response of flexible retaining structures. Ph.D. Thesis, Sapienza University of Rome. (in Italian).

Papadimitriou A. G., Bouckovalas G. D. (2002). Plasticity model for sand under small and large cyclic strains: a multiaxial formulation, Soil Dynamics and Earthquake Engineering, 22: 191-204.

Papadimitriou A. G., Bouckovalas G. D., Dafalias Y. F. (2001). Plasticity model for sand under small and large cyclic strains, Journal of Geotechnical and Geoenvironmental Engineering, ASCE, 127(11): 973-983.

Zienkiewicz O.C. and Shiomi T. (1984). Dynamic behavior of saturated porous media; the generalized Biot formulation and its numerical solution. International Journal for Numerical Methods in Geomechanics, 8, 71-96.

5 SIMULATION OF THE SITE RESPONSE OF A SOIL COLUMN TO A SEISMIC EXCITATION

5.1 INTRODUCTION

A reliable prediction of the seismic response of a soil column represents another challenging goal in Geotechnical Earthquake Engineering problems. The critical issues connected to the simulation of such a problem dramatically increase if the column is made of liquefiable soil. This is due to the complexity of the phenomenon that becomes extremely hard to be simulated when boundary value problems are considered. In addition, the presence of liquefiable soils implies effective stress analysis and this raises, in turn, both the complication of numerical modeling and the computational demand. Indeed, the nonlinear response of the material under earthquake loadings requires a proper description of the stress and strain distribution in the soil domain; additionally, the filtering effect exercised by the soil on the input motion should be appropriately caught (Visone et al., 2010). To this aim, the use of dynamic finite element or finite difference analysis is vital to try to reproduce the soil behaviour at a high strain level. In this framework, the soil nonlinearity can be only reliably considered using a valid constitutive model.

To understand the differences that arise using different constitutive models, developed for the same scope (i.e., the simulation of liquefiable soils behaviour), and to evaluate how the implemented constitutive model responds, the chapter focuses on the response of a 20 m-thick soil column of Nevada sand subjected to different input motions. The analysis is conducted in OpenSees by adopting the three bounding surface constitutive models previously described (cf. §2.4.1, §2.4.2 and §2.4.3): NTUASand02 (Papadimitriou and Bouckovalas, 2002), which has been implemented in OpenSees in the framework of the current study, SANISAND (Dafalias and Manzari, 2004), and

PM4SAND (Boulanger and Ziotopoulou, 2017). Some of the results reported in this chapter are in Fierro et al. (2022).

5.2 FINITE ELEMENT MODEL

As previously indicated, the model of the soil column is built in OpenSees: it consists of a 20 m-soil column of Nevada sand with a 0.66 initial void ratio. The Nevada sand was selected because this sand has been widely adopted in different studies (see, for example, Taiebat et al., 2010; Andrade et al., 2013; Kamai and Boulanger, 2013; Papadimitriou and Bouckovalas, 2002; Andrianopoulos et al., 2010), and, consequently, calibrations are available in the literature. The adoption of a largely studied soil is made to avoid the introduction of additional bias and to compare the resulting responses. The height of 20 m is selected because works are available in the literature reporting centrifuge tests on liquefiable soils reproducing case studies, where the height at prototype scale of the column corresponds to about 20 m (see, among others, Ramirez et al., 2018; Fasano et al., 2021).

The numerical model is composed of 40 bi-dimensional SSPquadUP elements (McGann et al., 2012). The dimensions of quad elements are 1.0 x 0.5 m^2 with a unit out-of-plane thickness. The size of the elements was selected with a view to permitting the transmission of frequencies up to 20 Hz, a threshold of interest for Earthquake Engineering problems. Consistently, real accelerograms are selected for the analyses.

The side boundaries of the model are treated by tying the nodes at the same height to simulate periodic boundaries. The groundwater table coincides with the ground level. At the base nodes of the numerical model, two Lysmer dashpots (Lysmer and Kuhlemeyer, 1969) are applied in both horizontal and vertical directions to account for the impedance contrast between the soft soil and the underlying bedrock. As suggested by Joyner and Chen (1975), the dashpot coefficients (C_n and C_p) are defined as the product between mass density and shear wave velocity of the underlying bedrock along the horizontal direction (5.1) and mass density times the P-wave velocity of the underlying bedrock in vertical direction, as reported in (5.2).

$$C_n = \rho_{bed} \cdot V_{s,bed} \tag{5.1}$$

$$C_p = \rho_{bed} \cdot V_{P,bed} \tag{5.2}$$

The coefficients are then multiplied by the tributary area of the base nodes. The bedrock is modelled adopting a unit weight γ_{bed}=24.5 kN/m^3 and a shear wave velocity V_s=950 m/s.

The dynamic load is applied following the Joyner and Chen (1975) procedure as a nodal force proportional to the velocity time-history of the selected ground motion.

The dynamic analysis is performed in three different stages: an elastic gravity stage, which is performed in order to properly reproduce the desired initial conditions, and where the equilibrium under the soil weight is evaluated assuming an elastic behaviour (i.e., considering the elastic formulation of the selected constitutive model, which is hypoelastic for the models considered in this study), an elasto-plastic gravity stage, where the equilibrium under the soil unit weight is calculated by activating the plastic formulation of the constitutive model, and, finally, the dynamic stage, where the dynamic excitation is applied at the base of the model. The coefficient of permeability is assumed to be 1.5 x 10^{-3} m/s.

Analyses are performed applying kinematic constraints exploiting the Penalty Method with penalty coefficients 1x10^{14} and a Krylov-Newton solution algorithm. The Plain numberer is selected to renumber DOFs and a Sparse General system of equation solver is considered. Finally, the Generalized Alpha method is selected as an integrator with coefficients α_M=1.0 and α_F=0.8. In this way, the unconditional stability $\alpha_M > \alpha_F > 0.5$ is guaranteed. The response is investigated at different depths along the soil column: 1 m, 10 m and 15 m below the ground level (Figure 5.1).

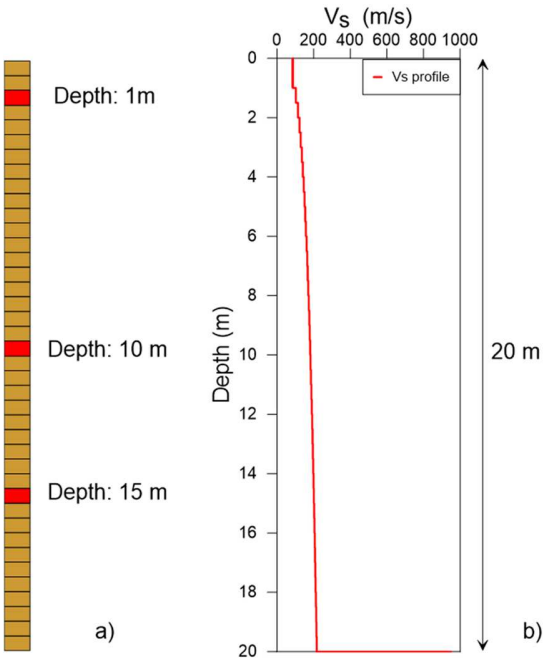

Figure 5.1. Discretized soil column with control points (a) and shear wave velocity profile (b).

5.2.1 CONSTITUTIVE PARAMETERS

As it was stressed before, with a view to avoiding the introduction of any bias related to the calibration procedure, the Nevada Sand, whose calibrations referred to the selected constitutive models are widely available in the literature, is considered. Specifically, parameters for NTUASand02 are obtained by Papadimitriou and Bouckovalas (2002) on the basis of monotonic and cyclic, drained and undrained triaxial and direct simple shear tests performed within the framework of the VELACS project (Arulmoli et al., 1992). The latter are exploited in this study (see §3) to validate the implementation of the constitutive model in OpenSees. The same tests were considered by Taiebat et al. (2010) to calibrate SANISAND for the same sand. Constitutive parameters for PM4SAND, instead, were obtained by Kamai and Boulanger (2013), based on undrained cyclic triaxial tests, undrained isotropically consolidated torsional hollow cylinder tests, and undrained one-dimensionally consolidated direct simple shear tests. Among others, in the calibration procedure of PM4SAND, tests performed by Arulmoli et al. (1992) have been exploited. The

parameters considered for NTUASand02 are reported in Table 4.2, and the latter is here reposted for the sake of clarity (see Table 5.1).

Table 5.1. NTUASand02 constitutive parameters referred to Nevada sand adopted for site response analyses (from Papadimitriou and Bouckovalas, 2002).

Parameter	**Value**	**Meaning**
$(e_{cs})_a$	0.809	CSL Location in the e-ln(p) space
λ	0.022	CSL Location in the e-ln(p) space
M_c^c	1.25	Critical state strength in triaxial compression
M_e^c	0.9	Critical state strength in triaxial extension
B	520	Elastic shear modulus constant
a_1	0.67	Non-linearity of the elastic shear modulus
γ_1	0.00025	Strain limit of elastic modulus degradation
ν	0.31	Poisson's ratio
k_c^b	1.45	Effect of ψ on peak stress ratio
k_c^d	0.3	Effect of ψ on stress ratio at PT
A_o	2.1	Dilatancy constant
h_o	5000	Plastic modulus constant
H_o	68000	Fabric index constant
ζ	1.0	Effect of major principal stress on fabric index
m	0.0625	Yield surface constant

Accordingly, in the following Table 5.2, the parameters for the SANISAND constitutive model calibrated by Taiebat et al. (2010) are shown.

Table 5.2. SANISAND constitutive parameters referred to Nevada sand calibrated by Taiebat et al. (2010).

Parameter	**Value**	**Meaning**
G_0	150	Elastic material constant
ν	0.05	Poisson's ratio
M^c	1.14	Critical-state stress ratio
c	0.78	Ratio of critical-state stress ratio in extension and compression
λ_c	0.027	State line constant
e_0	0.83	Void ratio at p=0
ξ	0.45	State line constant
h_0	9.7	Plastic modulus constant
c_h	1.02	Plastic modulus constant
n^b	2.56	Plastic modulus constant
A_0	0.81	Dilatancy constant
n^d	1.05	Dilatancy constant
z_{max}	5.0	Fabric-dilatancy tensor parameter
c_z	800	Fabric-dilatancy tensor parameter

Finally, the available PM4SAND parameters for Nevada sand (Kamai and Boulanger, 2013) are shown in Table 5.3.

Table 5.3. PM4SAND constitutive parameters referred to Nevada sand calibrated by Kamai and Boulanger (2013).

Parameter	**Value**	**Meaning**
D_r (%)	40	Apparent relative density
G_0	685	Shear modulus coefficient
h_0	0.5	Plastic modulus to elastic modulus ratio variable
h_{po}	0.065	Contraction rate parameter
e_{max}	0.793	Maximum void ratio
e_{min}	0.486	Minimum void ratio
Φ_{cv} (°)	32	Critical state effective friction angle
Q	9.5	Critical state constant
R	0.7	Critical state constant

Considering the above-mentioned parameters, the profiles of the initial deviatoric stress ratios M_c^b and M_c^d as well as the profile of the state parameter in initial conditions are reported in the following Figure 5.2. The profiles are obtained by considering the initial conditions in terms of void ratio, state parameter, critical state variables, and constants regulating the effect of ψ on peak stress ratio and stress ratio at phase transformation.

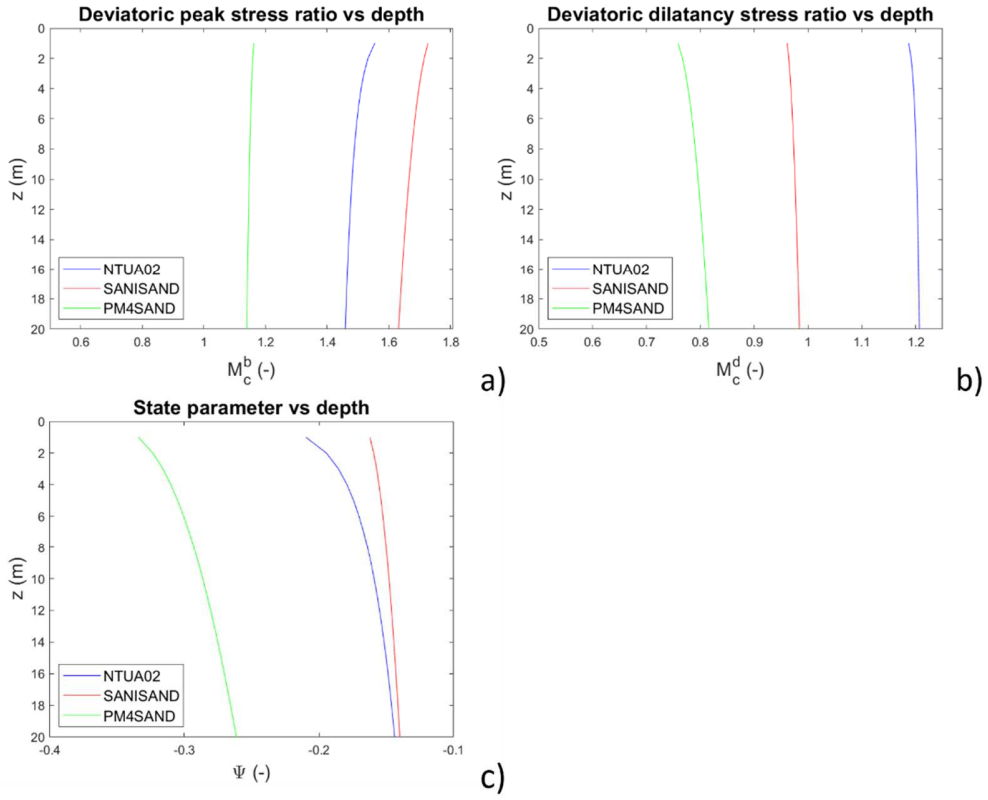

Figure 5.2. Profiles of peak (a) and dilatancy (b) deviatoric stress ratios and state parameter (c) based on the calibrations from literature.

Observing the so-obtained profiles, some parameters have been modified in order to increase as possible the matching between the variation of the initial deviatoric stress ratios and of the state parameter along with the depth considering the different constitutive models adopted in this study. Furthermore, especially for PM4SAND, if some parameters were not calibrated in the reference paper, the value suggested by Boulanger and Ziotopioulou (2017) is adopted. It is worth noticing that perfect matching cannot be guaranteed due to the different formulations provided by the

models. Assuming the calibration for Nevada sand as a benchmark, the parameters for SANISAND and PM4SAND are modified accordingly. The parameter m, which accounts for the "diameter" of the yield surface, is set to 0.0625 for each model: as stated by Manzari and Dafalias (1997), this value can be assumed equal to 5% of the critical state stress ratio (cf. §2.4.1).

In this framework, in order to guarantee that the initial shear wave velocity profile reported in Figure 5.1 is actually considered in the model, a key role is played by the definition of the parameter that controls the shear modulus (i.e., B in NTUASand02 and G_o for both SANISAND and PM4SAND), on the basis of the relation $V_s = \sqrt{G/\rho}$ where G is the shear modulus and ρ is the soil density. Consequently, the values for G_0 in both SANISAND and PM4SAND and B in NTUASand02 are calculated from the equality of (2.33), (2.67), and (2.97) in initial conditions in order to ensure the same initial shear wave velocity profiles for all the models. The resulting values are considered in site response analysis. The parameters calculated in this manner, are reported in the following Table 5.4 and Table 5.5.

Table 5.4. SANISAND constitutive parameters referred to Nevada sand adopted for site response analyses.

Parameter	**Value**	**Meaning**
G_0	267.42	Elastic material constant
ν	0.31	Poisson's ratio
M^c	1.25	Critical-state stress ratio
c	0.2	Ratio of critical-state stress ratio in extension and compression
λ_c	0.027	State line constant
e_0	0.83	Void ratio at p=0
ξ	0.45	State line constant
h_0	9.7	Plastic modulus constant
c_h	1.02	Plastic modulus constant
n^b	1.1	Plastic modulus constant
A_0	0.81	Dilatancy constant
n^d	0.25	Dilatancy constant
z_{max}	5.0	Fabric-dilatancy tensor parameter
c_z	800	Fabric-dilatancy tensor parameter

Table 5.5. PM4SAND constitutive parameters referred to Nevada sand adopted for site response analyses.

Parameter	**Value**	**Meaning**
D_r (%)	$\frac{e_{max} - e}{e_{max} - e_{min}}$	Apparent relative density
G_0	859.62	Shear modulus coefficient
h_{po}	0.065	Contraction rate parameter
h_0	0.5	Plastic modulus to elastic modulus ratio variable
e_{max}	0.793	Maximum void ratio
e_{min}	0.486	Minimum void ratio
n^b	1.1	Plastic modulus constant
n^d	0.25	Dilatancy constant
A_{do}	$\frac{1}{0.4}\frac{\sin^{-1}(M^b/2) - \sin^{-1}(M/2)}{M^b - M^d}$	Dilatancy constant
z_{max}	$0.28\exp(6.1D_r) < 40.0$	Fabric-dilatancy tensor parameter
c_z	250	Fabric-dilatancy tensor parameter
c_e	$-10D_r + 8.5 < 5.0$	Parameter controlling the strain accumulation in undrained cyclic loading
Φ_{cv} (°)	31.15	Critical state effective friction angle
ν	0.31	Poisson's ratio
C_{GD}	2.0	Shear modulus degradation factor
C_{DR}	$5 + 25(D_r) - 0.35 \leq 10$	Factor controlling rotation of dilatancy surface
$C_{K\alpha f}$	0.0	Parameter controlling the effect of sustained static shear stresses on plastic modulus
Q	8.0	Critical state constant
R	1.0	Critical state constant
m	0.0625	Yield surface constant
$F_{sed,min}$	$0.03\exp(2.6D_r) \leq 0.99$	Moduli reduction factor during reconsolidation
$p'_{sed,o}$	$-p_{atm}/5$	Mean effective stress up to which reconsolidation strains are enhanced
cr_{hg}	0.005	Nominal plastic shear strength ratio at initialization
c_{hg}	$\min(cr_{hg} \cdot p; 0.0)$	Nominal plastic shear strength at initialization

The resulting profiles of the deviatoric stress ratios and of the state parameter are shown in the following Figure 5.3.

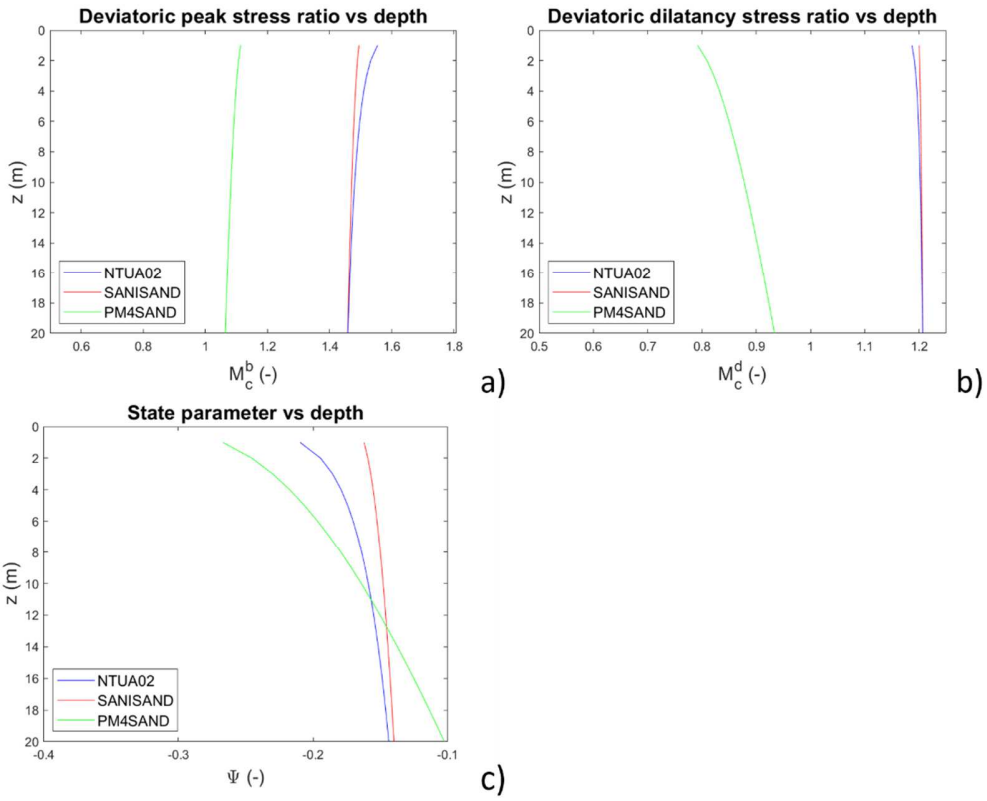

Figure 5.3. Profiles of peak (a) and dilatancy (b) deviatoric stress ratios and state parameter (c) obtained through the modified set of parameters.

The cyclic triaxial test exploited in §4.8 has been here performed once more to compare the resulting curves for NTUASand02 and SANISAND. The $G_s/G_{s,max}$-γ and G-γ curves are reported in Figure 5.4 and Figure 5.5, respectively, where it is clear that the same initial conditions are well-reproduced. It is worth noting that the test cannot be conducted with reference to PM4SAND, being the latter developed for plane-strain conditions only (cf. §2.4.3).

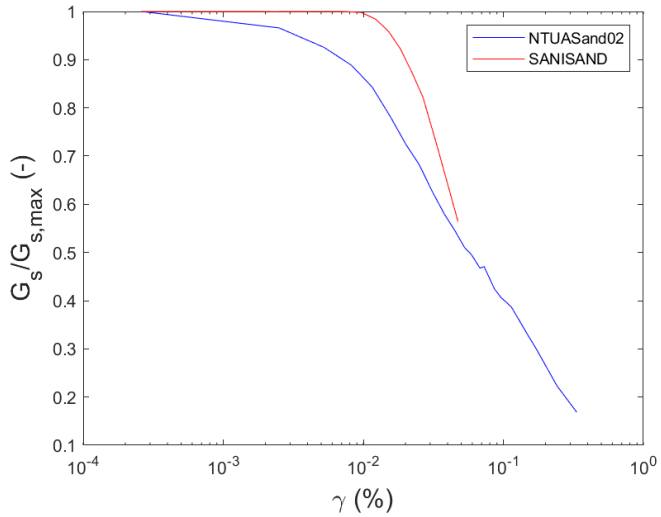

Figure 5.4. Comparison between modulus reduction curves obtained from cyclic triaxial tests for NTUASand02 and SANISAND.

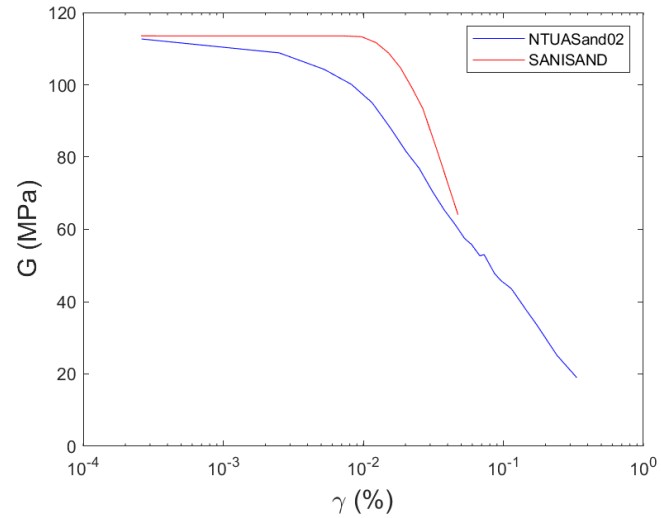

Figure 5.5. Comparison between G_s vs shear strain curves obtained from cyclic triaxial tests for NTUASand02 and SANISAND.

5.2.2 INPUT SELECTION

The input motions to be applied to the column are selected among real accelerograms downloaded from the Engineering Strong Motion Database (Luzi et al., 2016) and PEER Ground Motion Database. Two waveforms are selected to examine both cases

of liquefaction being triggered or not. Furthermore, the response is tested in both drained and undrained conditions. In the former case, a unit permeability is assigned to the soil elements. The main features of the selected motions are reported in Table 5.6, while acceleration time series and Fourier amplitude spectra are shown in Figure 5.6 and Figure 5.7. The two inputs are referenced in the following recalling the name of the recording station. The sampling interval adopted for the analyses corresponds to 0.0005 s.

Table 5.6. List of the main features of the selected motions.

Date	**Event**	**Station**	**M_w (-)**	**PGA (g)**
01/18/2017	Central Italy	Accumoli (ACC)	5.1	0.104
01/16/1995	Kobe	Kakogawa (CUE90)	6.8	0.345

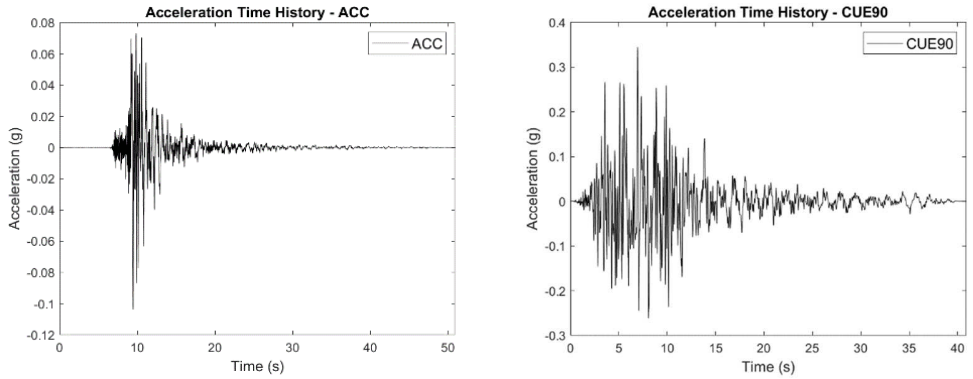

Figure 5.6. Input motions adopted for the analyses.

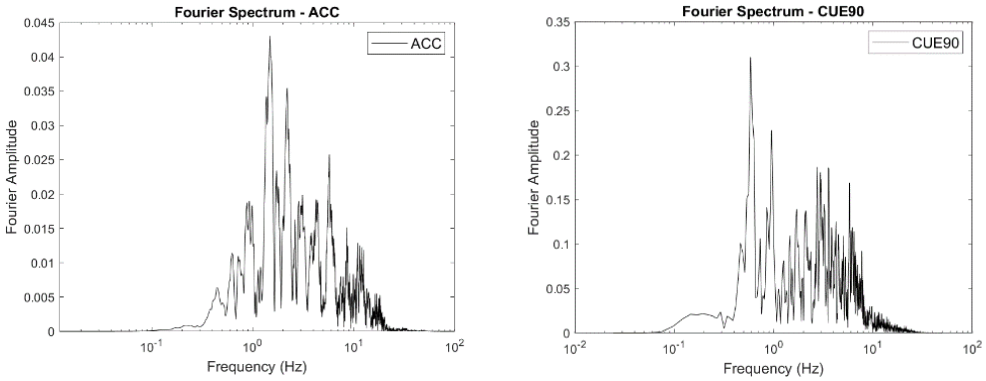

Figure 5.7. Fourier spectra of the selected input motions.

5.2.3 RAYLEIGH DAMPING

An additional Rayleigh damping is considered in the numerical model to take into account for an additional damping at low strain level. The coefficients of the Rayleigh damping formulation are evaluated following the procedure suggested by Kwok et al. (2007) with two control frequencies. These frequencies correspond to the fundamental (f_1) and the third natural (f_3) frequencies of the soil column. The latter have been evaluated through linear elastic analyses with the Strata tool (Kottke and Rathje, 2008). In particular, a sine sweep with a frequency varying up to 200 Hz has been applied. The first five natural frequencies are $f_1 = 2.86$ Hz, $f_2 = 7.63$ Hz, $f_3 = 12.28$ Hz, $f_4 = 17.03$ Hz, and $f_5 = 21.93$ Hz. For this reason, the first Rayleigh control frequency is set as 2.86 Hz and the second is set as $f_3 = 12.28$ Hz. In the following Figure 5.8, the dependence of the damping on the frequency is illustrated.

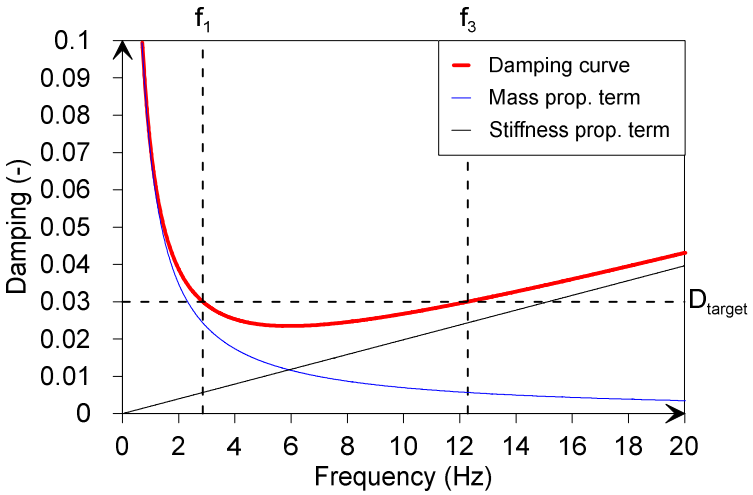

Figure 5.8. Rayleigh damping formulation adopted for the 20 m-thick soil column of Nevada Sand.

5.3 RESULTS

The obtained results are shown at the control points and elements located at 1 m, 10 m and 15 m below the ground level, in terms of time-histories of acceleration and their respective single-sided Fourier amplitude spectra, excess pore water pressure ratio in case of undrained conditions, stress-strain loops, displacement and profiles of peak

ground acceleration (PGA) and residual shear strain at the end of the signal. Worth noticing that the excess pore water pressure ratio r_u is computed as the ratio between excess pore water pressure and vertical effective stress $r_u=\Delta u/\sigma'_{v0}$. In §5.3.1 the results of the analyses conducted in drained conditions are shown, while in §5.3.2, the same input motion is applied under undrained conditions.

5.3.1 DRAINED CONDITIONS

The drained conditions are considered by assuming a unit permeability and this condition is respected by observing the resulting evolution of the excess pore water pressure ratio in the time, not reported here for the sake of brevity. In the following §5.3.1.1, the outputs deriving from the motion coded as ACC are shown, while in §5.3.1.2 the response of the column subjected to the CUE90 input is reported.

5.3.1.1 Input: ACC

Considering as input motion the one coded as ACC (cf. Figure 5.7), Figure 5.9, Figure 5.10, and Figure 5.11 reports acceleration time series, while Figure 5.12, Figure 5.13, and Figure 5.14 illustrates Fourier Amplitude Spectrum (FAS) at 1 m, 10 m, and 15 m below the ground level (g.l.). The PGA profile is shown in Figure 5.15. Then, displacement time series are in Figure 5.16, Figure 5.17, and Figure 5.18, while the strain profile at the end of the signal is reported in Figure 5.19. At the end, shear stress-shear strain loops are in Figure 5.20, Figure 5.21, and Figure 5.22.

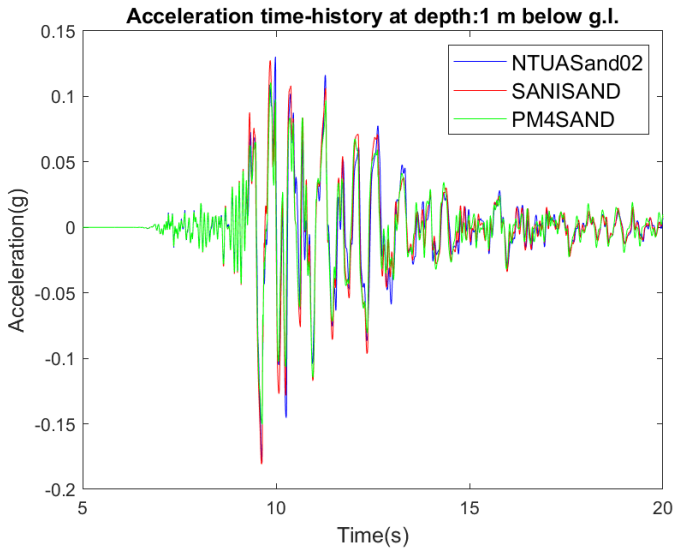

Figure 5.9. Acceleration time series for the input ACC at 1 m below g.l.

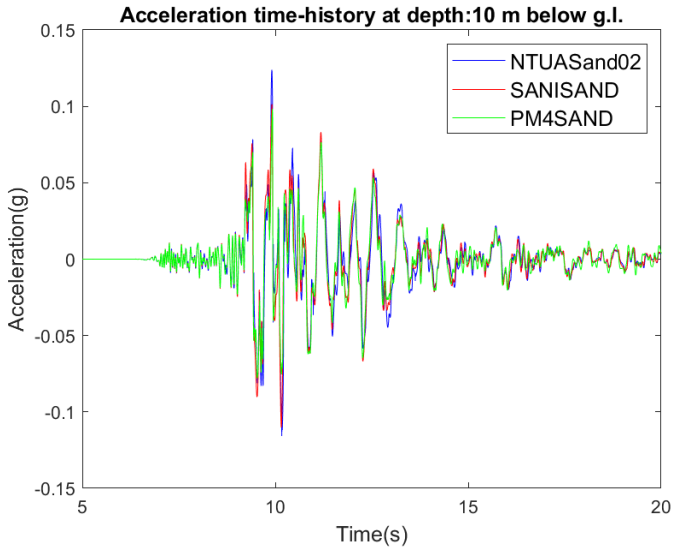

Figure 5.10. Acceleration time series for the input ACC at 10 m below g.l.

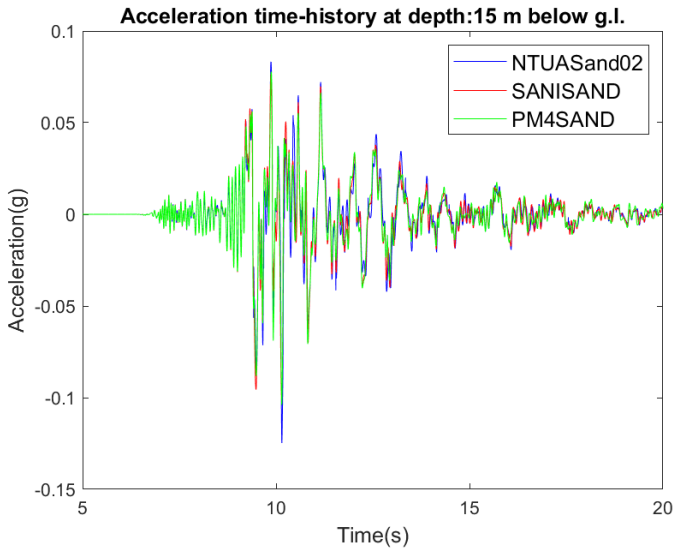

Figure 5.11. Acceleration time series for the input ACC at 15 m below g.l.

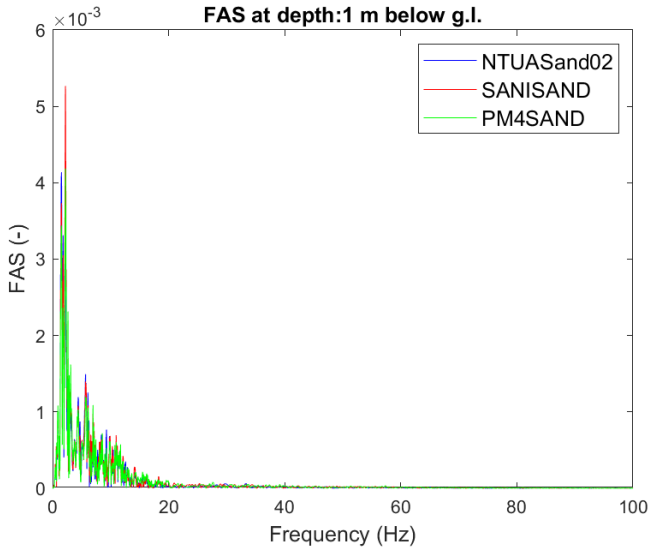

Figure 5.12. FAS for the input ACC at 1 m below g.l.

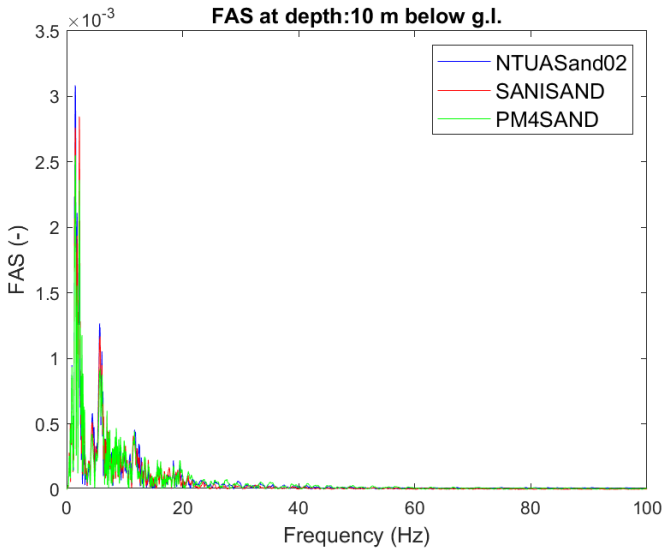

Figure 5.13. FAS for the input ACC at 10 m below g.l.

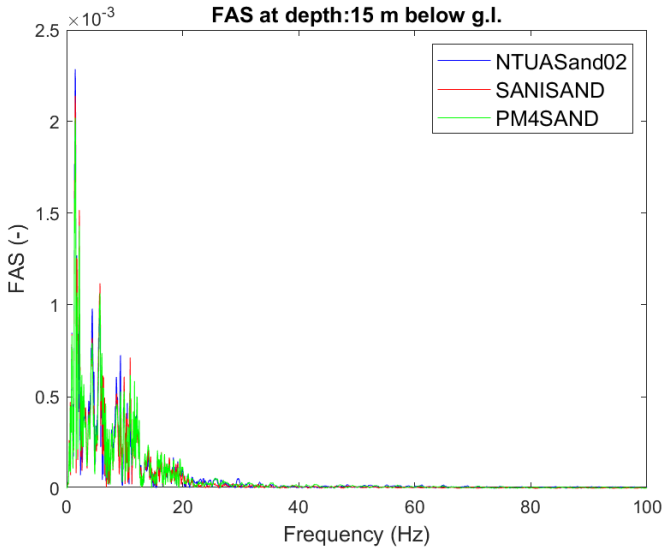

Figure 5.14. FAS for the input ACC at 15 m below g.l.

The contextual observation of acceleration time series reported in Figure 5.9, Figure 5.10, and Figure 5.11, and their Fourier amplitude spectra (Figure 5.12, Figure 5.13, Figure 5.14) highlights very satisfactory accordance in terms of time-series at each depth, while frequencies up to 20 Hz are excited. Furthermore, the amplitudes resulting from the accelerograms seem to be consistent among the three selected constitutive models.

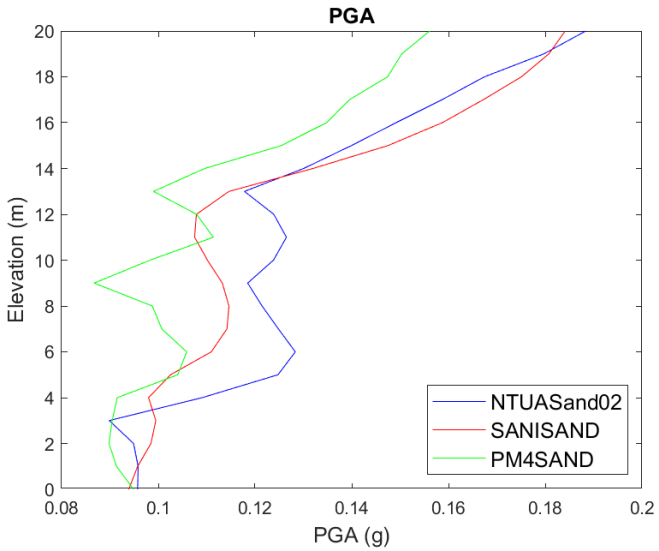

Figure 5.15. PGA profile for the input ACC.

The PGA profile resulting from the application of the ACC input motion in drained conditions (Figure 5.15) points out very good accordance between NTUASand02 and SANISAND in the topmost 5 m, while lower values of PGA are simulated with the Nevada Sand calibration of PM4SAND. In the middle 10 m (i.e., from 5 m to 15 m below the ground level), the highest amplification is provided by the NTUASand02 constitutive model, while PM4SAND shows once more the lowest PGA levels. Finally, from 15 m below g.l., and up to the bedrock, the solutions with the acceleration obtained using the three constitutive models are basically the same.

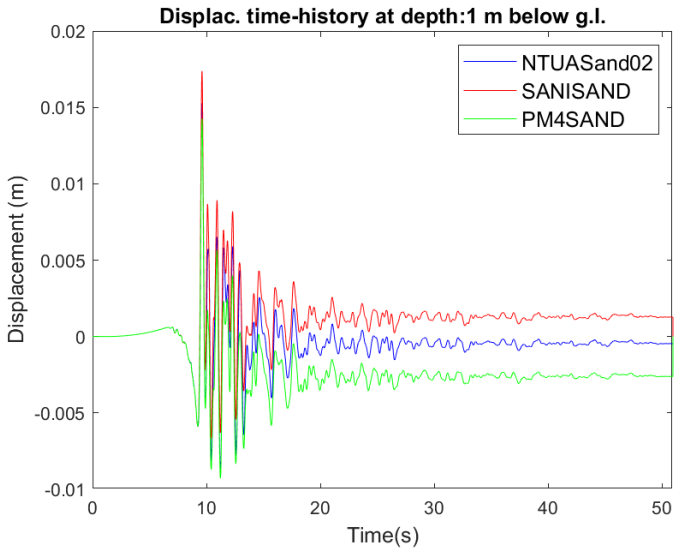

Figure 5.16. Displacement time series for the input ACC at 1 m below g.l.

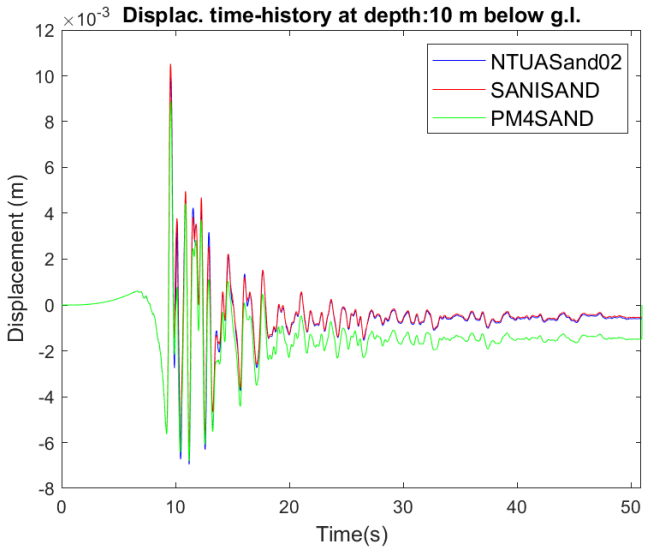

Figure 5.17. Displacement time series for the input ACC at 10 m below g.l.

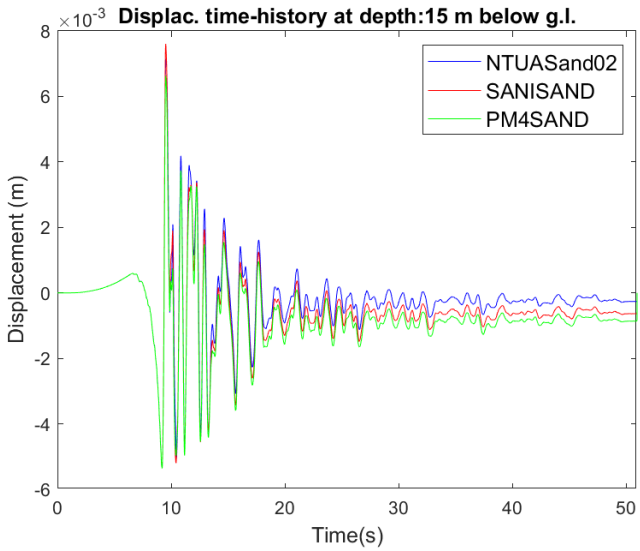

Figure 5.18. Displacement time series for the input ACC at 15 m below g.l.

The displacement time series are reported because they are notoriously not affected by high frequencies disturbance that can numerically arise. In fact, the plots reported in Figure 5.16, Figure 5.17, and Figure 5.18 show the same shapes for all the constitutive models, with very close amplitudes, mainly in the first 20 s of the time series. This confirms the effectiveness of the NTUASand02 constitutive model in the simulation of boundary value problems, even if compared to other constitutive models whose use is extremely widespread in the literature. The different residual displacements at the end of the signal just shown in Figure 5.16, Figure 5.17, and Figure 5.18 can be due to the different flow rules and hardening laws provided by the three models in the plastic response formulation.

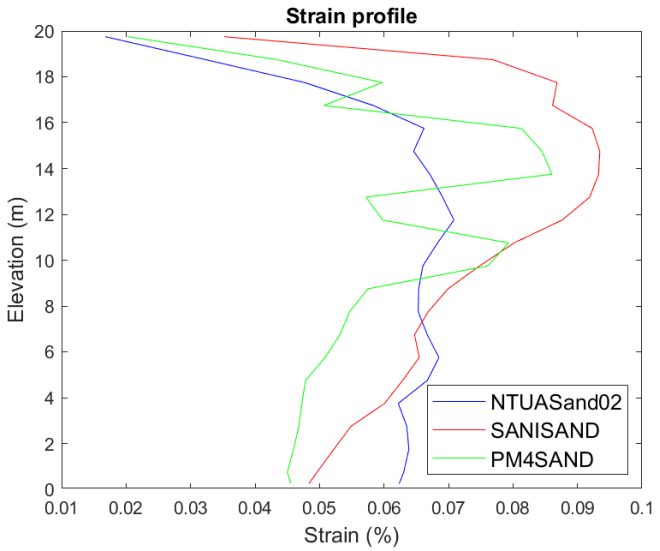

Figure 5.19. Strain profile for the input ACC.

In Figure 5.19 the resulting strain profile shows once more good accordance between the models. The highest strain levels are shown by NTUASand02 in the lowest 7 m, while in the first 3 m below the ground level there is good accordance with the strain level mobilized by PM4SAND. Here, SANISAND produces the highest deformation.

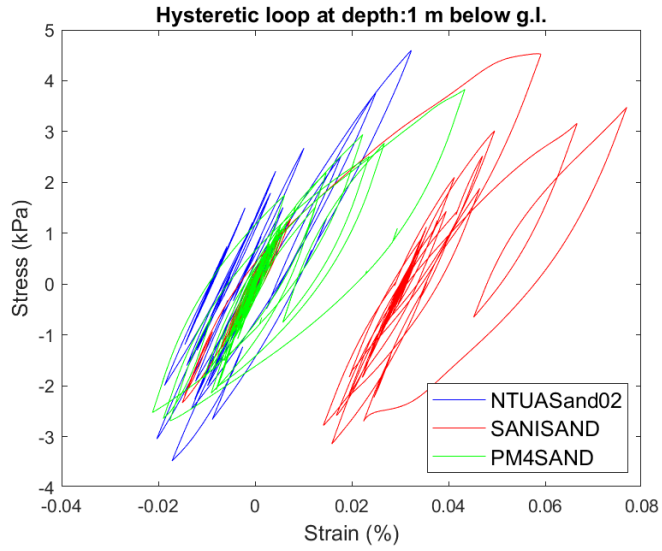

Figure 5.20. Hysteretic loops for the input ACC at 1 m below g.l.

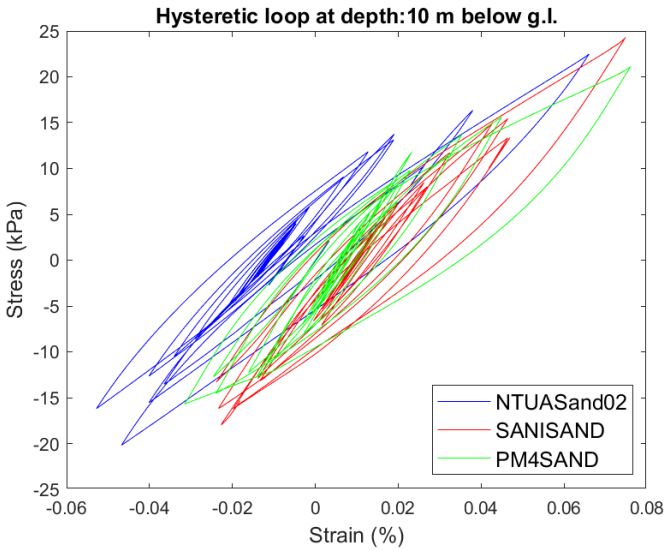

Figure 5.21. Hysteretic loops for the input ACC at 10 m below g.l.

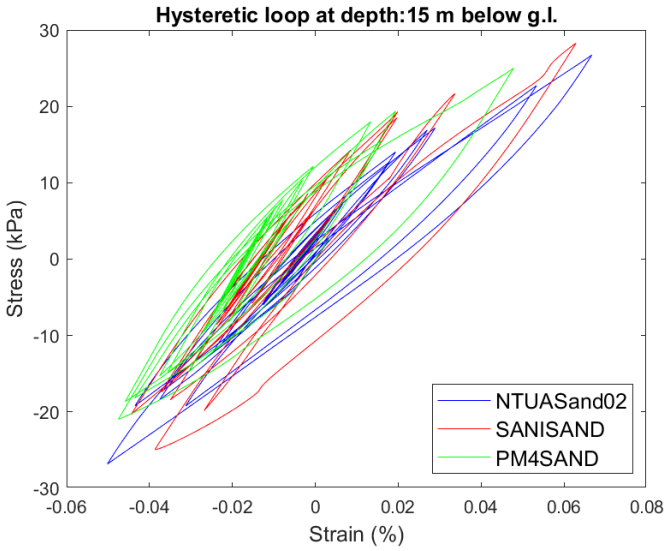

Figure 5.22. Hysteretic loops for the input ACC at 15 m below g.l.

The hysteretic loops reported in Figure 5.20, Figure 5.21, and Figure 5.22 highlight good accordance between the three constitutive models at the highest depths (i.e., 10 m and 15 m below the ground level), while the response in the upper control point seems to show some discrepancies, but with reference to the SANISAND constitutive model only. This observation is consistent with the shear strain profile of Figure 5.19,

where the simulation using SANISAND mobilizes the highest strain level in the upper part of the soil deposit.

5.3.1.2 Input: CUE90

With reference to the input CUE90 of Figure 5.7 applied in drained conditions, acceleration time series are shown in Figure 5.23, Figure 5.24, and Figure 5.25 at the three control points, while Figure 5.26, Figure 5.27, and Figure 5.28 illustrate Fourier Amplitude Spectra (FAS). PGA profile is reported in Figure 5.29, and the displacement time series are in Figure 5.30, Figure 5.31, and Figure 5.32. The residual shear strain profile is in Figure 5.33, and the hysteretic loops are represented in Figure 5.34, Figure 5.35, and Figure 5.36.

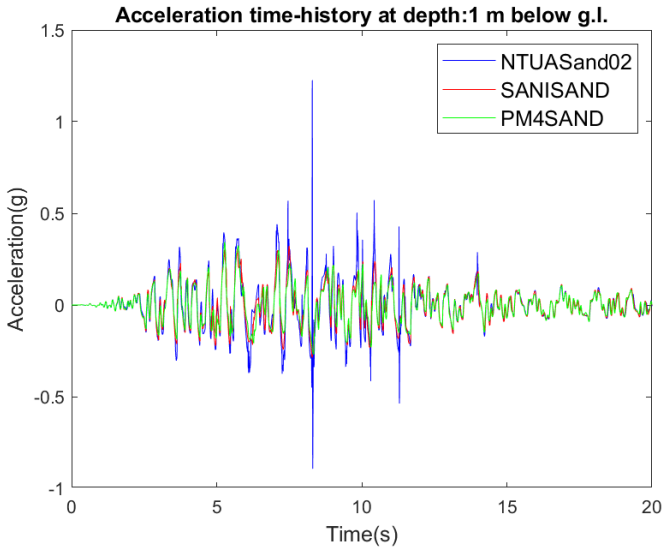

Figure 5.23. Acceleration time series for the input CUE90 at 1 m below g.l.

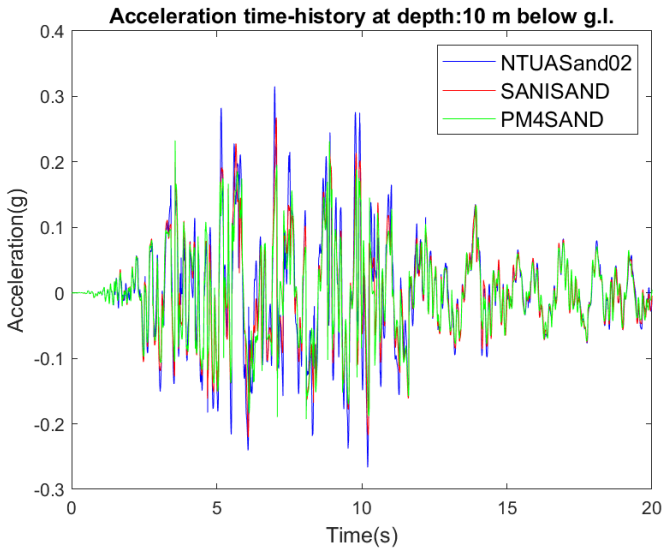

Figure 5.24. Acceleration time series for the input CUE90 at 10 m below g.l.

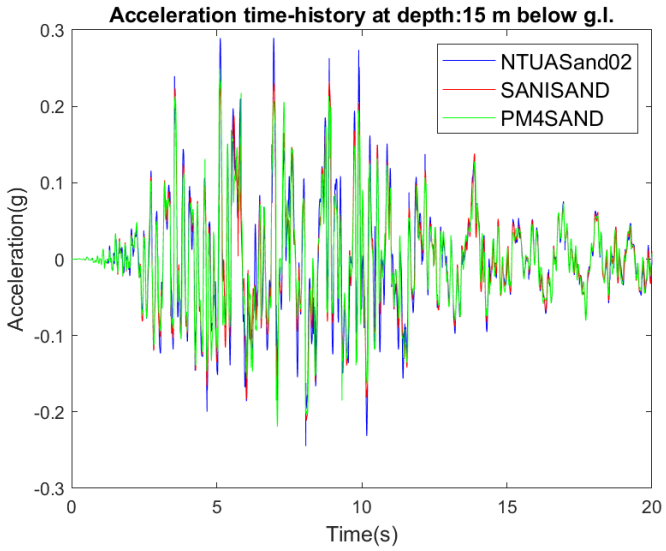

Figure 5.25. Acceleration time series for the input CUE90 at 15 m below g.l.

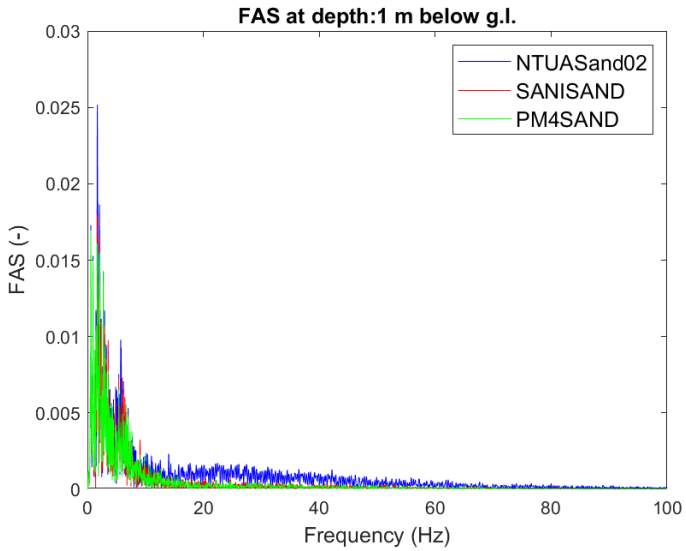

Figure 5.26. FAS for the input CUE90 at 1 m below g.l.

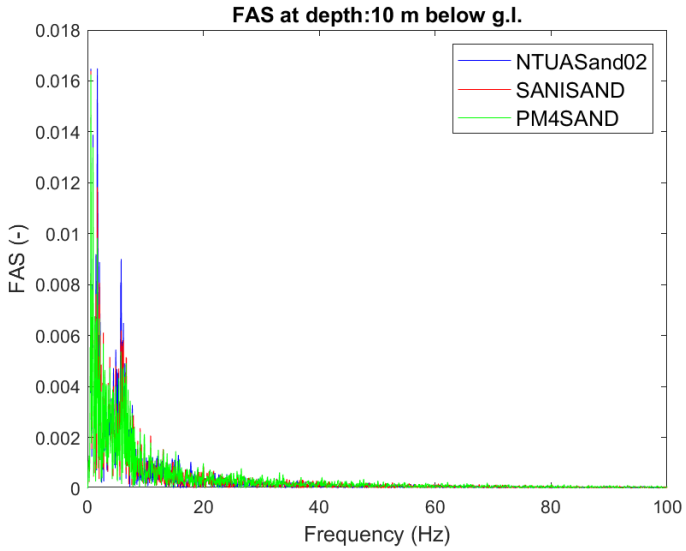

Figure 5.27. FAS for the input CUE90 at 10 m below g.l.

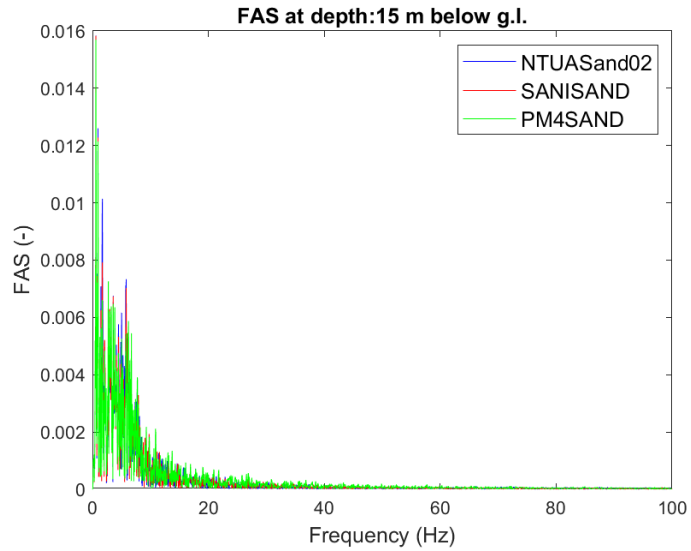

Figure 5.28. FAS for the input CUE90 at 15 m below g.l.

Very useful to understand the performances of the three constitutive models, keeping an eye on the one exhibited by NTUASand02, is the coupled observation of acceleration time-series (cf. Figure 5.23, Figure 5.24, Figure 5.25) and Fourier amplitude spectra (cf. Figure 5.26, Figure 5.27, Figure 5.28). In fact, it emerges that when a severe input motion is applied, NTUASand02 exhibits a higher amplification when comparing the response at the different control points using the different constitutive models. More pronounced peaks are individuable at 1 m below the ground level (Figure 5.23 and Figure 5.26), while the response at the remaining control points still appears satisfactory. The peaks at the uppest control points can even be distinguished in the corresponding Fourier amplitude spectrum, where frequencies belonging to the 20-40 Hz band are more excited in terms of spectral amplitude if compared to the FAS of the remaining constitutive models.

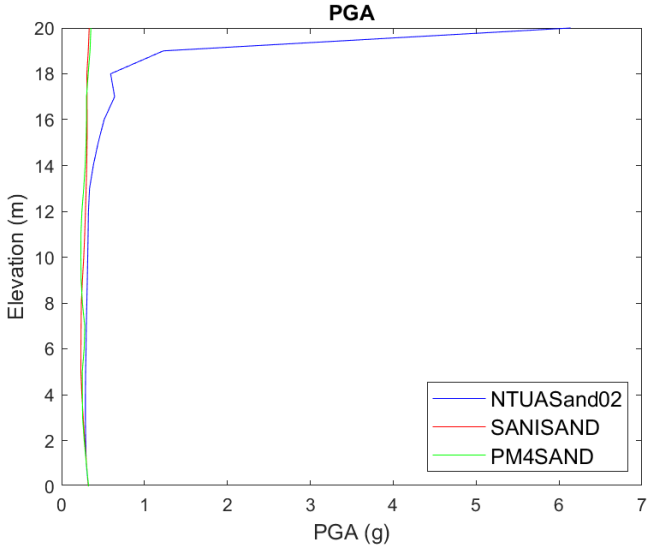

Figure 5.29. PGA profile for the input CUE90.

With reference to the PGA profile reported in Figure 5.29, the constitutive model NTUASand02 always exhibits the highest amplitude values, but on the most surficial nodes (i.e., on the ground surface), PGA reaching extremely high values is simulated.

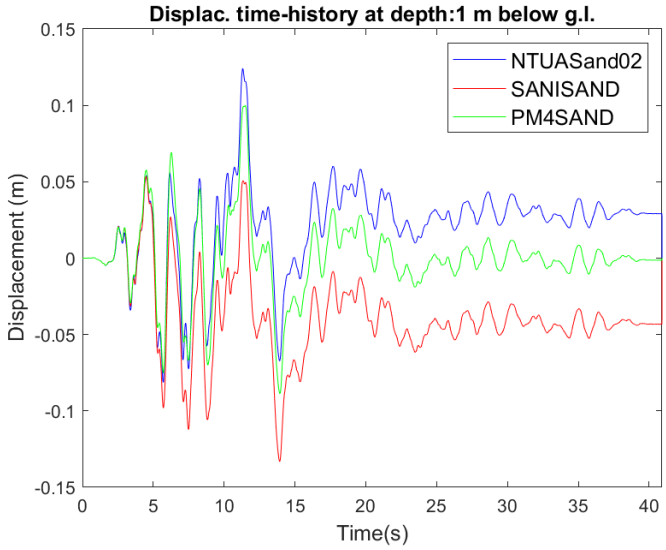

Figure 5.30. Displacement time series for the input CUE90 at 1 m below g.l.

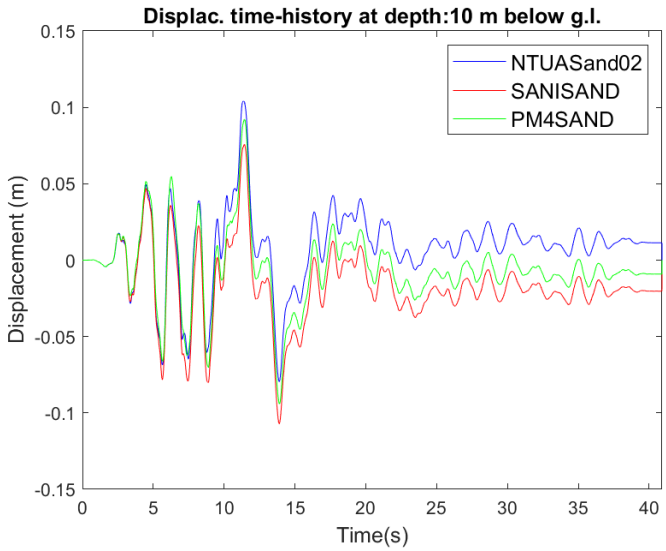

Figure 5.31. Displacement time series for the input CUE90 at 10 m below g.l.

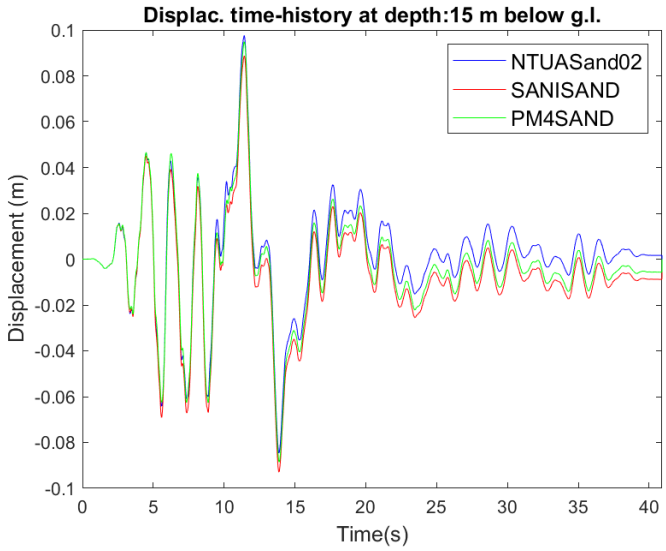

Figure 5.32. Displacement time series for the input CUE90 at 15 m below g.l.

As mentioned before, the displacement time-series are not affected by high frequencies disturbance and the observation of Figure 5.30, Figure 5.31, and Figure 5.32 confirm that the shapes of the displacement time-series are consistent among the three models at each depth.

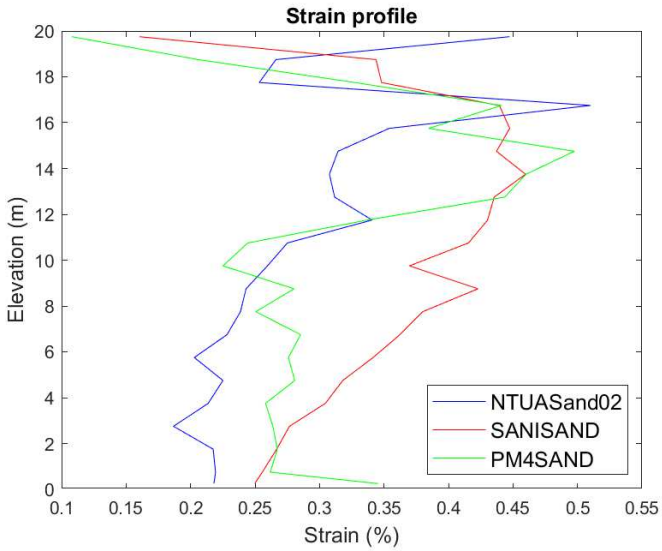

Figure 5.33. Strain profile for the input CUE90.

The strain profile resulting from the analyses highlights good accordance between the three constitutive models. In particular, up to 10 m below the ground level, SANISAND seems to show the highest mobilized strain, with the lowest values provided by NTUASand02. On the other hand, with reference to the topmost 5 m of the soil deposit, the three formulations show the same deformations. It is worth noting that the highest strain level is provided by NTUASand02 on surface, and this behaviour is also shown in the profile of Figure 5.29. The closest integration point to the surface is located at 0.25 m below the ground level because of the nature of SSPquadUP elements that, as stated in McGann et al. (2012), exploits the single point integration with the integration point located at the center of the element.

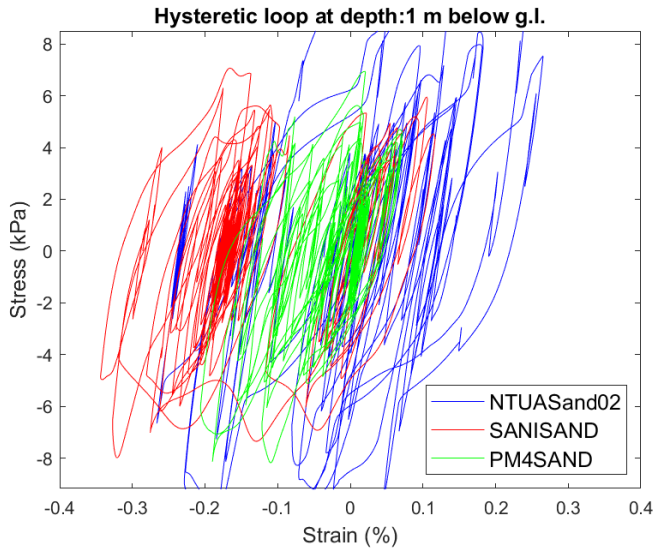

Figure 5.34. Hysteretic loops for the input CUE90 at 1 m below g.l.

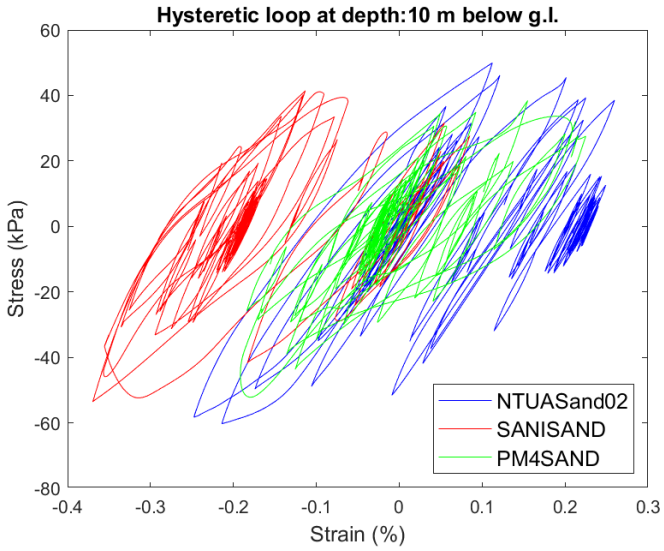

Figure 5.35. Hysteretic loops for the input CUE90 at 10 m below g.l.

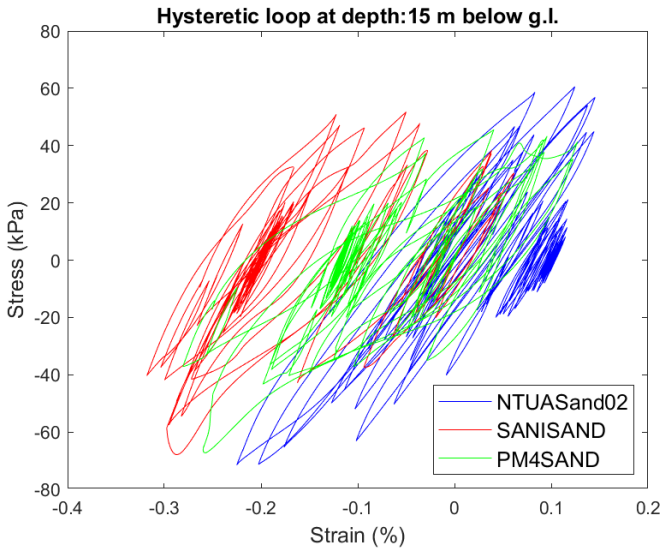

Figure 5.36. Hysteretic loops for the input CUE90 at 15 m below g.l.

The discussion referred to drained conditions can be concluded by some comments on the resulting hysteretic loops. In particular, very good accordance is reached at the lowest control points, and, as expected, a softer response if compared to the one exhibited when the input motion with the lower PGA is applied can be distinguished. Furthermore, another non-trivial aspect is related to the fact that the same initial stiffness is guaranteed in both input motions for the three constitutive models.

5.3.2 UNDRAINED CONDITIONS

In the following §5.3.2.1, the outputs deriving from the motion coded as ACC are shown, while in §5.3.2.2 the response for the column subjected to the CUE90 input is reported.

5.3.2.1 Input: ACC

With reference to the input ACC and reproducing undrained conditions, Figure 5.37, Figure 5.38, and Figure 5.39 plot the acceleration time series, while Figure 5.40, Figure 5.41, and Figure 5.42 depict Fourier amplitude spectra. Figure 5.43 shows the PGA profile and in Figure 5.44, Figure 5.45, and Figure 5.46, the evolution of the

displacement with time is reported. The strain profile is in Figure 5.47 and the hysteretic loops are shown in Figure 5.48, Figure 5.49, Figure 5.50. At the end, the excess pore water pressure ratio time series are reported in Figure 5.51, Figure 5.52, and Figure 5.53.

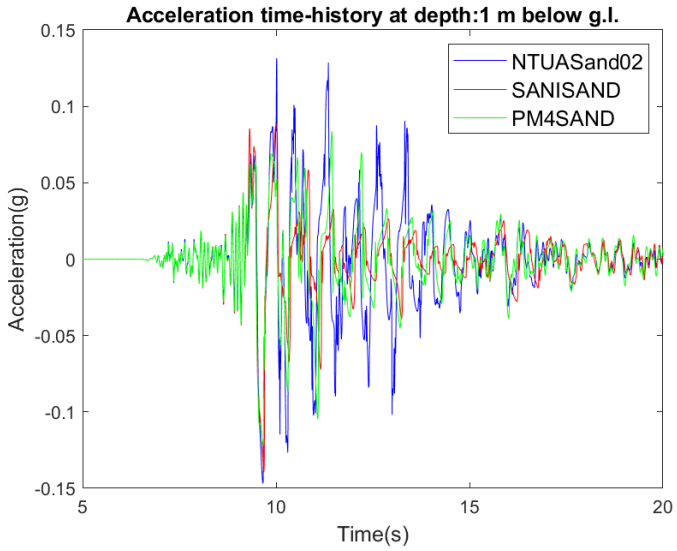

Figure 5.37. Acceleration time series for the input ACC at 1 m below g.l.

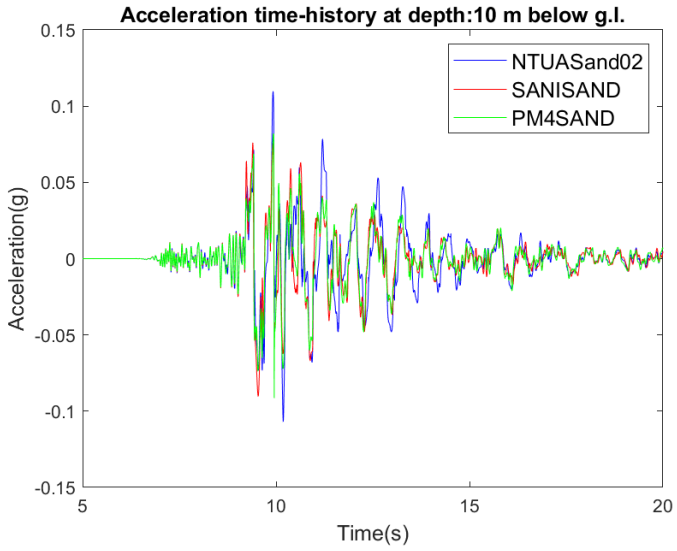

Figure 5.38. Acceleration time series for the input ACC at 10 m below g.l.

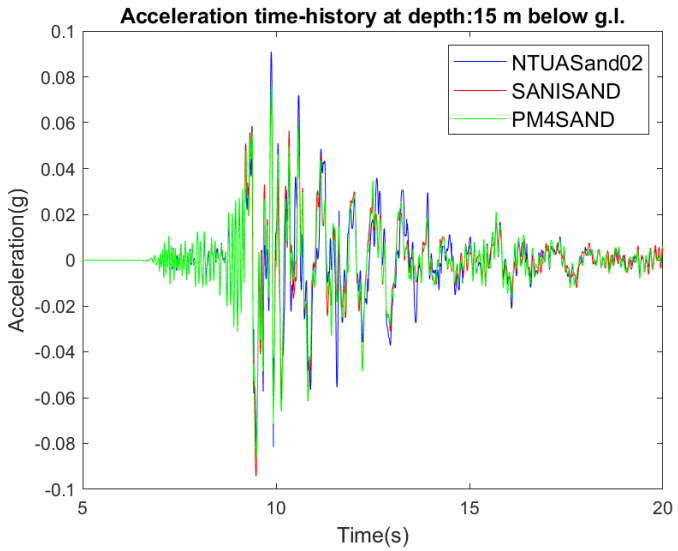

Figure 5.39. Acceleration time series for the input ACC at 15 m below g.l.

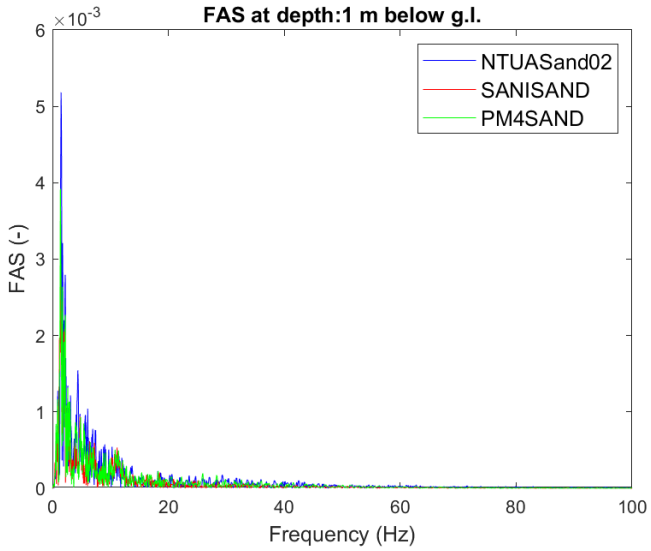

Figure 5.40. FAS for the input ACC at 1 m below g.l.

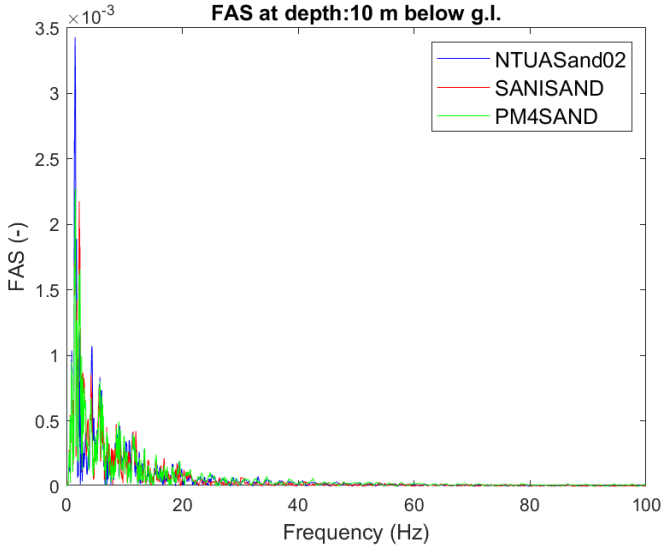

Figure 5.41. FAS for the input ACC at 10 m below g.l.

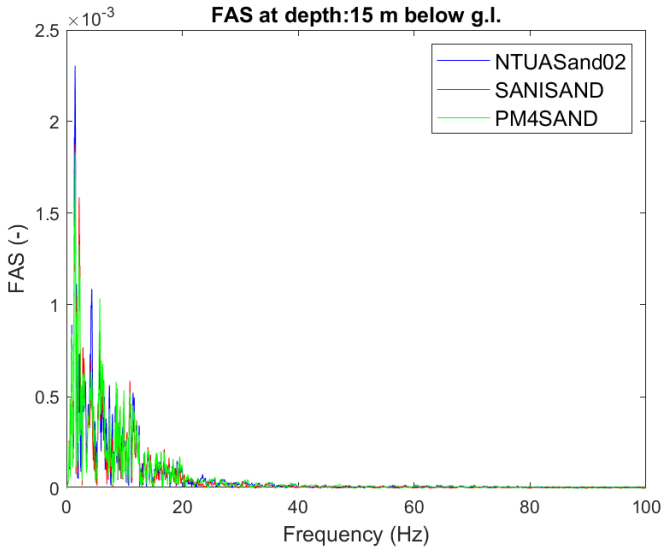

Figure 5.42. FAS for the input ACC at 15 m below g.l.

Acceleration time series (Figure 5.37, Figure 5.38, Figure 5.39) and Fourier amplitude spectra (Figure 5.40, Figure 5.41, Figure 5.42) point out good accordance between the response with the three constitutive models, but a significant overestimation of the response obtained with SANISAND and PM4SAND is observed using NTUASand02 in the central part of the time series at the highest control point. This is consistent with

what is observed in Fourier amplitude spectra, where the highest Fourier amplitudes in the whole band 0-20 Hz are observed with NTUASand02.

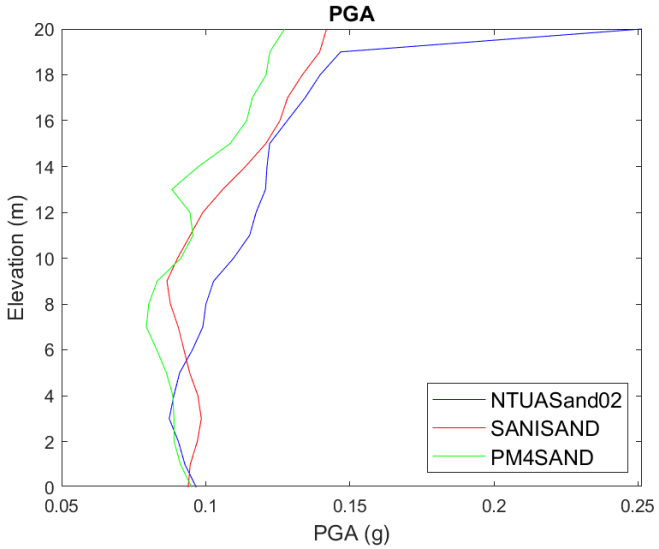

Figure 5.43. PGA profile for the input ACC.

Satisfactory accordance is pointed out even by the PGA profile of Figure 5.43, up to 1 m below the ground level, with the three models exhibiting essentially the same response. On the surface, a strong amplification is observed considering NTUASand02.

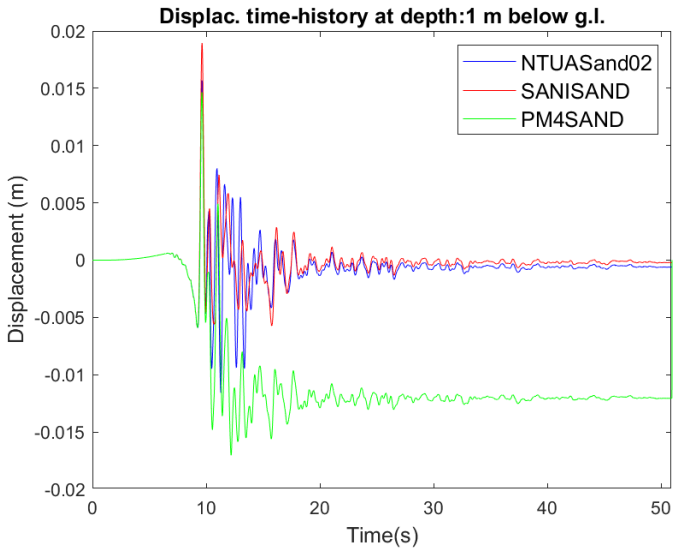

Figure 5.44. Displacement time series for the input ACC at 1 m below g.l.

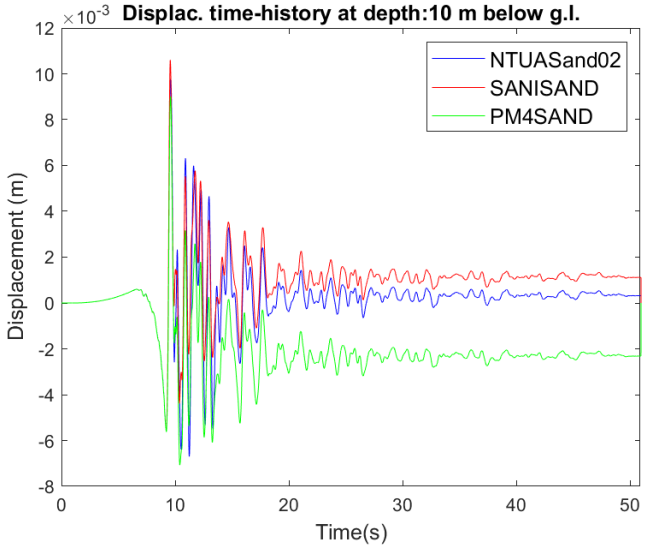

Figure 5.45. Displacement time series for the input ACC at 10 m below g.l.

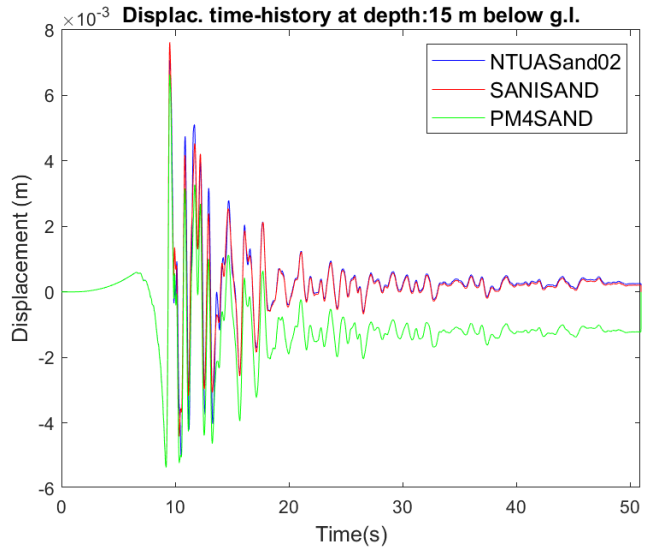

Figure 5.46. Displacement time series for the input ACC at 15 m below g.l.

The displacement time histories of Figure 5.44, Figure 5.45 Figure 5.46 point out a good coherence between the models at all the depths with reference to both amplitudes and shapes.

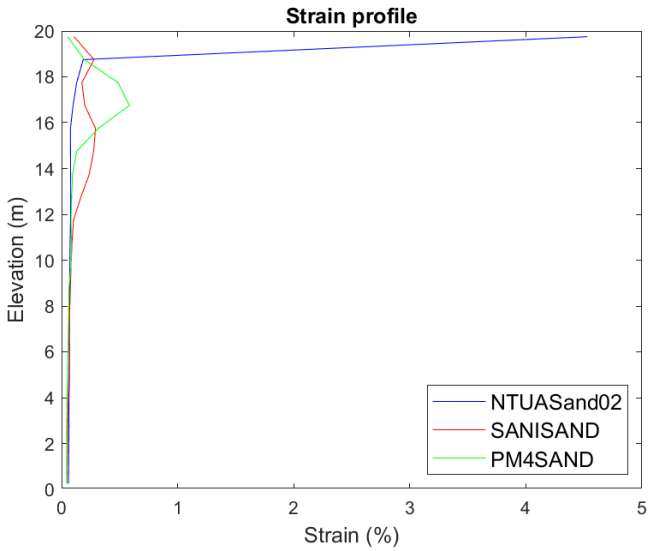

Figure 5.47. Strain profile for the input ACC.

The strain profile reported in Figure 5.47 evidences a very high strain level reached on the surface that appears to be consistent with the PGA profile reported in Figure 5.43. At the other locations, basically the same strain levels are reached.

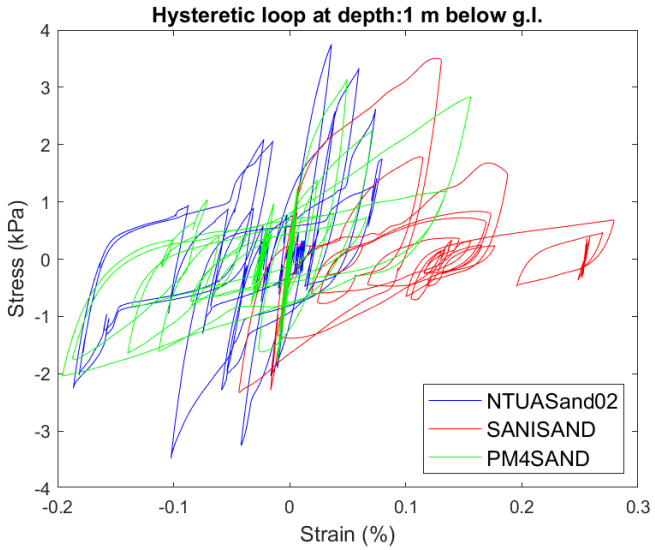

Figure 5.48. Hysteretic loops for the input ACC at 1 m below g.l.

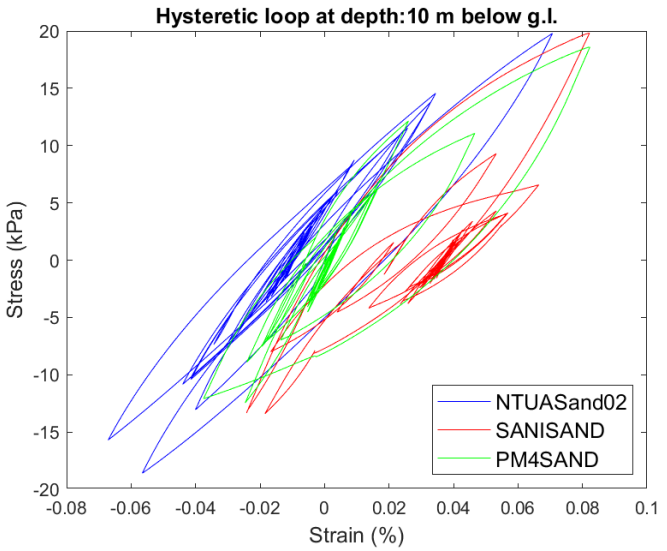

Figure 5.49. Hysteretic loops for the input ACC at 10 m below g.l.

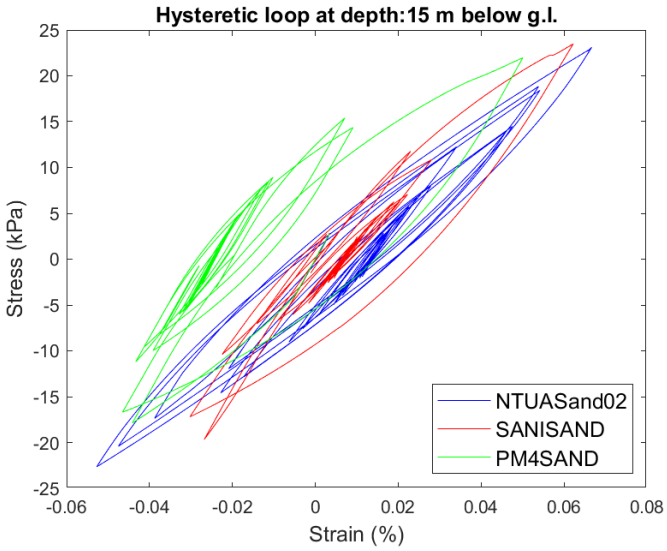

Figure 5.50. Hysteretic loops for the input ACC at 15 m below g.l.

Observing the response provided in terms of shear stress-shear strain cycles at the different depths, satisfactory accordance is achieved, in terms of strain amplitude. Generally speaking, the loops point out a strong non-linearity on the surface, highlighting the role of the development of excess pore water pressure. The non-linearity is more pronounced with the increasing depth. This feature is justified even by observing the simulated response in terms of excess pore water pressure ratio.

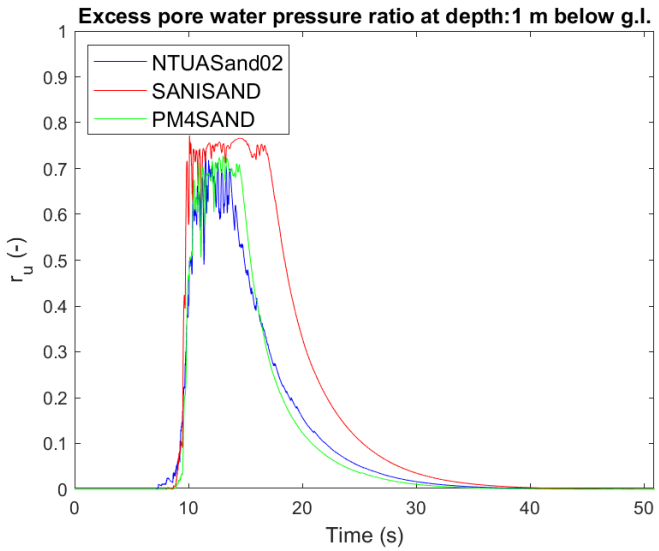

Figure 5.51. Excess pore water pressure ratio for the ACC input at 1 m below the g.l.

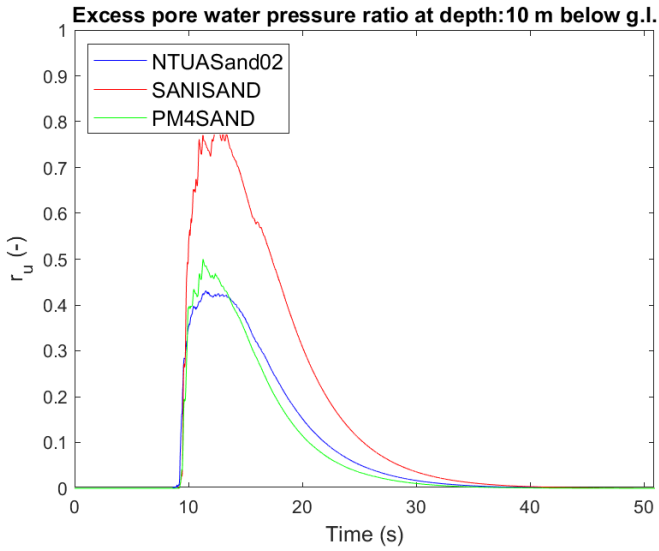

Figure 5.52. Excess pore water pressure ratio for the ACC input at 10 m below the g.l.

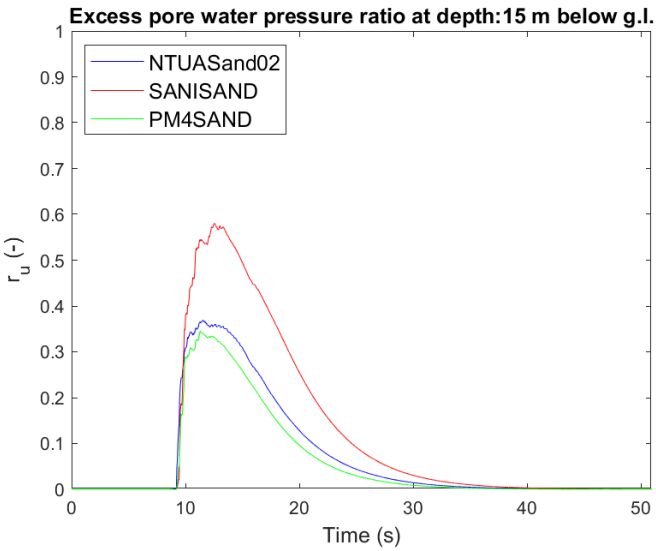

Figure 5.53. Excess pore water pressure ratio for the ACC input at 15 m below the g.l.

It is worth remembering how the excess pore water pressure ratio is evaluated: it represents the ratio between the excess pore water pressure Δu and the initial vertical effective stress σ'_{v0}. Generally, it is observed that higher values in terms of r_u are reached at 1 m below the ground level, and this is consistent with the observed stress-strain loops at the same depth. Good accordance even in terms of excess pore water pressure ratio is given by comparing the response obtained using both PM4SAND and NTUASand02, while SANISAND always exhibits the highest values of r_u.

5.3.2.2 Input: CUE90

Finally, an attempt to evaluate the performance of the implementation of NTUASand02 was made by considering the CUE90 input motion in undrained conditions. Provided that it is an extremely severe condition, this could help to understand how the model behaves when soil liquefaction develops. In fact, the analysis conducted considering the NTUASand02 constitutive model experiences convergence problems that seem to be strictly related to the condition $p<p_{min}$ in the upper 11 m of the column, discussed in §3.4 and to the development of high values of excess pore water pressures.

For the sake of clarity, some of the results obtained applying the CUE90 input motion are reported in the following plots. In particular, Figure 5.54, Figure 5.55, and Figure

5.56 show the acceleration time series of the simulated response after about 5 s for all the control points, while Figure 5.57 shows the Fourier spectrum at 15 m below the ground level. The displacement time series are shown in Figure 5.58, Figure 5.59, and Figure 5.60 and, at the end, stress-strain loops and excess pore water pressure ratio are in Figure 5.61-Figure 5.63 and Figure 5.64-Figure 5.66, respectively.

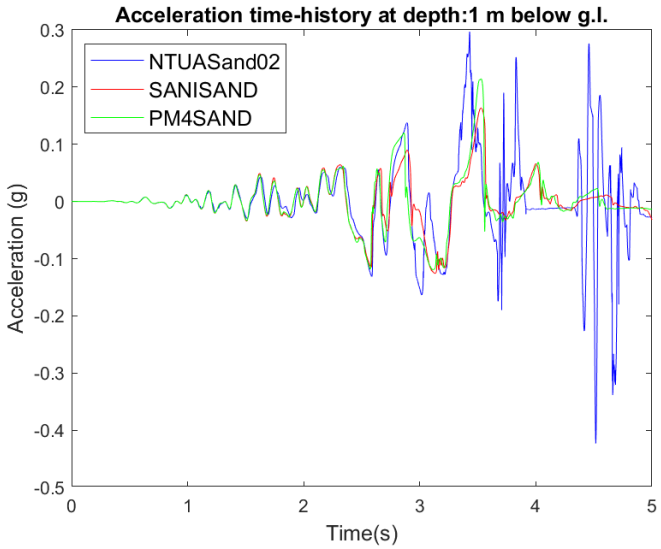

Figure 5.54. Acceleration time series for the input CUE90 at 1 m below g.l.

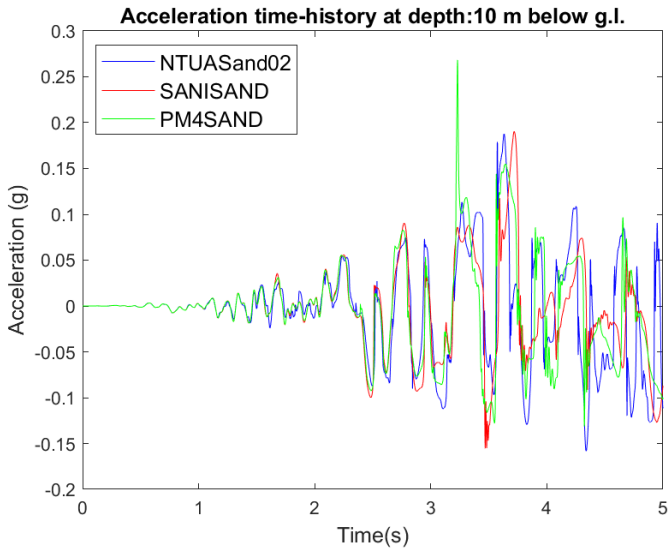

Figure 5.55. Acceleration time series for the input CUE90 at 10 m below g.l.

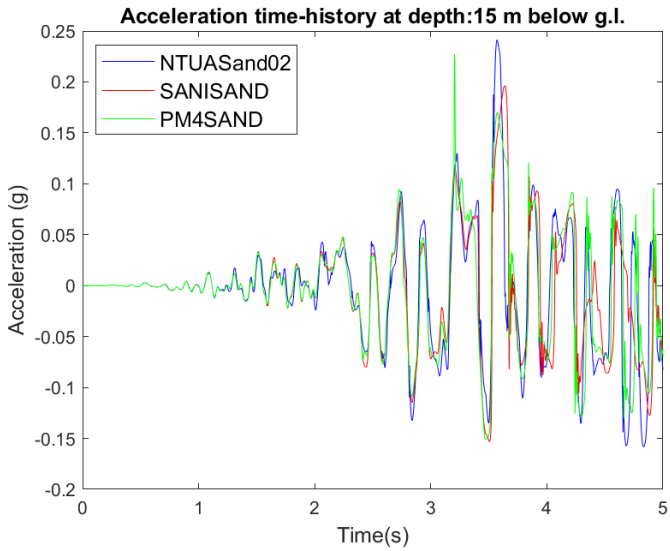

Figure 5.56. Acceleration time series for the input CUE90 at 15 m below g.l.

In Figure 5.54-Figure 5.56, the response observed comparing the performance of the constitutive models in the first 5 s highlights that good accordance is reached at 10 m and 15 m below the ground level, while on the surface, up to 3–4 s, the response is acceptable, then, contextually to the generation of high excess pore water pressures, it quickly becomes unstable.

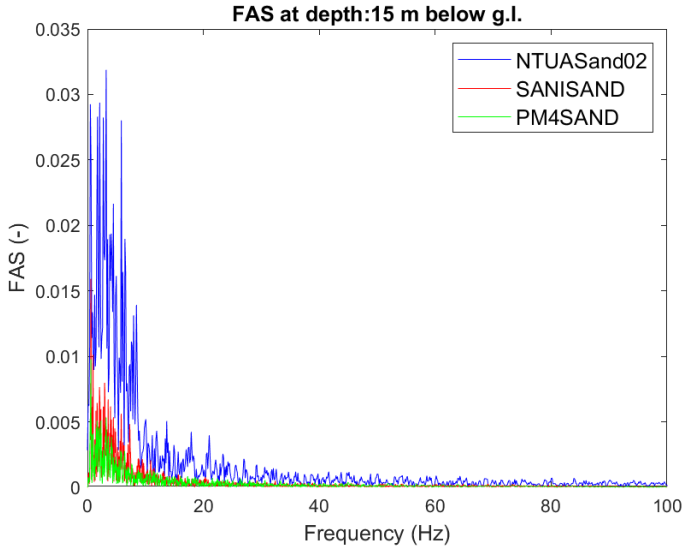

Figure 5.57. FAS for the input CUE90 at 15 m below g.l.

The Fourier amplitude spectrum of the signal at 15 m below the ground level is shown as an example in order to stress the high frequency content of the simulated signal provided by NTUASand02. This can be related either to the simulation of the specific case or to the constitutive platform.

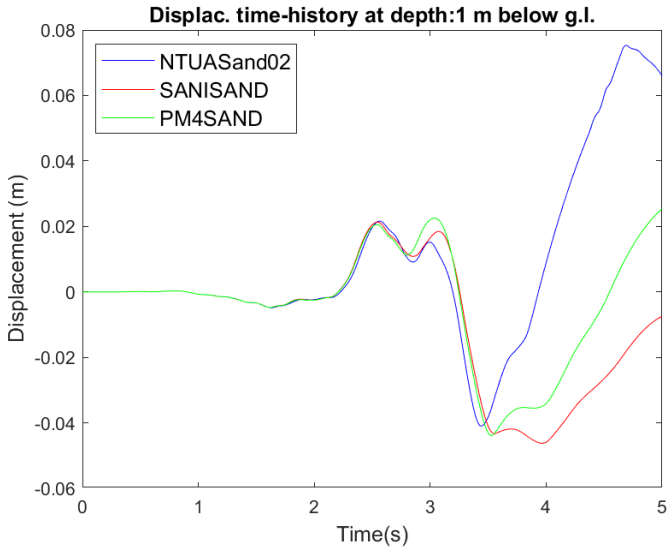

Figure 5.58. Displacement time series for the input CUE90 at 1 m below g.l.

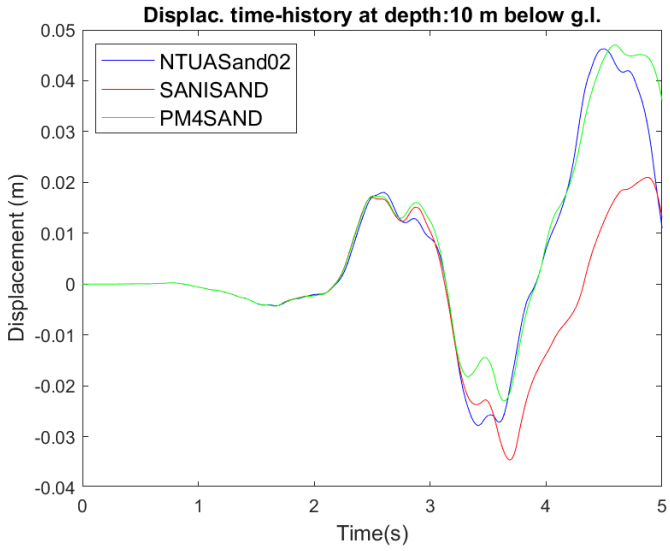

Figure 5.59. Displacement time series for the input CUE90 at 10 m below g.l.

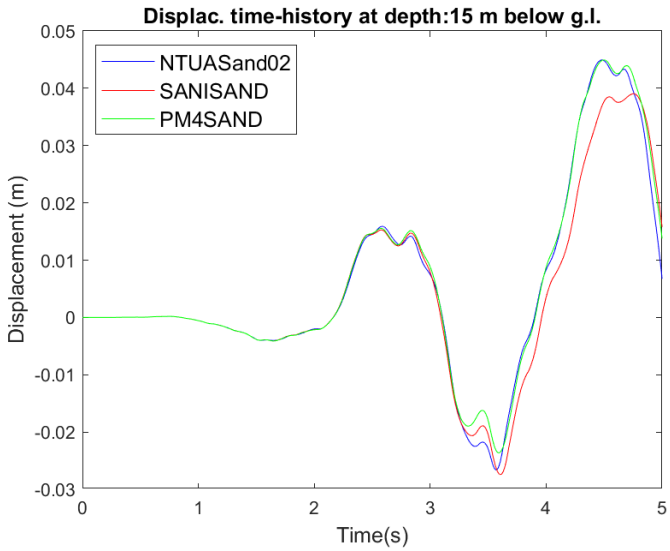

Figure 5.60. Displacement time series for the input CUE90 at 15 m below g.l.

As it was previously pointed out, the displacement time series are not affected by high-frequency disturbance. In fact, at the depths of 10 m and 15 m below the ground level, very satisfactory accordance is observed up to about 5 s, while the response on surface shows discrepancies at about 4 s.

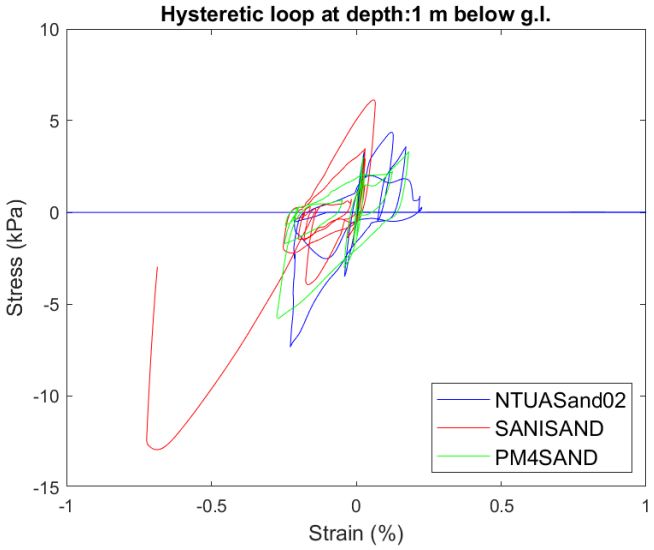

Figure 5.61. Hysteretic loops for the input CUE90 at 1 m below g.l.

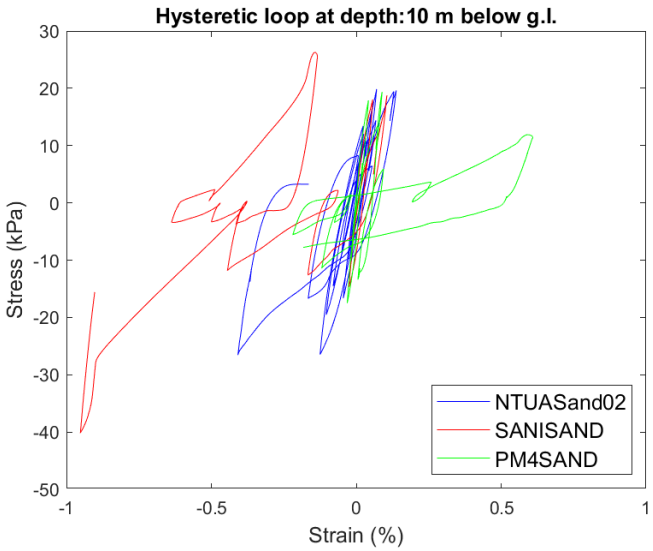

Figure 5.62. Hysteretic loops for the input CUE90 at 10 m below g.l.

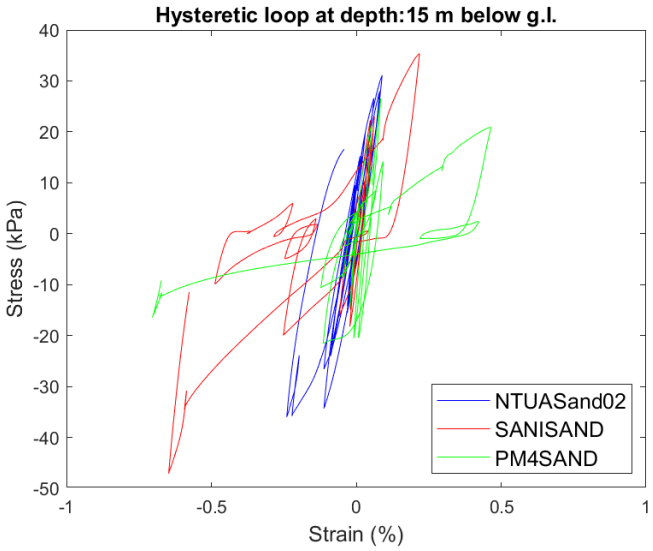

Figure 5.63. Hysteretic loops for the input CUE90 at 15 m below g.l.

Consequently, even high strain levels are mobilized. In fact, the hysteretic loops observed in Figure 5.61 point out very high strains for NTUASand02 that are contextual to severe and disturbed excess pore water pressure ratio, reaching even the value of 1, meaning that the excess pore water pressure is equal to the initial effective stress. However, in Figure 5.62 and Figure 5.63, a good accordance is observed among the models.

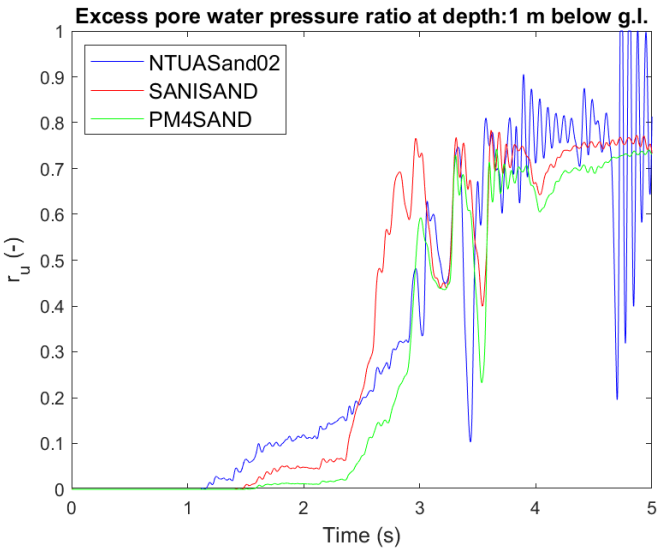

Figure 5.64. Excess pore water pressure ratio for the CUE90 input at 1 m below g.l.

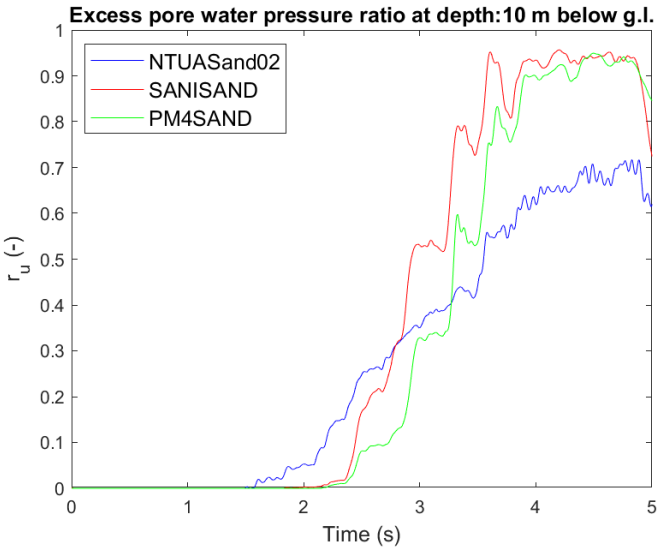

Figure 5.65. Excess pore water pressure ratio for the CUE90 input at 10 m below g.l.

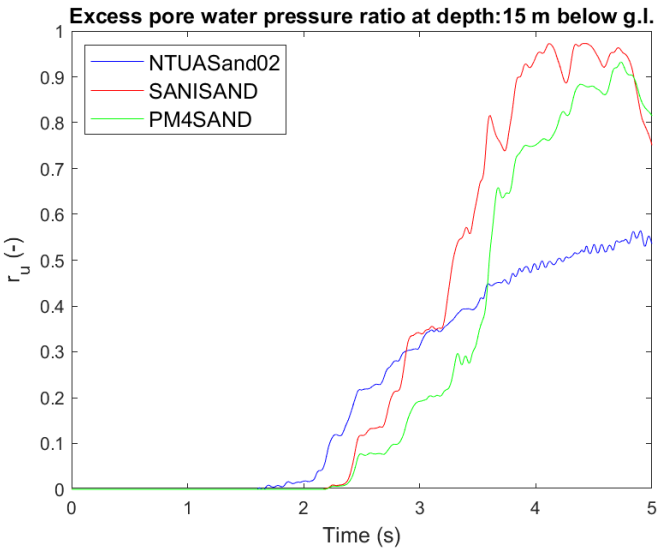

Figure 5.66. Excess pore water pressure ratio for the CUE90 input at 15 m below g.l.

What above mentioned appears extremely clear in Figure 5.64. In fact, with reference to the response at 1 m below the ground level, the condition r_u=1 for NTUASand02 is contextual to the discrepancies observed in acceleration time histories (cf. Figure 5.54). Furthermore, this response can be considered looking at the hysteretic loops of Figure 5.61.

5.4 DISCUSSION

The analyses reported in this chapter have a dual role: on the one hand they are conceived to understand how reliable the implementation of the NTUASand02 constitutive model is in the simulation of boundary value problems, even if characterized by a certain degree of simplicity (i.e., the simulation of a homogeneous sand soil column); on the other hand, they are willing to compare the different responses obtained using constitutive models widely adopted in the literature and whose calibration with reference to the Nevada sand is available. It is worth noting that the constitutive parameters have been slightly modified in order to fit the initial values of the image stress ratios and state parameter profile along with the depth of the deposit.

Overall, it can be asserted that the resulting response in drained conditions is satisfactory, even if a severe input motion is applied, considering the NTUASand02 implementation and comparing its response to that obtained using SANISAND and PM4SAND. All the observed responses (i.e., acceleration and displacement time series, excess pore water pressure ratio and shear stress-shear strain loops) gave realistic results, in particular at the highest depths.

More complex is the response reproduced when undrained conditions are applied: the response considering the motion ACC (with about 0.1 g PGA) highlighted very good accordance among the constitutive models at the higher depths. This appears clearly in the comparison of displacement time series and excess pore water pressure ratio. However, strong amplification with severe strain levels arises on surface, as it can be seen from the profile of PGA and deformation. On the other hand, the analyses conducted exploiting strong motion in undrained conditions point out a different response of NTUASand02 with respect to the other constitutive models. In fact, with the use of SANISAND and PM4SAND the convergence is reached and the whole accelerogram is reproduced, while with the use of NTUASand02, the analysis reaches the condition $p<p_{min}$ after about 5 s. However, it is worthwhile to mention that the input is very severe and satisfactory response is observed up to 3-4 s, when the excess pore water pressure ratio approaches 1. In addition, these models, except for PM4SAND are designed to detect the liquefaction triggering and not more complex phenomena, such as post-liquefaction. Furthermore, even if PM4SAND provides a formulation to model post-liquefaction behaviour, the developers give the users the possibility to activate it or not, and, in this case, this has not been considered.

With reference to the reaching of p_{min} by NTUASand02, limitations can be correlated to various factors, such as the numerical model of the soil column, the interaction between the constitutive framework and the finite element platform, and the constitutive model itself. These aspects will be investigated one-by-one in the further developments of the work, even by considering possible modification of the model or the implementation of its newer version (Andrianopoulos et al., 2010) by keeping yield

surface. Finally, considering the constitutive model in the version recalled in this study, worth mentioning that it has never been implemented and tested in a finite element code considering boundary value problems together with undrained conditions.

5.5 REFERENCES

Andrade J.E., Ramos A.M. and Lizcano A. (2013). Criterion for flow liquefaction instability. Acta Geotechnica. 8 (5): 525-535. https://doi.org/10.1007/s11440-013-0223-x

Andrianopoulos K. I., Papadimitriou A. G. and Bouckovalas G. D. (2010). Bounding surface plasticity model for the seismic liquefaction analysis of geostructures, Soil Dynamics and Earthquake Engineering, 30(10): 895-911.

Arulmoli, K., Muraleetharan, K., Hosain, M. and Fruth, L. (1992). Velacs laboratory testing program, soil data report. Rep. to the National Science Foundation, Earth Technology Corporation, Irvine, CA.

Boulanger R.W. and Ziotopoulou K. (2017). PM4Sand (version 3.1): A sand plasticity model for earthquake engineering applications. Report UCD/CGM-17/01, Center for Geotechnical Modeling, Dept. of Civil and Environmental Eng., University of California, Davis, CA.

Dafalias, Y.F. and Manzari, M.T. (2004). Simple plasticity sand model accounting for fabric change effects. J.Eng. Mech; 130(6):622–34. https://doi.org/10.1061/(ASCE)0733-9399.

Fierro T., Castiglia M., Santucci de Magistris F. (2022; in print). Performance of advanced constitutive models in site response analyses of liquefiable soils. Proceedings of the 4th International Conference on Performance-based Design in Earthquake Geotechnical Engineering. Beijing, July 15-17, 2022.

Joyner, W.B. and Chen, A.T.F. (1975). Calculation of nonlinear ground response in earthquakes, Bull. Seism. Soc. Am., 65, 1315-1336.

Kamai, R. and Boulanger, R.W. (2013). Simulations of a centrifuge test with lateral spreading and void redistribution effects. Journal of Geotechnical and Geoenvironmental Engineering. J. Geotech. Geoenviron. Eng. 2013.139:1250-1261.

Kwok, A. O. L., Stewart, J. P., Hashash Y. M. A., Matasovic N., Pyke R., Wang Z. and Yang, Z. (2007). Use of exact solutions of wave propagation problems to guide implementation of nonlinear seismic ground response analysis procedures. J. Geotech. Eng. 133 (11): 1385–1398.

Luzi, L., Puglia, R, Russo, E. and ORFEUS WG5 (2016). Engineering Strong Motion Database, ver. 1.0. Istituto Nazionale di Geofisica e Vulcanologia, Observatories & Research Facilities for European Seismology. Doi: 10.13127/ESM.

Lysmer, J. and Kuhlemeyer R.L. (1969). Finite dynamic model for infinite media. Journal of the Engineering Mechanics Division, ASCE, 95(EM4):859-877.

McGann, C.R., Arduino, P. and Mackenzie-Helnwein P. (2012). Stabilized single-point 4-node quadrilateral element for dynamic analysis of fluid saturated porous media. Acta Geotechnica 7 (4), 297-311.

McKenna, F., Fenves, G. L., Scott, M. H. and Jeremic, B. (2000). Open system for earthquake engineering simulation. http:// opensees.berkeley.edu.

Manzari, M.T. and Dafalias, Y.F. (1997). A critical state two-surface plasticity model for sand. Geotechnique; 47(2):255–72.

Papadimitriou, A.G. and Bouckovalas, G.D. (2002). Plasticity model for sand under small and large cyclic strains: a multiaxial formulation. Soil Dyn. And Earth. Engng. 22, 191-204.

Ramirez J., Barrero R.A., Chen L., Dashti S., Ghofrani A., Taiebat M. and Arduino P. (2018). Site response in a layered liquefiable deposit: evaluation of different numerical tools and methodologies with centrifuge experimental results. J Geotech Geoenviron ASCE 2018;144(10) https://doi.org/10.1061/(ASCE)GT.1943-5606.0001947.

Taiebat, M., Jeremic, B., Dafalias, Y.F., Kaynia, A.M. and Cheng, Z. (2010). Propagation of seismic waves through liquefied soils. Soil Dyn and Earthq Eng 30 236–257.

5. SIMULATION OF THE SITE RESPONSE OF A SOIL COLUMN TO A SEISMIC EXCITATION

Visone, C., Bilotta, E. and Santucci de Magistris, F. (2010). One-dimensional ground response as a preliminary tool for dynamic analyses in Geotechnical Earthquake Engineering. Journal of Earthquake Engineering, 14: 1, 131-162.

6 SIMULATION OF CENTRIFUGE TESTS

6.1 INTRODUCTION

The following chapter describes the numerical simulations of centrifuge tests conducted in the framework of the LIQUEFACT project (H2020-DRS-2015, Grant n. 700748), on Ticino sand, in order to show the applicability of the advanced constitutive models in site response analyses of liquefiable soils. In the LIQUEFACT project, a wide number of tests has been performed, considering both the cases of free-field conditions and with structural models installed inside the centrifuge (see Özcebe et al., 2020; Fasano et al., 2021). In particular, the free-field response was modelled by Özcebe et al. (2020) in OpenSees using the multi-surface Pressure-Dependent Multi-Yield02 constitutive model (PDMY02; Yang et al., 2003). The numerical model was built in plane-strain conditions, by implementing the whole box and reproducing even the boundary conditions of the container. In this study, an attempt to simulate the free-field response of the centrifuge tests modelling the centerline of the box through a soil column is made by using PM4SAND model and the calibration for Ticino sand proposed by Fasano et al. (2021). The response is investigated in terms of acceleration and excess pore water pressure time series, by comparing the simulations with the recorded data. The following paragraph §6.2 briefly illustrates the centrifuge tests that are going to be numerically reproduced, §6.3 describes the initial conditions of the tests and the adopted scaling laws; in §6.4 the numerical model is reported, while in §6.5 some details on the PM4SAND parameters which have been selected are indicated. Then, §6.6 together with §6.7 shows the achieved results. Finally, some comments are proposed in §6.8 regarding the results of the simulations.

6.2 CENTRIFUGE TESTS

The centrifuge tests were conducted on a 750 x 280 mm^2 soil deposit at the model scale that corresponds to a 37.5 m-large and 14 m-high prototype of Ticino Sand. In this

study, two different ground motions are considered. Data are obtained from Airoldi et al. (2018), released in the framework of LIQUEFACT project and from Fasano et al. (2021). The two different tests here considered were identified through the following codes:

1. M1_S1_GM17
2. M1_S1_GM34

These codes refer to the model M1, consisting of a homogeneous deposit of Ticino Sand (S1) with the application of the two ground motions identified as GM17 and GM34. The applied input motions at the model scale are reported in the following Figure 6.1 and Figure 6.2 (Airoldi et al., 2018).

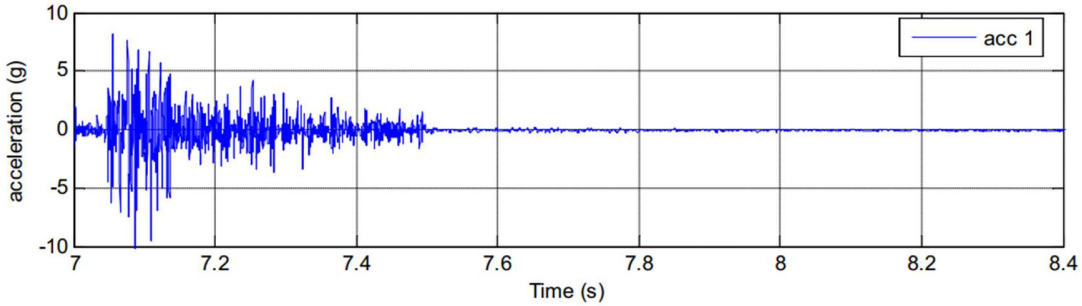

Figure 6.1. GM17 ground motion at model scale (from Airoldi et al., 2018)

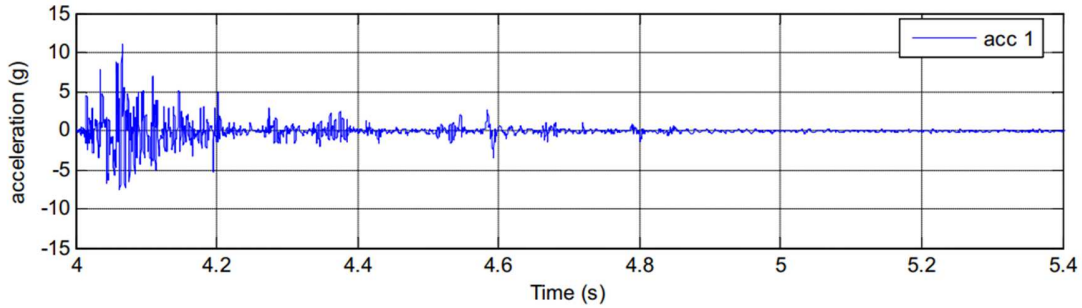

Figure 6.2. GM34 ground motion at model scale (from Airoldi et al., 2018).

6.3 MODEL PARAMETERS

In the report compiled by Airoldi et al. (2018), for each test, the following data are obtained. They are referred to the state of the model before the application of the centrifugal acceleration and immediately after the reconstitution stage:

1. Relative density, D_r and the corresponding void ratio, e (based on the values of e_{max} and e_{min} of Ticino Sand);
2. Centrifugal angular velocity, ω;
3. Saturated density of Ticino sand, ρ_{sat};

The model is reproduced using the OpenSees framework at the prototype scale. This choice was made because, generally, it is easier to interpret the obtained results at this scale. To this aim, all the measurements together with the model properties should be converted accordingly. The following scaling laws are adopted to obtain time (6.1), acceleration (6.2), pore pressure (6.3) and lengths (6.4) at prototype scale:

$$t_p = t_m \cdot a_c/g \tag{6.1}$$

$$a_p = \frac{a_m}{a_c/g} \tag{6.2}$$

$$u_m = u_p \tag{6.3}$$

$$l_m = l_p \cdot a_c/g \tag{6.4}$$

Here, t_m, a_m and u_m represent time, acceleration and pore water pressure at model scale, while t_p, a_p and u_p represent time, acceleration and pore water pressure at prototype scale. Finally, a_c is the centrifugal acceleration and l_m and l_p are lengths at model and prototype scales, respectively. g is gravity acceleration.

The report of Airoldi et al. (2018) allowed even to calculate the height of the model after reconstitution and the positions of the instruments. In particular, they are derived considering the centrifugal acceleration at each depth of the soil column as $\omega^2 r$, where r represents the distance from the centrifuge axis, and applying the above-mentioned scaling laws. Even the data of sensors locations refer to the state of the prototype after reconstitution and they are required to compare recorded and simulated data. A sketch of the centrifuge box at the model scale is shown in Figure 6.3, where the soil column to be modelled is highlighted through the red square.

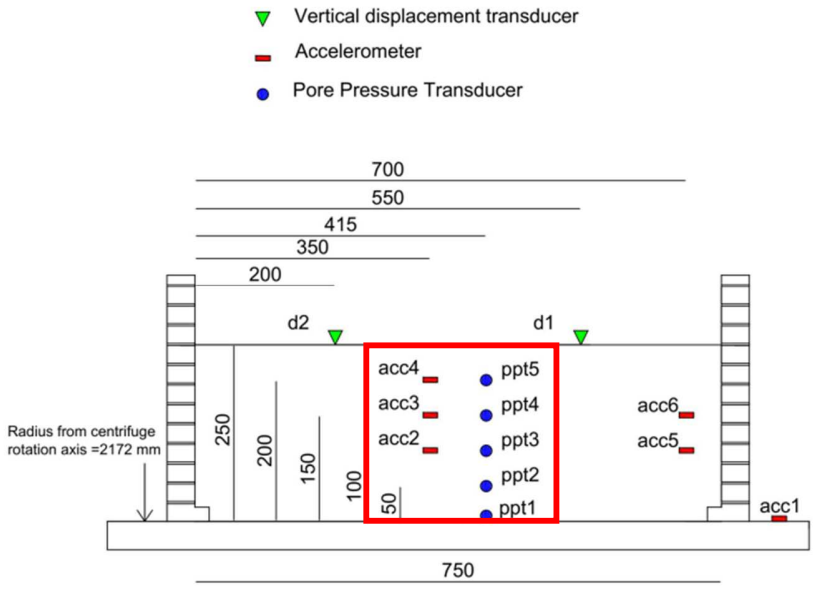

Figure 6.3. Centrifuge tests layout at model scale (from Airoldi et al., 2018).

As it is well-known, in a centrifuge model, some differences arise by considering either the actual acceleration (calculated as $\omega^2 r$) or the acceleration calculated at the effective radial distance, R_e (a_c=50g in this case). Generally, by selecting the effective radial distance properly, this gap should be neglectable. However, in the study (i.e., in the conversion from the model scale to the prototype scale), the scaling laws are referred to the actual acceleration $\omega^2 r$. The hydraulic permeability k is assigned to be 1.5×10^{-3} m/s (Fasano et al., 2021) that corresponds to an intrinsic permeability of 1.53×10^{-4} m^2/(kPa·s) calculated as $k/(\rho_w \cdot g)$ where ρ_w is the water density and g is gravity acceleration. Worth noticing that most of the data used to build the numerical model in OpenSees are obtained from Fasano et al. (2021). Finally, modelling the centerline of the box, the sensors located close to the sides have not been considered in the study.

6.4 NUMERICAL MODEL

As it was stressed before, numerical analyses have been performed at prototype scale and the numerical model is built in OpenSees considering SSPquadUP finite elements (McGann et al., 2012), while a single column of quadrilateral elements with 0.2 m-side

reproduces the centerline of the shaking table. Furthermore, in both Özcebe et al. (2020) and Fasano et al. (2021), the quadUP elements are adopted. After the reconstitution process, conducted at low density by air pluviation in physical tests, the height of the prototype is 11 m, slightly lower than the one reported in Figure 6.3 (i.e., 14 m). The groundwater table is assumed to be 0.6 m below ground level when the motion coded as GM17 is applied, while it is 1.4 m when GM34 is considered. The pore water pressure degree of freedom of the nodes above this depth has been constrained. Periodic boundaries are assigned by imposing that the nodes at the same height have the same displacements (equalDOF command in OpenSees) and a fixed base is implemented. A Uniform Excitation pattern is applied, and the relative acceleration is obtained through the recorders at the nodes corresponding to the sensors' positions.

The analysis is conducted by applying loads in three different stages (cf. §5.2):

1. Elastic gravity stage;
2. Elasto-plastic gravity stage (activation of the plastic formulation of the constitutive model);
3. Dynamic stage (application of the input motion).

The equations of motion have been integrated using the Newmark method, Krylov-Newton algorithm and a 0.01 s time step obtained by applying the scaling law for time (cf. equation (6.1). Constraints are enforced through the transformation equation method, while the convergence test is applied in terms of the norm of the displacement increment. The threshold value of the norm was set as $1x10^{-3}$. This choice has been oriented by Fasano et al. (2021), and in the above-mentioned study this value was relaxed to $1x10^{-2}$ for some convergence issues faced in the bi-dimensional model. A two-control frequencies Rayleigh damping was applied by setting damping D=1.5% at 0.2 Hz and 5 Hz. It is worth noting that the damping matrix has been assumed to be proportional to the initial stiffness matrix and not to the current stiffness matrix. All the above-mentioned data have been obtained by Fasano et al. (2021).

The soil nonlinearity is modelled using the bounding surface PM4SAND constitutive model (Boulanger and Ziotopoulou, 2017) which was implemented in OpenSees by Chen and Arduino (2021; see §2.4.3). The analyses are conducted using PM4SAND only, mainly because it has already been used to model the response of the Ticino sand in the framework of the LIQUEFACT project (Fasano et al., 2021) and, consequently, the set of calibrated parameters is already available in literature for this sand. Furthermore, even the possibility allowed to the PM4SAND users to assign only four mandatory parameters played a key role in the constiituive model choice. In fact, Boulanger and Ziotopoulou (2017) illustrate the relationships required to obtain the whole set of parameters starting from the mandatory ones. When these relationships are not available, default values suitable for most sands are provided. On the contrary, a large amount of laboratory tests is needed for the calibration of both NTUASand02 (cf. §2.4.1) and SANISAND. At the time of writing this thesis, the tests required for this calibration procedure are not available.

6.5 CONSTITUTIVE MODEL

The calibrated PM4SAND parameters for the Ticino sand are obtained from Fasano et al. (2021). In case the calibration of some optional parameters is not explained in Fasano et al. (2021), their suggested values are obtained from Ziotopoulou and Boulanger (2013) and Boulanger and Ziotopoulou (2017). The parameters are summarized in the following Table 6.1, with the reference adopted to obtain the parameter itself.

Table 6.1. PM4SAND constitutive parameters adopted for the centrifuge test simulations.

Parameter	**Value**	**Reference**
D_r (-)	Variable for each test	Airoldi et al. (2018)
G_0 (-)	$167 \cdot \sqrt{46D_r^2 + 2.5}$	Fasano et al. (2021)
h_{po}	0.15	Fasano et al. (2021)
ρ (t/m^3)	1.954	Airoldi et al. (2018)
p_{atm} (kPa)	101.3	-
h_0 (-)	$(0.25 + D_r)/2 > 0.30$	Boulanger and Ziotopoulou (2017)
e_{max} (-)	0.923	Airoldi et al. (2018)
e_{min} (-)	0.574	Airoldi et al. (2018)
n^b (-)	0.5	Fasano et al. (2021)
n^d (-)	0.1	Fasano et al. (2021)
A_{do} (-)	$\frac{1}{0.4}\frac{\sin^{-1}(M^b/2) - \sin^{-1}(M/2)}{M^b - M^d}$	Boulanger and Ziotopoulou (2017)
z_{max} (-)	$0.28\exp(6.1D_r) < 40.0$	Ziotopoulou and Boulanger (2013)
c_z (-)	250	Boulanger and Ziotopoulou (2017)
c_e (-)	$-10D_r + 8.5 < 5.0$	Ziotopoulou and Boulanger (2013)
Φ_{cv} (°)	33	Fasano et al. (2021)
ν (-)	0.3	Fasano et al. (2021)
C_{GD} (-)	2.0	Boulanger and Ziotopoulou (2017)
C_{DR} (-)	$5 + 25(D_R) - 0.35 \leq 10$	Boulanger and Ziotopoulou (2017)
$C_{K\alpha f}$ (-)	0.0	Ziotopoulou and Boulanger (2013)
Q (-)	10.0	Fasano et al. (2021)
R (-)	1.5	Fasano et al. (2021)
m (-)	0.01	Boulanger and Ziotopoulou (2017)
$F_{sed,min}$ (-)	$0.03\exp(2.6D_r) \leq 0.99$	Boulanger and Ziotopoulou (2017)
$p'_{sed,o}$ (-)	$-p_{atm}/5$	Boulanger and Ziotopoulou (2017)
cr_{hg} (-)	0.005	Boulanger and Ziotopoulou (2017)
c_{hg} (-)	$\min(cr_{hg} \cdot p; 0.0)$	Boulanger and Ziotopoulou (2017)

6.6 SIMULATION OF THE TEST M1_S1_GM17

The state of the prototype before the application of the centrifugal acceleration and of the motion, coded as GM17, is reported in Figure 6.4, extracted from Airoldi et al. (2018). In addition, relative density, D_r and saturated soil density, ρ_{sat} have been assigned to be 47.42% and 1.949 t/m^3, respectively.

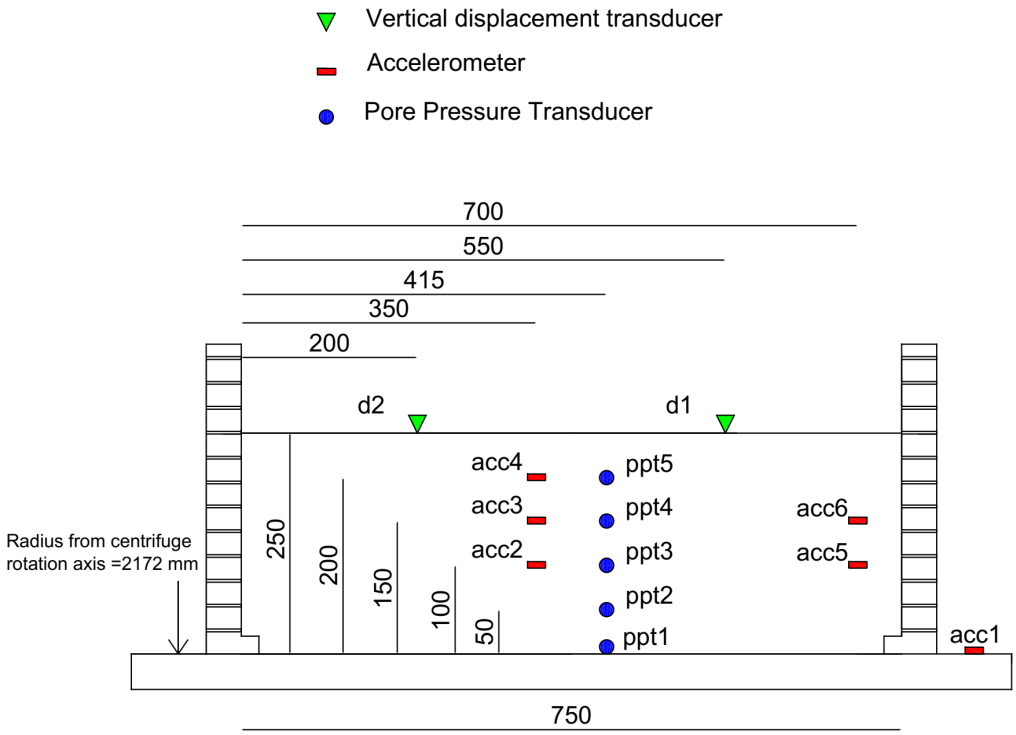

Figure 6.4. State of the model of the test M1_S1_GM17 before the application of the shock (from Airoldi et al., 2018).

The comparison in terms of acceleration time-histories of simulated response and recorded data at the prototype scale are reported in Figure 6.5, Figure 6.6, and Figure 6.7, while Figure 6.8 shows the input motion applied at the base of the model.

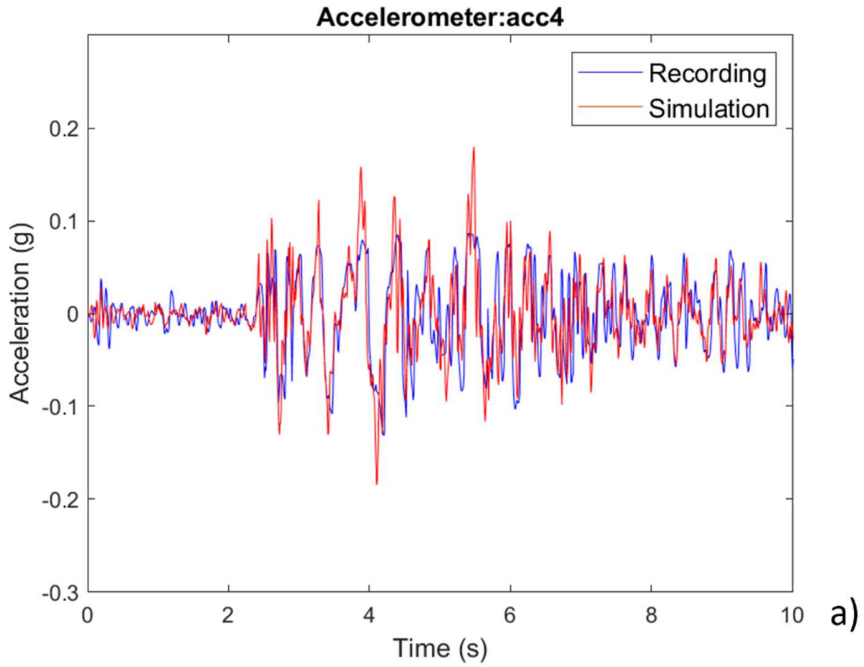

Figure 6.5. Simulated vs recorded acceleration time-series at acc4 sensor at prototype scale.

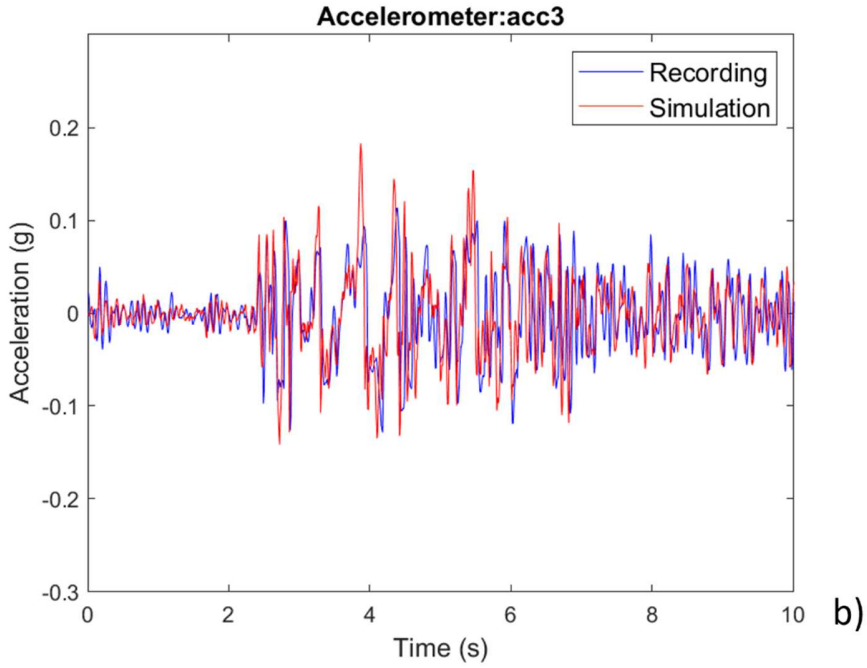

Figure 6.6. Simulated vs recorded acceleration time-series at acc3 sensor at prototype scale.

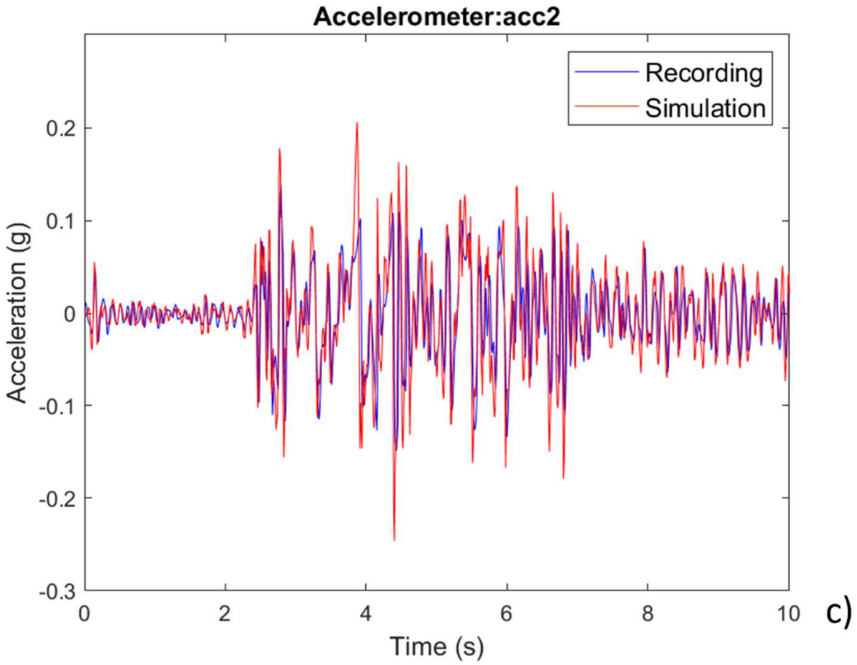

Figure 6.7. Simulated vs recorded acceleration time-series at acc2 sensor at prototype scale.

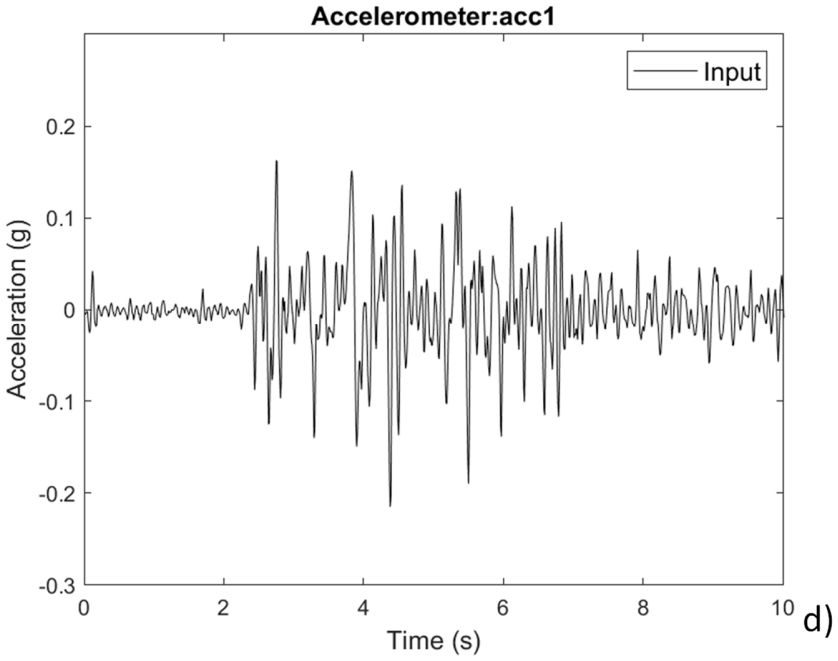

Figure 6.8 Input motion GM17 at prototype scale.

The comparison shown in Figure 6.5-Figure 6.7 highlights that the response is well caught in terms of acceleration time-series at all depths. A general slight overestimation of the recorded response is observed using PM4SAND.

Figure 6.9-Figure 6.13 report the comparison between simulated and recorded excess pore water pressures, obtained as $\Delta u = u(t) - u_0$, where u(t) represents the excess pore water pressure time-series, while u_0 indicates the pore water pressure in hydrostatic conditions.

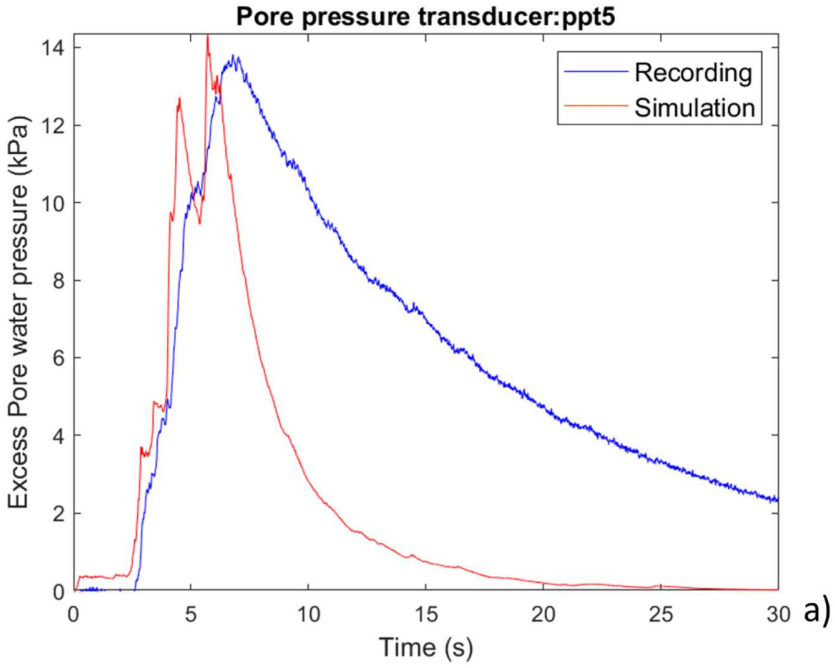

Figure 6.9. Simulated vs recorded excess pore water pressure at ppt5 sensor.

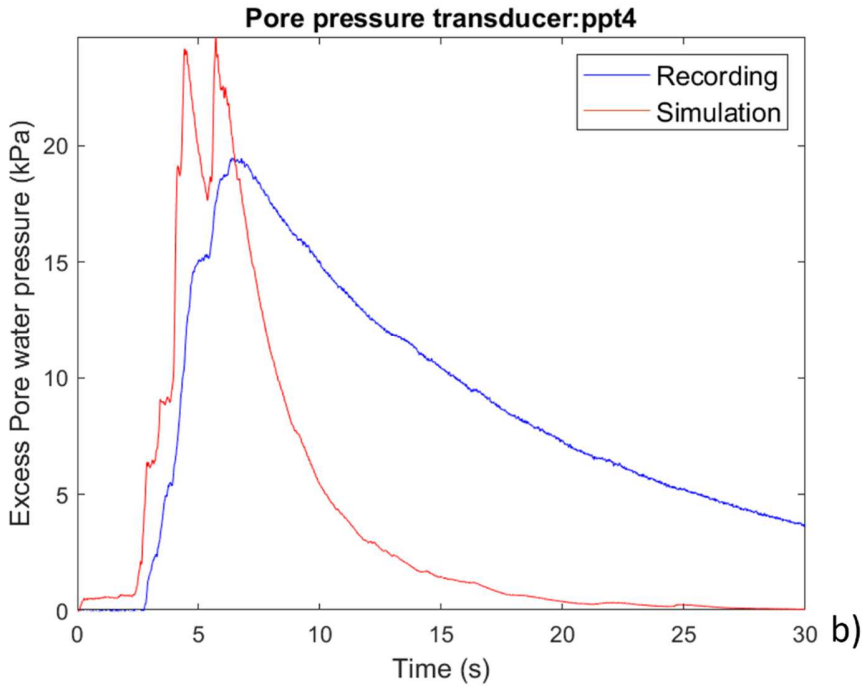

Figure 6.10. Simulated vs recorded excess pore water pressure at ppt4 sensor.

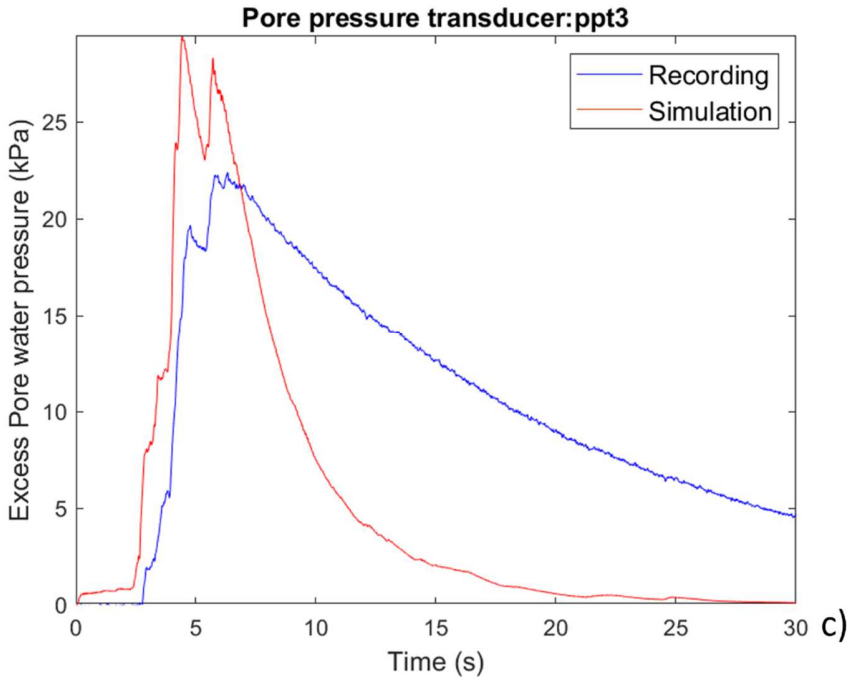

Figure 6.11. Simulated vs recorded excess pore water pressure at ppt3 sensor.

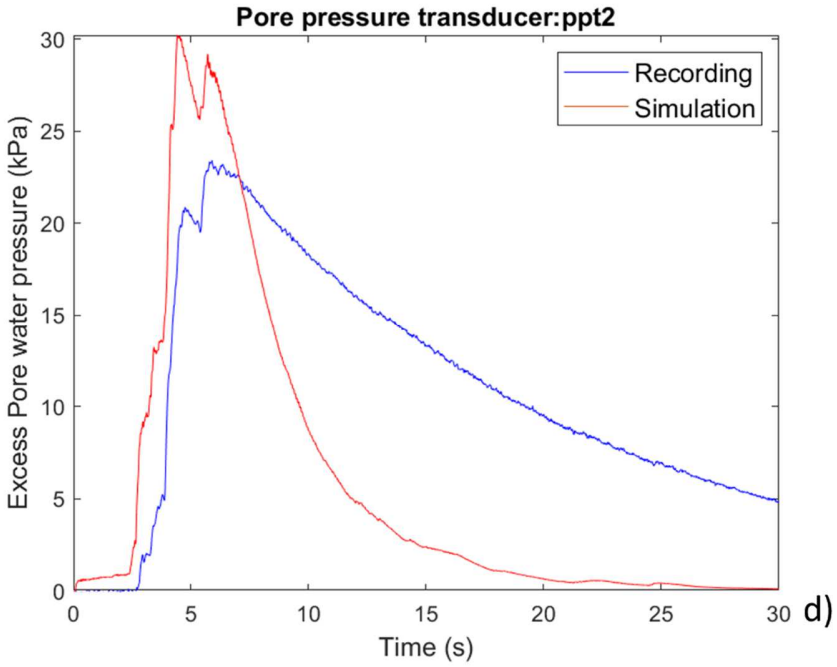

Figure 6.12. Simulated vs recorded excess pore water pressure at ppt2 sensor.

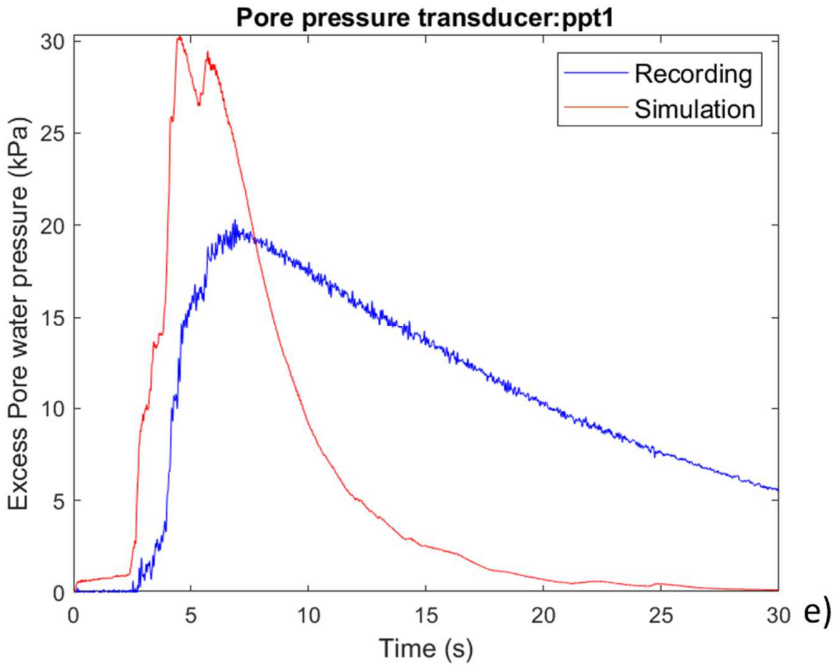

Figure 6.13. Simulated vs recorded excess pore water pressure at ppt1 sensor.

The time series just shown highlight that at the sensors coded as ppt5 (Figure 6.9), ppt4 (Figure 6.10), ppt3 (Figure 6.11), and ppt2 (Figure 6.12), the response seems to be correctly reproduced, showing a faster dissipation if compared to the recordings. Finally, the time-series at the lower depth (Figure 6.13) shows an overestimation of the recorded response together with a faster dissipation.

6.7 SIMULATION OF THE TEST M1_S1_GM34

As it was made for the GM17 ground motion, here, the state of the prototype before the application of the centrifugal acceleration for the test identified as M1_S1_GM34 is reported in Figure 6.14, extracted from Airoldi et al. (2018). Relative density, D_r and saturated soil density, ρ_{sat} were assigned to be 49.83% and 1.954 ton/m^3, respectively.

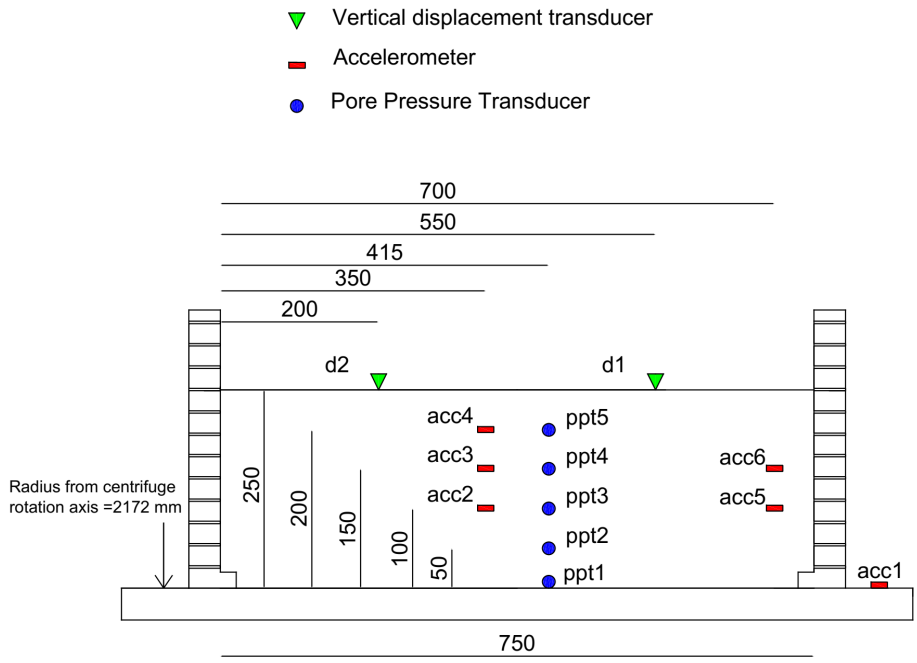

Figure 6.14. State of the model of the test M1_S1_GM34 before the application of the shock (from Airoldi et al., 2018).

Figure 6.15, Figure 6.16, Figure 6.17 report comparisons between simulations and recordings in terms of acceleration time-histories, while Figure 6.18 shows input motion at prorotype scale.

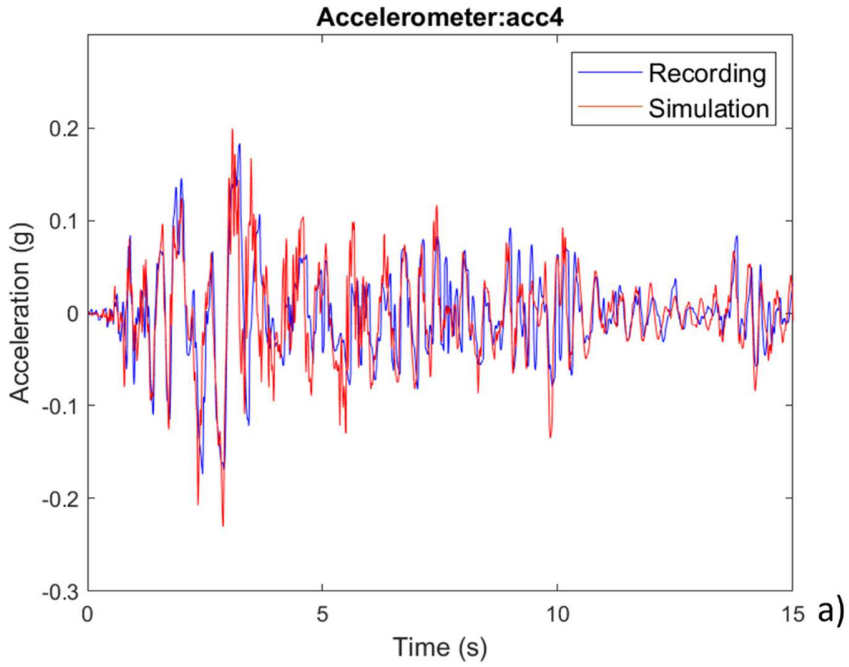

Figure 6.15. Simulated vs recorded acceleration time-series at acc4 sensor at prototype scale.

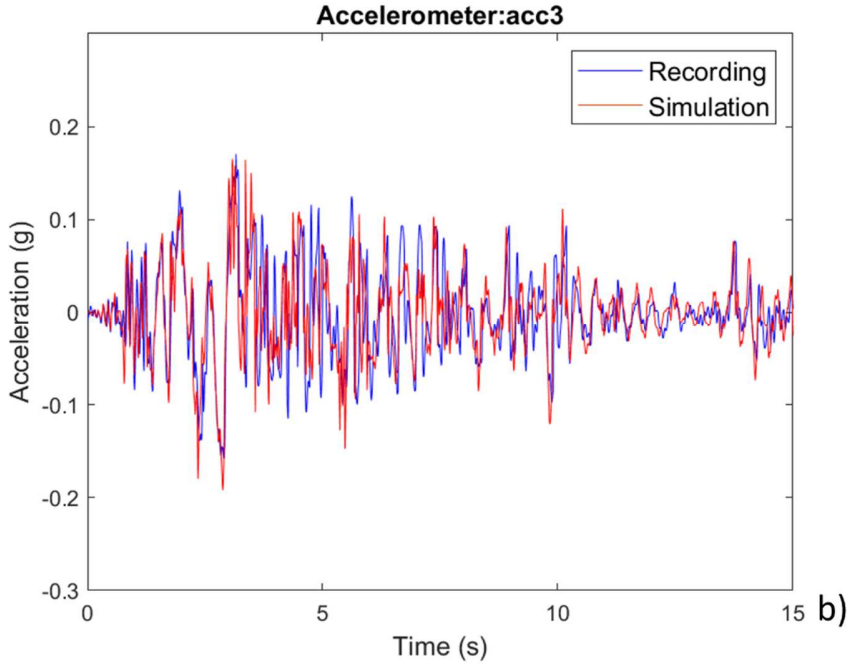

Figure 6.16. Simulated vs recorded acceleration time-series at acc3 sensor at prototype scale.

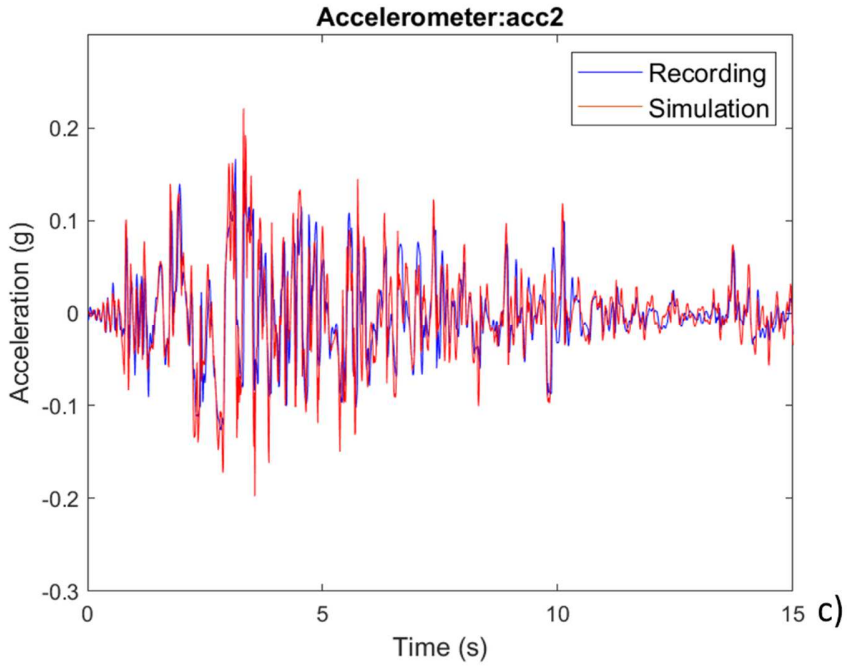

Figure 6.17. Simulated vs recorded acceleration time-series at acc2 sensor at prototype scale.

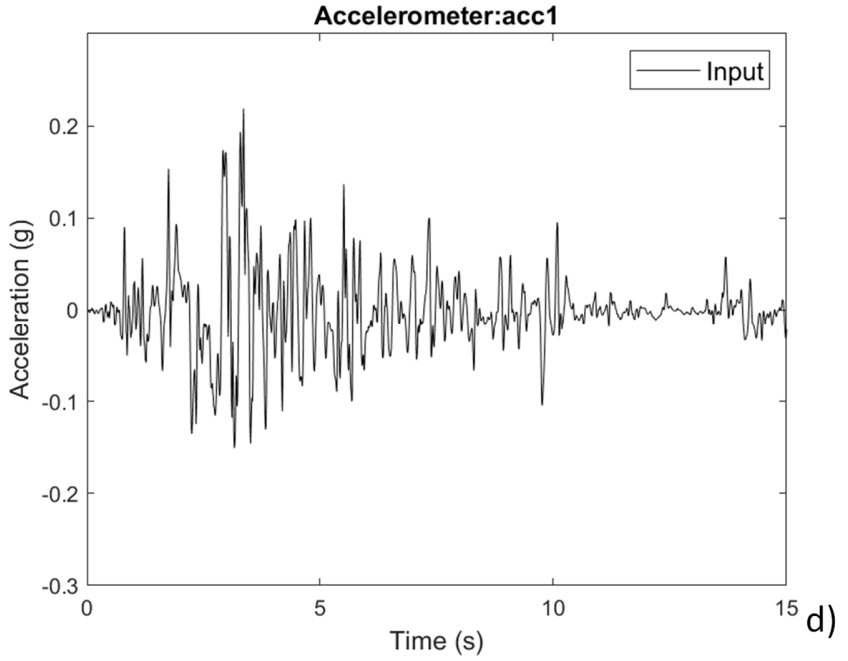

Figure 6.18. Input motion GM34 at prototype scale.

The results shown in Figure 6.15-Figure 6.17 highlight that the acceleration time-histories are well simulated at each depth and an overestimation lower than that exhibited for ground motion GM17 (cf. Figure 6.5-Figure 6.7) can be observed.

Finally, the following Figure 6.19-Figure 6.23 report the comparison between simulated and recorded excess pore water pressures for ground motion GM34.

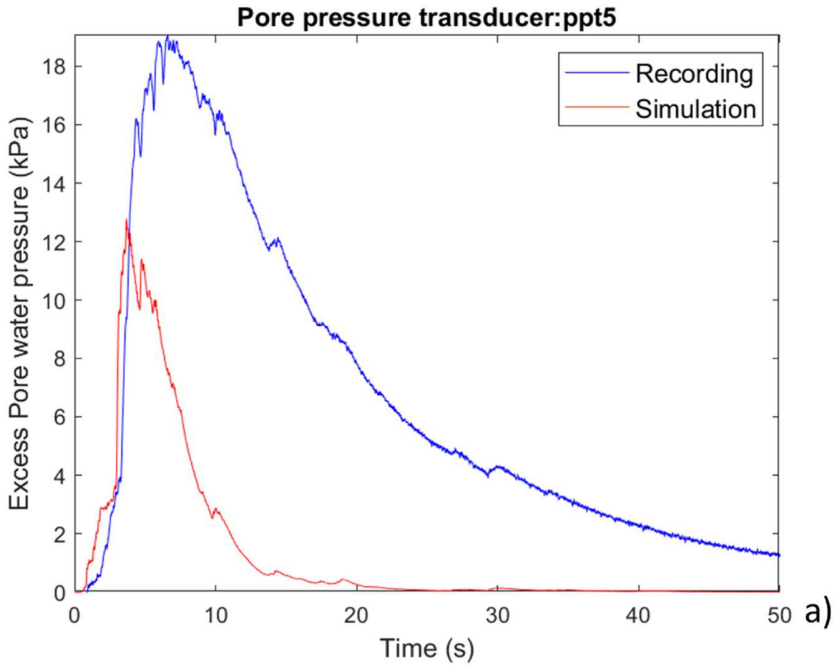

Figure 6.19. Simulated vs recorded excess pore water pressure at ppt5 sensor at prototype scale.

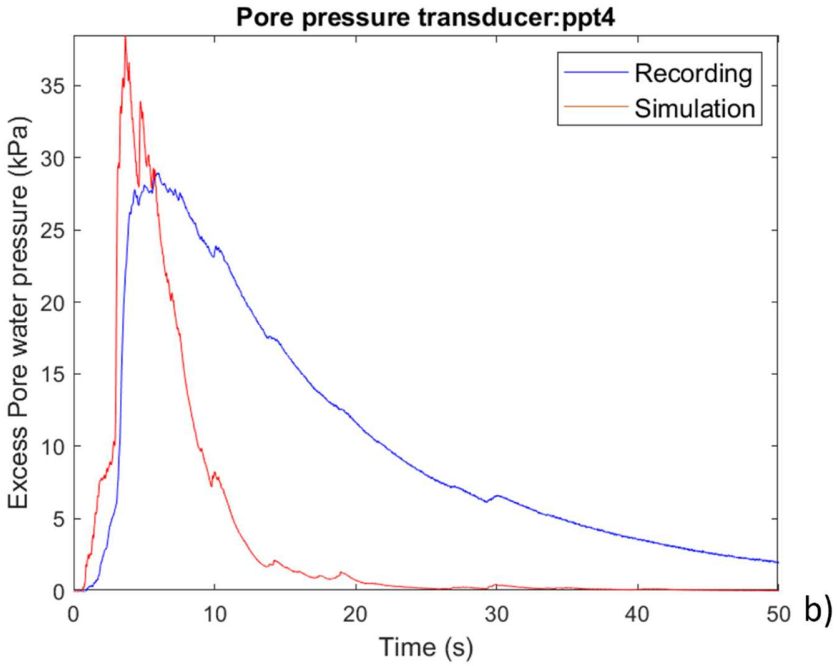

Figure 6.20. Simulated vs recorded excess pore water pressure at ppt4 sensor at prototype scale.

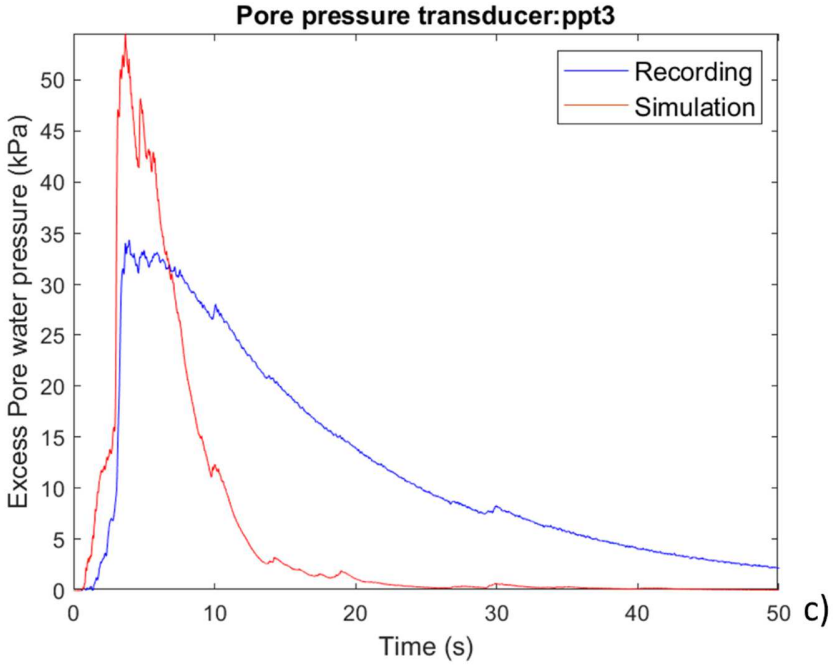

Figure 6.21. Simulated vs recorded excess pore water pressure at ppt3 sensor at prototype scale.

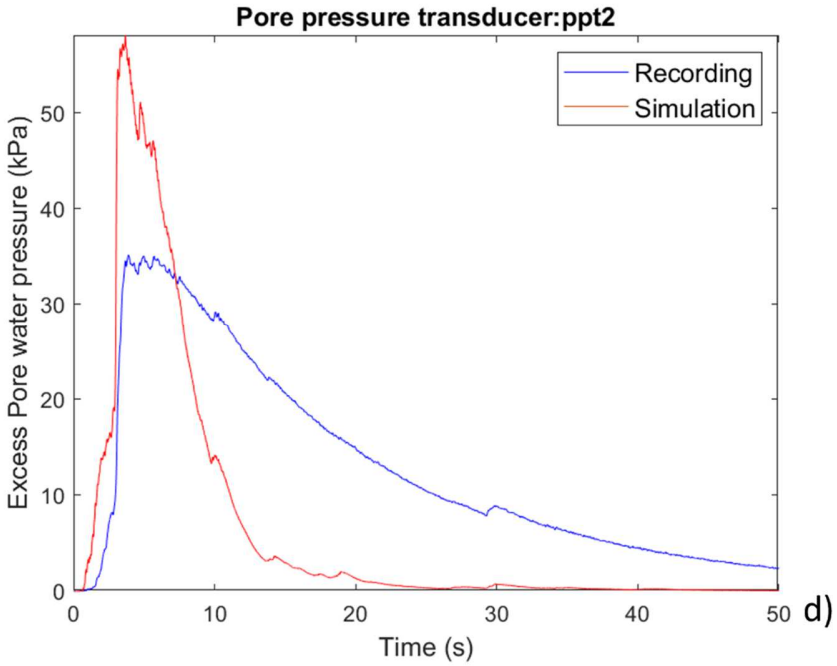

Figure 6.22. Simulated vs recorded excess pore water pressure at ppt2 sensor at prototype scale.

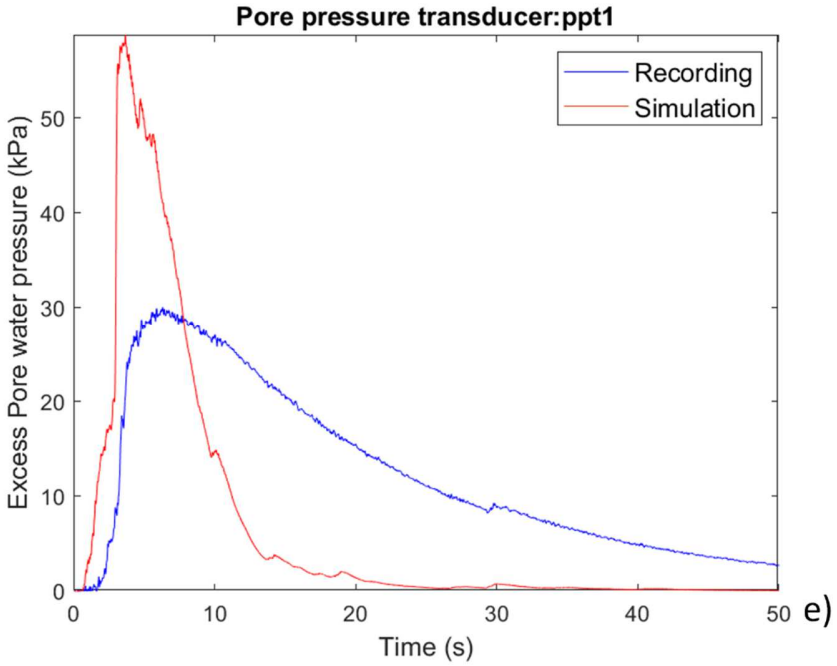

Figure 6.23. Simulated vs recorded excess pore water pressure at ppt1 sensor at prototype scale.

In Figure 6.19-Figure 6.23, a strong underestimation of the recorded response is detected at ppt5 (Figure 6.19), while the response is always overestimated at the other depths (Figure 6.20, Figure 6.21, Figure 6.22, Figure 6.23). A faster dissipation is always observed in the simulated data.

Generally, the response simulated in terms of acceleration time-histories seems to be correctly caught and it witnesses the goodness of the calibration performed in Fasano et al. (2021), while some issues arise for the reproduction of excess pore water pressure time-histories that cannot be correctly reproduced by the numerical model implemented in OpenSees.

6.8 DISCUSSION

The simulation of centrifuge tests here illustrated highlighted the ability of an advanced constitutive model, namely PM4SAND, to simulate the response of a homogeneous soil column under seismic loadings. Even if the problem is simulated in a simplified manner (i.e., only the centerline of the container is modelled in plane-strain conditions by considering a soil column), the response seems to be well caught in terms of acceleration time series. Furthermore, some issues arise with reference to excess pore water pressure. In fact, the simulations generally overestimate the excess pore water pressures, showing a faster dissipation as well.

However, these discrepancies can be due even to uncertainties of the test procedures, such as groundwater table depth, permeability and sensor positions after shaking. These aspects are always very difficult to be caught and a back analysis is useful to understand their influence on the results.

Obviously, further developments can be oriented towards the calibration of other constitutive models (SANISAND, NTUASand02) for the Ticino sand, observing whether the response is more or less accurate than what resulted with the adoption of PM4SAND.

6.9 REFERENCES

Airoldi S., Fioravante V., Giretti D. and Moglie J. (2018). LIQUEFACT project. Deliverable D4.2. Report on validation of retrofitting techniques from small scale models v1.0.

Boulanger RW, and Ziotopoulou K (2017). PM4Sand (version 3.1): A sand plasticity model for earthquake engineering applications. Report UCD/CGM-17/01, Center for Geotechnical Modeling, Dept. of Civil and Environmental Eng., University of California, Davis, CA.

Chen L. and Arduino P. (2021). Implementation, verification and validation of the PM4SAND model in OpenSees. PEER Report No. 2021/02. Pacific Earthquake Engineering Research Center Headquarters, University of California, Berkeley, March 2021.

Fasano G., Nappa V., Özcebe A.G., Bilotta E. (2021). Numerical modelling of the effect of horizontal drains in centrifuge tests on soil-structure interaction in liquefiable soils. Bulletin of Earthquake Engineering 19:3895–3931 https://doi.org/10.1007/s10518-021-01084-2.

LIQUEFACT project (H2020-DRA-2015). Assessment and mitigation of Liquefaction potential across Europe: a holistic approach to protect structures/infrastructure for improved resilience to earthquake-induced Liquefaction disasters. H2020-DRA-2015. GA no. 700748.

McGann, C.R., Arduino, P. and Mackenzie-Helnwein P. (2012). Stabilized single-point 4-node quadrilateral element for dynamic analysis of fluid saturated porous media. Acta Geotechnica 7 (4), 297-311.

Özcebe, A.G., Giretti, D., Bozzoni, F., Fioravante V. and Lai C.G. (2021). Centrifuge and numerical modelling of earthquake-induced soil liquefaction under free-field conditions and by considering soil–structure interaction. Bull. Earthquake Eng. 19, 47–75 https://doi.org/10.1007/s10518-020-00972-3.

Yang Z., Elgamal A., Parra E. (2003). Computational model for cyclic mobility and associated shear deformation. J Geotech Geoenvironmental Eng 129:1119–1127.

Ziotopoulou, K., and Boulanger, R. W. (2013). Calibration and implementation of a sand plasticity plane-strain model for earthquake engineering applications. Journal of Soil Dynamics and Earthquake Engineering, 53, 268-280, 10.1016/j.soildyn.2013.07.009.

7 NUMERICAL APPROACHES TO THE SITE RESPONSE: THE CASE-HISTORY OF SAN GIULIANO DI PUGLIA VALLEY

7.1 INTRODUCTION

The following chapter describes nonlinear bi-dimensional site response analyses performed exploiting the capabilities of OpenSeesSP for the case study of the village of San Giuliano di Puglia, in Molise region, which was hit by the Molise earthquake in 2002 where an elementary school collapsed and caused the death of a teacher and 27 students.

This study represents a step further in the numerical modelling of the problem, after the research carried out by Puglia (2008), Puglia et al. (2007; 2009; 2013) and Fierro et al. (2019; 2020b) in terms of bi-dimensional site response analyses. It is worth noticing that it should be the first time that the model of the village is implemented into a nonlinear code to study the response of the San Giuliano di Puglia basin, and this has been possible due to the advent of the increasing availability of HPC (High Performance Computing) resources. This numerical analysis aims at showing the ability of OpenSees to model very large domains and to show accurate results in this sense, if compared to real data. Furthermore, the use of the advanced constitutive model pressure-independent multi-yield (Yang et al., 2008), whose parameters are obtained by in-situ and laboratory tests, is pointed out and critically discussed.

The case of San Giuliano di Puglia is extremely significant and paradigmatic for the whole Italian Geotechnical Engineering community because, on the one hand, it boosted the development of the New Codes of Construction together with Microzonation studies in Italy, and, on the other hand, even if a large amount of in-situ and laboratory tests have been performed, the geotechnical characterization of the soil is still not clear and shared. The great availability of tests is due to the fact that, in the

aftermath of the earthquake, reconnaissance activities evidenced a strongly non-uniform damage distribution in the epicentral area, and this encouraged a wide research work in the town. This damage pattern suggested that site amplification dramatically affected the seismic response of the town.

However, even if a multitude of tests was performed soon after the earthquake and for almost a decade, the different stages of investigations revealed discrepancies in terms of small-strain stiffness of the soil layers. The stiffness profiles resulting from the tests were critically investigated in several studies through site response back-analysis. This was possible by exploiting the precious and helpful hand provided by the installation of an accelerometric network in the town, even in the form of vertical arrays. The seismic stations installed immediately after the earthquake and those installed about ten years later, in 2012, as a part of the Italian Accelerometric Network (RAN) were exploited to estimate the goodness of numerical models by trying to fit the simulated data with the recordings of the accelerometers installed in the town. Exploiting the more recent data in terms of both shear wave velocity profiles and recordings, it emerged that the consensus shear wave velocity profile can be re-evaluated by assuming higher stiffness values. In addition, different buried morphologies were analyzed and the one providing the more complex geometry of the contact between bedrock and soft soil has revealed to perform better.

Based on that, the rest of the chapter focuses on the implementation of the above-mentioned consensus model of the cross-section of San Giuliano di Puglia in the parallel module OpenSeesSP (Single Parallel OpenSees interpreter), exploiting the valuable computational resources provided by the infrastructure DesignSafe-CI (Rathje et al., 2017). Being the strain level induced by the recorded accelerograms very low, the numerical model is built in OpenSees using an advanced constitutive platform and evaluating whether some differences arise if compared to the results obtained by the adoption of a linear elastic behaviour.

In the following paragraphs, it is first briefly described the background of the case study of San Giuliano di Puglia (§7.2); then, the new shear wave velocity profiles and the

seismic monitoring system that was deployed in the village are critically discussed in §7.3. Later, in §7.4, the data available from the monitoring system are adopted as a benchmark to validate the numerical models, while §7.5 provides a brief state-of-art on the site response analyses performed at the site. Finally, in §7.6, a description of the model implementation in OpenSees and the nonlinear site response analyses performed are detailed.

Overall, the research highlighted that the reliability of the geotechnical characterization is crucial for the solution of a Geotechnical Earthquake Engineering problem. Furthermore, the effectiveness of the geotechnical characterization can be dramatically improved by the use of accelerometric stations, arranged in vertical arrays. Furthermore, OpenSees has been revealed to be successful in modelling even large numerical domains with a certain grade of accuracy.

It is worth noting that only an early and rapid introduction on the state-of-art is here reported together with the problem statement, while the interested reader can refer to Fierro et al. (2020b) for an extended summary of the state-of-art on the numerical simulations performed at the site. Some of the more relevant site response analyses treated in Fierro et al. (2020b) are reported in Appendix B. This chapter mainly aims at underlining the results of the numerical analyses obtained using the OpenSees framework. In addition, the results presented here are reported in Fierro et al. (2022).

7.2 BACKGROUND

San Giuliano di Puglia, a small village located at about 200 km E of Rome, drew the attention of the national chronicles because, on October 31st, 2002, it suffered the most dramatic consequences of an earthquake of magnitude M_w=5.74 that hit the Molise Region, Italy. The earthquake can be considered moderate for the geodynamics of the area, but it reached a worldwide relevance due to the collapse of the “F. Jovine” elementary school and the consequent death of 27 children and a teacher.

7. NUMERICAL APPROACHES TO THE SITE RESPONSE: THE CASE-HISTORY OF SAN GIULIANO DI PUGLIA VALLEY

The main event happened on October 31st, 2002, at 10:33:00 UTC (11:33:00 local time) with a moment magnitude M_w=5.74 (M_L=5.4). The epicenter was located 1 km SW of the village of Bonefro (CB), approximately 200 km E of Rome, at a depth of about 10 km. This main earthquake was preceded, on October 2002, by two foreshocks of duration magnitude M_d=3.2 (01:25 a.m. local time) and M_d=3.5 (03:27 a.m. local time), respectively, and followed by another mainshock of M_w=5.72 (November 1st, 15:08 UTC) with an epicenter located at about 6 km W from the first event. No additional casualties were induced by the event. Only twelve permanent accelerometer stations (seven digital and five analog) belonging to the Italian seismic network were activated. Due to the low-seismicity level assumed for that area, and to the relatively small spread of the stations at that time, none of them was located in the near-field, being the epicentral distance of the triggered instruments in the range 25÷190 km.

This earthquake represented a turning point for the whole Earthquake Engineering field in Italy because it highlighted the necessity to update seismic codes and to review the seismic hazard guidelines in the country. It is worthwhile to mention that San Giuliano was considered as a non-seismic village according to the previous Code of Construction and the collapse of the elementary school, with children fatalities together with the strongly non-uniform observed damage distribution highlighted the need for deeper studies with reference to the seismicity of Italian regions.

In particular, a few weeks after the earthquake, the Order of the President of the Council of Ministers n. 3274 of 20 March 2003 (OPCM 3274, 2003) released new Criteria for the identification of seismic zones that was at the base of the nowadays study of seismic hazard at the national level (Working Group MPS, 2004). This document was legally approved in Italy in 2006 (OPCM 3519, 2006).

In the same OPCM 3274, technical seismic standards for buildings, bridges, foundations and retaining walls were released. On the basis of this document, among others, the guidelines Geotechnical Aspect of the Design in Seismic Areas (AGI, 2005) and the new technical codes for constructions (NTC, 2008; NTC 2018) were developed.

Later on, the Department of Civil Protection created a working group to define the Addresses and Criteria for Seismic Microzonation (Working Group, 2008) that were applied and updated subsequently to the 2009 Abruzzo earthquake (AA. VV., 2011).

In Molise, after the earthquake, it was promoted the seismic microzonation of all the municipalities belonging to the district of Campobasso (Molise Region, 2003–2009). This legislative production together with a strong effort performed by the scientific community made available to the general public a large geotechnical dataset that was employed, among others, for scientific purposes (Fabbrocino et al., 2015; Forte et al., 2017).

As it was just mentioned, a peculiar aspect of the earthquake was the strongly non-uniform damage distribution observed in the epicentral area. This feature suggested that site amplification significantly affected the seismic response of the town. Therefore, very soon after the event and for almost ten years, the first stage of analysis, consisting of very detailed soil investigations, was conducted. This led to a very detailed characterization of the San Giuliano di Puglia subsoil. Numerical simulations were carried out to try to understand whether and to what extent, the possible site effects took place in the village. This was made in the context of different studies and research projects.

To this aim, beyond the soil properties investigations, a crucial role is played by the geotechnical monitoring. In fact, soon after the main events, a temporary monitoring system was installed in the town. Furthermore, more than ten years later, in 2012, the second stage of investigations was conducted in the framework of the installation of permanent seismic stations, even arranged in vertical arrays. Here, in-situ tests revealed a stiffer shear wave velocity profile if compared to that obtained in the first stage of tests. This profile was confirmed by the results from mono- and bi-dimensional site response back-analyses reported in Fierro et al. (2019; 2020a; 2020b) using Strata (Kottke e al., 2013) and QUAD4M (Hudson et al., 1994) codes. Therefore, it is very challenging to try to understand if more recent data, including new geotechnical tests and more recent recordings, together with the adoption of a nonlinear finite element

code would confirm the previous findings with the aim to detect the spatial distribution of the related ground motion amplification. In these research activities, the significance of both soil investigation and monitoring is highlighted, and it is also very engaging to evaluate the effectiveness of the previous findings in the light of the newly available data.

7.3 THE SUBSOIL MODEL AT SAN GIULIANO DI PUGLIA

The village of San Giuliano di Puglia rises on the top of a narrow SSE-NNW elongated ridge, with elevation ranging from 450 to 460 m a.s.l. The historical core of the village is located on the southern hilltop, while the more recently developed area extends across the ridge, shaped like a saddle, which connects the original hill-town to a higher hill in the north direction.

As it was stressed before, a large number of boreholes (129) is available, and consequently, this led to a clear and shared definition of surface geology. To this purpose, a geological map of the area is shown in Figure 7.1a. In the area, two main stratigraphic units were identified: the calcareous-marly unit and the clayey-marly unit. The calcareous-marly unit is the oldest one and it is formed by a well-bedded succession of limestones and marly limestones, differently fractured and fissured, with intercalations of marls and clayey marls (Miocene Faeto Flysch formation). This unit essentially crops out in the northern part of the ridge and in the southern one where the historical core of the village is built. The Faeto Flysch formation is stratigraphically overlain by the clayey-marly unit formed by bluish-grey clays and marly clays with sandy intercalations (Miocene Toppo Capuana Marls formation). The clayey-marly unit outcrops in the middle and gentler part of the ridge where the recent part of the village lies. Finally, cover deposits varying in thickness from a few decimeters to a few meters overlie the uppermost clay layers along the ridge. They consist of man-made fill and accumulations of landslide deposits.

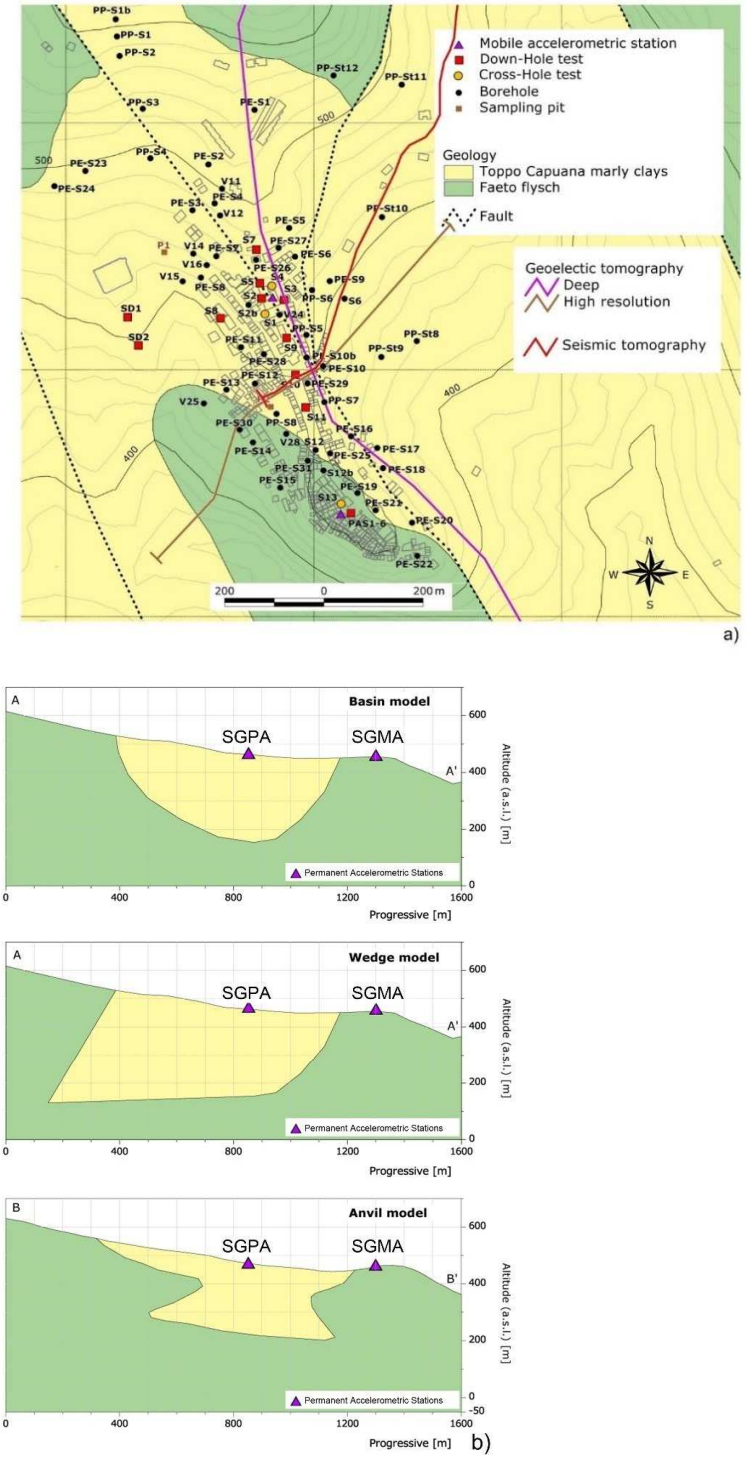

Figure 7.1. Geological map for San Giuliano di Puglia together with the main investigations (a) and different models of the buried morphology proposed for the longitudinal section of the village (b) (modified after Puglia, 2008). The trace of the section plane is reported in the following Figure 7.3.

7. NUMERICAL APPROACHES TO THE SITE RESPONSE: THE CASE-HISTORY OF SAN GIULIANO DI PUGLIA VALLEY

As reported in Puglia (2008), the Toppo Capuana marly clay formation in San Giuliano di Puglia consists of three principal subunits:

1. a "debris cover", of less than five meters thickness, including black organic carbonaceous elements, lumps, and lenses of white powdery calcite and small calcareous litho-clasts;
2. a layer, of two to ten meters thickness, of "weathered tawny clays" (referred to as "tawny clays" in this study), characterized by medium to intense fissuring, resulting from the weathering and disturbance of the uppermost part of Toppo Capuana marly clays;
3. a deep layer of Toppo Capuana marly clays, called "grey clays" hereinafter. The thickness of this layer seems to be around three hundred meters, as back-figured from the natural frequencies of the aftershocks recorded in the new part of the town. Worth noticing that the grey Toppo Capuana marly clays are less intensely fissured than the weathered tawny clays.

As it is shown in Figure 7.1b, some uncertainties regarded the definition of the contact between the two different stratigraphic units (i.e., Faeto flysch and Toppo Capuana marly clays) and the geometry of their contact, in spite of the availability of a remarkably large amount of geological, geophysical, and geotechnical data. This was due to a lack of direct information about the geometry of the upper bound of the flysch formation beneath and around the marly clay. On the other hand, the unusual density of borehole distribution allowed describing, in detail, the Faeto flysch and the Toppo Capuana marly clay (Silvestri et al., 2006; Puglia, 2008; d'Onofrio et al., 2009).

Three different models of increasing complexity and developed exploiting different techniques (e.g., adopting investigation and back-analysis of seismic signals of the aftershocks recorded in two specific locations of the village) were identified (Figure 7.1b): a "Basin" model, proposed by Baranello et al. (2003) and employed by Lanzo and Pagliaroli (2009) for their analyses; a "Wedge" model (Giaccio et al., 2004) and

an "Anvil" model, developed and adopted by Puglia (2008) and Puglia et al. (2007; 2009; 2013).

A detailed description of the physical and mechanical properties of the soil formations is in Silvestri et al. (2006) and d'Onofrio et al. (2009). However, in this chapter, only those used to define the subsoil models adopted for the seismic response analyses are reported. The shear wave velocity profiles resulting from the first stage of analyses were carried out from the joint interpretation of the results of both resonant column (RC) tests at small shear strain level and in-situ Down-Hole (DH) and Cross-Hole (CH) tests (the test locations are in Figure 7.1a). Larger stiffness values emerged from the latter (CH tests) and were not employed to build up the models, because a non-polarized source type is adopted to carry out the tests. Indeed, site response analyses recently performed in Fierro et al. (2020a) confirmed the inconsistency of shear wave velocity profiles obtained by these Cross-Hole tests. The adopted procedure to obtain Vs-z profiles is reported in d'Onofrio et al. (2009).

As it was mentioned before, the shear wave velocity profile obtained from this first stage of tests was adopted firstly by Puglia et al. (2007; 2009; 2013) and Puglia (2008). Then, Fierro et al. (2019; 2020b) exploited the same model to evaluate its performance in 1D and 2D equivalent linear site response analyses. In the following, the above-mentioned model is briefly recalled in order to highlight the differences with the newly developed model in terms of shear wave velocity profile, built in OpenSeesSP.

With reference to Debris cover, the same value of shear wave velocity is assigned to the whole stratum, while for Tawny clay and Grey clay (the Toppo Capuana marly clay), a discretization of the layers was performed to follow the equations obtained from the available tests. The profiles are reported in Figure 7.2 together with the data obtained from all the tests. Finally, for the Faeto flysch, the profile measured through Down-Hole tests was adopted. In Table 7.1, the main elastic parameters are reported, while in Table 7.2, the dependency of the shear modulus G and damping ratio D on the shear strain level is presented. It was carried out from the interpolation of the experimental resonant column test data using Ramberg-Osgood regression, being

$D(\gamma)=D_0+D$ and assuming a non-zero initial damping ratio D_0 (see, for instance, d'Onofrio et al., 2004). As reported in the above-referenced papers, for the marly clay the damping ratio was obtained by the results of the laboratory tests only; for the flysch, instead, the small-strain shear modulus was inferred by in-situ tests, while the damping ratio was assumed to be D_0=0.5%.

Table 7.1. Mechanical properties of the soil deposits significant for the seismic response of San Giuliano di Puglia (modified after d'Onofrio et al., 2009).

Unit	**Soil unit weight** γ **(kN/m^3)**	**Shear wave velocity Vs (m/s)**	**Poisson's ratio** ν **(–)**	**Compression wave velocity** V_p **(m/s)**	**Small strain damping ratio** D_0 **(%)**
Debris cover	19.60	122	0.493	1010	3.0
Tawny clay	21.10	$162(17+9.8z)^{0.104}$	0.489	f (V_s,ν)	2.3
Grey clay	21.20	$202(17+9.8z)^{0.108}$	0.477-0.485	f (V_s,ν)	2.5
Faeto flysch	22.00	400-1350	0.392-0.456	1400-3200	0.5

Table 7.2. Stiffness and damping ratio of the soil deposits significant for the seismic response of San Giuliano di Puglia (modified after d'Onofrio et al., 2009).

Unit	**Normalized shear modulus** $G=G(\gamma)/G_0$ **(-)**	**Damping ratio** $D(\gamma)$ **(%)**
Debris cover	$\gamma(\bar{G}) = \left(\frac{1-\bar{G}}{365627\cdot\bar{G}^{2.71}}\right)^{\frac{1}{2.71-1}}$	$\gamma(\bar{D}) = \left(\frac{\bar{D}}{1950798\cdot(1-\bar{D})^{3.29}}\right)^{\frac{1}{3.29-1}}$
Tawny clay	$\gamma(\bar{G}) = \left(\frac{1-\bar{G}}{14903068\cdot\bar{G}^{3.17}}\right)^{\frac{1}{3.17-1}}$	$\gamma(\bar{D}) = \left(\frac{\bar{D}}{3910\cdot(1-\bar{D})^{2.28}}\right)^{\frac{1}{2.28-1}}$
Grey clay	$\gamma(\bar{G}) = \left(\frac{1-\bar{G}}{1.31\cdot10^{9}\cdot\bar{G}^{3.75}}\right)^{\frac{1}{3.75-1}}$	$\gamma(\bar{D}) = \left(\frac{\bar{D}}{1000000\cdot(1-\bar{D})^{3.05}}\right)^{\frac{1}{3.05-1}}$
Faeto flysch	Linear	Linear

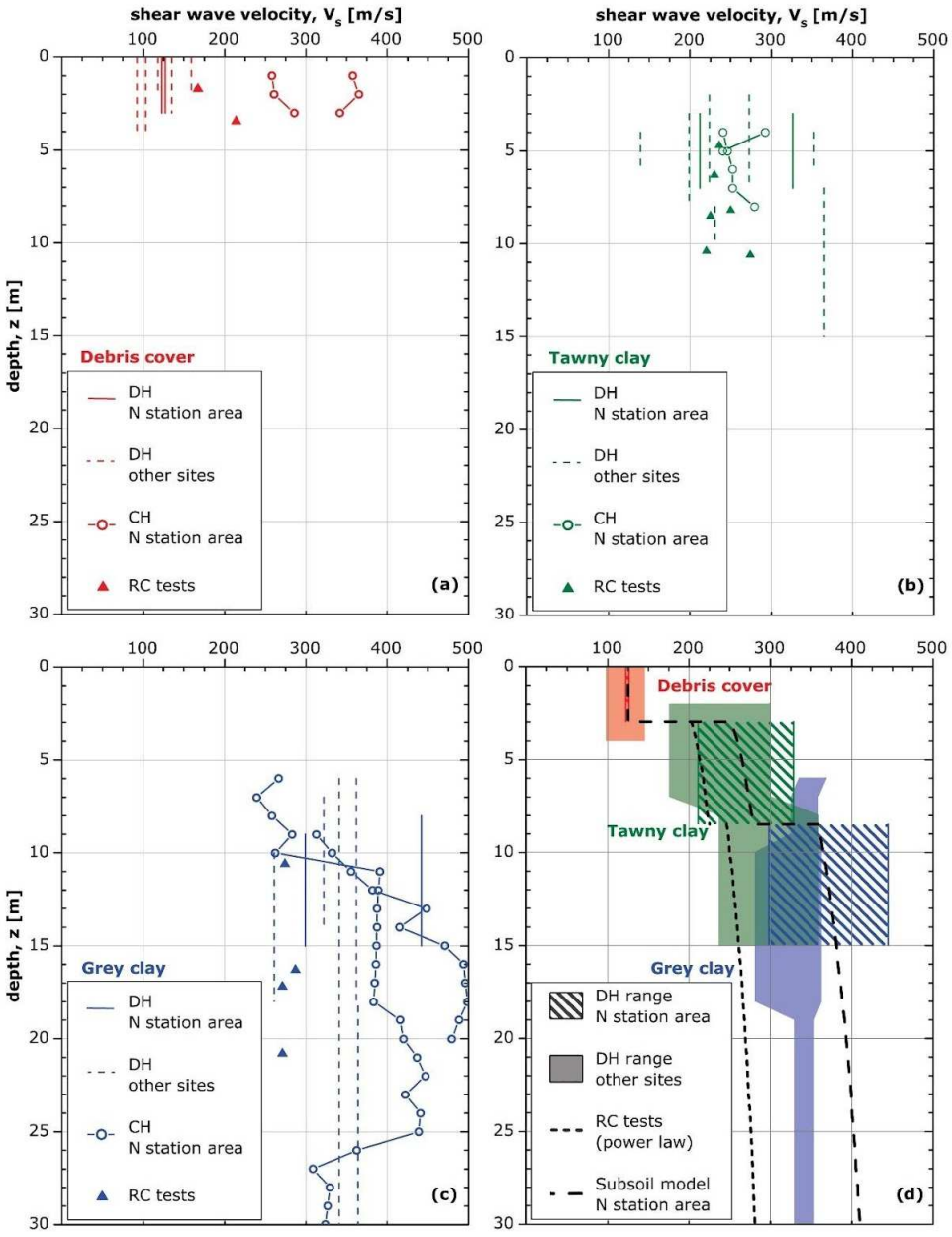

Figure 7.2. Shear wave velocity profiles obtained for the different formations from in-situ and laboratory tests: debris cover (a), tawny clay (b), grey clay (c), and comparison between the different trends (d) (Silvestri et al., 2006).

7.4 THE NEW STRUCTURAL AND GEOTECHNICAL MONITORING SYSTEM

In 2012, a permanent accelerometric network was added to the National Accelerometric Network (RAN) of the Italian Department of Civil Protection (DPC). Three different stations are included in the network (see Figure 7.3a):

1. SGMA, near Palazzo Marchesale (Marchesale Palace that is the City Hall), in the historical center on the stiff calcareous-marly unit. It is a single sensor, located at a depth of 10 m;
2. SGPA, installed at the "Parco della Memoria" (Memory Park) where the collapsed elementary school was located, on the clayey marly unit. This station is formed by a two-accelerometers array, located at the ground surface and at a depth of 53 m, respectively;
3. SGSC, another vertical array, near the new "F. Jovine" school on the clayey unit, consisting of a surface sensor and another located at a depth of 30 m.

The current study is developed on the basis of the information obtained by the SGMA and SGPA stations and on the soil investigation performed in the framework of study and research carried out at the site.

Here, the new Down-Hole tests performed contextually to the seismic network installation, show overall higher values of the shear wave velocity and, thus, a generally higher small-strain stiffness for the investigated soils. The newly available shear wave velocity profiles at the collapsed school (DH-S2) and at the city hall (DH-S3) are compared in Figure 7.3b with those adopted in the study of Puglia (2008) and derived papers at the same locations. The former test (DH-S2) reached a depth of 10 m from g.l., while the test DH-S3 reached -60 m from g.l. The deriving measurements confirm that the vertical array of the SGPA station is located in a softer site compared to the position where the embedded SGMA station is placed.

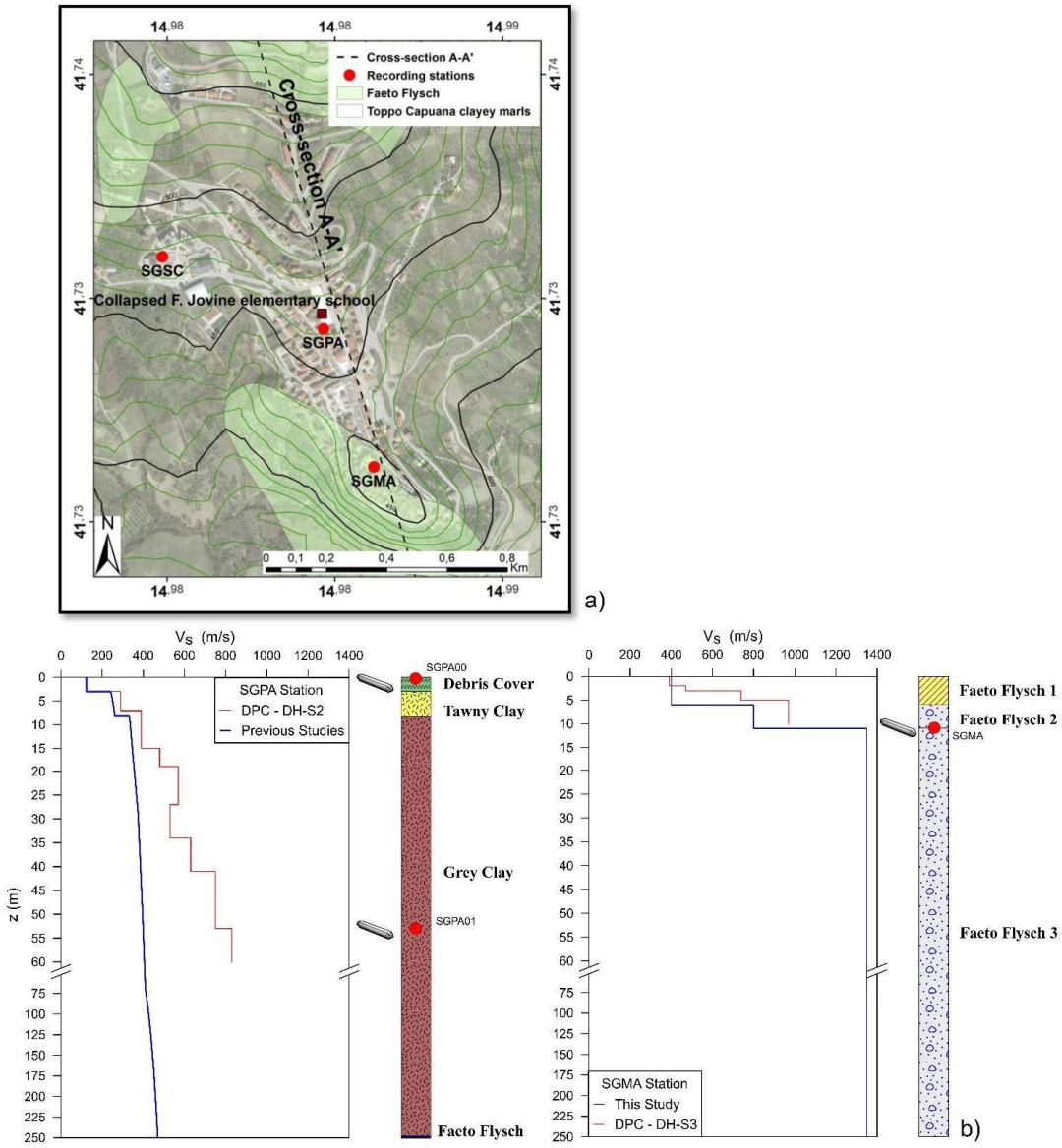

Figure 7.3. Plan view with the location of the new accelerometric network (a) and comparison between shear wave profiles assumed by Puglia (2008) and those measured by DPC (Sanò et al., 2015) at the collapsed school, SGPA and Palazzo Marchesale, SGMA (b).

No specific data about the stations are reported on the website of Luzi et al. (2016). However, additional information is provided by Sanò et al. (2015). The stations are made up of a 24-bit A/D converter and sensors for reading the three components of the seismic motion having 2g full scale, DC-200 Hz bandwidth, and 155 dB dynamic range; the stations are equipped with timing absolute GPS and telephone connection.

Recorded waveforms are collected and available in the Engineering Strong-Motion database (ESM). At the time to develop this thesis, in the catalog, for SGMA station manually processed records from 20 events from December 29th, 2013, to August 16th, 2018 in an M_W range 3.9÷6.5 were available, with the epicentral distance that belongs to the range 2.6÷199.1 km and the PGA is in the interval $6.22x10^{-5}$÷$2.37x10^{-2}$g. The buried sensor for the SGPA station recorded data from 13 events from December 29th, 2013 to August 16th, 2018 in an M_W range 4.0÷6.5, with epicentral distance 2.2÷198.8 km and PGA in the interval $3.13x10^{-4}$÷$4.37x10^{-2}$g, while the corresponding surface station recorded data from 30 events in the same time interval, in an M_W range 3.9÷6.5, with epicentral distance 2.2÷200.3 km and PGA in the interval $4.59x10^{-5}$÷$2.26x10^{-1}$g.

Overall, in the ESM catalog, thirteen earthquakes produced waveforms available at the basin level (i.e., recorded by both the stations at the SGPA site and at SGMA). The accelerograms are generated mainly by the seismic sequence that hit Central Italy starting from August 24th, 2016 as well as the one that affected the Molise Region in August 2018. The main features of the events are summarized in Table 7.3, and an ID code is assigned to each event. Some additional details on the recordings are reported in Fierro et al. (2019). It is worth noting that all the selected signals are marked in the ESM-ITACA database as 'Manually Processed'. This means that a detailed processing procedure to estimate and remove the noise is applied to each signal. This scheme (Paolucci et al., 2011; Pacor et al., 2011) is the same exploited by PEER (Pacific Earthquake Engineering Research Center) for the Next Generation Attenuation project (NGA; Power et al., 2008) with a slight difference related to the polynomial order adopted for detrending and it was widely tested by Boore et al. (2012).

Table 7.3. Main features of events recorded for SGPA and SGMA stations (data modified from Luzi et al., 2016).

ID	Event name	Date	Mw	Average epicentral distance R_{epi} (km)	Station	PGA (cm/s^2)	PGV (cm/s)	PGD (cm)
GM1	Caserta	2013-12-29 17:08:00	5.0	54.8	SGMA -10 m	0.851	0.104	0.079
					SGPA - 53 m	0.745	0.112	0.074
					SGPA 0 m	2.354	0.162	0.061
GM2	Campobasso	2014-12-24 11:40:10	4.0	2.4	SGMA -10 m	23.277	0.881	0.057
					SGPA - 53 m	42.868	1.238	0.112
					SGPA 0 m	221.707	6.828	0.247
GM3	Adriatic Sea	2015-12-06 16:24:40	4.5	77.1	SGMA -10 m	0.262	0.018	0.002
					SGPA - 53 m	0.307	0.017	0.002
					SGPA 0 m	1.367	0.052	0.003
GM4	Southern Italy	2016-01-16 18:55:11	4.3	35.2	SGMA -10 m	0.893	0.046	0.012
					SGPA - 53 m	1.179	0.055	0.012
					SGPA 0 m	2.981	0.125	0.016
GM5	Central Italy	2016-08-24 01:36:32	6.0	181.9	SGMA -10 m	1.029	0.300	0.221
					SGPA - 53 m	1.142	0.326	0.231
					SGPA 0 m	1.977	0.336	0.233
GM6	Central Italy	2016-08-24 02:33:29	5.3	193.7	SGMA -10 m	0.397	0.070	0.039
					SGPA - 53 m	0.360	0.062	0.037
					SGPA 0 m	0.985	0.072	0.038
GM7	Central Italy	2016-10-30 06:40:18	6.5	199.0	SGMA -10 m	2.493	0.720	0.661
					SGPA - 53 m	2.241	0.767	0.579
					SGPA 0 m	5.416	0.744	0.604
GM8	Central Italy	2017-01-18 10:14:12	5.5	167.7	SGMA -10 m	0.258	0.064	0.057
					SGPA - 53 m	0.353	0.076	0.057
					SGPA 0 m	0.875	0.086	0.057
GM9	Central Italy	2017-01-18 10:25:26	5.4	166.5	SGMA -10 m	0.404	0.068	0.041
					SGPA - 53 m	0.424	0.070	0.037
					SGPA 0 m	1.093	0.080	0.040
GM10	Southern Italy	2018-04-25 09:48:44	4.3	23.1	SGMA -10 m	1.069	0.084	0.013
					SGPA - 53 m	1.234	0.060	0.010
					SGPA 0 m	5.810	0.135	0.013
GM11	Southern Italy	2018-08-14 21:48:30	4.6	24.6	SGMA -10 m	4.262	0.285	0.042
					SGPA - 53 m	3.303	0.232	0.038
					SGPA 0 m	12.833	0.470	0.050
GM12	Southern Italy	2018-08-16 18:19:06	5.1	22.5	SGMA -10 m	7.468	0.517	0.111
					SGPA - 53 m	7.701	0.520	0.126
					SGPA 0 m	44.897	1.131	0.143
GM13	Southern Italy	2018-08-16 20:22:36	4.4	21.3	SGMA -10 m	5.156	0.439	0.044
					SGPA - 53 m	3.642	0.222	0.045
					SGPA 0 m	16.115	0.686	0.056

7.5 EQUIVALENT LINEAR SITE RESPONSE ANALYSES

The site response of the village of San Giuliano was firstly studied by Baranello et al. (2003) in the framework of the development of the microzonation studies of the area. Subsequently, several studies presented mono-, bi- and tri-dimensional analyses of the valley by considering increasing degrees of soil heterogeneity (Puglia, 2008; Puglia et al., 2007; 2009; 2013; Lanzo and Pagliaroli, 2009; Santucci de Magistris et al., 2014; Sanò et al., 2015), by always considering the equivalent linear approach. The data coming from the geotechnical monitoring were a precious source of information and were widely exploited. Most of the data came from the two mobile accelerometer stations installed by the Italian Civil Protection Department (DPC) after the earthquake on the outcropping flysch (CHI) and on the marly clay formation (SCL) in San Giuliano di Puglia (cf. Figure 7.1). Both the stations were removed in 2003.

Data obtained from the accelerometric network were adopted as a benchmark to test the goodness of the numerical models. Specifically, Puglia (2008) and derived papers calibrated their models on the available recordings of the two main aftershocks, while Lanzo and Pagliaroli (2009) tried to adapt their simulation to catch three recorded signals from aftershocks. Then, the calibrated model was employed to try to justify the observed damage distribution in the village of San Giuliano di Puglia (Dolce et al., 2004; Vona et al., 2009).

From this wide research work, it emerged that 1-D models significantly underestimated the observed amplification and they were only useful to detect the bedrock depth below the “Jovine” elementary school through the fundamental frequency of the deposit. On the other hand, 3-D models do not have enough resolution to catch the details of the modification of wave characteristics in the village, and this was related to the fact that a proper resolution was incompatible with reasonable computational time. This finding was obtained by Puglia (2013), where 2D models showed a better performance than 3D. This was probably due to the limitations in terms of geometry, extension, and resolution in subsoil description (Puglia, 2013). For this reason, further studies are needed in this sense in terms of in-situ tests oriented towards the definition of the

contact between flysch and marly clays and in terms of resolution of the numerical model, exploiting, for example, more powerful computational tools (i.e., parallel computing) allowing the development of large models that can be resolved in an acceptable computational time. Limiting the discussion to the results of the 2-D analyses performed along the main stratigraphic section of the village sketched in Figure 7.1, in the framework of the above-mentioned studies, the "Anvil" schema proved to be the most satisfying model, with respect to alternative hypotheses on the geometry of the top of the flysch bedrock (Puglia et al., 2007; Puglia, 2008).

For the so-called "Anvil IDW model" (because obtained through Inverse Distance Weight technique by exploiting the available boreholes), some results obtained by Santucci de Magistris et al. (2014) are shown in Figure 7.4. In particular, Figure 7.4a shows the surface response spectra (structural damping 5%) computed at regular steps of 100 m using as a reference input motion the synthetic acceleration time history simulated for the October 31st, 2002 event. Overall, the response spectra indicate a significant ground motion amplification on the surface of the marly clay deposit.

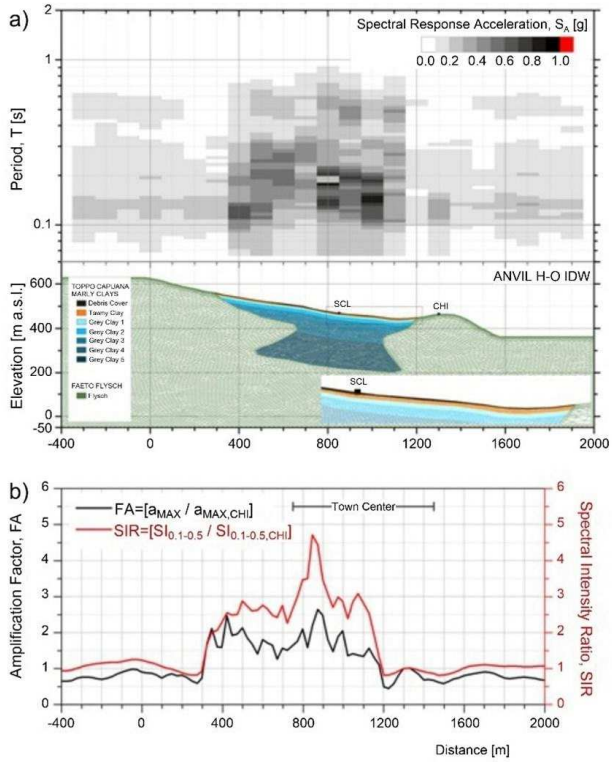

Figure 7.4. Response spectra of horizontal pseudo-acceleration (a) and amplification factors (b) for the event of October 31, 2002, simulated along the main section of the village of San Giuliano di Puglia (Santucci de Magistris et al., 2014).

In Figure 7.4b, the surface response is summarized in terms of Amplification Factor (AF) and Spectral Intensity Ratio (SIR) (see (7.1) and (7.2)):

$$\mathrm{AF} = \frac{\mathrm{a_{MAX}}}{\mathrm{a_{MAX,CHI}}} \tag{7.1}$$

$$\mathrm{SIR} = \frac{\mathrm{SI_{0.1-0.5}}}{\mathrm{SI_{0.1-0.5,CHI}}} = \frac{\int_{0.1}^{0.5} \mathrm{PSV(T)dT}}{\int_{0.1}^{0.5} \mathrm{PSV_{CHI}(T)dT}} \tag{7.2}$$

In particular, the amplification factors (FA) and the spectral intensity ratio (SIR), respectively expressed in terms of peak ground acceleration (a_{MAX}) and Housner Intensity ($SI_{0.1\text{-}0.5}$), were computed throughout the range of periods T representative of medium-size buildings (about 0.1 to 0.5 s) and, for this reason, the subscript "0.1-0.5" was added. Following the definition of Housner Intensity, PSV represents the pseudo-

velocity response spectrum ordinates. Both the indicators (FA and SIR) are expressed by the ratio between the ground motion parameters calculated at the surface on the analyzed vertical (a_{MAX} and $SI_{0.1\text{-}0.5}$) and those evaluated on bedrock outcropping conditions ($a_{MAX,CHI}$ and $SI_{0.1\text{-}0.5}$, CHI). Furthermore, the subscript "CHI" refers to the location of the temporary station previously described, which was installed on the outcropping Flysch.

The response of such a model in terms of SIR appears qualitatively able to reproduce the damage pattern observed in San Giuliano di Puglia after the main seismic event that was mapped according to the EMS scale (Dolce et al., 2004) showing that the earthquake produced the largest intensity in the central part of the village, where the collapsed school was located.

Finally, in the latest work proposed by Fierro et al. (2020b), whose results are reported in Appendix B, equivalent linear mono- and bi-dimensional site response analyses have been performed. In particular, the shear wave velocity profile was re-evaluated in the light of the new in-situ tests (cf. Figure 7.3b) comparing the simulated accelerograms with the recordings of the permanent accelerometers installed in the town in 2012. In the study, the responses obtained using the softer and the stiffer shear wave velocity profiles (cf. Figure 7.3b) are investigated. Furthermore, even the performances of "Anvil" and "Basin" models were evaluated. It was concluded that the best fitting of the recorded data was provided by the adoption of the "Anvil model" with the stiffer profile. Statistical indicators were selected to quantify the goodness of the simulations. Nevertheless, in Fierro et al. (2020a), a parametric study is conducted to understand the effect of the shear wave velocity and the bedrock depth on the site response in mono-dimensional conditions. It emerged that bedrock level has minimum influence on the comparison between simulated and recorded data, while the best-fit profile is consistent with the one adopted in Fierro et al. (2020b).

The latter studies are here recalled because the same geometrical model used in Puglia (2008), Santucci de Magistris et al. (2014) and Fierro et al. (2020b), among others, is considered in this research. In the following, a series of nonlinear numerical analyses

aiming at simulating three of the available seismic records at SGPA and SGMA stations are presented. In particular, bi-dimensional nonlinear site response analyses are performed using the parallel framework OpenSeesSP and implementing the so-called "Anvil" model, proposed by Puglia (2008; Figure 7.5), with the modification of the shear wave velocity profile based on Sanò et al. (2015) and exploited by Fierro et al. (2019; 2020b). Then, the comparison with the response obtained adopting a linear elastic model for the soil is shown.

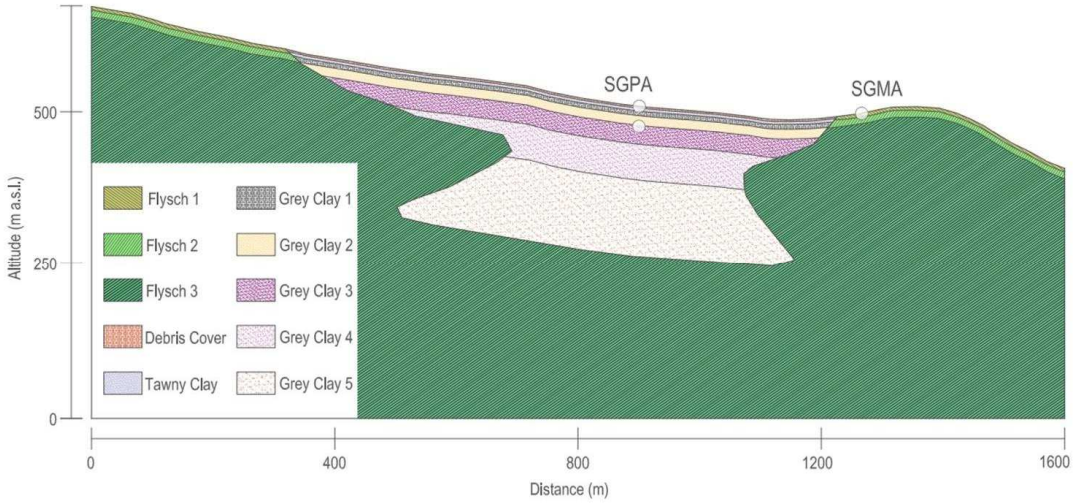

Figure 7.5. Main cross-section along the village of San Giuliano di Puglia considering the "Anvil" subsoil model by Puglia (2008) and the location of both the SGPA and SGMA seismic stations.

7.6 NONLINEAR SITE RESPONSE ANALYSES

The bi-dimensional "Anvil" model of the cross section of San Giuliano di Puglia is implemented in OpenSees and its response is observed under the excitation of three of the available accelerograms reported in Table 7.3. The goodness of the numerical model is evaluated by comparing the response at the nodes corresponding to the locations of the recording stations with the recorded data in terms of acceleration time series. As it is quite clear from Table 7.3 and as it was repeatedly stressed in the manuscript, the accelerometric network captured weak motions only.

The numerical model is extended for a width of 1600 m and has a total height of about 680 m. For this reason, being the computational time required for every single analysis on a single core processor considered unacceptable, the HPC resources provided by OpenSeesSP on the Cyber-Infrastructure (CI) DesignSafe have been exploited.

7.6.1 OPENSEESSP ON DESIGNSAFE-CI

The analyses are conducted with the parallel module of OpenSees, OpenSeesSP, in order to save computational time. OpenSeesSP represents the Single OpenSees Parallel Interpreter (McKenna and Fenves, 2008). It was conceived for the analysis of very large models or for input motions too long to be processed on a single processor. Furthermore, a deep knowledge of parallel computing is not required. Generally speaking, the model is firstly built on a single processor (P0), while, when the analyze() command (cf. §3.2) is called in the script, the model is going to be partitioned among the assigned processors and the elements are distributed among the machines. Then, the equations can be solved either in parallel or not and this depends on the choice of the system of equation solver. In fact, additional solvers are provided with respect to the sequential interpreter: Mumps, Petsc and SuperLU. Worth noticing that the outputs are given in .xml format.

OpenSeesSP, among other softwares, has been implemented into the Design-Safe CI (Rathje et al., 2017). The latter is a Cyber-Infrastructure providing cloud-based tools with a view to managing, analyzing, understanding, and publishing research data to better understand the impact of natural hazards. In addition, it allows performing numerical simulations exploiting advanced HPC resources and taking advantage of the supercomputers at TACC (Texas Advanced Computing Center). These capabilities are available at no-cost to the researchers. The infrastructure makes a repository, called Data Depot, available to the researchers where, with the aid of an interface, they can interact with data. Further technical details on the cyber infrastructure employed for the analyses can be found in www.designsafe-ci.org.

7.6.2 INPUT MOTIONS

The analyses here presented are conducted exploiting three manually processed accelerograms recorded between 2016 and 2018, coded in Table 7.3 as GM4, GM5 and GM13. The accelerograms used along the main section of the town (Section A-A' in Figure 7.3a) are obtained from the combination of the two horizontal components of the recordings, as in (7.3)

$$a(t)_{n344} = a(t)_{NS} \cdot \cos(16°) - a(t)_{EW} \cdot \text{sen}(16°) \quad (7.3)$$

The resulting time histories adopt the "n344" subscript, because the main axis of the town provides a clockwise orientation of 344° from the NS direction. The main features of the resulting motions, recorded at SGMA, deconvolved at the bedrock outcropping conditions and rotated along the AA' section, are reported in Table 7.4.

Table 7.4. Main features of the selected input motions.

Event ID	Event Name	Date	Time	M_w (-)	R_{epi} (km)	PGA (g)	Predominant period (s)
GM4	Southern Italy	2016-01-16	18:55	4.3	35.2	0.00082	0.26
GM5	Central Italy	2016-08-24	01:36	6.0	181.9	0.00098	0.42
GM13	Southern Italy	2018-08-16	20.22	4.8	22.7	0.00477	0.34

Figure 7.6 shows the time histories considered as input motions (at the outcropping bedrock conditions), obtained from a mono-dimensional deconvolution of the recordings available at the SGMA station. The mono-dimensional deconvolution was performed exploiting the Strata program (Kottke et al., 2013). The same procedure was adopted in Fierro et al. (2020a, b) to perform mono- and equivalent linear bi-dimensional analyses, to evaluate the shear wave velocity profile at the same site.

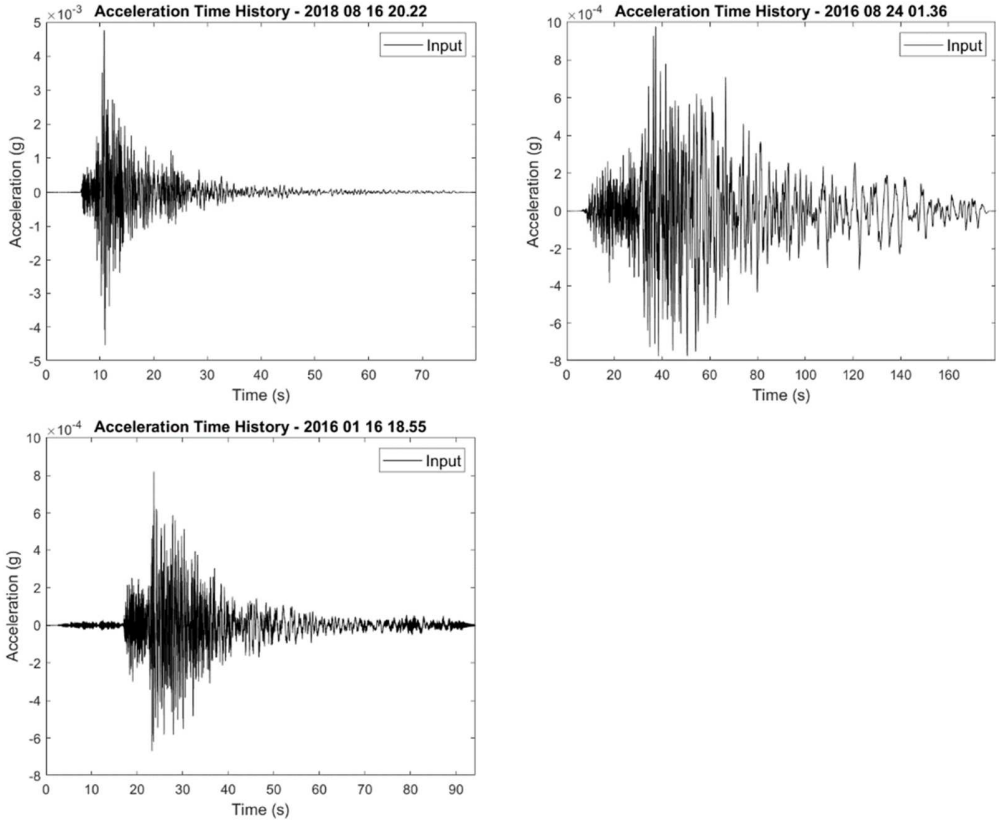

Figure 7.6. Input motions adopted for the bi-dimensional analyses.

7.6.3 NUMERICAL MODEL

The model is extended for a width of 1600 m and has a total height of about 680 m. It has been developed exploiting the GiD pre-processor (Coll et al., 2018), on the basis of that adopted for the equivalent linear analyses conducted with QUAD4M, while the nodes and the elements are obtained through Gid+OpenSees Interface (Papanikolaou et al., 2017). The layer discretization is shown in Figure 7.7, where the three main units of the San Giuliano di Puglia subsoil are switched into subunits based on the shear wave velocity profile. The model represents the implementation in OpenSeesSP of the geometry just shown in Figure 7.5. A detail of the mesh at the contact between Toppo Capuana marly clays and Faeto flysch (treated as bedrock) is reported in Figure 7.8.

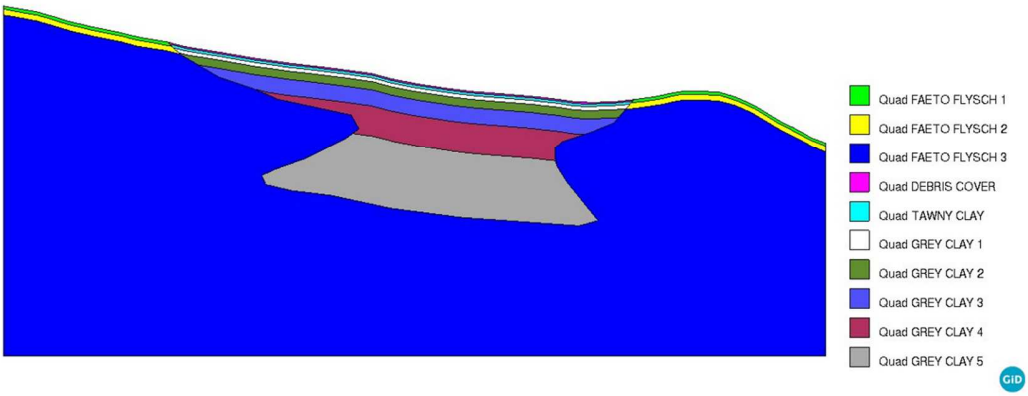

Figure 7.7. Layer discretization for the bi-dimensional model of San Giuliano di Puglia.

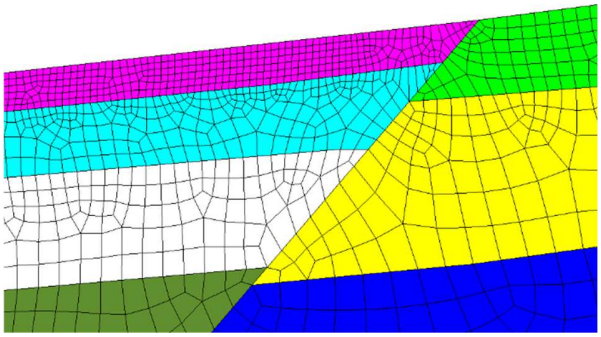

Figure 7.8. Detail of the contact between the meshed units.

Figure 7.9 focuses on the shear wave velocity profiles available in the village at the two sites of interest. Sanò et al. (2015) correspond to down-hole results performed at the time of array installation, and, consequently, a simplified profile that follows the latter is adopted in this study.

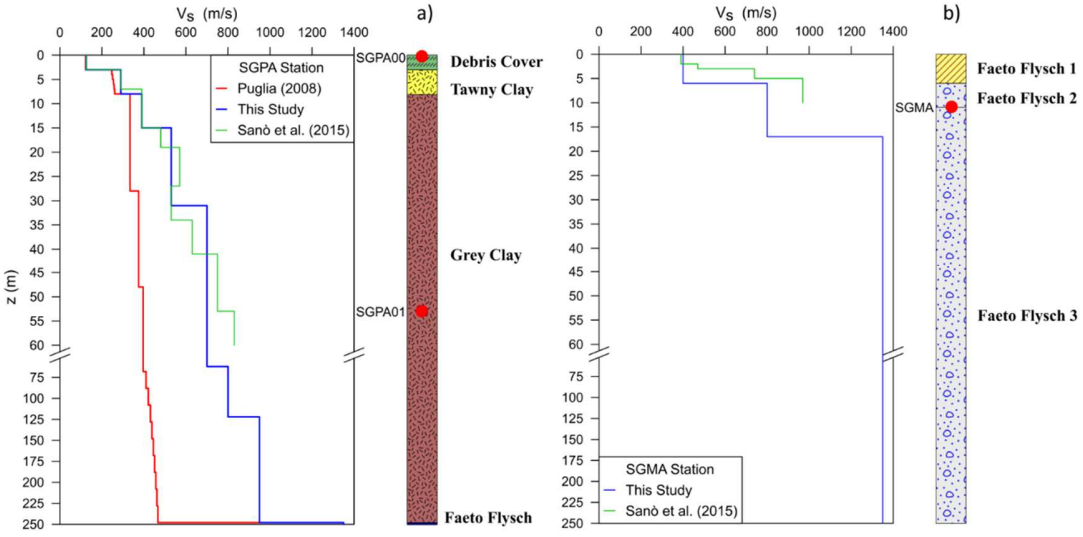

Figure 7.9. Vs profiles at SGPA (a) and SGMA (b) locations used for site response analyses.

The soil deposit is modelled using quadrilateral elements with a single-stabilization point (McGann et al., 2012), referred to as SSPquad in OpenSees. 80134 elements and 81695 nodes are used for the definition of the whole model. The SSPquad elements replicate the functions of the quad element implemented in OpenSees, by contextually exploiting the physically stabilized single-point integration (SSP), as in SSPquadUP and SSPbrickUP (cf. §4). The choice of a dynamic total stress analysis without considering pore water pressure generation can be justified by the use of weak motions for the tests that are, in turn, the only available recordings common to all the stations.

The dimensions of the elements are selected to allow the transmission of frequencies up to f_{max}=20 Hz, where the maximum height of the elements (H_{max}) is computed as $V_s/(10 \cdot f_{max})$. For each subunit, the following Table 7.5 summarizes the height of the element considered.

Table 7.5. Shear wave velocity adopted for each subunit, maximum height and selected height for the elements.

Unit	**V_s (m/s)**	**H_{max} (m)**	**H (m)**
Debris cover	125	0.625	0.5
Tawny clay	290	1.450	1.0
Grey clay 1	390	1.950	1.5
Grey clay 2	530	2.650	2.0
Grey clay 3	700	3.500	3.0
Grey clay 4	800	4.000	3.5
Grey clay 5	950	4.750	4.0
Faeto Flysch 1	400	2.000	1.0
Faeto Flysch 2	800	4.000	2.0
Faeto Flysch 3	1350	6.750	5.0

Surveys identified three layers of Faeto flysch, characterized by different levels of fracturing and fissuring, namely "Faeto flysch 1", "Faeto flysch 2", and "Faeto flysch 3". Their unit weight, shear wave velocity, P-wave velocity and Poisson's ratio are obtained from Puglia (2008) and d'Onofrio et al. (2009), as assumed in Fierro et al. (2019, 2020a, b). An elastic isotropic material is used to model their response in OpenSees. The Young modulus was consequently calculated based on the well-known elastic relationships reported in (7.4).

$$E = 2 \cdot (1 + \nu) \cdot G \tag{7.4}$$

where ν and G are Poisson's ratio and shear modulus of the soil, respectively. The latter is obtained as $G = \rho \cdot V_s^2$, on the basis of soil density and its shear wave velocity. The values of ν and ρ are obtained from Table 7.1, while the V_s profile is the one of Table 7.5.

The soft soil in the basin can be sub-divided into debris cover, tawny clay, and grey clay (d'Onofrio et al., 2009). To account for the increase of stiffness with the depth of the grey clay, it is divided into five subunits each of them with constant stiffness. According to Puglia (2008), the contact between Toppo Capuana marly clay and Faeto Flysch along the SGPA vertical is at 248m depth.

Soft soil is modelled using both elastic and pressure-independent multi-yield material. The pressure-independent multi-yield (PIMY) model was developed at the University of California San Diego and implemented in OpenSees (Yang et al., 2008). The model was conceived to simulate the behaviour of clays subjected to fast loading conditions and exploits the multi-surface concept. In this model, the plasticity can be developed only in the deviatoric plane, while the volumetric response is linear elastic. The structure of the model in the octahedral τ-γ plane is shown in Figure 7.10.

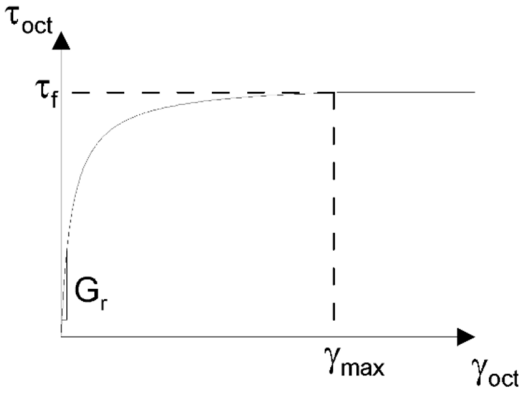

Figure 7.10. Pressure independent multi-yield constitutive model in octahedral τ-γ plane (reproduced from Yang et al., 2008).

Shear (G) and bulk (B) moduli are calculated based on the shear wave velocity profiles shown in Figure 7.9, using the following equations (7.5) and (7.6):

$$G = G_r \cdot \left(\frac{p'}{p'_r}\right)^d \tag{7.5}$$

$$B = B_r \cdot \left(\frac{p'}{p'_r}\right)^d \tag{7.6}$$

where G_r and B_r represent the reference shear and bulk moduli of the soil, respectively. In this study, the coefficient d, which accounts for the variation of the stiffness as a function of the effective mean confinement pressure, is assumed to be zero, to reproduce homogeneous layers (constant stiffness).

Soil density and modulus reduction curves used in the numerical model are from d'Onofrio et al. (2009). By specifying modulus reduction curves, the nested surfaces of pressure-independent multi-yield model are consequently generated, and their number is defined accordingly. Once user-defined yield surfaces are defined, the constitutive model ignores the values given for friction angle and cohesion and compute them as a function of the mean stress.

For all the clays in the model, it is used the value of the peak shear strain and effective reference pressure suggested in the manual for clays (0.1 and 100 kPa, respectively).

Absorbing boundaries in both horizontal and vertical directions are successfully implemented in the model to avoid wave reflection, using Lysmer dashpots (Lysmer and Kuhlemeyer, 1969), as shown in Durante et al. (2018). Seismic motions are applied at each node of the base of the model through nodal forces proportional to the velocity time-history of the input according to Joyner and Chen (1975).

Rayleigh viscous damping is applied to the model to guarantee a small amount of numerical damping. In this study, the approach with two control frequencies is adopted, using the procedure suggested by Hudson et al. (1994). The control frequencies correspond to the fundamental frequency of the model and n-times the fundamental frequency, where n is the odd integer that rounds up the ratio between the predominant frequency of the input and the fundamental frequency of the model. In this case, the fundamental frequency of the soil model is obtained from eigenvalue analysis carried out to perform simulations with an equivalent linear approach using QUAD4M by Fierro et al. (2020b). Figure 7.11 shows the schematic of the adopted Rayleigh damping formulation for one of the input motions used in this study.

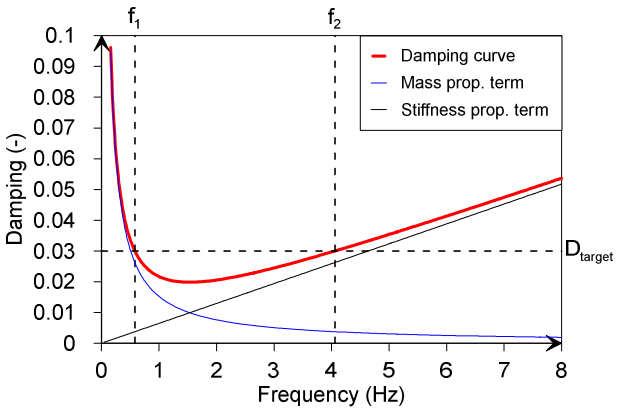

Figure 7.11. Rayleigh damping formulation for the input motion GM13.

The analyses are performed into three different steps: firstly, the gravity loads are applied considering an elastic behaviour of the soils. Then, the constitutive models are activated through the updateMaterialStage command in OpenSees. In these stages, a Transient analysis is performed exploiting Newmark integrator with β and γ coefficients equal to 0.5 and 0.25, respectively and the Krylov Newton algorithm. The Penalty method is adopted as a constraint handler, whose coefficients are chosen to be $1x10^{18}$. The convergence is evaluated in terms of the norm of displacement increments with a $5x10^{-3}$ tolerance value. Finally, the Mumps system of equation solver is adopted, switching the -INCTL14 option to 50%. The same analysis parameters are applied to the following dynamic stage, by only changing the Penalty parameters to $1x10^{20}$. The above-mentioned analyses are conducted using the OpenSeesSP v.3.3 interpreter on Stampede2, one of the supercomputers available at the TACC. It has 4200 KNL (Knight Landing) nodes. In order to resolve this model, 1 node with 64 parallel processors has been selected.

7.6.4 RESULTS

This section shows the comparisons between the numerical simulations and the recorded motions at the SGMA and SGPA stations.

Figure 7.12 shows the comparison between the recorded and the simulated acceleration time series for the input GM4 at the selected stations, obtained using the nonlinear

numerical model (PIMY). Figure 7.12a, Figure 7.12b, and Figure 7.12c suggest that a satisfactory agreement is obtained in terms of time-histories amplitude at all the locations. A slight overestimation is observed at a higher depth (Figure 7.12b), while the simulations underestimate the recorded response at the surface (Figure 7.12a, c). However, the PGA seems to be correctly reproduced.

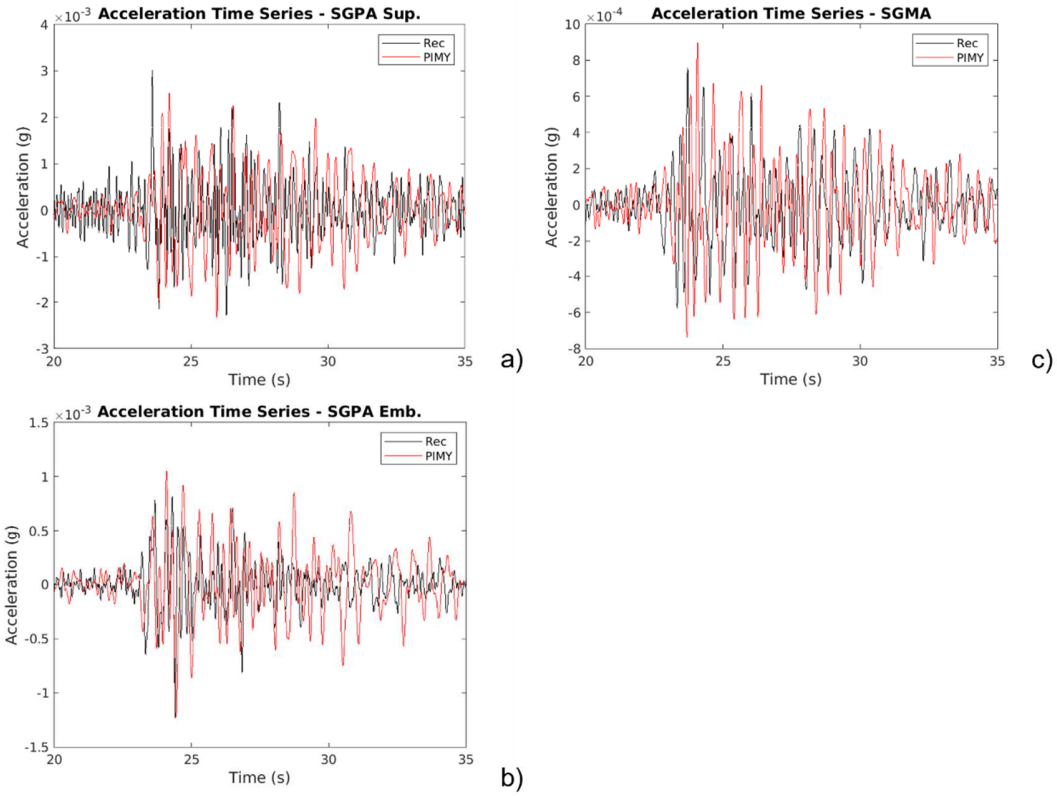

Figure 7.12. Comparison between recordings and simulations using pressure independent multi-yield constitutive model at SGPA at surface (a) and in depth (b), and surficial SGMA (c) stations for the event GM4.

In Figure 7.13, the comparison in terms of acceleration response spectra (5% structural damping) is presented for the GM4 motion for the sake of brevity.

Overall, a good performance is noticed, with the simulated response always overestimating the spectra from the recordings. Acceptable congruence is reached at the SGMA and SGPA embedded stations, considering both amplitude and spectral shapes. In both cases, the simulations overestimate a peak located at 0.5 s, and the

response seems to be overestimated even for the period range 0.25-1 s (see Figure 7.13b, c). This peculiarity can be found in the comparison at the SGPA surficial station as well, but the spectral shape seems not to be correctly captured in the above-mentioned period range (Figure 7.13a). This can be due to the definition of the Rayleigh parameters considered in this study. Further studies are needed for the evaluation of the performance of the model when soil non-linearity is reached.

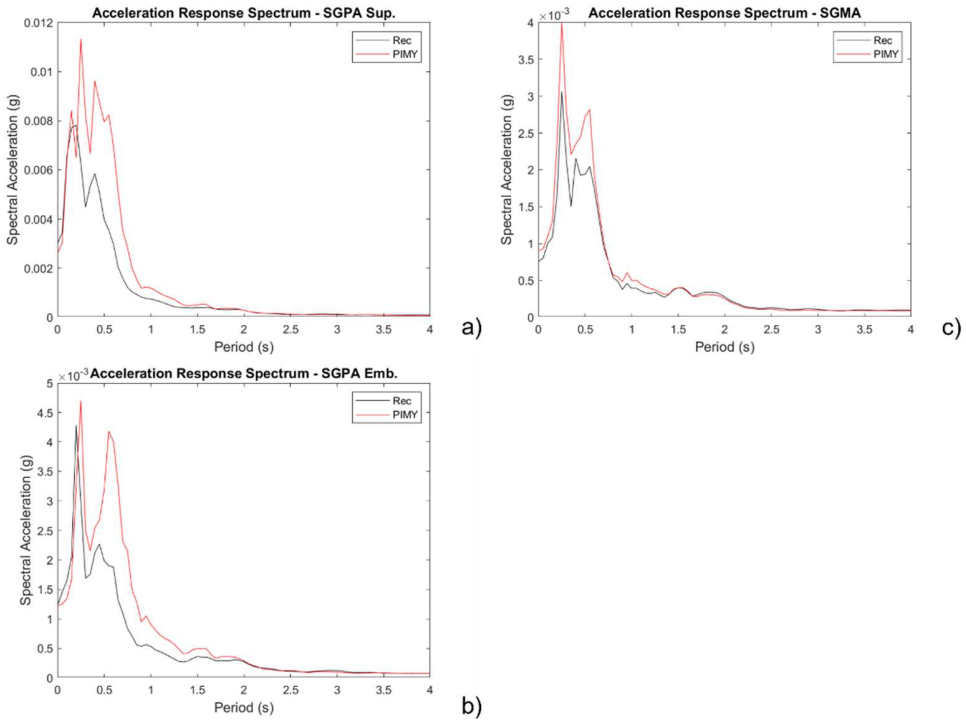

Figure 7.13. Comparison between recorded and simulated acceleration response spectra using pressure independent multi-yield model at surficial SGPA (a), embedded SGPA (b) and SGMA (c) locations for the event GM4.

Figure 7.14 shows the comparison between the recorded and the simulated acceleration time series for the event GM5 at the selected stations, obtained using the nonlinear numerical model. Model responses in terms of acceleration time-series can be considered satisfactory for the SGPA surficial and SGMA sensors (Figure 7.14a, c, respectively), while a widespread overestimation of acceleration amplitude is observed at the SGPA in-depth accelerometer (Figure 7.14b). For this motion, a time delay of about 0.5 s is observed in the simulations that could be related to three-dimensional site

response effects, that are neglected in the current 2D plane-strain model. This aspect needs further investigation, and it will be the object of further studies.

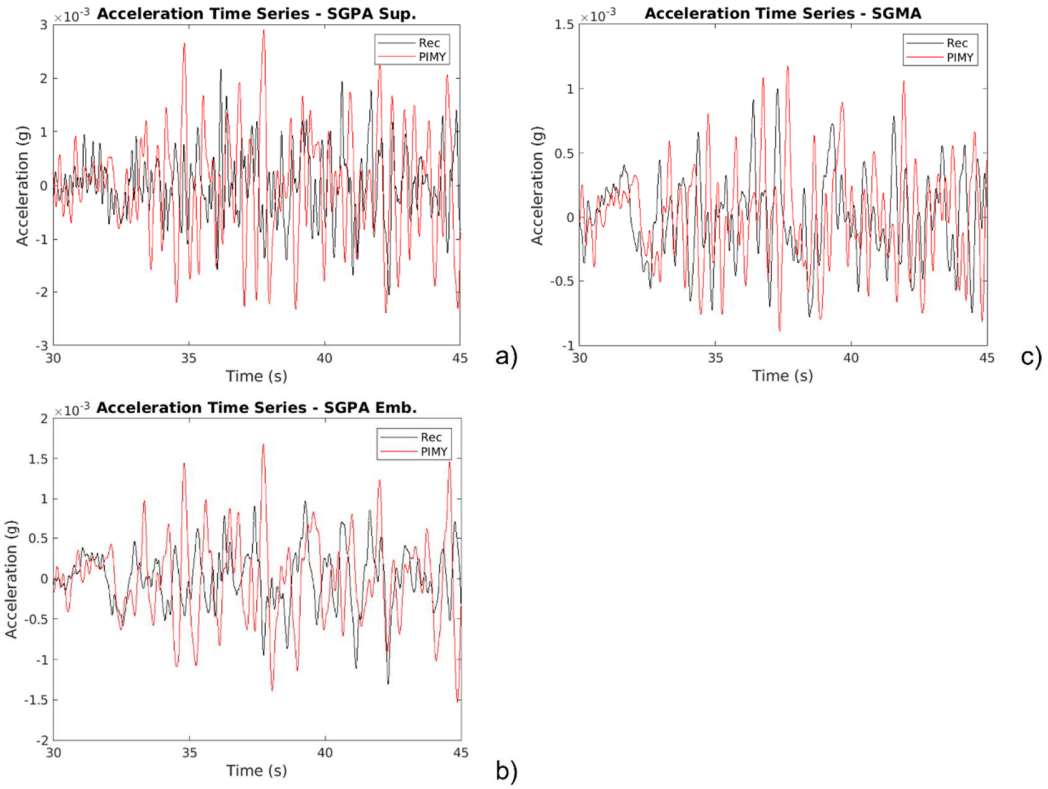

Figure 7.14. Comparison between recordings and simulations using the pressure-independent multi-yield constitutive model at surficial (a) and embedded (b) SGPA and SGMA (c) stations for the event GM5.

Figure 7.15 shows the comparison between the recorded and the simulated acceleration time series for the event GM13 at the selected stations, obtained using the nonlinear numerical model. A good agreement is always observed, despite a small overestimation produced by the simulations. It should be noted that the amplitude at the SGMA station seems to be more accurately reproduced than that at the SGPA vertical array.

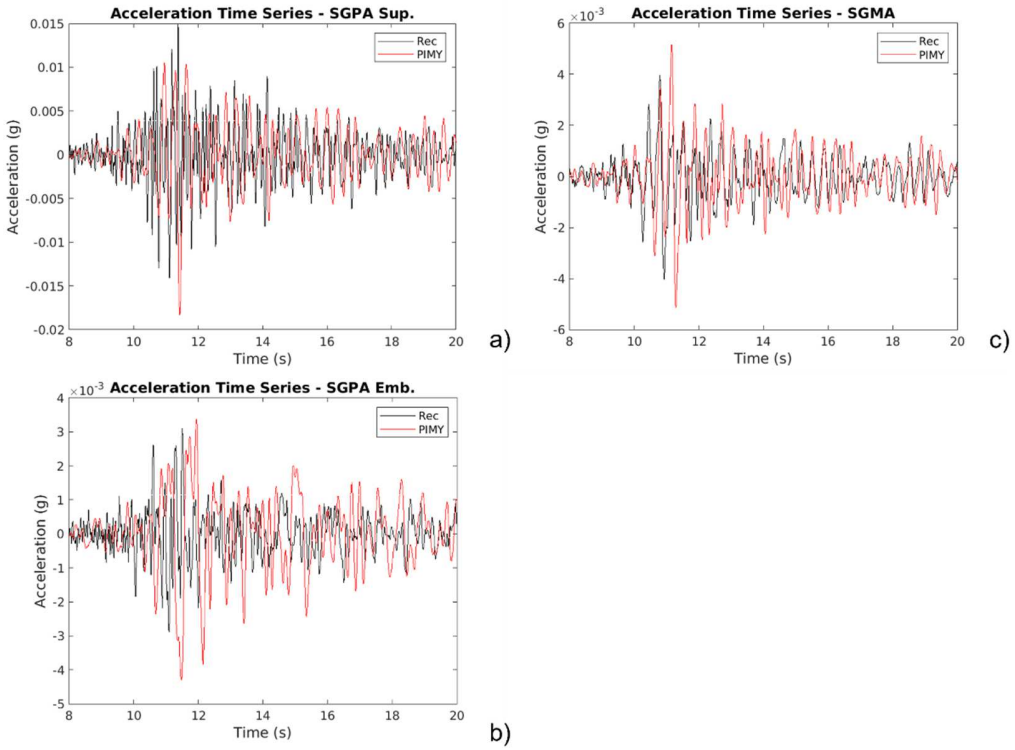

Figure 7.15. Recorded versus simulated acceleration time series at surficial SGPA (a), embedded SGPA (b) and SGMA (c) locations for event GM13, obtained using nonlinear model (PIMY).

Then, the response obtained using the advanced PIMY constitutive model is compared to that resulting from the adoption of a linear elastic behaviour for all the units previously mentioned, showing a good fit. This match is justified by the low strain level induced by the input motions. In fact, it has been observed that no degradation is applied to the materials in the model. For the sake of clarity, the comparison is reported with reference to the event GM13, only, in Figure 7.16.

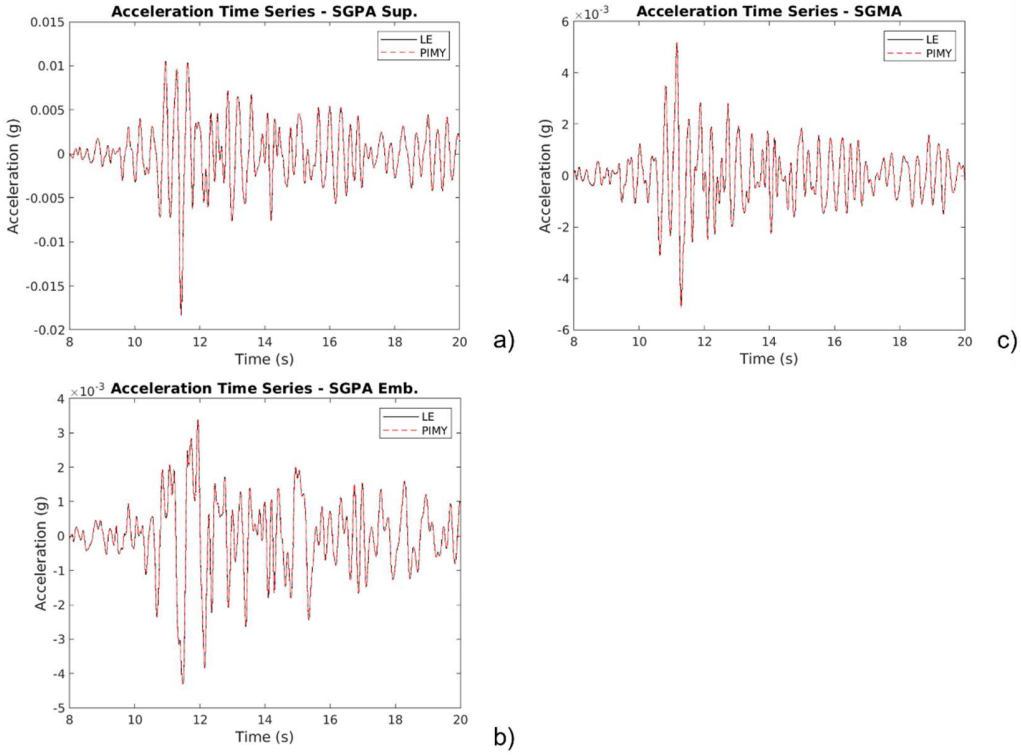

Figure 7.16. Linear elastic versus pressure independent multi-yield model results at surficial SGPA (a), embedded SGPA (b) and SGMA (c) locations for the event GM13.

Finally, the PGA and amplification factor profiles obtained along both SGMA and SGPA verticals are shown in the following Figure 7.17, Figure 7.18, Figure 7.19, and Figure 7.20, respectively, referred to the motion coded as GM4. Worth noticing that the amplification factor (AF) is calculated through the ratio between the simulated PGA and the PGA of the input.

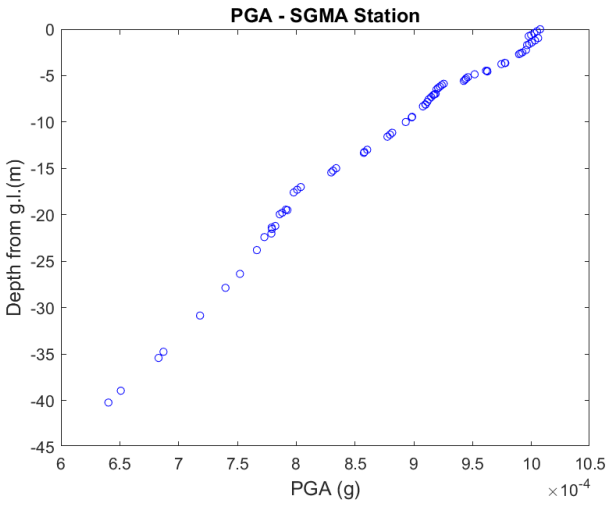

Figure 7.17. PGA profile along the SGMA vertical with reference to the motion GM4.

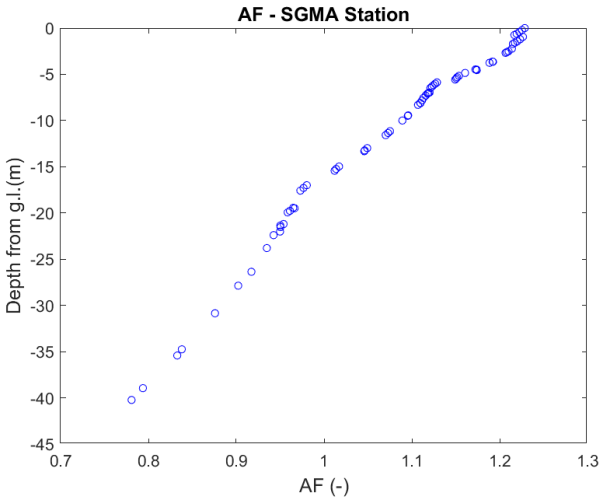

Figure 7.18. Amplification factor profile along the SGMA vertical with reference to the motion GM4.

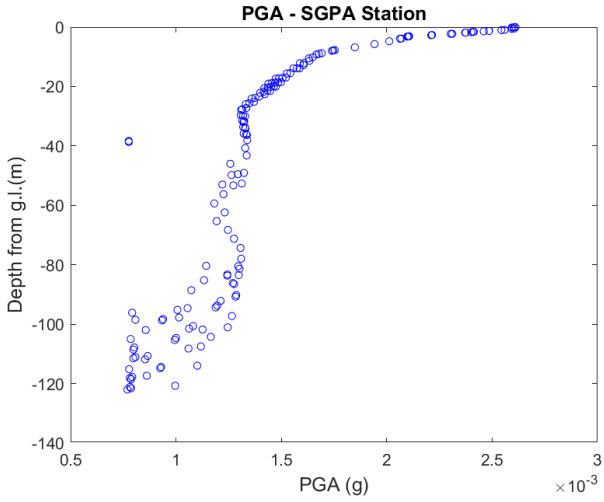

Figure 7.19. PGA profile along the SGPA vertical with reference to the motion GM4.

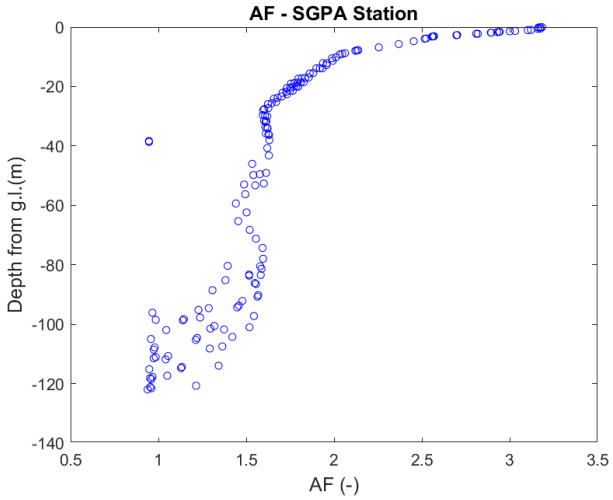

Figure 7.20. Amplification factor profile along the SGPA vertical with reference to the motion GM4.

In the following, Figure 7.21, Figure 7.22, Figure 7.23, and Figure 7.24 report the PGA and amplification factors profiles referred to the motion GM5.

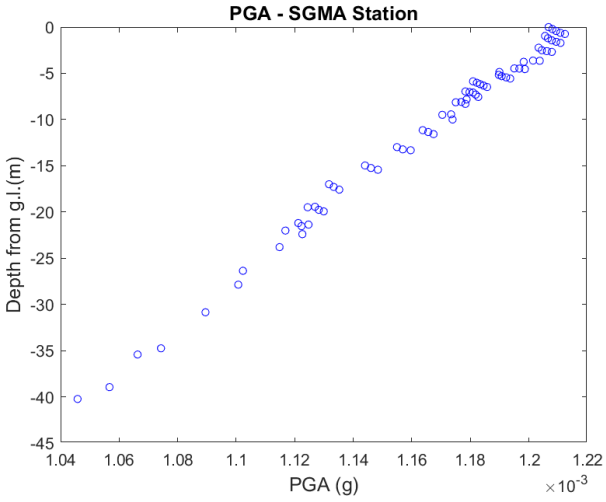

Figure 7.21. PGA profile along the SGMA vertical with reference to the motion GM5.

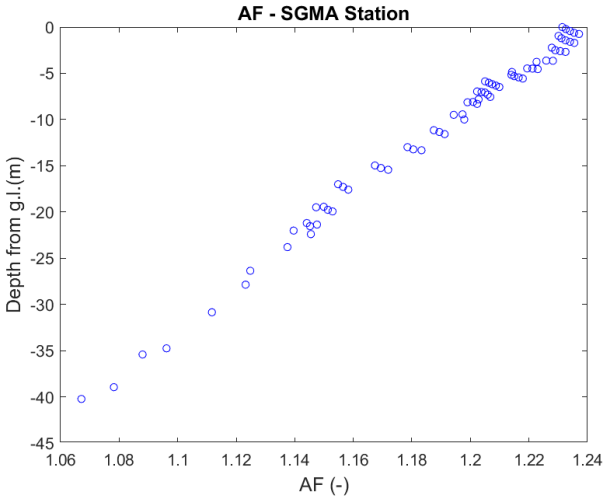

Figure 7.22. Amplification factor profile along the SGMA vertical with reference to the motion GM5.

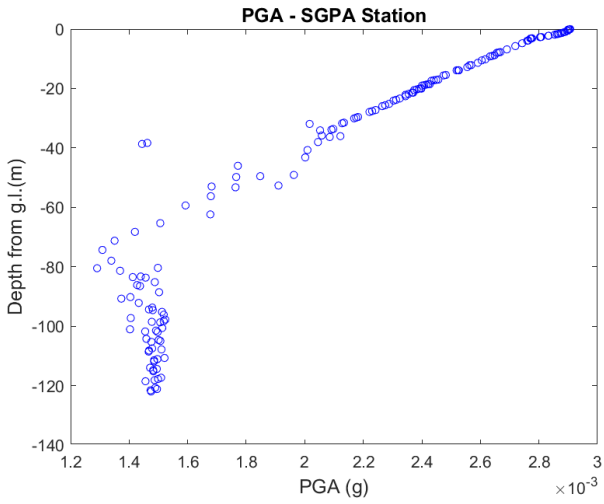

Figure 7.23. PGA profile along the SGPA vertical with reference to the motion GM5.

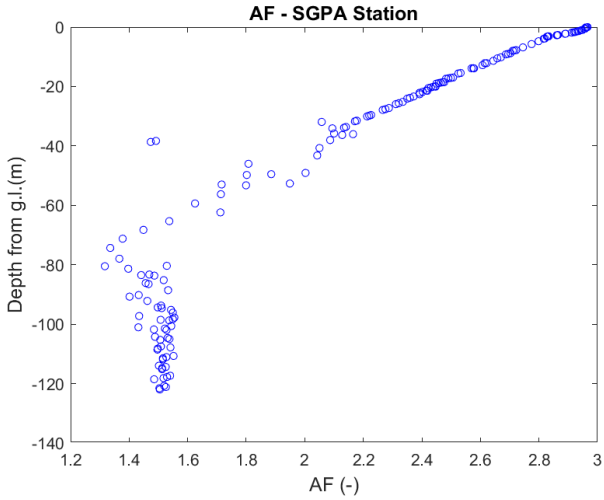

Figure 7.24. Amplification factor profile along the SGPA vertical with reference to the motion GM5.

Finally, peak ground acceleration and amplification factor profiles are shown for the motion GM13.

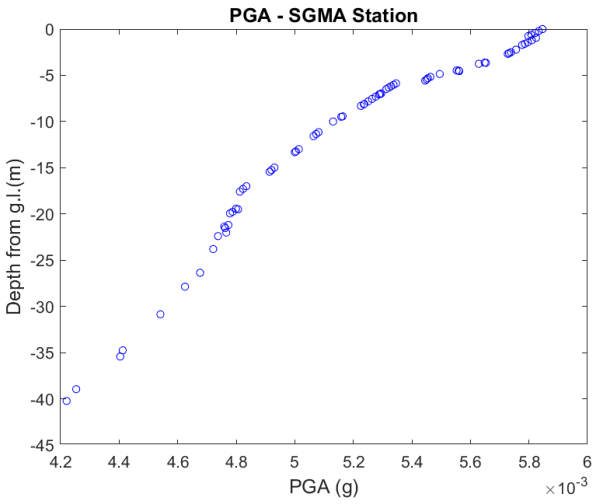

Figure 7.25. PGA profile along the SGMA vertical with reference to the motion GM13.

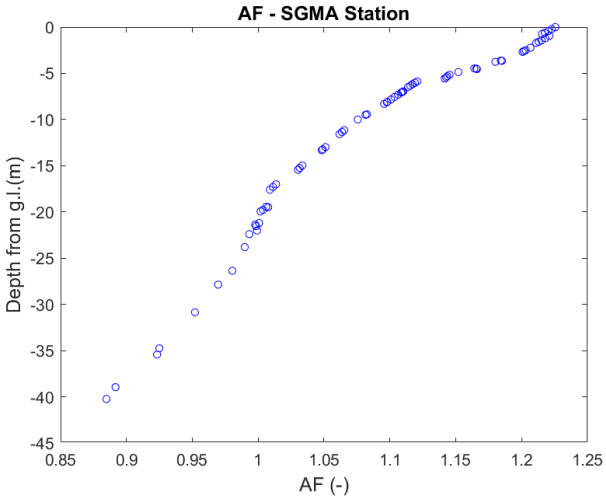

Figure 7.26. Amplification factor profile along the SGMA vertical with reference to the motion GM13.

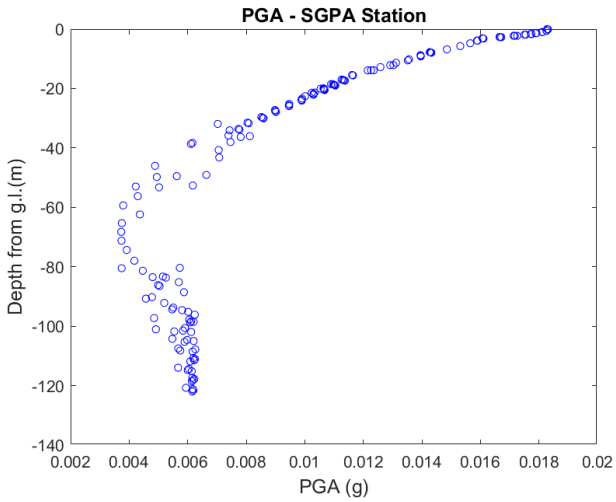

Figure 7.27. PGA profile along the SGPA vertical with reference to the motion GM13.

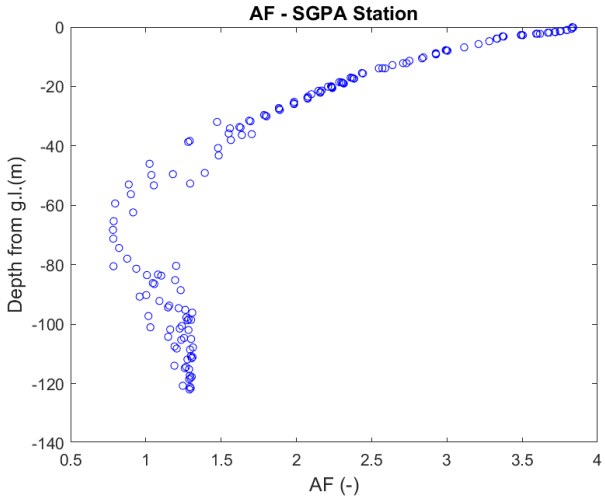

Figure 7.28. Amplification factor profile along the SGPA vertical with reference to the motion GM13.

Generally speaking, the observations provided by the previous studies are confirmed even with the analyses performed in OpenSeesSP. In fact, the profiles in terms of PGA and, consequently, in terms of AF, are consistent among the different input motions in shapes and amplitudes. With reference to SGPA, amplification occurs in the upper 40 m, highlighting a strong amplification on the surface, with AF ranging from 3 to 4. This is consistent even with the damage distribution observed after the earthquake. Along SGMA vertical, the surficial AF reaches the values of 1.2, evidencing that very small amplification takes place here, where the historical core is located. However, at the

higher depths, it assumes the values of 0.85-0.9, which means deamplification. This can be related to the interaction between the buried contact between the clay soils and the flysch, which can generate focalization effects towards the center of the valley.

7.7 DISCUSSION

The research presented herein has been focused on the site response analysis of the village of San Giuliano di Puglia, where high macroseismic intensity during the 2002 Molise earthquake was observed. The peculiar distribution of the damage and the tragic collapse of the "F. Jovine" elementary school have prompted numerous in-depth studies aimed at evaluating possible local amplification effects. Starting from this wide background of knowledge, the revised consensus model proposed in previous studies has been implemented in OpenSees, exploiting high HPC resources made available by the DesignSafe-CI. The available seismic signals recorded by the sensors installed in the town are used to test the goodness of the model implementation for the subsoil of the village.

Three weak motion accelerograms recorded by the network are exploited to assess whether the previous findings are confirmed, even adopting an advanced constitutive model. The results are then observed in terms of PGA and amplification factor, and they are compared to those obtained by assuming a linear elastic behaviour for the soil.

Overall, the numerical simulations revealed able to reproduce the motion at the depth of the recording stations satisfactorily. The simulated accelerograms show good accordance with the recorded data, with a slight overestimation of the response along the SGPA vertical, if compared to the embedded SGMA station, where the historical core of the village is built. On the other hand, the observation of PGA and AF profiles highlighted that the model is consistent with the observed damage after the 2002 events: the highest amplification factor (up to 3.5) has been reached on the surface along SGPA vertical, where the school collapsed, while a slight amplification can be identified in the historical core, which translates in deamplification at the higher depths. This can be due to focalization effects provided by the buried geometry towards the

center of the San Giuliano basin. On the other hand, the response in frequency domain requires deeper studies.

Furthermore, the study strengthens the previous findings, assessing a good performance of the numerical model already exploited in the recent studies. This model was built on the basis of new findings in terms of shear wave velocity profiles. For this reason, the adoption of soil monitoring through the use of vertical arrays installation as a valuable tool to back-analyze complex geometries and to verify the soil characterization, strongly emerges from the study. This finding can be considered an important starting point to underline the usefulness of the recordings obtained from the seismic stations. In fact, it arises that, for an area of geological and morphological complexity like that under study, although abundantly analyzed and investigated, the acquisition of additional information from the seismic station is of paramount importance to validate the numerical models through site response back-analyses. As a matter of fact, in the field of Geotechnical Earthquake Engineering, when advanced numerical analyses are performed, the results are always very difficult to evaluate in terms of their reliability, even for a relatively simple class of problems such as the local seismic response. This is due to the required high quality and a large amount of data to calibrate the models.

Last but not least, it is worthwhile to mention that numerical analyses with appropriate constitutive models for the soil are an essential tool for assessing site effects. The reliability of numerical models needs to be evaluated based on case histories, implying that effective tools can be obtained to analyze such contexts with practical implications of preservations and design. In the case under study, a relatively easy determination of the parameters to be assigned to the advanced pressure-independent multi-yield model was possible only thanks to the wide database of geotechnical data with reference to the soil units in San Giuliano di Puglia. On the other hand, this amount of data is not always available in the current practice. The study also highlights that the non-linearity has not been mobilized adopting the weak motion, as expected, being the obtained results identical to those obtained considering linear elastic behaviour of soils. This

points out that, sometimes, the implementation of such complex and large numerical domains (i.e., the buried morphology of the San Giuliano basin) is more relevant than the use of advanced constitutive models. For this reason, a wide background is required to the modeler.

On this basis, a key role was played by the HPC resources provided by DesignSafe-CI and OpenSeesSP. The availability of these resources led us to resolve this complex geometry in a relatively brief computational time. Please note that for the motion coded as GM5, about 6 days were needed to perform the analysis on a common sequential machine. This computational time has been reduced to 7 hours exploiting the DesignSafe platform. The increasing availability of such infrastructures, together with an increment of the documentation, is going to encourage researchers to adopt complex numerical codes like OpenSees, thought for research purposes, but with extremely high simulative potential. Once more, even if initially developed for structural purposes, OpenSees revealed extremely capable to simulate geotechnical problems.

7.8 REFERENCES

AA. VV. (2011). Supplement to the Earthquake Engineering Journal (in Italian). Anno XXVIII, n.2, 2011.

AGI (2005). Italian Geotechnical Association – Guidelines. Geotechnical Aspects of the design in seismic areas (in Italian). Patron Editore, Bologna.

Baranello S., Bernabini M., Dolce M., Pappone G., Rosskopf C., Sanò T., Cara P. L., De Nardis R., Di Pasquale G., Goretti A., Gorini A., Lembo P., Marcucci S., Marsan P., Martini M. G. and Naso G. (2003). Final Report on the Seismic Microzonation of the village of San Giuliano di Puglia (in Italian). Italian Department of Civil Protection, Rome.

Boore D.M., Azari Sisi A. and Akkar S. (2012). Using pad-stripped acausally filtered strong-motion data. Bull Seismol Soc Am 102(2):751–760. https://doi.org/10.1785/0120110222.

Castiglia M. and Santucci de Magistris F. (2016). Influence of the focal mechanism on the ground motion characteristics. Proceedings of the 1st IMEKO TC-4 International Workshop on Metrology for Geotechnics, Benevento (BN), Italy.

Coll A., Ribó R., Pasenau M., Escolano E., Perez J.S., Melendo A., Monros A. and Gárate J. (2018). GiD v.14 User Manual (pdf). (accessed 2020 May 25). www.gidhome.com.

d'Onofrio A., Santucci de Magistris F. and Sica S. (2004). Studies on the seismic zonation of the city of Benevento. In: The many facets of seismic risk – Multidisciplinary approach to the seismic risk problem, p. 125-133. CRDC - AMRA Università degli Studi di Napoli Federico II.

d'Onofrio A., Vitone C., Cotecchia F., Puglia R., Santucci de Magistris F. and Silvestri F. (2009). Geotechnical Characterization of the San Giuliano di Puglia subsoil (in Italian). In Rivista Italiana di Geotecnica (Italian Geotechnical Journal) 3, 43 –61.

DISS Working Group (2018). Database of Individual Seismogenic Sources (DISS), Version 3.2.1: A compilation of potential sources for earthquakes larger than M 5.5 in Italy and surrounding areas.http://diss.rm.ingv.it/diss/, Istituto Nazionale di Geofisica e Vulcanologia; DOI:10.6092/INGV.IT-DISS3.2.1.

Dolce M., Masi A., Samela C., Santarsiero G., Vona M., Zuccaro G., Cacace F. and Papa F. (2004). Analysis of the typological and damage features of the building heritage in San Giuliano di Puglia (in Italian). XI National Conference "L'ingegneria Sismica in Italia", ANIDIS, Rome.

Fabbrocino S., Lanzano G., Forte G., Santucci de Magistris F. and Fabbrocino G. (2015). SPT blow count vs. shear wave velocity relationship in the structurally complex formations of the Molise Region (Italy). Engineering Geology 187, 84-97.

Fierro T., Mignelli L., Scasserra G., Pagliaroli A. and Santucci de Magistris F. (2019). Key role of soil investigation and monitoring for the assessment of site effects for the village of San Giuliano di Puglia (CB), Italy. In VII International Conference on Earthquake Geotechnical Engineering, Rome, Italy, paper n.10120.

Fierro T., Mignelli L., Scasserra G., Pagliaroli A. and Santucci de Magistris F. (2020a). The use of seismic records for updating the geotechnical model for a site in

San Giuliano di Puglia (Italy). VI CNRIG Italian Conference of Researchers in Geotechnical Engineering, Lecco, Italy, July 2019.

Fierro T., Mignelli L., Scasserra G., Pagliaroli A. and Santucci de Magistris F. (2020b). Updating the Site Response Analyses at San Giuliano di Puglia (CB), Italy. Italian Geotechnical Journal, 2020(4), pp. 5-40.

Fierro T., Durante M.G., Castiglia M. and Santucci de Magistris F. (2022). Effects of local soil conditions on the seismic response of the historical area in San Giuliano di Puglia (Italy). From: Proceedings of Third international symposium on Geotechnical Engineering for the Preservation of Monuments and Historic Sites, TC301. Naples, June 22-24, 2022. (in print)

Forte G., Fabbrocino S., Fabbrocino G., Lanzano G., Santucci de Magistris F. and Silvestri F. (2017). A geolithological approach to seismic site classification: an application to the Molise Region (Italy). Bull Earthquake Eng (2017) 15: 175. https://doi.org/10.1007/s10518-016-9960-1.

Giaccio B., Ciancia S., Messina P., Pizzi A., Saroli M., Sposato A., Cittadini A., Di Donato V., Esposito P. and Galadini F. (2004). Geological-geomorphological features and site effects in San Giuiano di Puglia (CB) and in the villages hit by the seismic sequence of October-November 2002 (in Italian). Il Quaternario, 17(1), Ed. Aiqua, pagg. 83-99.

Hudson M.B., Beikae M. and Idriss I.M. (1994). QUAD4M, a Computer Program to Evaluate the Seismic Response of Soil Structures Using Finite Element Procedures and Incorporating a Compliant Base. Center for Geotechnical Modeling, Department of Civil and Environmental Engineering, University of California, Davis.

Joyner W.B. and Chen A.T.F. (1975). Calculation of nonlinear ground response in earthquakes, Bull. Seism. Soc. Am., 65, 1315-1336.

Kottke A.R., Wang X. and Rathje E.M. (2013). Technical Manual for Strata. Geotechnical Engineering Center Department of Civil, Architectural, and Environmental Engineering, University of Texas.

Lanzo G. and Pagliaroli A. (2009). Numerical Modeling of Site Effects at San Giuliano di Puglia (Southern Italy) during the 2002 Molise Seismic Sequence. J. of Geotech. and Geoenviron. Eng., ASCE.

Luzi L., Puglia R., Russo E. and ORFEUS WG5 (2016). Engineering Strong Motion Database, version 1.0. Istituto Nazionale di Geofisica e Vulcanologia, Observatories & Research Facilities for European Seismology. doi: 10.13127/ESM

Lysmer J. and Kuhlemeyer R.L. (1969). Finite dynamic model for infinite media. Journal of the Engineering Mechanics Division, ASCE, 95(EM4):859-877.

McGann C.R., Arduino P. and Mackenzie-Helnwein P. (2012). Stabilized single-point 4-node quadrilateral element for dynamic analysis of fluid saturated porous media. Acta Geotechnica 7 (4), 297-311.

McKenna F. and Fenves G.L. (2008). Using the OpenSees Interpreter on Parallel Computers. Network for Earthquake Engineering Simulations (NEES) TN-2007-16. UC Berkeley.

McKenna F., Fenves G. L., Scott M. H. and Jeremic B. (2000). Open system for earthquake engineering simulation. http:// opensees.berkeley.edu.

Molise Region, Working Group MS (2003). Guidelines for the Seismic Microzonation of the villages of the Campobasso Province with particular attention to those hit by the October 31st, 2002 Earthquake (in Italian). C. D. n.14/2003.

NTC (2008). Technical Codes for Constructions (in Italian). DM 14 gennaio 2008, Gazzetta Ufficiale, n. 30 del 4 febbraio 2008, Istituto Poligrafico e Zecca dello Stato, Roma.

NTC (2018). Technical Codes for Constructions (in Italian). DM 17 gennaio 2018, Gazzetta Ufficiale, n. 42 del 20 febbraio 2018, Supplemento Ordinario n.8, www.cslp.it, Istituto Poligrafico e Zecca dello Stato, Roma.

OPCM 3274 (2003). First elements for the definition of the general criteria for the seismic classification of the national territory and for the technical codes for constructions in seismic areas (in Italian). Gazzetta Ufficiale della Repubblica Italiana, n. 105-8/5/03.

OPCM 3519 (2006). General criteria for the definition of the seismic areas and for the the updating of the lists for the same areas (in Italian). Gazzetta Ufficiale della Repubblica Italiana, n. 108-11/5/06.

Pacor F., Paolucci R., Luzi L., Sabetta F., Spinelli A., Gorini A., Nicoletti M., Marcucci S., Filippi V. and Dolce M. (2011). Overview of the Italian strong-motion database ITACA 1.0. Bull Earthq Eng 9(6):1723–1739. https://doi.org/10.1007/s10518-011-9327-6.

Paolucci R., Pacor F., Puglia R., Ameri G., Cauzzi C. and Massa M. (2011). Record processing in ITACA, the new Italian strong-motion database. In: Akkar S, Gulkan P, van Eck T (eds) Chapter 8 of the book earthquake data in engineering seismology—predictive models, data management and networks. ISBN: 978-94-007-0151-9 (printed version) 978-94-007-0152-6 (E-book version). Geotechnical, geological, and earthquake engineering, vol 14, Springer, Netherlands.

Power M., Chiou B., Abrahamson N., Bozorgnia Y., Shantz T. and Roblee C. (2008). An overview of the NGA project. Earthq Spectra 24(1):3–21.

Puglia R. (2008). Analysis of the seismic response of San Giuliano di Puglia (in Italian). Ph.D. Thesis in Geotechnical Engineering, University of Calabria.

Puglia R., Klin P., Pagliaroli A., Ladina C., Priolo E., Lanzo G. and Silvestri F. (2009). Analysis of the site response of San Giuliano di Puglia with 1D, 2D and 3D models (in Italian). Rivista Italiana di Geotecnica (Italian Geotechnical Journal), Pagg. 62-71.

Puglia R., Lanzo G., Pagliaroli A., Sica S. and Silvestri F. (2007). Ground motion amplification in San Giuliano di Puglia (Southern Italy) during the 2002 Molise earthquake. In IV International Conference on Earthquake Geotechnical Engineering, Thessaloniki, Greece, paper no. 1611.

Puglia R., Russo E., Luzi L., D'Amico M., Felicetta C., Pacor F. and Lanzano G. (2018). Strong-motion processing service: a tool to access and analyse earthquakes strong-motion waveforms. Bull Earthquake Eng 16, 2641–2651. https://doi.org/10.1007/s10518-017-0299-z.

Puglia R., Vona M., Klin P., Ladina C., Masi A., Priolo E. and Silvestri F. (2013). Analysis of site response and building damage distribution induced by the 31 October 2002 earthquake at San Giuliano di Puglia (Italy). Earthquake Spectra, 29(2):497-526. doi: 10.1193/1.4000134.

Rathje E., Dawson C. Padgett J.E., Pinelli J.-P., Stanzione D., Adair A., Arduino P., Brandenberg S.J., Cockerill T., Dey C., Esteva M., Haan Jr. F.L., Hanlon M., Kareem A., Lowes L., Mock S. and Mosqueda G. (2017). DesignSafe: A New Cyberinfrastructure for Natural Hazards Engineering, ASCE Natural Hazards Review, doi:10.1061/(ASCE) NH.1527-6996.0000246.

Sanò T., Bongiovanni G., Clemente P., and Rinaldis D. (2015). Modelling of local effects based on accelerometric recordings at the site (in Italian). In ANIDIS 2015 – XVI Convegno.

Santucci de Magistris F., d'Onofrio A., Penna A., Puglia R. and Silvestri F. (2014). Lessons learned from two case histories of seismic microzonation in Italy. Nat. Hazards, 74, 2005–2035.

Silvestri F., Vitone C., d'Onofrio A., Cotecchia F., Puglia R. and Santucci de Magistris F. (2006). The influence of meso-structure on the mechanical behaviour of a marly clay from low to high strains. In Symposium to celebrate Prof. Tatsuoka's 60th birthday, Roma, Italy.

Vona M., Puglia R., Masi A. and Silvestri F. (2009). Comparison between the observed damage on the buildings in San Giuliano di Puglia after the 2002 Earthquake and the estimated damage on the basis of different models for the definition of the seismic input (in Italian). In Rivista Italiana di Geotecnica (Italian Geotechnical Journal), 72 – 82.

Working Group MPS (2004). Development of the seismic hazard map required by OPCM 3274 of March, 20th, 2003 (in Italian). Final report for the Department of Civil Protection, INGV, Milan-Rome, April 2004, 65 pp. + 5 annexes.

Working Group MS (2008). Addresses and criteria for the seismic microzonation (in Italian). Conference of the Italian Regions and Provinces – Department of Civil Protection, Rome, 3 vol. e Dvd.

Yang, Z., Lu J. and Elgamal, A. (2008). OpenSees Soil Models and Solid-Fluid Fully Coupled Elements. User's Manual. v1.0. Department of Structural Engineering, University of California, San Diego.

8 CONCLUSIONS AND FURTHER DEVELOPMENTS

A reliable numerical modelling in Geotechnical Earthquake Engineering, particularly when considering the local seismic response, poses its basis on different features: a solid constitutive framework to model soil behaviour, a widely tested software platform, and a proper definition of the geometry of the problem under analysis.

The constitutive modelling of soils, mainly when high strain levels are mobilized and under undrained conditions, is still an open issue and the researchers have proposed different solutions over the years to try to describe mathematically the response of soils, even when liquefaction is reached. A practical aspect that a constitutive framework should satisfy to be effective deals with the simplicity of its mathematical formulation and with the explicit physical meaning of the constitutive parameters that render the model suitable to be adopted in numerical codes. In addition, codes developed for research purposes, such as OpenSees, used in this research, are generally overlooked by practitioners for their complexity, as compared with commercial codes. In this framework, the thesis can be viewed as a summary for the users that would like to afford the arduous tasks to implement and use advanced constitutive models in OpenSees.

Some interesting aspects emerged from the development of the thesis.

Firstly, the constitutive model proposed by Papadimitriou and Bouckovalas (2002), due to its peculiarities in simulating the nonlinear hysteretic response of sands at low strain level, together with the possibility to account for fabric orientation with a scalar index, has successfully been implemented in OpenSees. The comparison with a wide range of element tests has shown an excellent agreement, in terms of stress paths and hysteretic loops. In particular, drained and undrained direct simple shear tests and triaxial tests have been simulated, even using different finite elements. The simulations reported in the original works of the Authors have been correctly and satisfactorily reproduced. Then, the response is evaluated also under monotonic loadings at the element level;

different integration schemes have been checked and the ability of the model to reproduce the modulus reduction curve of certain sand generated valuable results.

Overall, the implementation of the model in OpenSees can be considered acceptable, and this provides an additional tool for the OpenSees users when a constitutive platform to model behaviour of liquefiable soils is required. In addition, the capability of OpenSees to add a complex bounding surface constitutive model in the framework is highlighted.

The next step of the research in this sense will be oriented towards other applications using the constitutive model NTUASand02, to strengthen the implementation of the code in order to make it available to all the OpenSees users. In addition, the implementation of the code can also be adopted to introduce the slight modifications to the constitutive platform provided by Andrianopoulos et al. (2010), with a view to showing the difference with the 2002 version of the model.

A key role in the implementation of an advanced numerical model in a software framework is played by the integration schemes: in general, most constitutive frameworks work well for simple scenarios but have problems when used in large models (crashing analysis or taking unacceptable computational time because of the dimension of the domain). Schemes that can be used in large models become obsolete very quickly. To this aim, future developments of the work can be even oriented towards the implementation of more robust and efficient schemes, both implicit or semi-explicit (e.g., Backward Euler and cutting plane).

Generally speaking, the model has revealed its capability to simulate the response of a 20 m-thick soil column of Nevada sand in undrained and drained conditions under moderate input with PGA=0.104 g and in drained conditions with an input whose PGA is 0.345g. The good accordance among the different models, evaluated in terms of acceleration and displacement time series, hysteretic loops, strain and PGA profiles, and, in undrained conditions, even considering excess pore water pressure ratios to monitor soil liquefaction, can be considered satisfactory. This also strengthens the slight modification of the model constants to fit the state parameter profile. Overall, the advantages of the NTUASand02 constitutive model with respect to the other models

consist in its ability to simulate a more realistic behaviour of sands in the low-strain range, if compared to SANISAND. Furthermore, its three-dimensional formulation renders it more versatile if compared to PM4SAND. However, the latter requires less parameters to be calibrated.

Based on the Author's knowledge, the constitutive framework NTUASand02 has never been implemented in a numerical code to conduct fully-coupled analyses for boundary value problems. Overall, the potential sources of error will be carefully investigated in further developments of the research, and some sensitivity analyses of the soil column considering both constitutive parameters and column height will be conducted, mainly exploiting the HPC resources provided by the DesignSafe Cyber-Infrastructure or elsewhere.

The analysis of the two case-studies conducted in this thesis highlighted once more the capabilities of OpenSees to simulate complex problems in terms of the constitutive behaviour of soils (i.e., providing advanced constitutive frameworks) and in the numerical solution of complicated domains (i.e., the analysis of large models and strictly multi-dimensional geometries resolved in an acceptable computational time). In particular, the simulation of centrifuge tests, using PM4SAND and exploiting calibrated parameters available in the literature for Ticino sand, revealed very good accordance in terms of comparison between recorded and simulated acceleration time series. However, non-neglectable differences arise when the excess pore water pressure response is observed. These discrepancies can be due to different factors, such as initial conditions of the soil in terms of groundwater table depth, permeability and sensor positions after shaking. These aspects are always very difficult to detect, and a back analysis could be extremely useful to understand their influence on the results. In this sense, it would be extremely interesting evaluating the response considering SANISAND and NTUASand02 constitutive models. However, proper calibration of the constitutive parameters is required and, with reference to the Ticino sand, the tests needed for the calibration are not completely available. Furthermore, it is worth noting that PM4SAND has been adopted due to the possibility to calibrate only 4 parameters and taking advantage of the correlations between the former and the other constants.

On the contrary, with reference to SANISAND and NTUASand02, there is a greater number of parameters that need to be calibrated.

Then, the simulation of the seismic response of the San Giuliano di Puglia basin was conducted in order to understand whether a nonlinear advanced constitutive model exploiting the multi-surface theory together with the use of the OpenSees numerical framework would confirm the previous findings in terms of both buried morphology and soil stiffness of the valley. Therefore, the analysis has been conducted in a relatively brief computational time only by the use of the parallel module of OpenSees (OpenSeesSP) and its implementation onto the DesignSafe Cyber Infrastructure.

The analyses of the basin have inferred a very good performance of the implemented model compared to the recorded data. In fact, the small town experienced the 2002 earthquake, and a strongly non-uniform damage distribution was observed: the historical core of the town was hit by limited damage, while the newly built area was characterized by significant structural collapses, and this was related to amplification effects. Even if a wide number of tests was available, the bi-dimensional model of the valley together with the stiffness of the layers has been continuously re-evaluated. In the study, the model exploited in the latest analyses was adopted and the simulated data have been compared to the accelerograms obtained by the seismic network of the town. Good accordance has been observed in terms of simulated PGA, while the better congruence is obtained at the station installed below the historical core of the town (where the SGMA station was installed). A slight overestimation of the recorded data in terms of time series has been encountered along with the vertical corresponding to the newly built area (location of the SGPA vertical array).

Furthermore, even the response in terms of amplification factor profiles along both the verticals can be considered consistent with the damage distribution observed after the 2002 Molise Earthquake. Strong amplification effects were estimated along the SGPA vertical, with AF that reaches values ranging from 3 to 4 on the surface, while a slight amplification took place along the SGMA vertical on the surface (AF=1.20) and slight deamplification effects were encountered at the higher depths. The latter finding can

be connected to the interaction between the buried morphology of the clayey soils and the bedrock.

This study is also oriented towards the comparison between the response obtained with the pressure-independent multi-yield model and the use of linear elastic behaviour of soils. No difference arose, highlighting that a key role is played by the buried morphology and to the strictly bi-dimensionality of the problem under study. Here, the use of vertical array recordings was of vital importance, and their use was essential to validate the numerical model. In addition, the large number of tests made the definition of the constitutive parameters relatively easy.

Finally, the calibrated model can be adopted in further research developments oriented towards microzonation studies with the application of more severe input excitations and to the calibration of more advanced bounding surface constitutive models (e.g., Bounding Cam-Clay, PM4Silt), exploiting the large amount of available data. Furthermore, the multiple parallel OpenSees interpreter, conceived to carry out parametric analysis of large models, namely OpenSeesMP implemented on the DesignSafe platform, can be exploited to apply different inputs to the model and to vary constitutive parameters.

This thesis, once the calibration and the use of constitutive models in the platform OpenSees was completed, paved the way to the use of this system in the advanced simulations of a large variety of problems that interest the research in structural and geotechnical engineering. Such problems can be analysed taking the advantage of the enormeous computational ability of the software. Worth mentioning, for instance, the study of the lifelines, the seismic response of large areas, using HPC and parallel computation, the analysis of a series of civil problems of soil-structure interaction.

APPENDIX A. DERIVATIVES OF THE CONSTITUTIVE EQUATIONS TO INTEGRATE AN IMPLICIT METHOD

The selection of the Modified Euler integration scheme for the implementation of the NTUASand02 constitutive model in OpenSees has been performed after checking different integration techniques. In this framework, the Backward Euler scheme, widely described in Ghofrani (2018) for SANISAND, has been implemented, but no reliable results have been achieved. Worth noticing that the latter is an implicit method, and, for this reason, the output solution is automatically consistent not requiring a stress correction. However, this can be guaranteed at the cost of some additional derivatives that are reported in the following. It must be emphasized that future developments of this work can consist in the implementation of additional integration schemes and these derivatives can be useful for the purpose.

In order to compare the response obtained using different integration strategies, the structure of the Backward Euler integration scheme has been implemented for the NTUASand02 constitutive model as made in Ghofrani (2018) for the SANISAND constitutive model.

In such a scheme, given a strain increment and assuming a fully elastic trial stress, the vector of residuals ($\mathbf{R_1}$, $\mathbf{R_2}$, $\mathbf{R_3}$ and $\mathbf{R_4}$) is built to start Newton iterations to find the state at which residual vector is zero as in Ortiz and Simo (1986), and as it is shown in (A.1), (A.2), (A.3) and (A.4).

$$\mathbf{R_1} = \boldsymbol{\varepsilon}^{\mathbf{e}} - \boldsymbol{\varepsilon}^{\mathbf{e}}_{\mathbf{tr}} + \Lambda \cdot \mathbf{R} \tag{A.1}$$

$$\mathbf{R_2} = \boldsymbol{\alpha} - \boldsymbol{\alpha}_{\mathbf{cur}} - \Lambda \cdot \bar{\boldsymbol{\alpha}} \tag{A.2}$$

APPENDIX A.

$$\mathbf{R_3} = \mathbf{F} - \mathbf{F_{cur}} - \Lambda \cdot \bar{\mathbf{F}} \tag{A.3}$$

$$\mathrm{R}_4 = \mathrm{f}(\boldsymbol{\sigma}, \boldsymbol{\alpha}) \tag{A.4}$$

where $\bar{\boldsymbol{\alpha}}$ and $\bar{\mathbf{F}}$ are defined by (A.5) and (A.6):

$$\bar{\boldsymbol{\alpha}} = \mathrm{h_b} \cdot \mathrm{h_f} \cdot \left(\boldsymbol{\alpha^b} - \boldsymbol{\alpha}\right) \tag{A.5}$$

$$\bar{\mathbf{F}} = \mathrm{H}(\mathrm{D}\mathbf{I} - \langle -\mathrm{D}\rangle(\mathrm{C}\mathbf{n} + \mathbf{f})) \tag{A.6}$$

Then, the derivatives required for all the quantities are calculated in the following. The derivative of the yield function can be split as in (A.7):

$$\frac{\mathrm{df}}{\mathrm{d}\boldsymbol{\sigma}} = \frac{\partial \mathrm{f}}{\partial \mathbf{s}} + \frac{\partial \mathrm{f}}{\partial \mathrm{p}}\frac{\mathbf{I}}{3} = \mathbf{L} \tag{A.7}$$

and

$$\frac{\partial \mathrm{f}}{\partial \mathbf{s}} = \frac{(\mathbf{s} - \mathrm{p}\boldsymbol{\alpha})}{\sqrt{(\mathbf{s} - \mathrm{p}\boldsymbol{\alpha}) : (\mathbf{s} - \mathrm{p}\boldsymbol{\alpha})}} = \mathbf{n} \tag{A.8}$$

$$\frac{\partial \mathrm{f}}{\partial \mathrm{p}} = -\boldsymbol{\alpha} : \frac{(\mathbf{s} - \mathrm{p}\boldsymbol{\alpha})}{\sqrt{(\mathbf{s} - \mathrm{p}\boldsymbol{\alpha}) : (\mathbf{s} - \mathrm{p}\boldsymbol{\alpha})}} - \sqrt{\frac{2}{3}}\mathrm{m} = -\boldsymbol{\alpha} : \mathbf{n} - \sqrt{\frac{2}{3}}\mathrm{m} \tag{A.9}$$

that yields

$$\frac{\partial \mathrm{f}}{\partial \boldsymbol{\sigma}} = \mathbf{n} + \left(-\boldsymbol{\alpha} : \mathbf{n} - \sqrt{\frac{2}{3}}\mathrm{m}\right)\frac{\mathbf{I}}{3} = \mathbf{n} - \frac{\mathrm{V}}{3}\mathbf{I} \tag{A.10}$$

Defining the norm as in (A.11),

APPENDIX A.

$$\|\mathbf{s}-\mathrm{p}\boldsymbol{\alpha}\| = \sqrt{(\mathbf{s}-\mathrm{p}\boldsymbol{\alpha}):(\mathbf{s}-\mathrm{p}\boldsymbol{\alpha})} \tag{A.11}$$

the derivative of the normal to the yield surface with respect to $\boldsymbol{\alpha}$ is (A.12):

$$\frac{\partial \mathbf{n}}{\partial \boldsymbol{\alpha}} = \frac{(-\mathrm{p}\mathbf{I}+\mathrm{p}\mathbf{n}\cdot\mathbf{n})}{\|\mathbf{s}-\mathrm{p}\boldsymbol{\alpha}\|} = \frac{\mathrm{p}(\mathbf{n}\cdot\mathbf{n}-\mathbf{I})}{\|\mathbf{s}-\mathrm{p}\boldsymbol{\alpha}\|} \tag{A.12}$$

The derivative of the normal to the yield surface with respect to $\boldsymbol{\sigma}$ is reported in (A.13):

$$\frac{\partial \mathbf{n}}{\partial \boldsymbol{\sigma}} = \frac{\partial \mathbf{n}}{\partial \mathbf{s}} + \frac{\partial \mathbf{n}}{\partial \mathrm{p}}\frac{\mathbf{I}}{3} \tag{A.13}$$

where

$$\frac{\partial \mathbf{n}}{\partial \mathbf{s}} = \frac{(\mathbf{I}-\mathbf{n}\cdot\mathbf{n})}{\|\mathbf{s}-\mathrm{p}\boldsymbol{\alpha}\|} \tag{A.14}$$

$$\frac{\partial \mathbf{n}}{\partial \mathrm{p}} = \frac{(\boldsymbol{\alpha}:\mathbf{n}\cdot\mathbf{n}-\boldsymbol{\alpha})}{\|\mathbf{s}-\mathrm{p}\boldsymbol{\alpha}\|} \tag{A.15}$$

$$\frac{\partial \mathbf{n}}{\partial \boldsymbol{\sigma}} = \frac{(\mathbf{I}-\mathbf{n}\cdot\mathbf{n})}{\|\mathbf{s}-\mathrm{p}\boldsymbol{\alpha}\|} + \frac{\boldsymbol{\alpha}:\mathbf{n}\cdot\mathbf{n}-\boldsymbol{\alpha}}{\|\mathbf{s}-\mathrm{p}\boldsymbol{\alpha}\|}\frac{\mathbf{I}}{3} = \frac{\mathbf{I}-\frac{\mathbf{I}}{3}\boldsymbol{\alpha}-\mathbf{n}\cdot\mathbf{n}+\frac{\mathbf{I}}{3}(\boldsymbol{\alpha}:\mathbf{n})\cdot\mathbf{n}}{\|\mathbf{s}-\mathrm{p}\boldsymbol{\alpha}\|} \tag{A.16}$$

With reference to the state parameter ψ, it is a function of $\boldsymbol{\sigma}$, so its derivative is (A.17):

$$\frac{\partial \psi}{\partial \boldsymbol{\sigma}} = \frac{\lambda \mathbf{I}}{3\mathrm{p}} \tag{A.17}$$

Furthermore, the derivative of the elastic strain rate direction **R** is required with respect to $\boldsymbol{\sigma}$ and $\boldsymbol{\alpha}$. For this reason, some other derivatives need to be calculated, such as:

$$\frac{\partial \mathrm{d}^{\mathrm{d}}}{\partial \boldsymbol{\sigma}} = \frac{\partial\left(\boldsymbol{\alpha}^{\mathbf{d}}-\boldsymbol{\alpha}\right)}{\partial \boldsymbol{\sigma}}\mathbf{n} + \left(\boldsymbol{\alpha}^{\mathbf{d}}-\boldsymbol{\alpha}\right)\frac{\partial \mathbf{n}}{\partial \boldsymbol{\sigma}} \tag{A.18}$$

where

$$\frac{\partial\left(\boldsymbol{\alpha}^{\mathbf{d}}-\boldsymbol{\alpha}\right)}{\partial\boldsymbol{\sigma}}=\frac{\partial\boldsymbol{\alpha}^{\mathbf{d}}}{\partial\boldsymbol{\sigma}} \tag{A.19}$$

Recalling that the stress ratio tensor is:

$$\bar{\mathbf{r}}=\mathbf{r}-\boldsymbol{\alpha} \tag{A.20}$$

The derivatives of this parameter are required with respect to $\boldsymbol{\sigma}$ and $\boldsymbol{\alpha}$, such as:

$$\frac{\partial\bar{\mathbf{r}}}{\partial\boldsymbol{\sigma}}=\frac{\partial\bar{\mathbf{r}}}{\partial\mathbf{s}}+\frac{\partial\bar{\mathbf{r}}}{\partial\mathrm{p}}\frac{\mathbf{I}}{3} \tag{A.21}$$

$$\frac{\partial\bar{\mathbf{r}}}{\partial\mathbf{s}}=\frac{\partial(\mathbf{r}-\boldsymbol{\alpha})}{\partial\mathbf{s}}=\frac{\partial\left(\frac{\mathbf{s}}{\mathrm{p}}-\boldsymbol{\alpha}\right)}{\partial\mathbf{s}}=\frac{\mathbf{I}}{\mathrm{p}} \tag{A.22}$$

$$\frac{\partial\bar{\mathbf{r}}}{\partial\mathrm{p}}=\frac{\partial(\mathbf{r}-\boldsymbol{\alpha})}{\partial\mathrm{p}}=\frac{\partial\left(\frac{\mathbf{s}}{\mathrm{p}}-\boldsymbol{\alpha}\right)}{\partial\mathrm{p}}=(-1)\left(\frac{\mathbf{s}}{\mathrm{p}^{2}}\right) \tag{A.23}$$

$$\frac{\partial(\mathbf{r}-\boldsymbol{\alpha})}{\partial\boldsymbol{\sigma}}=\frac{\mathbf{I}}{\mathrm{p}}-\frac{\mathbf{r}}{3\mathrm{p}}=\frac{1}{\mathrm{p}}\left(\mathbf{I}-\frac{\mathbf{r}}{3}\right) \tag{A.24}$$

$$\frac{\partial(\mathbf{r}-\boldsymbol{\alpha})}{\partial\boldsymbol{\alpha}}=-\mathbf{I} \tag{A.25}$$

Then, the derivatives of the invariants can be calculated as:

$$\frac{\partial\bar{\mathrm{J}}_{2}}{\partial\boldsymbol{\sigma}}=\frac{1}{2}\left(\frac{1}{\mathrm{p}}\left(\mathbf{I}-\frac{\mathbf{r}}{3}\right)(\mathbf{r}-\boldsymbol{\alpha})\right) \tag{A.26}$$

$$\frac{\partial\bar{\mathrm{J}}_{3}}{\partial\boldsymbol{\sigma}}=\frac{1}{3}(\bar{\mathbf{r}}\cdot\bar{\mathbf{r}})\frac{1}{\mathrm{p}} \tag{A.27}$$

APPENDIX A.

$$\frac{\partial \bar{J}_2}{\partial \boldsymbol{\alpha}} = \left(-\mathbf{I}(\mathbf{r} - \boldsymbol{\alpha})\right) \tag{A.28}$$

$$\frac{\partial \bar{J}_3}{\partial \boldsymbol{\alpha}} = \frac{1}{3}(\bar{\mathbf{r}} \cdot \bar{\mathbf{r}})(-\mathbf{I}) \tag{A.29}$$

Furthermore, the derivative of cos3θ with respect to $\boldsymbol{\sigma}$ and $\boldsymbol{\alpha}$ are

$$\frac{\partial \cos 3\theta}{\partial \boldsymbol{\sigma}} = \frac{\frac{3\sqrt{3}}{2}\left(\frac{\partial \bar{J}_3}{\partial \boldsymbol{\sigma}} \bar{J}_2^{\frac{3}{2}} - \frac{3}{2}\bar{J}_3 \bar{J}_2^{0.5} \frac{\partial \bar{J}_2}{\partial \boldsymbol{\sigma}}\right)}{\bar{J}_2^3} \tag{A.30}$$

$$\frac{\partial \cos 3\theta}{\partial \boldsymbol{\alpha}} = \frac{\frac{3\sqrt{3}}{2}\left(\frac{\partial \bar{J}_3}{\partial \boldsymbol{\alpha}} \bar{J}_2^{\frac{3}{2}} - \frac{3}{2}\bar{J}_3 \bar{J}_2^{0.5} \frac{\partial \bar{J}_2}{\partial \boldsymbol{\alpha}}\right)}{\bar{J}_2^3} \tag{A.31}$$

In the following, the derivatives of $M_{c,e}^{b,d}$ are reported. Being the latter dependent on $\boldsymbol{\sigma}$ only, consequently, the derivative with respect to $\boldsymbol{\sigma}$ is required. In particular, the Heaviside function centered in 0 is defined as follows (A.32):

$$\Xi(x) = \begin{cases} 1 \text{ for } x > 0 \\ 0 \text{ for } x \leq 0 \end{cases} \tag{A.32}$$

This is required in order to define the derivative of the argument of the Macauley brackets. In particular:

$$\frac{\partial M_e^b}{\partial \boldsymbol{\sigma}} = k_e^b \cdot \Xi(-\psi)\left(-\frac{\partial \psi}{\partial \boldsymbol{\sigma}}\right) \tag{A.33}$$

$$\frac{\partial M_e^d}{\partial \boldsymbol{\sigma}} = k_e^d \frac{\partial \psi}{\partial \boldsymbol{\sigma}} \tag{A.34}$$

APPENDIX A.

$$\frac{\partial M_c^d}{\partial \boldsymbol{\sigma}} = k_c^d \frac{\partial \psi}{\partial \boldsymbol{\sigma}} \tag{A.35}$$

Then, the derivative of $c^{b,d}$ is (A.36):

$$\frac{\partial c^{b,d}}{\partial \boldsymbol{\sigma}} = \frac{\frac{\partial M_e^{b,d}}{\partial \boldsymbol{\sigma}} M_c^{b,d} - M_e^{b,d} \frac{\partial M_c^{b,d}}{\partial \boldsymbol{\sigma}}}{\left(M_c^{b,d}\right)^2} \tag{A.36}$$

Furthermore, the derivatives of $g(\cos 3\theta, c)$ and $g(-\cos 3\theta, c)$ are obtained considering that $\cos 3\theta = -\cos 3(\theta + \pi)$.

$$\begin{aligned} \frac{\partial g(\cos 3\theta, c^{b,d})}{\partial \boldsymbol{\sigma}} = & \frac{2\frac{\partial c^{b,d}}{\partial \boldsymbol{\sigma}}\left[\frac{1+c^{b,d}}{2} - \frac{1-c^{b,d}}{2}\cos 3\theta\right]}{\left[\frac{1+c^{b,d}}{2} - \frac{1-c^{b,d}}{2}\cos 3\theta\right]^2} + \\ & - \frac{2c^{b,d}\left[\frac{1}{2}\frac{\partial c^{b,d}}{\partial \boldsymbol{\sigma}} + \left(\frac{1}{2}\frac{\partial c^{b,d}}{\partial \boldsymbol{\sigma}}\cos 3\theta - \frac{1-c^{b,d}}{2}\frac{\partial \cos 3\theta}{\partial \boldsymbol{\sigma}}\right)\right]}{\left[\frac{1+c^{b,d}}{2} - \frac{1-c^{b,d}}{2}\cos 3\theta\right]^2} + \\ & - \left[\frac{1}{2}\frac{\partial c^{b,d}}{\partial \boldsymbol{\sigma}} - \frac{1}{2}\frac{\partial c^{b,d}}{\partial \boldsymbol{\sigma}}\cos 3\theta + \frac{1-c^{b,d}}{2}\frac{\partial \cos 3\theta}{\partial \boldsymbol{\sigma}}\right] \end{aligned} \tag{A.37}$$

$$\frac{\partial g(\cos 3\theta, c^c)}{\partial \boldsymbol{\sigma}} = \frac{2c^c}{\left[\frac{1+c^c}{2} - \frac{1-c^c}{2}\cos 3\theta\right]^2}\left(-\frac{1-c^c}{2}\frac{\partial \cos 3\theta}{\partial \boldsymbol{\sigma}}\right) - \frac{1-c^c}{2}\frac{\partial \cos 3\theta}{\partial \boldsymbol{\sigma}} \tag{A.38}$$

$$\frac{\partial g(\cos 3\theta, c^{c,b,d})}{\partial \boldsymbol{\alpha}} = \frac{2c^{c,b,d}}{\left[\frac{1+c^{c,b,d}}{2} - \frac{1-c^{c,b,d}}{2}\cos 3\theta\right]^2}\left(-\frac{1-c^{c,b,d}}{2}\frac{\partial \cos 3\theta}{\partial \boldsymbol{\alpha}}\right) - \frac{1-c^{c,b,d}}{2}\frac{\partial \cos 3\theta}{\partial \boldsymbol{\alpha}} \tag{A.39}$$

APPENDIX A.

$$\frac{\partial g(-\cos 3\theta, c^{b,d})}{\partial \boldsymbol{\sigma}} = \frac{2\frac{\partial c^{b,d}}{\partial \boldsymbol{\sigma}} \cdot \left[\frac{1+c^{b,d}}{2} + \frac{1-c^{b,d}}{2}\cos 3\theta\right]}{\left[\frac{1+c^{b,d}}{2} + \frac{1-c^{b,d}}{2}\cos 3\theta\right]^2} +$$

$$- \frac{-2c^{b,d}\left[\frac{1}{2}\frac{\partial c^{b,d}}{\partial \boldsymbol{\sigma}} + \left(\frac{1}{2}\frac{\partial c^{b,d}}{\partial \boldsymbol{\sigma}}\cos 3\theta - \frac{1-c^{b,d}}{2}\frac{\partial \cos 3\theta}{\partial \boldsymbol{\sigma}}\right)\right]}{\left[\frac{1+c^{b,d}}{2} + \frac{1-c^{b,d}}{2}\cos 3\theta\right]^2} + \tag{A.40}$$

$$- \left[\frac{1}{2}\frac{\partial c^{b,d}}{\partial \boldsymbol{\sigma}} + \frac{1}{2}\frac{\partial c^{b,d}}{\partial \boldsymbol{\sigma}}\cos 3\theta - \frac{1-c^{b,d}}{2}\frac{\partial \cos 3\theta}{\partial \boldsymbol{\sigma}}\right]$$

$$\frac{\partial g(-\cos 3\theta, c^{c})}{\partial \boldsymbol{\sigma}} = \frac{2c^{c}}{\left[\frac{1+c^{c}}{2} + \frac{1-c^{c}}{2}\cos 3\theta\right]^2}\left(\frac{1-c^{c}}{2}\frac{\partial \cos 3\theta}{\partial \boldsymbol{\sigma}}\right) + \frac{1-c^{c}}{2}\frac{\partial \cos 3\theta}{\partial \boldsymbol{\sigma}} \tag{A.41}$$

$$\frac{\partial g(-\cos 3\theta, c^{c,b,d})}{\partial \boldsymbol{\alpha}} = \frac{2c^{c,b,d}}{\left[\frac{1+c^{c,b,d}}{2} + \frac{1-c^{c,b,d}}{2}\cos 3\theta\right]^2}\left(\frac{1-c^{c,b,d}}{2}\frac{\partial \cos 3\theta}{\partial \boldsymbol{\alpha}}\right) + \frac{1-c^{c,b,d}}{2}\frac{\partial \cos 3\theta}{\partial \boldsymbol{\alpha}} \tag{A.42}$$

Now, derivatives of $\alpha_{\theta}^{b,c,d}$ and $\alpha_{\theta+\pi}^{b,c,d}$ with respect to $\boldsymbol{\sigma}$ and $\boldsymbol{\alpha}$ can be easily obtained:

$$\frac{\partial \alpha_{\theta}^{b,d}}{\partial \boldsymbol{\sigma}} = \frac{\partial g(\cos 3\theta, c^{b,d})}{\partial \boldsymbol{\sigma}} M_c^{b,d} + g(\cos 3\theta, c^{b,d}) \frac{\partial M_c^{b,d}}{\partial \boldsymbol{\sigma}} \tag{A.43}$$

$$\frac{\partial \alpha_{\theta}^{c}}{\partial \boldsymbol{\sigma}} = M_c^{c} \frac{\partial g(\cos 3\theta, c^{c})}{\partial \boldsymbol{\sigma}} \tag{A.44}$$

$$\frac{\partial \alpha_{\theta}^{c,b,d}}{\partial \boldsymbol{\alpha}} = M_c^{c,b,d} \frac{\partial g(\cos 3\theta, c^{c,b,d})}{\partial \boldsymbol{\alpha}} \tag{A.45}$$

$$\frac{\partial \alpha_{\theta+\pi}^{b,d}}{\partial \boldsymbol{\sigma}} = \frac{\partial g(-\cos 3\theta, c^{b,d})}{\partial \boldsymbol{\sigma}} M_c^{b,d} + g(-\cos 3\theta, c^{b,d}) \frac{\partial M_c^{b,d}}{\partial \boldsymbol{\sigma}} \tag{A.46}$$

$$\frac{\partial \alpha_{\theta+\pi}^{c}}{\partial \boldsymbol{\sigma}} = M_c^{c} \frac{\partial g(-\cos 3\theta, c^{c})}{\partial \boldsymbol{\sigma}} \tag{A.47}$$

APPENDIX A.

$$\frac{\partial \alpha_{\theta+\pi}^{c,b,d}}{\partial \boldsymbol{\alpha}} = M_c^{c,b,d} \cdot \frac{\partial g(-\cos 3\theta, c^{c,b,d})}{\partial \boldsymbol{\alpha}} \tag{A.48}$$

while the derivatives of $\boldsymbol{\alpha}^{\mathbf{c,b,d}}$ are:

$$\frac{\partial \boldsymbol{\alpha}^{\mathbf{c,b,d}}}{\partial \boldsymbol{\sigma}} = \sqrt{\frac{2}{3}}\left(\frac{\partial \alpha_\theta^{c,b,d}}{\partial \boldsymbol{\sigma}}\mathbf{n} + \alpha_\theta^{c,b,d} \cdot \frac{\partial \mathbf{n}}{\partial \boldsymbol{\sigma}}\right) \tag{A.49}$$

$$\frac{\partial \boldsymbol{\alpha}^{\mathbf{c,b,d}}}{\partial \boldsymbol{\alpha}} = \sqrt{\frac{2}{3}}\left(\frac{\partial \alpha_\theta^{c,b,d}}{\partial \boldsymbol{\alpha}}\mathbf{n} + \alpha_\theta^{c,b,d}\frac{\partial \mathbf{n}}{\partial \boldsymbol{\alpha}}\right) \tag{A.50}$$

$$\frac{\partial\left(\boldsymbol{\alpha}^{\mathbf{c,b,d}} - \boldsymbol{\alpha}\right)}{\partial \boldsymbol{\sigma}} = \frac{\partial \boldsymbol{\alpha}^{\mathbf{c,b,d}}}{\partial \boldsymbol{\sigma}} \tag{A.51}$$

$$\frac{\partial\left(\boldsymbol{\alpha}^{\mathbf{c,b,d}} - \boldsymbol{\alpha}\right)}{\partial \boldsymbol{\alpha}} = \frac{\partial \boldsymbol{\alpha}^{\mathbf{c,b,d}}}{\partial \boldsymbol{\alpha}} - \mathbf{I} \tag{A.52}$$

Then, the derivatives of $d^{c,b,d}$ and D are calculated as:

$$\frac{\partial d^{c,b,d}}{\partial \boldsymbol{\sigma}} = \frac{\partial\left(\boldsymbol{\alpha}^{\mathbf{c,b,d}} - \boldsymbol{\alpha}\right)}{\partial \boldsymbol{\sigma}}\mathbf{n} + \left(\boldsymbol{\alpha}^{\mathbf{c,b,d}} - \boldsymbol{\alpha}\right)\frac{\partial \mathbf{n}}{\partial \boldsymbol{\sigma}} = \frac{\partial \boldsymbol{\alpha}^{\mathbf{c,b,d}}}{\partial \boldsymbol{\sigma}}\mathbf{n} + \left(\boldsymbol{\alpha}^{\mathbf{c,b,d}} - \boldsymbol{\alpha}\right)\frac{\partial \mathbf{n}}{\partial \boldsymbol{\sigma}} \tag{A.53}$$

$$\frac{\partial d^{c,b,d}}{\partial \boldsymbol{\alpha}} = \frac{\partial\left(\boldsymbol{\alpha}^{\mathbf{c,b,d}} - \boldsymbol{\alpha}\right)}{\partial \boldsymbol{\alpha}}\mathbf{n} + \left(\boldsymbol{\alpha}^{\mathbf{c,b,d}} - \boldsymbol{\alpha}\right)\frac{\partial \mathbf{n}}{\partial \boldsymbol{\alpha}} = \left(\frac{\partial \boldsymbol{\alpha}^{\mathbf{c,b,d}}}{\partial \boldsymbol{\alpha}} - \mathbf{I}\right)\mathbf{n} + \left(\boldsymbol{\alpha}^{\mathbf{c,b,d}} - \boldsymbol{\alpha}\right)\frac{\partial \mathbf{n}}{\partial \boldsymbol{\alpha}} \tag{A.54}$$

$$\frac{\partial D}{\partial \boldsymbol{\sigma}} = A_0 \frac{\partial d^d}{\partial \boldsymbol{\sigma}} \tag{A.55}$$

$$\frac{\partial D}{\partial \boldsymbol{\alpha}} = A_0 \frac{\partial d^d}{\partial \boldsymbol{\alpha}} \tag{A.56}$$

Now, the derivative of the normal to the plastic potential surface can be obtained:

APPENDIX A.

$$\frac{\partial \mathbf{R}}{\partial \boldsymbol{\sigma}} = \frac{\partial \mathbf{n}}{\partial \boldsymbol{\sigma}} + \frac{\partial \mathrm{D}}{\partial \boldsymbol{\sigma}} \frac{\mathbf{I}}{3} \tag{A.57}$$

$$\frac{\partial \mathbf{R}}{\partial \boldsymbol{\alpha}} = \frac{\partial \mathbf{n}}{\partial \boldsymbol{\alpha}} + \frac{\partial \mathrm{D}}{\partial \boldsymbol{\alpha}} \frac{\mathbf{I}}{3} \tag{A.58}$$

Furthermore, d^b_{ref} needs to be derivated with respect to $\boldsymbol{\sigma}$ and $\boldsymbol{\alpha}$:

$$\frac{\partial d^b_{ref}}{\partial \boldsymbol{\sigma}} = \sqrt{\frac{2}{3}} \left(\frac{\partial \alpha^b_\theta}{\partial \boldsymbol{\sigma}} + \frac{\partial \alpha^b_{\theta+\pi}}{\partial \boldsymbol{\sigma}} \right) \tag{A.59}$$

$$\frac{\partial d^b_{ref}}{\partial \boldsymbol{\alpha}} = \sqrt{\frac{2}{3}} \left(\frac{\partial \alpha^b_\theta}{\partial \boldsymbol{\alpha}} + \frac{\partial \alpha^b_{\theta+\pi}}{\partial \boldsymbol{\alpha}} \right) \tag{A.60}$$

Finally, h_b is required to obtain the derivatives of $\bar{\boldsymbol{\alpha}}$

$$\frac{\partial h_b}{\partial \boldsymbol{\sigma}} = h_0 \left[(\mu - 1) \left(\frac{p}{p_{atm}} \right)^{\mu-2} \frac{I}{3 p_{atm}} \frac{|d^b|}{\langle d^b_{ref} - |d^b| \rangle} \right] +$$

$$+ \left(\frac{p}{p_{atm}} \right)^{\mu-1} \left(\frac{\frac{|d^b|}{d^b} \frac{\partial d^b}{\partial \boldsymbol{\sigma}} \langle d^b_{ref} - |d^b| \rangle - |d^b| \Xi(d^b_{ref} - |d^b|) \left(\frac{\partial d^b_{ref}}{\partial \boldsymbol{\sigma}} - \frac{|d^b|}{d^b} \frac{\partial d^b}{\partial \boldsymbol{\sigma}} \right)}{\langle d^b_{ref} - |d^b| \rangle^2} \right) \tag{A.61}$$

$$\frac{\partial h_b}{\partial \boldsymbol{\alpha}} = h_0 \left[(\mu - 1) \left(\frac{p}{p_{atm}} \right)^{\mu-2} \frac{I}{3 p_{atm}} \frac{|d^b|}{\langle d^b_{ref} - |d^b| \rangle} \right] +$$

$$+ \left(\frac{p}{p_{atm}} \right)^{\mu-1} \left(\frac{\frac{|d^b|}{d^b} \frac{\partial d^b}{\partial \boldsymbol{\alpha}} \langle d^b_{ref} - |d^b| \rangle - |d^b| \Xi(d^b_{ref} - |d^b|) \left(\frac{\partial d^b_{ref}}{\partial \boldsymbol{\alpha}} - \frac{|d^b|}{d^b} \frac{\partial d^b}{\partial \boldsymbol{\alpha}} \right)}{\langle d^b_{ref} - |d^b| \rangle^2} \right) \tag{A.62}$$

and:

APPENDIX A.

$$\frac{\partial \bar{\boldsymbol{\alpha}}}{\partial \boldsymbol{\sigma}} = \mathrm{h_f}\left(\frac{\partial \mathrm{h_b}}{\partial \boldsymbol{\sigma}}\left(\boldsymbol{\alpha}^{\mathbf{b}} - \boldsymbol{\alpha}\right) + \mathrm{h_b}\left(\frac{\partial \boldsymbol{\alpha}^{\mathbf{b}}}{\partial \boldsymbol{\sigma}} - \mathbf{I}\right)\right) \tag{A.63}$$

$$\frac{\partial \bar{\boldsymbol{\alpha}}}{\partial \boldsymbol{\alpha}} = \mathrm{h_f}\left(\frac{\partial \mathrm{h_b}}{\partial \boldsymbol{\alpha}}\left(\boldsymbol{\alpha}^{\mathbf{b}} - \boldsymbol{\alpha}\right) + \mathrm{h_b}\left(\frac{\partial \boldsymbol{\alpha}^{\mathbf{b}}}{\partial \boldsymbol{\alpha}} - \mathbf{I}\right)\right) \tag{A.64}$$

Now, also the derivatives relative of the fabric tensor with respect to $\boldsymbol{\sigma}$ and $\boldsymbol{\alpha}$ can be written as:

$$\frac{\partial \bar{\mathbf{F}}}{\partial \boldsymbol{\sigma}} = \mathrm{H}\left(\frac{\partial \mathrm{D}}{\partial \boldsymbol{\sigma}}\mathbf{I} - \Xi(-\mathrm{D})\frac{\partial \mathrm{D}}{\partial \boldsymbol{\sigma}}(\mathrm{C}\mathbf{n} + \mathbf{f}) - \langle -\mathrm{D}\rangle \mathrm{C}\frac{\partial \mathbf{n}}{\partial \boldsymbol{\sigma}}\right) \tag{A.65}$$

$$\frac{\partial \bar{\mathbf{F}}}{\partial \boldsymbol{\alpha}} = \mathrm{H}\left(\frac{\partial \mathrm{D}}{\partial \boldsymbol{\alpha}}\mathbf{I} - \Xi(-\mathrm{D})\frac{\partial \mathrm{D}}{\partial \boldsymbol{\alpha}}(\mathrm{C}\mathbf{n} + \mathbf{f}) - \langle -\mathrm{D}\rangle \mathrm{C}\frac{\partial \mathbf{n}}{\partial \boldsymbol{\alpha}}\right) \tag{A.66}$$

In the end, the derivatives with respect to fabric are reported:

$$\frac{\partial \mathbf{f}}{\partial \mathbf{F}} = \mathbf{I} - \frac{\mathbf{I}}{3} \tag{A.67}$$

$$\frac{\partial \bar{\mathbf{F}}}{\partial \mathbf{F}} = -\langle -\mathrm{D}\rangle \mathrm{H}\mathbf{I} \tag{A.68}$$

$$\frac{\partial \mathrm{h_f}}{\partial \mathbf{F}} = \frac{1 + 2\langle \mathbf{F}:\mathbf{I}\rangle \Xi(\mathbf{F}:\mathbf{I})(\mathbf{I}\cdot\mathbf{I})(1 + \langle \mathbf{F}:\mathbf{n}\rangle) - \left(1 + \langle \mathbf{F}:\mathbf{I}\rangle^2 \Xi(\mathbf{F}:\mathbf{n})(\mathbf{I}\cdot\mathbf{n})\right)}{(1 + \langle \mathbf{F}:\mathbf{n}\rangle)^2} \tag{A.69}$$

$$\frac{\partial \bar{\boldsymbol{\alpha}}}{\partial \mathbf{F}} = \mathrm{h_b}\frac{\partial \mathrm{h_b}}{\partial \mathbf{F}}\left(\boldsymbol{\alpha}^{\mathbf{b}} - \boldsymbol{\alpha}\right) \tag{A.70}$$

APPENDIX A.

A.1 REFERENCES

Ghofrani A. (2018). Development of Numerical Tools For the Evaluation of Pile Response to Laterally Spreading Soil. Ph.D. Thesis, The University of Washington, Seattle

Ortiz M., Simo J. C. (1986). An analysis of a new class of integration algorithms for elastoplastic constitutive relations. International Journal for Numerical Methods in Engineering, 23 (3). pp. 353-366. ISSN 0029-5981.

APPENDIX B. EQUIVALENT LINEAR SITE RESPONSE ANALYSES AT SAN GIULIANO DI PUGLIA

In the following, the mono- and bi-dimensional equivalent linear analyses reported in Fierro et al. (2020b) are briefly illustrated to complete the discussion referred to the case study of San Giuliano di Puglia.

B.1 1-D ANALYSES

Mono-dimensional analyses are conducted exploiting the software Strata (Kottke et al., 2013). This numerical tool is used to carry out equivalent linear site response analyses in the frequency domain using acceleration time-series as input motions and adopting algorithms similar to those introduced, firstly, in SHAKE (Schnabel et al., 1972; Idriss and Sun, 1992).

B.1.1 ANALYSES AT MEMORY PARK SITE USING THE MOTION RECORDED AT THE EMBEDDED SGPA STATION

The first set of 1-D analyses performed along the SGPA soil column is developed considering the following approach: the recorded signals at the embedded station (SGPA -53 m) are applied as an input motion at the depth of the accelerometers (cf. Table 7.3), and then the response at the top of the soil column is computed. Finally, the calculated response is compared with the recorded motion at the ground level. The geotechnical data used to implement the SGPA soil column are reported in Table B.1, based on the shear wave velocity profile carried out in the previous studies by Puglia (2008), starting from the available geotechnical and geophysical tests.

APPENDIX B.

Table B.1. Geotechnical parameters for 1-D seismic response analyses along the SGPA soil column.

Depth (m)	**Soil formation**	**Thickness (m)**	**Soil unit weight γ (kN/m³)**	**Shear wave velocity Vs (m/s)**	**Modulus Reduction curve G=G(γ)/G₀**	**Damping curve D (γ)**
0	Debris cover	3	19.60	122	Table 7.2	Table 7.2
3	Tawny clay	1	21.15	247		
4	Tawny clay	1	21.15	251		
5	Tawny clay	1	21.15	255		
6	Tawny clay	1	21.15	258		
7	Tawny clay	1	21.15	261		
8	Grey clay	20	21.20	334		
28	Grey clay	20	21.20	375		
48	Grey clay	20	21.20	396		
68	Grey clay	20	21.20	410		
88	Grey clay	20	21.20	421		
108	Grey clay	20	21.20	431		
128	Grey clay	20	21.20	438		
148	Grey clay	20	21.20	445		
168	Grey clay	20	21.20	451		
188	Grey clay	20	21.20	457		
208	Grey clay	20	21.20	462		
228	Grey clay	20	21.20	466		
248	Faeto flysch 3	Bedrock	22.00	1350	1	0.5

The sensors of the seismic network are oriented along the North-South and East-West directions, and, for this reason, the recorded time-series should be composed to obtain the resultant motion on the main axis of the town, as made in Puglia (2008; cf. (7.3). Comparison is presented in terms of median elastic response spectra in acceleration with 5% damping.

In this first stage of analysis, led by the standard of practice about the conditions to be implemented at the embedded sensor depth, “Within” motion option is first considered. Adopting this approach, an overestimation of the surficial response is observed (cf. Figure B.1).

This result should not be completely surprising because it can be related to a damping of the motion produced by the wave scattering effect developed in the field, as already pointed out in previous studies (Pecker, 1995; Kaklamanos et al., 2013; Zalachoris and Rathje, 2015; Cabas and Rodriguez-Marek, 2017; Afshari et al., 2019; Tao and Rathje, 2019; see Appendix C for further details). This phenomenon is proper of the in-situ conditions, and it has been widely studied and analzyed over the years. Consequently, it is impossible to be reproduced using laboratory apparatuses. For this reason, in order to try to account for wave scattering in numerical simulations, in the current practice it is common to add a supplemental low strain level damping between 0% and 5% (see Stewart and Kwok, 2008; Yee et al., 2013; Stewart et al., 2014) or to amplify the "laboratory-based" low-strain damping D_0 by a factor between 1.5 and 5.5 (Tao and Rathje, 2019).

In this study, the effect of additional low-strain damping in mono-dimensional analyses is investigated to understand how the surficial response could be modified. To this aim, supplemental mono-dimensional analyses are therefore conducted by increasing the low-strain damping obtained from laboratory tests by a quantity of 2% and 5%, respectively. The fitting undoubtfully improved, but it still appears unsatisfying (Figure B.1), in terms of spectral shapes.

APPENDIX B.

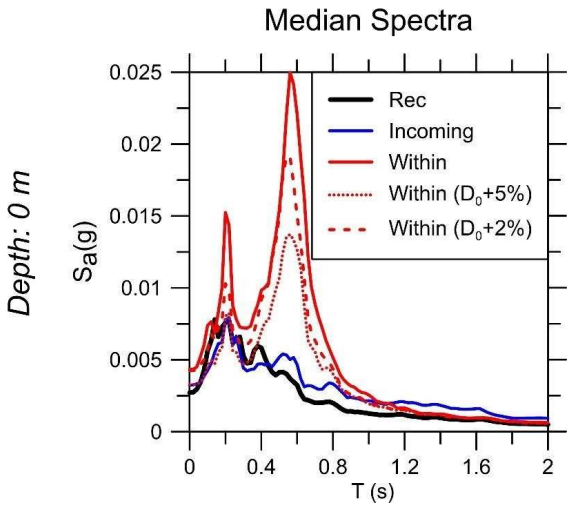

Figure B.1. Comparison between the computed and measured median response spectra for mono-dimensional analyses on the SGPA soil column.

Nevertheless, some literature studies reported a better fitting between recorded and simulated data obtained by considering the upward propagating waves only at the embedded sensor instead of both upward and downward waves. In this framework, Bonilla et al. (2002) analyzed the well-known Garner Valley Downhole Array (GVDA), made by seven down-hole instruments ranging from surficial to 500 m depth sensors, and observed that the downgoing wave effect is strongly predominant in the first 87 m and is then attenuated at the highest depths, because most of the energy is trapped into the surficial layers. In fact, in the frequency domain, the interference between both downgoing and incident wave fields may produce spectral holes (Steidl et al., 1996). Furthermore, Thompson et al. (2009) investigated the response of 13 Kiban-Kyoshin network stations, installed as vertical arrays and excited by ground motions with maximum acceleration lower than 0.2 g, finding that, in a non-neglectable amount of cases, better accordance with recordings is obtained considering in the simulations the upgoing wave only (the so-called “Incoming” motion option in Strata), even if the downgoing component is certainly included in the spectra carried out from recordings at the embedded sensor depth.

APPENDIX B.

On the basis of what above discussed, Figure B.1 reports median spectra carried out considering the small-strain damping values measured in laboratory tests and both input motion options provided by Strata ("Within" and "Incoming"). In the same Figure, spectra calculated by increasing the small strain damping of the three units by a quantity of 2% and 5%, respectively, adopting the 'Within" motion option are illustrated. The input motions considered for the analyses are those shown in Table 7.3, except for the December, 24th, 2014 event, whose exclusion will be detailed later. From the observation of the results, the better performance obtained by considering the upward propagating wave only is clear.

Therefore, this interesting result could be due to the limits in the theoretical formulation for the specific case of a deep down-hole instrument location, whose limits can be identified in the absence of the full wavefield modelling or in the lack of a spatially-correlated variability of the soil seismic characteristics (see Thompson et al., 2009). A better mapping of the mono-dimensional soil profile onto spectral amplification could help to overcome these limits. The resulting strong overestimation can be overcome through a bi-dimensional modelling of the problem with the application of the "Within" motion option as well. Consequently, in this paragraph and with reference to the mono-dimensional model of the problem, the acceleration response spectra obtained using the "Incoming" motion, by assigning the soil damping values from RC and CT tests as benchmarks, as in Table 7.2, are considered. Then, those results will be compared to the ones obtained from bi-dimensional simulations and considering both upward and downward propagating waves, which are more representative of the physical phenomena. The resulting difference between computed and recorded spectra need to be quantified numerically. To this aim, some statistical indicators are introduced. Specifically, in the period range T=0÷2 s, one can compute an absolute standard deviation obtained from (B.1), where $SA_{pred}(T_i)$ is the computed spectral ordinate at the period T_i, $SA_{rec}(T_i)$ is the spectral ordinate from recording at the same period and n is

the number of observations in the selected period range. This indicator, reported in (B.1), is already adopted in Fierro et al. (2019; 2020a; 2020b).

$$d = \frac{1}{n}\sqrt{\sum_{i=1}^{n}\left(SA_{rec}(T_i) - SA_{pred}(T_i)\right)^2} \tag{B.1}$$

For the same range of periods, additional indicators are evaluated for each couple of accelerograms (i.e., the recorded and the computed ones), namely the root mean square deviation, D_{rms} (Acunzo et al., 2014; see (B.2)), the mean absolute error (MAE) and the normalized standard deviation (B.3) (S; cf. (B.4)).

$$D_{rms} = \frac{1}{n}\sqrt{\sum_{i=1}^{n}\left(\frac{SA_{rec}(T_i)}{PGA_{rec}} - \frac{SA_{pred}(T_i)}{PGA_{pred}}\right)^2} \tag{B.2}$$

$$MAE = \frac{1}{n}\sum_{i=1}^{n}\left|SA_{rec}(T_i) - SA_{pred}(T_i)\right| \tag{B.3}$$

$$S = \sqrt{\frac{1}{n}\sum_{i=1}^{n}\left(\frac{SA_{rec}(T_i) - SA_{pred}(T_i)}{SA_{rec}(T_i)}\right)^2} \tag{B.4}$$

For all the available signals introduced in Table 7.3, the resulting statistical parameters are reported in Table B.2, taking into account for the “Incoming” motion option only. Each accelerogram is recalled using the ID number provided in Table 7.3.

APPENDIX B.

Table B.2. Statistical parameters showing differences between predicted and recorded signals along the SGPA soil column.

ID	n344 direction			
	Incoming			
	d **(g x 10^{-3})**	**D_{rms}** **(-)**	**MAE** **(g x 10^{-3})**	**S** **(-)**
GM1	1.241	0.055	1.096	0.721
GM2	105.536	0.025	45.580	0.327
GM3	0.474	0.044	0.281	0.594
GM4	0.973	0.028	0.610	0.584
GM5	2.354	0.054	2.164	0.692
GM6	0.679	0.077	0.613	0.690
GM7	3.887	0.065	3.516	0.701
GM8	0.498	0.085	0.335	0.404
GM9	0.709	0.077	0.592	0.679
GM10	2.524	0.044	1.223	0.626
GM11	4.448	0.034	2.881	0.572
GM12	19.970	0.064	10.558	0.653
GM13	5.466	0.032	3.219	0.583
Average	11.443	0.053	5.590	0.602
Median	2.354	0.054	1.223	0.626

The observation of Table B.2 highlights that a greater reliability can be obtained by considering the statistical parameters measuring absolute difference between recorded and simulated spectral accelerations (i.e., d and MAE reported in the expressions (B.1) and (B.3). In fact, the normalized statistical parameters (D_{rms}, which is normalized with respect to PGA and S, normalized to S_a from recording at the spectral period T_i), tend to estimate the accordance between spectral shapes only, without considering their absolute scattering in terms of spectral values.

This issue is clearly identified analyzing the near-field event that happened on December, 24th, 2014 (R_{epi} = 2.2 km from SGPA station) and the abovementioned difference is highlighted in Table B.2. The normalized statistical parameters (i.e., D_{rms} and S) pointed out satisfactory accordance between recordings and simulations, while observing the absolute statistical parameters (i.e., d and MAE), a marked gap is

underlined. The short epicentral distance could allow that near-field conditions in this recording may arise. Being the quasi-vertical propagation of the waves, required for the analyses, not guaranteed in this situation, the event is excluded.

B.1.2 ANALYSES AT MEMORY PARK SITE USING THE MOTION RECORDED AT MARCHESALE PALACE SGMA STATION

An additional stage of mono-dimensional site response analyses is performed considering the SGMA site. This is performed to define a proper reference motion on outcropping bedrock as in previous studies (Puglia, 2008; cf. Figure 7.3a and Figure 7.5). In fact, even if the calcareous materials detected at this site are relatively stiff, in order to overcome the fissured superficial layer (cf. Figure 7.3b), the station is installed at about 10 m from the ground level, where shear wave velocity is V_s=800 m/s. For this reason, deconvolution analyses to obtain the reference motion at outcropping bedrock conditions (Faeto Flysch 3 in Table B.1) are conducted. In this case, the motion recorded at the depth of the station is certainly strongly influenced by both upward and downward propagating waves because of its close distance to the ground surface and to the surficial alteration, which can provide reflection effects. As a consequence, the "Within" motion option should be considered in Strata. Additionally, the impedance contrast between the units referred as Faeto Flysch 3 (V_s=1350 m/s) and Faeto Flysch 2 (V_s=800 m/s) could generate stratigraphic effects in the reference rock motion. Linear elastic deconvolution analyses were performed, by assuming a damping ratio value D=0.5%, as in Puglia (2008). The geotechnical data for the SGMA vertical model are summarized in the following Table B.3.

APPENDIX B.

Table B.3. Geotechnical parameters adopted for mono-dimensional seismic response analyses at the SGMA site.

Depth (m)	**Soil formation**	**Thickness (m)**	**Soil unit weight, γ (kN/m²)**	**Shear wave velocity Vs (m/s)**	$\bar{G} = \frac{G(\gamma)}{G_0}$	**D (γ) (%)**
0	Faeto flysch 1	6	22.00	400	1	0.5
6	Faeto flysch 2	11	22.00	800		
17	Faeto flysch 3	Bedrock	22.00	1350		

The signals resulting from the deconvolution process are then directly applied along the SGPA soil column considering the bedrock outcropping condition and using the subsoil model developed by Puglia (2008) and adopted in derived papers. During the upward propagation, this time-series obtained by 1-D numerical analyses is compared with the recorded data available at level -53 m from g.l. (where the sensors are located) and at the surface. For the sake of comparison, the output accelerograms at the deeper station are carried out considering both the available motion options ("Within" and "Incoming") to show how the inclusion or the exclusion of the downward propagating wave influences the results.

In Table B.4, the differences between measurements and simulated time-series in terms of statistical predictors for both the output motion options at the surface and at the depth of the embedded station (-53 m) are reported. Referring to the latter, a widespread better performance by choosing the "Incoming" motion option instead of "Within" is noticed for all the selected statistical parameters. From the observation of the resulting statistical indicators, among them, the normalized parameters do not exhibit a strong variation throughout the events, while the absolute parameters increase apparently as the epicentral distance decreases. Furthermore, lower values of all the statistical parameters (meaning a better recorded-computed agreement) are obtained by considering the comparison between recordings and simulations at the deeper station (-53 m from g.l.) with respect to the response at the surface and this can be due to the bi-dimensional effects that condition the response of the village of San Giuliano di Puglia.

Table B.4. Statistical indicators showing differences between predicted and recorded signals at the SGPA site at -53 m and 0 m. Seismic motion is applied at bedrock level (-248 m from g.l.).

ID	n344 direction											
	-53 m from g.l.								Surface			
	Incoming				Within							
	d ($g \times 10^{-3}$)	D_{rms} (-)	MAE ($g \times 10^{-3}$)	S (-)	d ($g \times 10^{-3}$)	D_{rms} (-)	MAE ($g \times 10^{-3}$)	S (-)	d ($g \times 10^{-3}$)	D_{rms} (-)	MAE ($g \times 10^{-3}$)	S (-)
GM1	0.490	0.067	0.376	0.324	0.639	0.094	0.499	0.536	1.597	0.087	1.088	0.629
GM3	0.189	0.069	0.121	0.398	0.231	0.071	0.156	0.481	0.866	0.109	0.372	0.413
GM4	0.695	0.065	0.416	0.368	0.704	0.065	0.473	0.619	1.686	0.063	0.900	0.640
GM5	1.023	0.078	0.877	0.352	1.200	0.122	1.008	0.498	1.650	0.106	1.204	0.520
GM6	0.386	0.057	0.329	0.436	0.390	0.106	0.337	0.558	0.578	0.061	0.408	0.538
GM7	1.567	0.039	1.392	0.317	1.739	0.081	1.367	0.332	2.101	0.064	1.783	0.321
GM8	0.273	0.063	0.220	0.389	0.242	0.078	0.202	0.395	0.538	0.089	0.353	0.413
GM9	0.249	0.036	0.199	0.308	0.282	0.064	0.219	0.515	0.680	0.076	0.427	0.559
GM10	0.581	0.038	0.415	0.423	0.524	0.048	0.382	0.502	3.678	0.065	1.434	0.472
GM11	1.546	0.048	1.084	0.352	1.791	0.067	1.287	0.428	7.831	0.082	3.506	0.431
GM12	4.550	0.079	3.419	0.391	4.988	0.075	3.938	0.491	28.603	0.135	12.553	0.543
GM13	1.730	0.058	1.144	0.396	2.469	0.065	1.239	0.485	9.612	0.074	4.310	0.427
Average	2.548	0.057	1.550	0.377	2.665	0.075	1.633	0.483	17.385	0.081	7.723	0.496
Median	0.695	0.058	0.416	0.389	0.704	0.071	0.499	0.491	1.686	0.076	1.204	0.520

For example, the comparison referred to the composed motion of January 18th, 2017 Central Italy earthquake, is reported in Figure B.2. The simulations are made considering, for the surficial station, both the input motions applied at the depth of the deeper station adopting the “Incoming” motion option (-53 m; “LSR 0m Conv” in the

graph, where "0m" refers to the depth where outputs are requested) and using the full soil column by applying at bedrock the motion obtained by deconvolution analysis ("LSR 0m"). The latter is exploited also to obtain the acceleration response spectra at -53 m from g.l ("LSR 53m"). As it can be observed, a generalized underestimation of the recorded spectrum at -53 m from g.l. occurred, while, on the surface, the underestimation is confined up to the period of 0.5 s. No significant differences in the different input motion applications are highlighted.

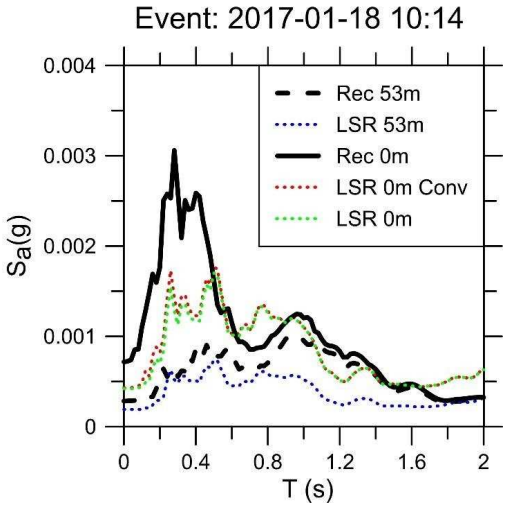

Figure B.2. Comparison between the computed and measured response spectra for 1-D at the SGPA site at -53 m from g.l. and at the surface with reference to the January 18th, 2017 Central Italy earthquake.

B.2 2-D EQUIVALENT LINEAR ANALYSES

After the introductory investigation of the mono-dimensional response of both SGMA and SGPA sites, full analyses considering the main cross-section of San Giuliano di Puglia using the finite-element code QUAD4M are conducted. This code exploits an equivalent linear viscoelastic approach and a Rayleigh damping formulation using two control frequencies to model damping properties (Hudson et al., 1994).

APPENDIX B.

The first set of analyses is executed adopting the "Anvil" model previously sketched in Figure 7.5 and employing the same soil properties, as indicated in §7. The soil domain is meshed using triangular elements and can be visualized in Figure B.3. An important aspect that needs to be accounted for when large models are under analysis consists of the possibility that uncontrolled wave reflections at the boundaries can take place. For this reason, the size of the model was made large enough to accomplish for the indications given by Lanzo and Pagliaroli (2009) on the same site. When the input motion is applied, the horizontal components only are considered: this allows an easier comparison with mono-dimensional analysis results.

As input signals, the 1-D deconvolution at the outcropping bedrock conditions of the motion recorded at SGMA station during the previously reported earthquakes (cf. Table 7.3) are applied. The NS and EW components of the motion are composed and projected, as already made for the 1-D analyses, along the n344 direction (i.e., the orientation of the selected cross-section), following the indications provided by Puglia (2008).

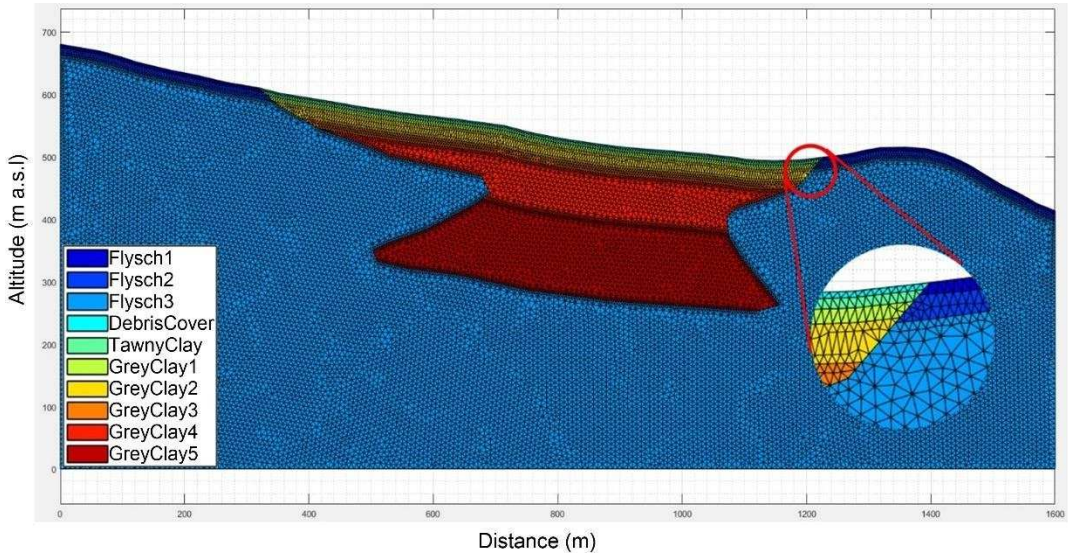

Figure B.3. Adopted mesh for the "Anvil" model employed for 2-D analyses conducted with QUAD4M.

APPENDIX B.

The reliability of the model is assessed by means of the comparison of measured and computed elastic response spectra at the SGPA station, where recording stations take place, i.e., at ground level and at a depth of -53 m from the ground level.

Taking once more the January 18th, 2017 Central Italy earthquake as example, the comparison is reported in Figure B.4. Acceptable values are provided by the numerical analyses when the comparison is made at the surface and for a period lower than 0.5 s as well as at the depth of the deeper station for the range of periods 0.4÷1s, while it is clear a general overestimation of the spectral accelerations otherwise. In Figure B.5, a comparison is shown in terms of average and median spectra, considering all the signals. Similar considerations are reported in Sanò et al. (2015) using a limited number of earthquakes and computing spectra through the BESOIL code. The observation of the spectra reveals that simulations hardly overestimate recordings at -53 m from g.l. for a specified range of periods, while the the recorded data are significantly underestimated at the surface up to 0.3 s.

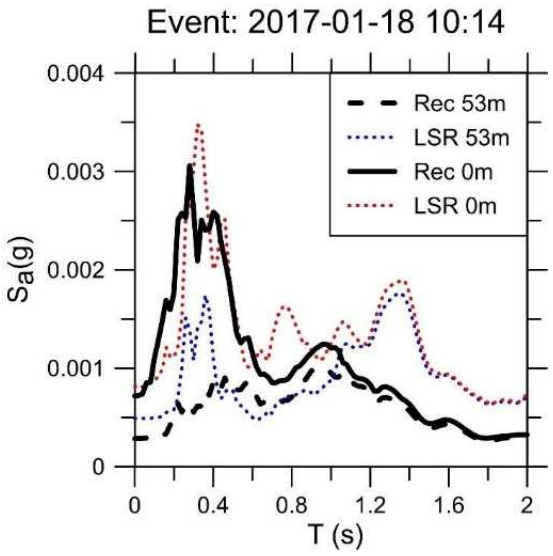

Figure B.4. Comparison between the computed and measured response spectra for 2-D analyses at the SGPA site at -53 m from g.l. and at the surface with reference to the January 18th, 2017 Central Italy earthquake.

APPENDIX B.

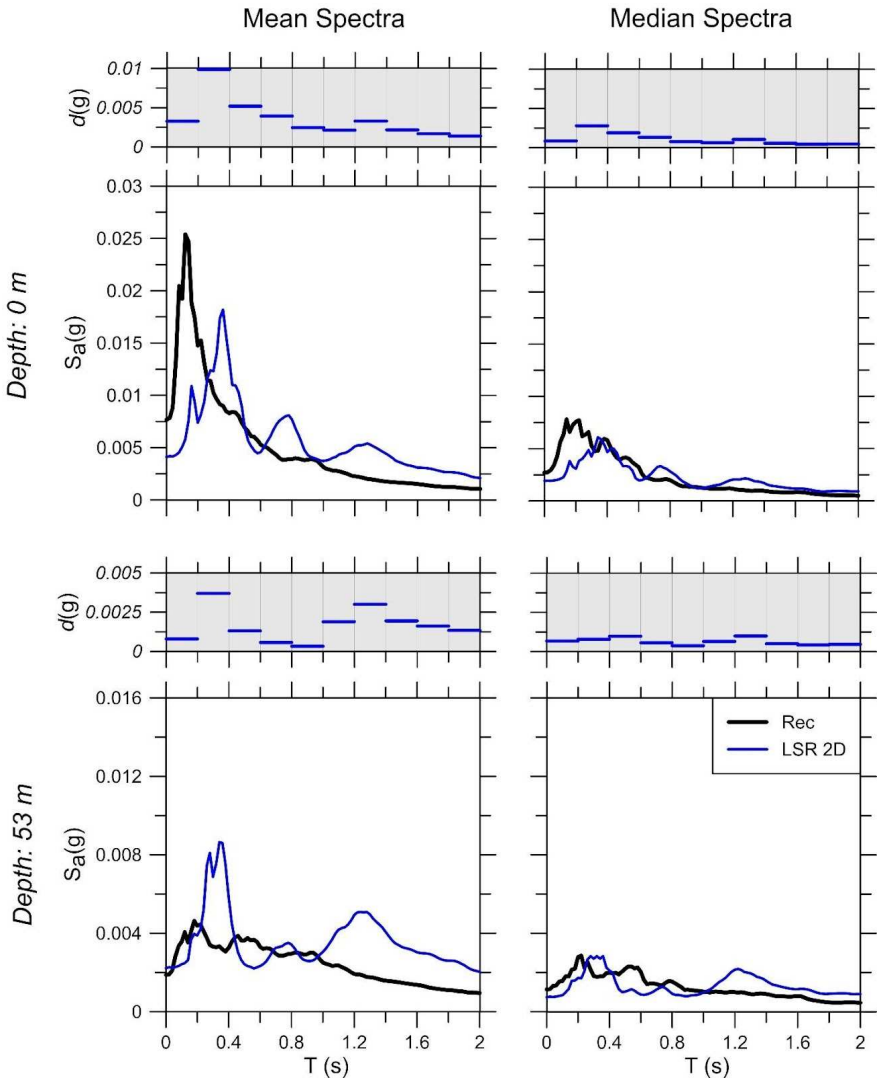

Figure B.5. Comparison between average and median, computed and measured response spectra for 2-D analyses at the SGPA site at -53 m from g.l. and at the surface, using the stiffness profile proposed by Puglia (2008). Input motion for earthquakes listed in Table 7.3.

Table B.5 reports the differences between measurements and numerical analyses quantified through the above-mentioned statistical indicators.

APPENDIX B.

Table B.5. Statistical parameters showing differences between predicted and recorded signals at the SGPA site at level -53 m and 0 m using the 2-D "Anvil" model proposed by Puglia (2008).

ID	-53 m from g.l.				Surface			
	d ($g \times 10^{-3}$)	**D_{rms}** (-)	**MAE** ($g \times 10^{-3}$)	**S** (-)	**d** ($g \times 10^{-3}$)	**D_{rms}** (-)	**MAE** ($g \times 10^{-3}$)	**S** (-)
GM1	0.831	0.061	0.799	0.695	2.026	0.073	1.352	0.639
GM3	0.220	0.089	0.156	0.804	0.696	0.072	0.346	0.701
GM4	0.804	0.127	0.642	1.429	1.392	0.079	0.922	1.144
GM5	3.745	0.153	2.831	1.451	3.761	0.148	3.151	1.282
GM6	0.715	0.107	0.602	1.126	0.821	0.110	0.667	0.965
GM7	4.567	0.090	3.758	1.084	5.255	0.063	4.221	0.937
GM8	0.489	0.096	0.389	0.973	0.554	0.066	0.452	0.849
GM9	0.649	0.130	0.533	1.505	0.875	0.075	0.733	1.335
GM10	0.788	0.100	0.615	1.189	3.484	0.091	1.650	0.970
GM11	3.092	0.085	2.414	1.161	8.674	0.102	5.407	0.964
GM12	8.035	0.085	6.144	1.125	28.143	0.133	14.985	1.045
GM13	4.027	0.078	2.292	1.257	10.360	0.096	6.157	1.071
Average	2.330	0.100	1.765	1.150	5.503	0.092	3.337	0.992
Median	0.818	0.093	0.720	1.144	2.755	0.085	1.501	0.968

The overestimation of the acceleration response spectra obtained from recordings by those obtained from numerical simulations together with the availability of additional down-hole tests with respect to those exploited by Puglia (2008), suggested to reconsider the geotechnical subsoil model and, in particular, to re-evaluate the reliability of the shear wave velocity profiles in the light of the newly available data (Figure 7.3b). As previously stressed, such profiles return a greater stiffness compared to what was assumed in previous studies, here considered as the first reference. Then, the new geotechnical subsoil model in the central part of the village is summarized in Table B.6, which has been developed using the V_s-values coming from the down-hole test. However, the model for Faeto flysch below the historical center was left unchanged as summarized in Table B.3 (see, for instance, Fierro et al., 2019).

APPENDIX B.

Table B.6. Updated geotechnical model for the central part of San Giuliano di Puglia, based on shear wave velocity profiles by Sanò et al. (2015).

Depth (m)	**Soil formation**	**Thickness (m)**	**Soil unit weight, γ (kN/m³)**	**Shear wave velocity, Vs (m/s)**	$\overline{G} = \frac{G(\gamma)}{G_0}$	**D(γ)**
0	Debris cover	3	19.60	125	Table 7.2	Table 7.2
3	Tawny clay	5	21.15	290		
8	Gray clay 1	7	21.20	390		
15	Gray clay 2	16	21.20	530		
31	Gray clay 3	31	21.20	700		
62	Gray clay 4	60	21.20	800		
122	Gray clay 5	126	21.20	950		
248	Faeto flysch	Bedrock	22.00	1350	1	0.5

In Figure B.6 and Figure B.7, the comparisons carried out by adopting the new shear wave velocity profile, respectively for the reference event of January 18th, 2017 Central Italy earthquake and for the average and median spectra for all the events are presented. In Figure B.7, with a view to highlighting the differences with the mono-dimensional response, even the average and median spectra as obtained from 1-D analyses are reported, confirming again the need to consider the bi-dimensional effects for the village of San Giuliano di Puglia and to point out their key role in the amplification of motion at the site. The resulting statistical parameters from 1-D analyses are reported in Table B.7. For the sake of clarity, it is underlined that, in the above-mentioned figures, output spectra are carried at SGPA site, at both surficial (0 m) and deep (-53 m from g.l.) stations. In addition, considering the former (surficial station, 0 m), the spectral shapes obtained from the following sets of analyses are reported and then compared to the acceleration response spectra of the recordings at the surface:

1. bi-dimensional analyses ("LSR 2D");
2. mono-dimensional analyses using, as input motions, the accelerograms recorded at SGMA station (-10 m) and then deconvolved to obtain outcropping bedrock condition ("LSR 1D);
3. mono-dimensional analyses performed through the application of the recorded motion at the depth of the embedded station (-53 m; "LSR 1D

Conv") using the "Incoming" motion option (i.e., the upward propagating waves are considered only).

Table B.7. Statistical parameters showing differences between predicted and recorded signal at the SGPA site at level -53 m and 0 m using the 1-D model with updated geotechnical parameters.

ID	1-D updated model											
	-53 m from g.l.				Surface (Input SGMA)				Surface (Input SGPA)			
	d (g x10^{-3})	D_{rms} (-)	MAE (g x10^{-3})	S (-)	d (g x10^{-3})	D_{rms} (-)	MAE (g x10^{-3})	S (-)	d (g x 10^{-3})	D_{rms} (-)	MAE (g x10^{-3})	S (-)
GM1	0.517	0.043	0.434	0.359	1.167	0.041	0.703	0.283	1.102	0.040	1.001	0.716
GM3	0.176	0.036	0.117	0.401	0.760	0.071	0.303	0.261	0.375	0.031	0.248	0.588
GM4	0.626	0.036	0.385	0.365	1.391	0.043	0.635	0.283	1.988	0.032	0.976	0.660
GM5	1.108	0.048	1.023	0.394	1.227	0.078	0.874	0.274	2.228	0.071	1.862	0.477
GM6	0.407	0.051	0.359	0.476	0.499	0.043	0.331	0.272	0.646	0.070	0.579	0.687
GM7	1.817	0.050	1.670	0.381	1.429	0.038	1.045	0.195	3.951	0.047	3.634	0.707
GM8	0.265	0.049	0.237	0.425	0.438	0.062	0.246	0.236	0.537	0.082	0.478	0.680
GM9	0.337	0.043	0.262	0.382	0.646	0.064	0.397	0.306	0.653	0.073	0.552	0.671
GM10	0.508	0.049	0.382	0.432	3.192	0.049	1.138	0.274	1.851	0.032	1.093	0.628
GM11	1.415	0.040	1.125	0.379	6.575	0.055	2.641	0.231	3.139	0.021	2.435	0.567
GM12	3.992	0.044	3.222	0.403	24.83	0.078	9.957	0.311	15.323	0.053	8.674	0.643
GM13	1.492	0.050	1.009	0.389	8.251	0.056	3.636	0.338	3.201	0.021	2.352	0.582
Av.	1.055	0.045	0.852	0.399	4.200	0.057	1.825	0.272	2.916	0.048	1.990	0.634
Med.	0.571	0.046	0.410	0.392	1.309	0.056	0.788	0.274	1.920	0.043	1.047	0.651

On the other hand, referring to the embedded station (-53 m), the comparison is made by exploiting the following sets:

1. bi-dimensional analyses ("LSR 2D");
2. mono-dimensional analyses using, as input motions, the accelerograms recorded at SGMA station (-10 m) and then deconvolved to obtain outcropping bedrock condition ("LSR 1D").

APPENDIX B.

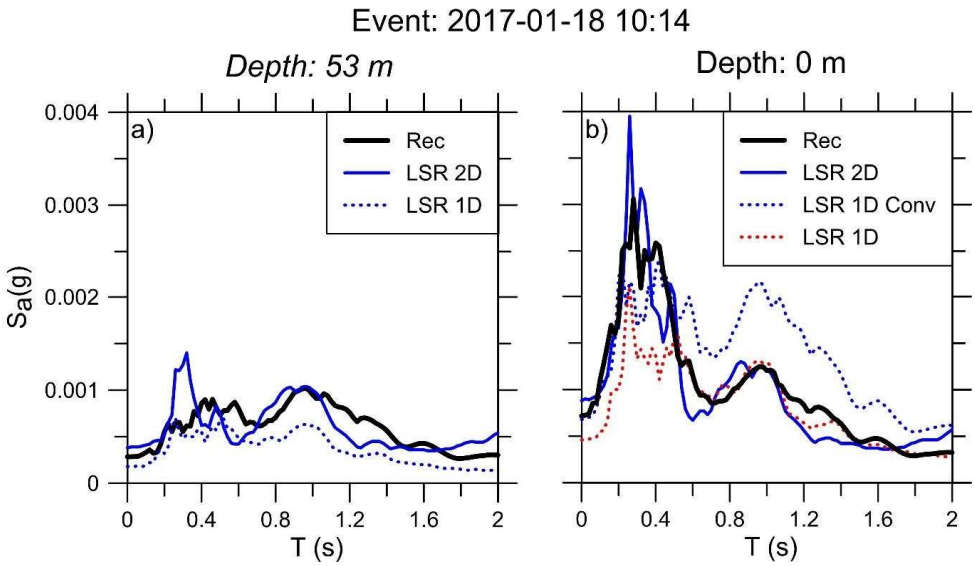

Figure B.6. Comparison between the computed and measured response spectra for 1-D and 2-D analyses at SGPA site at -53 m from g.l. (a) and at the surface (b) with reference to the January 18th, 2017 Central Italy earthquake, using an updated geotechnical model.

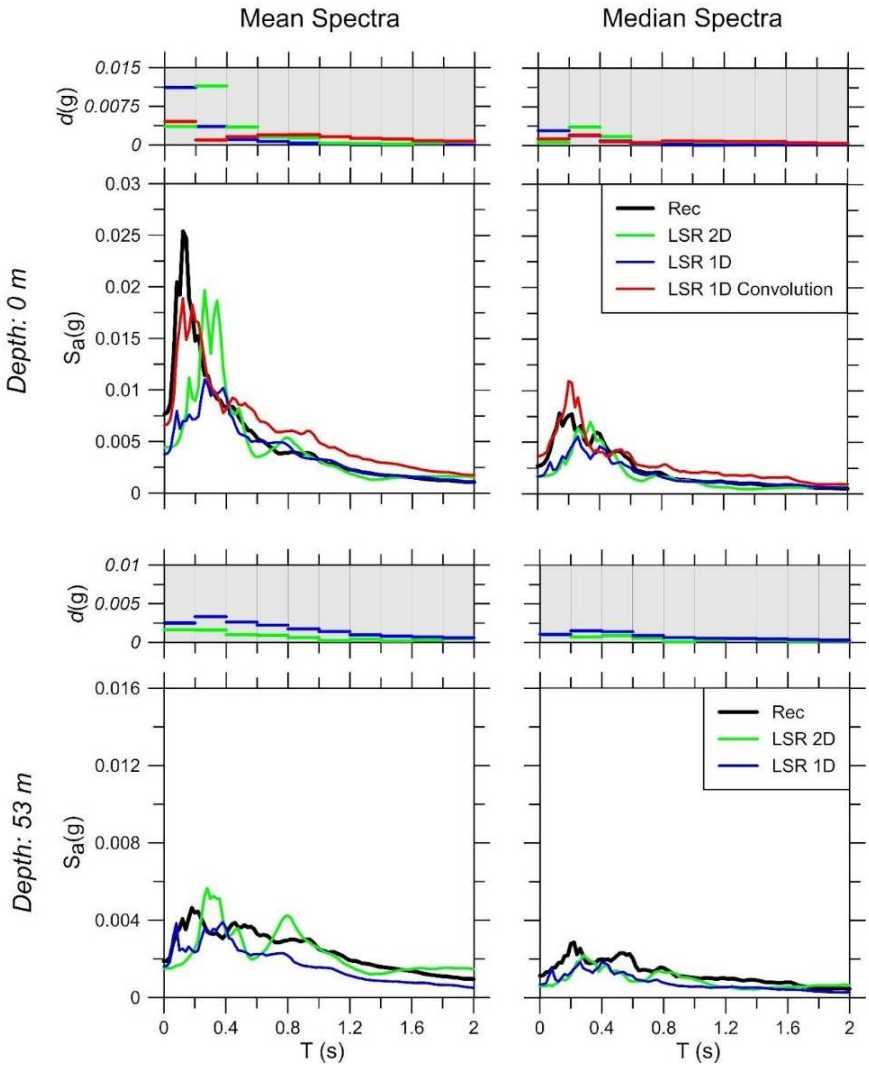

Figure B.7. Comparison between the average and median, computed and measured response spectra for 1-D and 2-D analyses at SGPA site at -53 m from g.l. and at the surface, using an updated geotechnical model.

From the updated graphs, it is possible to observe the more satisfactory congruence between the recorded data and those obtained from numerical analyses on the revised model characterized by a greater stiffness at the small strain level. The same conclusion can be obtained also from statistical parameters as reported in Table B.8. With reference to the Figure B.7, it is worth noting that at the surface, even if a bi-dimensional model is considered, the latter does not appear able to detect the peak at about 0.15 s (observable

in both mean and median spectra from recordings). By contrast, this peak seems to be correctly reproduced if the mono-dimensional model is considered, applying input motions at the depth of the embedded station. Overall, this could lead to assert that spectra obtained from mono-dimensional analyses fit recordings better than those obtained from bi-dimensional ones. However, this result could be explained by considering that signals used as inputs at -53 m, being recorded, could include three-dimensional effects, and the mono-dimensionality of the problem only refers to the topmost 53 m. On the other hand, in the bi-dimensional analyses, the inputs are carried out from mono-dimensional deconvolution, while the simulation is bi-dimensional up to the surface. These conclusions strongly underline the key role played by the accelerometers installed as array stations.

Table B.8. Statistical parameters showing differences between predicted and recorded signals at the SGPA site at level -53 m and 0 m using the 2-D "Anvil" model with updated geotechnical parameters.

ID	2-D updated model							
	-53 m from g.l.				Surface			
	d ($g \times 10^{-3}$)	D_{rms} (-)	MAE ($g \times 10^{-3}$)	S (-)	d ($g \times 10^{-3}$)	D_{rms} (-)	MAE ($g \times 10^{-3}$)	S (-)
GM1	0.881	0.068	0.853	0.744	2.012	0.057	1.485	0.711
GM3	0.184	0.068	0.111	0.379	0.673	0.055	0.267	0.303
GM4	0.713	0.102	0.422	0.527	1.351	0.066	0.723	0.482
GM5	0.869	0.085	0.702	0.374	1.383	0.083	0.988	0.372
GM6	0.304	0.083	0.254	0.463	0.615	0.071	0.437	0.486
GM7	1.148	0.051	0.806	0.238	3.082	0.057	1.617	0.315
GM8	0.217	0.085	0.163	0.385	0.308	0.050	0.218	0.291
GM9	0.188	0.048	0.130	0.415	0.518	0.064	0.326	0.430
GM10	0.544	0.062	0.356	0.435	3.494	0.081	1.455	0.462
GM11	1.764	0.069	1.218	0.422	7.646	0.090	3.767	0.389
GM12	4.867	0.091	3.451	0.476	26.447	0.099	11.854	0.465
GM13	2.165	0.067	1.243	0.395	10.119	0.084	4.881	0.540
Average	1.154	0.073	0.809	0.438	4.804	0.071	2.335	0.437
Median	0.791	0.069	0.562	0.419	1.697	0.069	1.222	0.446

Furthermore, considering that the adopted bi-dimensional code (QUAD4M) considers both upward and downward propagating waves (i.e., "Within" motion option in Strata), the accordance between the simulated and recorded spectra improves clearly with respect to the 1-D analyses. This more accurate and sophisticated level of analysis apparently allows to overcome some typical discrepancies observed in the mono-dimensional condition when borehole recordings are available, as it can be observed.

Finally, the obtained positive results encouraged us to test whether a simpler geometric model for the subsoil of San Giuliano di Puglia can lead to satisfactory results too, keeping unchanged the latest physical and mechanical properties of the materials. To this end, the comparison between simulated and recorded elastic response spectra is made considering the "Basin" geometry, which is simpler and often adopted when no direct information on the buried geometry is available and whose mesh discretization is reported in Figure B.8.

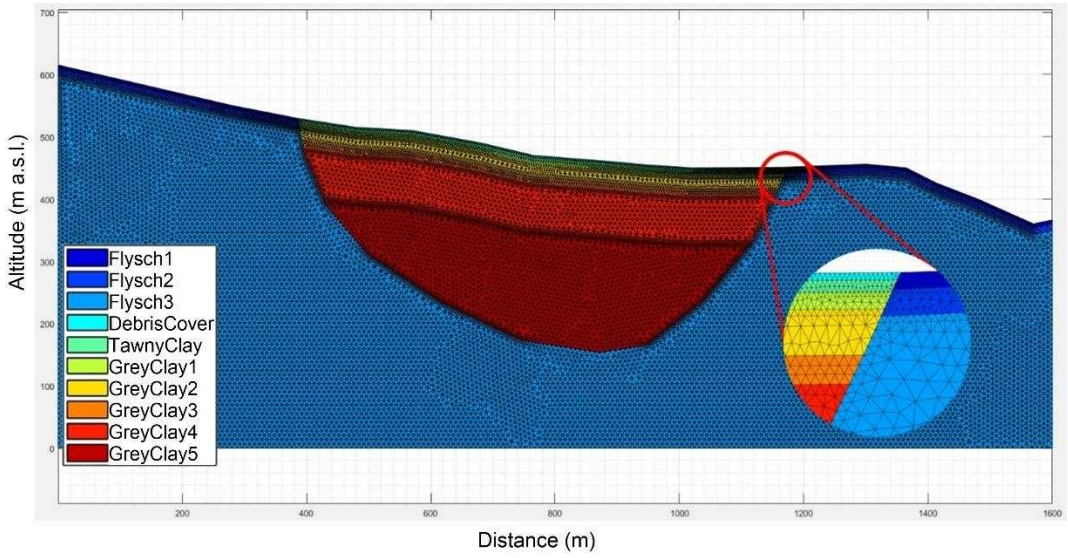

Figure B.8. Adopted mesh for the "Basin" model employed for 2-D QUAD4M analyses.

Using both the mean and median spectra for all the considered events, results are graphically reported in Figure B.9 and their corresponding statistical indicators are

shown in Table B.9. In the same figure, even the mean spectra as obtained from 1-D analyses are reported. A strong overestimation of the spectra with the “Basin” model at the deeper station level is observed, while a good agreement with the recordings is noticed at the surface, but only for periods higher than 0.3 s, as it happens for the previous “Anvil” model. Overall, from what above-mentioned, it seems, therefore, that initial soil stiffness rather than details in bedrock geometry plays a major role in governing the seismic response of the village of San Giuliano di Puglia. The good performance showed by mono-dimensional analysis applying recordings at -53 m from g.l. (Figure B.7 and Figure B.9) could suggest that the use of their deconvolution as input motions, could offer more satisfactory results.

APPENDIX B.

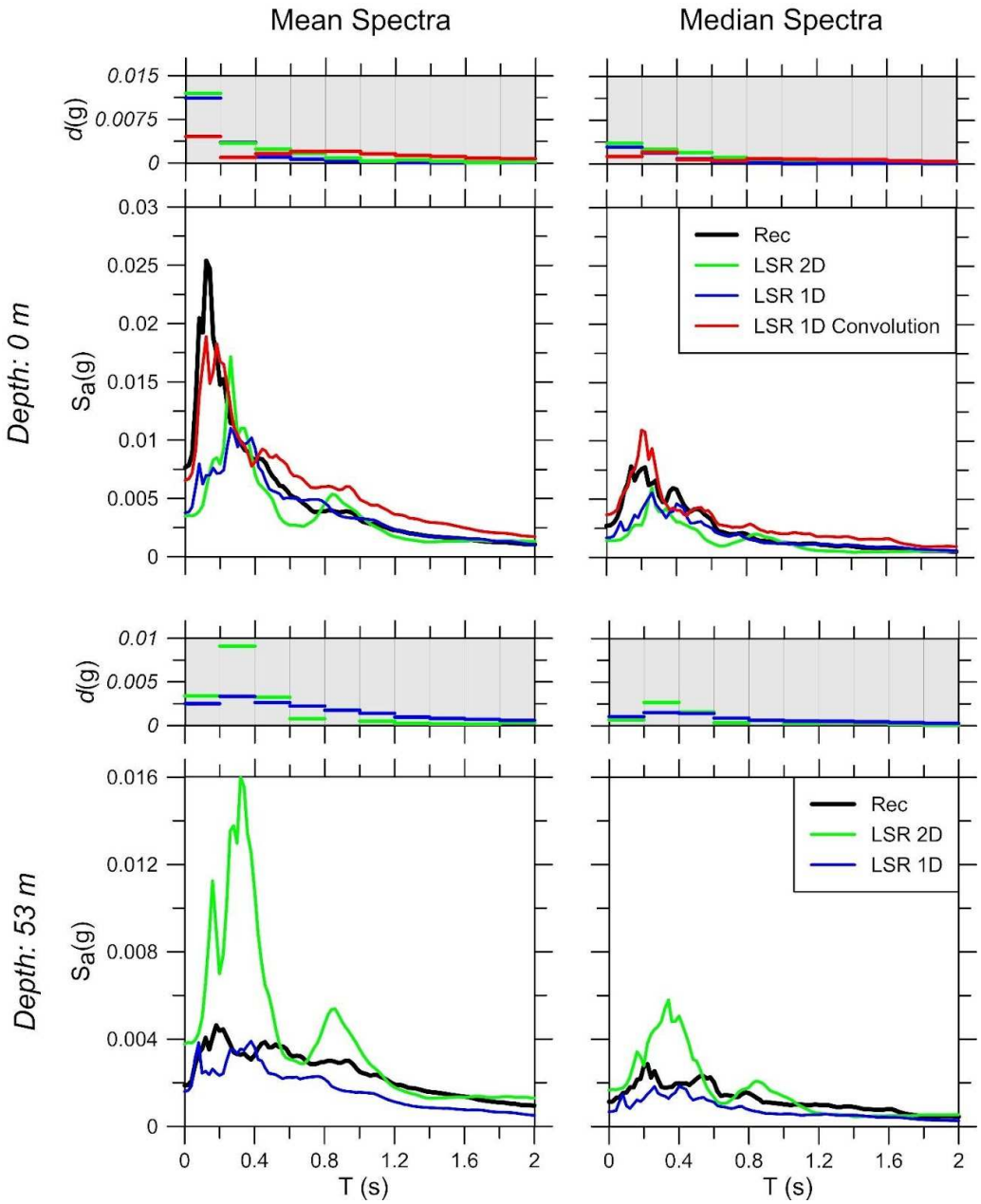

Figure B.9. Comparison between the mean and median, computed and measured response spectra for 1-D and 2-D analyses at the SGPA site at -53 m from g.l. and on the surface, using a "Basin" shape geometry of the subsoil and the updated geotechnical model.

APPENDIX B.

Table B.9. Statistical parameters showing differences between predicted and recorded signals along the vertical SGPA at level -53 m and 0 m using the 2-D "Basin" with updated geotechnical parameters.

ID	2-D updated model							
	-53 m from g.l.				Surface			
	d ($g \times 10^{-3}$)	D_{rms} (-)	MAE ($g \times 10^{-3}$)	S (-)	d ($g \times 10^{-3}$)	D_{rms} (-)	MAE ($g \times 10^{-3}$)	S (-)
GM1	0.704	0.088	0.646	0.673	2.246	0.045	1.706	0.763
GM3	0.536	0.069	0.237	0.855	0.724	0.055	0.340	0.360
GM4	1.219	0.073	0.608	0.678	1.579	0.059	0.890	0.408
GM5	1.578	0.074	1.146	0.635	1.456	0.099	1.121	0.328
GM6	0.871	0.119	0.537	1.210	0.584	0.059	0.422	0.405
GM7	4.028	0.107	2.353	0.937	2.259	0.058	1.555	0.254
GM8	0.700	0.124	0.431	1.242	0.341	0.050	0.242	0.262
GM9	0.594	0.063	0.377	0.798	0.691	0.064	0.425	0.364
GM10	1.939	0.057	0.974	1.180	3.489	0.089	1.380	0.399
GM11	6.018	0.093	2.954	1.113	7.990	0.081	3.771	0.362
GM12	14.810	0.080	7.237	1.202	26.053	0.092	11.012	0.379
GM13	9.565	0.065	5.004	1.801	8.971	0.080	3.980	0.373
Average	3.547	0.084	1.875	1.027	4.699	0.069	2.237	0.388
Median	1.399	0.077	0.810	1.025	1.913	0.062	1.251	0.368

In Figure B.10, the mean and median acceleration response spectra obtained from bi-dimensional analyses only are compared to those resulting from recordings and two different morphologies of the buried geometry are considered. In addition, with reference to the "Anvil model" both the shear wave velocity profiles considered in this study are taken into account. At the depth of -53 m from g.l. the best agreement is given by the use of the Anvil model with updated geotechnical parameters; at the same time, a strong overestimation is generated by the Basin Model up to 0.5 s which is going to attenuate as the period increases, showing also a good performance in the higher range of periods. This could be due to focalization effects related to the basin shape. Considering acceleration response spectra at the location of the surficial sensor, despite an underestimation that takes place for all the models in the lower periods range (0÷0.3 s), the best performance seems to be shown by the Basin model as well as the Anvil one with updated parameters. This suggests once more the need to reconsider the consensus

geotechnical model of the town in terms of shear stiffness. In addition, the inability of the models to catch the seismic response at lower periods could be related to the lateral heterogeneity of the main section of San Giuliano di Puglia as it was stressed in Fierro et al. (2019), where the comparison between Anvil model with both old and updated parameters was already pointed out.

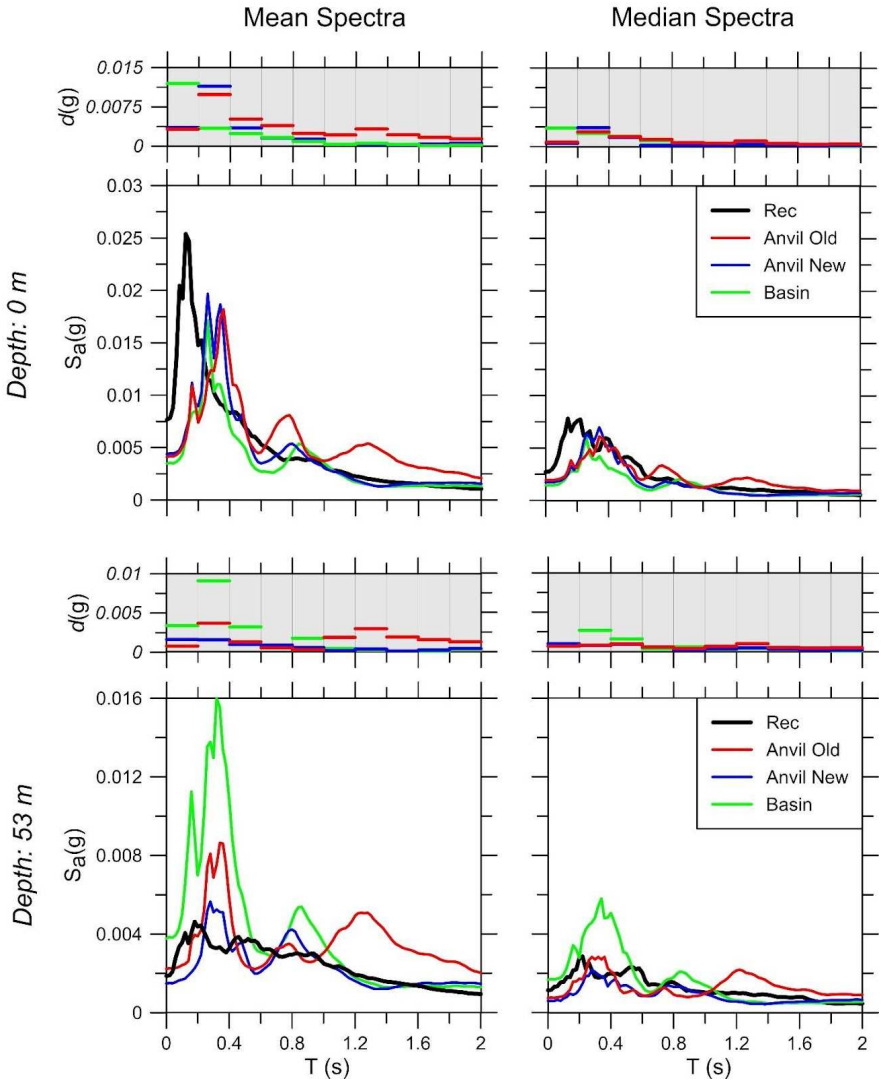

Figure B.10. Comparison between the averaged and median, computed and measured response spectra for 2-D analyses at SGPA site at -53 m from g.l. and at the surface, using "Anvil" and "Basin" shape geometry of the subsoil with old and updated geotechnical parameters.

B.3 REFERENCES

Acunzo G., Pagliaroli A. and Scasserra G. (2014). In-Spector: a software for supporting the selection of natural spectrum-compatible accelerograms for geotechnical and structural analyses (in Italian). 33° Convegno Nazionale GNGTS, Bologna 25- 27 November 2014, volume 2, 107-114, ISBN 978-88-940442-2-5.

Afshari K. and Stewart J.P. (2019). Insights from California Vertical Arrays on the Effectiveness of Ground Response Analysis with Alternative Damping Models. Bulletin of the Seismological Society of America 109 (4): 1250-264.

Bonilla L. F., Steidl J. H., Gariel J.-C. and Archuleta R. J. (2004). Borehole response studies at the Garner Valley Downhole Array, Southern California. Bull. Seismol. Soc. Am., 92(8), 3165–3179.

Cabas A. and Rodriguez-Marek A. (2017). What Can We Learn from Kappa (κ) to Achieve a Better Characterization of Damping in Geotechnical Site Response Models? Geotechnical Frontiers 2017: Seismic Performance and Liquefaction. GSP 281.

Fierro T., Mignelli L., Scasserra G., Pagliaroli A. and Santucci de Magistris F. (2019). Key role of soil investigation and monitoring for the assessment of site effects for the village of San Giuliano di Puglia (CB), Italy. In VII International Conference on Earthquake Geotechnical Engineering, Rome, Italy, paper n.10120.

Fierro T., Mignelli L., Scasserra G., Pagliaroli A. and Santucci de Magistris F. (2020a). The use of seismic records for updating the geotechnical model for a site in San Giuliano di Puglia (Italy). VI CNRIG Italian Conference of Researchers in Geotechnical Engineering, Lecco, Italy, July 2019.

Fierro T., Mignelli L., Scasserra G., Pagliaroli A. and Santucci de Magistris F. (2020b). Updating the Site Response Analyses at San Giuliano di Puglia (CB), Italy. Italian Geotechnical Journal, 2020(4), pp. 5-40.

Hudson M.B., Beikae M. and Idriss I.M. (1994). QUAD4M, a Computer Program to Evaluate the Seismic Response of Soil Structures Using Finite Element Procedures

and Incorporating a Compliant Base. Center for Geotechnical Modeling, Department of Civil and Environmental Engineering, University of California, Davis.

Idriss I.M. and Sun J.I. (1992). Shake91: A computer program for conducting equivalent linear seismic response analysis of horizontally layered soil deposits. User's Guide. Center for Geotechnical Modeling, Civil Engineering Department, UC Davis.

Kaklamanos J., Bradley B.A., Thompson E.M. and Baise L.G. (2013). Critical parameters affecting bias and variability in site-response analyses using KiK-net downhole array data. Bulletin of the Seismological Society of America, 103: 1733-1749.

Kottke A.R., Wang X. and Rathje E.M. (2013). Technical Manual for Strata. Geotechnical Engineering Center Department of Civil, Architectural, and Environmental Engineering, University of Texas.

Lanzo G. and Pagliaroli A. (2009). Numerical Modeling of Site Effects at San Giuliano di Puglia (Southern Italy) during the 2002 Molise Seismic Sequence. J. of Geotech. and Geoenviron. Eng., ASCE.

Pecker A. (1995). Validation of small strain properties from recorded weak seismic motions. Soil Dynamics and Earthquake Engineering 14 (6): 399-408 (1995).

Puglia R. (2008). Analysis of the local seismic response of San Giuliano di Puglia (in Italian). Ph.D. Thesis in Geotechnical Engineering, Universiy of Calabria.

Schnabel P.B., Lysmer J. and Seed H.B. (1972). SHAKE - A computer program for earthquake analysis of horizontally layered sites. Earthquake Engineering Research Center, University of California, Berkeley, Report No. EERC 72-12.

Steidl J. H., Tumarkin A. G. and Archuleta R. J. (1996). What is a reference site? Bull. Seism. Soc. Am. 86, 1733–1748.

Stewart J.P. and Kwok A.O. (2008). Nonlinear seismic ground response analysis: code usage protocols and verification against vertical array data. ASCE Geotechnical Special Publication No. 181, Geotechnical Engineering and Soil Dynamics IV, Sacramento, CA.

APPENDIX B.

Stewart J.P., Afshari K. and Hashash Y.M.A. (2014). Guidelines for performing hazard-consistent one- dimensional ground response analysis for ground motion prediction. In: PEER Report 2014.

Tao Y. and Rathje E.M. (2019). Insights into Modeling Small-Strain Site Response Derived from Downhole Array Data. Journal of Geotechnical and Geoenvironmental Engineering 145 (7): 04019023.

Thompson E., Baise L., Kayen R. and Guzina B. (2009). Impediments to predicting site response: Seismic property estimation and modelling simplifications. Bull. Seismol. Soc. Am., 99(5), 2927–2949.

Yee E., Stewart J.P. and Tokimatsu K. (2013). Elastic and large-strain nonlinear seismic site response from analysis of vertical array recordings. ASCE, J. Geotech. Eng., 139(10): 1789–1801.

Zalachoris G. and Rathje E. M. (2015). Evaluation of one-dimensional site response techniques using borehole arrays. J. Geotech. Geoenviron. Eng. 141 (12): 04015053. https://doi.org/10.1061/(ASCE)GT.1943 -5606.0001366.

APPENDIX C. SOME NOTES ON THE ROLE OF SOIL DAMPING IN SEISMIC RESPONSE ANALYSES

It is well-known that a key role for a reliable site response analysis is played by the soil damping. The latter can be assigned in different manners, such as through damping curves or it can be deduced hysteretically from τ-γ loops in nonlinear analysis. In order to consider damping even at low strain levels, the Rayleigh formulation is adopted to add numerical damping to the models. Obviously, the choice depends on the selected analysis approach.

To this aim, a research work was developed over the years to try to understand the different sources of soil damping. In this framework, the importance of the vertical arrays, which are rapidly increasing in number as time goes on, is highlighted because they represent a vital tool to back-analyze the recorded data and have been revealed a precious source of information. In fact, data coming from vertical arrays evidenced that wave scattering definitely influence the site response of a soil deposit and this aspect should be considered in the implementation of a numerical model. Due to its own nature, laboratory procedures to evaluate small strain-damping cannot account for the wave scattering effects that develop in the field. Consequently, an overestimation of the measured response of the site could occur, in some cases, if the laboratory-based small-strain damping is adopted. A wide body of research was developed to quantify the additional low-strain damping to be introduced to numerically reproduce the phenomenon and, as it has been just mentioned, data from array recordings in well-characterized sites were analyzed in detail. For example, Tao and Rathje (2019) suggest multiplying the "laboratory-based" low-strain damping D_0 by a factor between 1.5 and 5.5, in order to improve the consistency of recordings and simulations. Afshari et al.

(2019) underlined that the adoption of laboratory-based damping models leads to an overestimation of the observed data provided by simulations because site attenuation is, in turn, underestimated. Zalachoris and Rathje (2015) also observed a better fit obtained with higher damping than that estimated considering the Darendeli (2001) laboratory-based model. Pecker (1995) selected D_0 values considered reasonable to build his model, concluding that a rate-dependent low-strain damping ratio is needed to try to take into account for wave scattering effects. Kaklamanos et al. (2013) critically analyzed the response obtained using both linear and equivalent linear approaches highlighting that adopting the former, modulus reduction and damping curves are based on peak strain, which is, in turn, dependent on the long-period ground motion, leading to inaccuracy in the short-period ground-motion predictions. Otherwise, Yee et al. (2013) proposed to increase the laboratory-based low-strain damping by a quantity falling in a range of 2% and 5% with a view to capturing recorded motion data; on the contrary, Stewart and Kwok (2008) did not observe the necessity to increase D_0 to reach a better fit, while Stewart et al. (2014) considered appropriate, in some cases, even an additional low-strain level damping between 0% to 5%. Other studies (see, for instance, Cabas and Rodriguez-Marek, 2017; Ktenidou et al., 2015) discussed the differences observed in the site response analyses where vertical arrays are available, considering both the site-specific decay parameter κ_0 and the laboratory-based models to define soil damping.

Considering this wide research body, in the case-study proposed in Appendix B, the amplification obtained in mono-dimensional simulations considering the "Within" motion option could be related to an underestimation of the low-strain soil damping.

On the other hand, it is worth noting that some studies (see, for example, Bonilla et al., 2002; Thompson et al., 2009) have demonstrated that sometimes a better fitting between simulated and recorded signals is observed considering the upward propagating wave only (i.e., the condition simulated adopting the "Incoming" motion option in Strata), rather than both upward and downward propagating waves ("Within" motion option in

Strata), even if the downward propagating wave is certainly recorded by the sensor. They stated that this phenomenon could be connected to the limited assumptions in the theoretical formulation rather than the uncertainties proper of the soil properties definition. Furthermore, the basic problem is related to the definition of a "laboratory-based" damping curve. All the referenced studies use empirical relationships (e.g., Darendeli, 2001; Menq, 2003; Zhang et al., 2005, etc.), certainly calibrated on a large amount of laboratory tests. On the contrary, in this research, a wide number of laboratory tests (resonant column and cyclic torsion tests) were specifically conducted to evaluate the damping curves D-γ and the low-strain damping ratio D_0. Therefore, for the sake of exhaustiveness, low-strain damping in the middle of each unit is calculated adopting the Darendeli (2001) formulation. It emerged that at low-strain level, the curves obtained by d'Onofrio et al. (2009) always overlie those calculated on the basis of the above-mentioned Darendeli (2001) formula. In the following Figure C.1, Figure C.2 and Figure C.3, the comparison just described is shown for debris cover, tawny clay and grey clay, respectively.

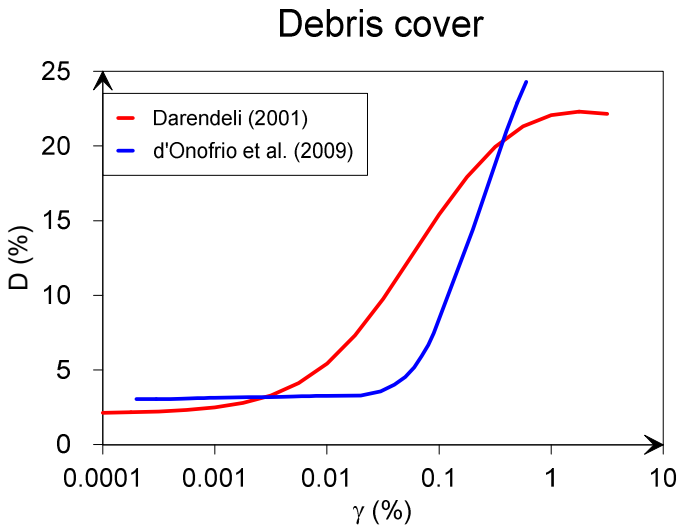

Figure C.1. Comparison between damping curves obtained by laboratory tests (blue curve; d'Onofrio et al., 2009) and by adopting the Darendeli (2001; red curve) formula for debris cover.

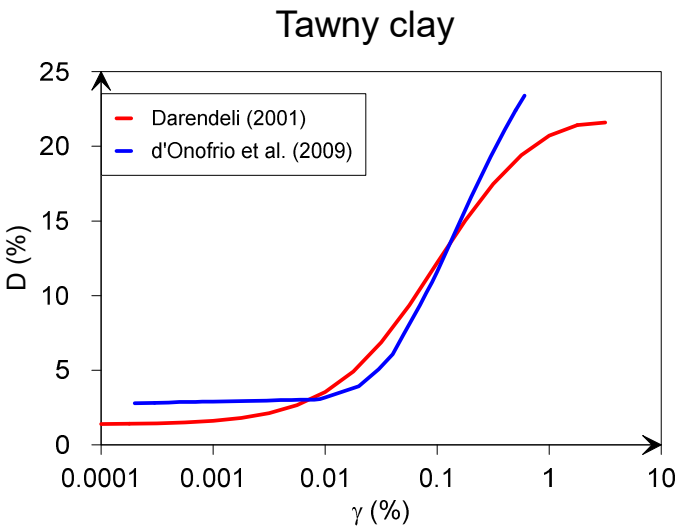

Figure C.2. Comparison between damping curves obtained by laboratory tests (blue curve; d'Onofrio et al., 2009) and by adopting the Darendeli (2001; red curve) formula for tawny clay.

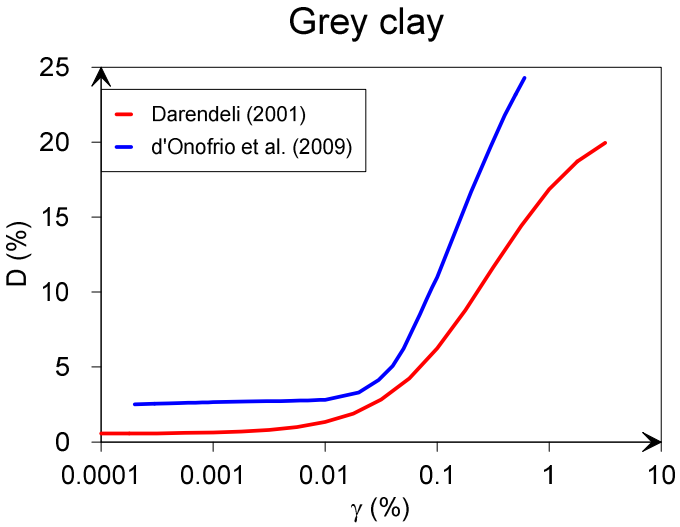

Figure C.3. Comparison between damping curves obtained by laboratory tests (blue curve; d'Onofrio et al., 2009) and by adopting the Darendeli (2001; red curve) formula for grey clay.

For these reasons, in this study, the damping properties obtained from laboratory tests, directly, are adopted without any additional damping, considering also the results provided by the bi-dimensional analysis, which allows overcoming the strong

overestimation of the recorded motions observed in the mono-dimensional analyses adopting the “Within” motion option.

C.1 REFERENCES

Afshari K. and Stewart J.P. (2019). Insights from California Vertical Arrays on the Effectiveness of Ground Response Analysis with Alternative Damping Models. Bulletin of the Seismological Society of America 109 (4): 1250-264.

Bonilla L. F., Steidl J. H., Gariel J.-C. and Archuleta R. J. (2002). Borehole response studies at the Garner Valley Downhole Array, Southern California. Bull. Seismol. Soc. Am., 92(8), 3165–3179.

Cabas A. and Rodriguez-Marek A. (2017). What Can We Learn from Kappa (κ) to Achieve a Better Characterization of Damping in Geotechnical Site Response Models? Geotechnical Frontiers 2017: Seismic Performance and Liquefaction. GSP 281.

d’Onofrio A., Vitone C., Cotecchia F., Puglia R., Santucci de Magistris F. and Silvestri F. (2009). Geotechnical Characterization of the San Giuliano di Puglia Subsoil. In Rivista Italiana di Geotecnica (Italian Geotechnical Journal) 3, 43 –61.

Darendeli M. B. (2001). Development of a new family of normalized modulus reduction and material damping curves. Ph.D. dissertation, Univ. of Texas at Austin, Austin, TX, 396.

Kaklamanos J., Bradley B.A., Thompson E.M. and Baise L.G. (2013). Critical parameters affecting bias and variability in site-response analyses using KiK-net downhole array data. Bulletin of the Seismological Society of America, 103: 1733-1749.

Ktenidou O.-J., Abrahamson, N.A., Drouet S. and Cotton F. (2015). Understanding the physics of kappa (κ): insights from a downhole array. Geophys. J. Int. 203, 678-691. doi: 10.1093/gji/ggv315.

Menq F.Y. (2003). Dynamic Properties of Sandy and Gravelly Soils. Ph.D. Thesis, Department of Civil Engineering, University of Texas, Austin, TX.

APPENDIX C.

Pecker A. (1995). Validation of small strain properties from recorded weak seismic motions. Soil Dynamics and Earthquake Engineering 14 (6): 399-408 (1995).

Stewart J.P. and Kwok A.O. (2008). Nonlinear seismic ground response analysis: code usage protocols and verification against vertical array data. ASCE Geotechnical Special Publication No. 181, Geotechnical Engineering and Soil Dynamics IV, Sacramento, CA.

Stewart J.P., Afshari K. and Hashash Y.M.A. (2014). Guidelines for performing hazard-consistent one- dimensional ground response analysis for ground motion prediction. In: PEER Report 2014.

Tao Y. and Rathje E.M. (2019). Insights into Modeling Small-Strain Site Response Derived from Downhole Array Data. Journal of Geotechnical and Geoenvironmental Engineering 145 (7): 04019023.

Thompson E., Baise L., Kayen R. and Guzina B. (2009). Impediments to predicting site response: Seismic property estimation and modelling simplifications. Bull. Seismol. Soc. Am., 99(5), 2927–2949.

Yee E., Stewart J.P. and Tokimatsu K. (2013). Elastic and large-strain nonlinear seismic site response from analysis of vertical array recordings. ASCE, J. Geotech. Eng., 139(10): 1789–1801.

Zalachoris G. and Rathje E. M. (2015). Evaluation of one-dimensional site response techniques using borehole arrays. J. Geotech. Geoenviron. Eng. 141 (12): 04015053. https://doi.org/10.1061/(ASCE)GT.1943 -5606.0001366

Zhang J., Andrus R. D. and Juang C. H. (2005). Normalized shear modulus and material damping ratio relationships. J. Geotech. Geoenv. Eng. 131, 453–4.